Contribution to the study and the modelling of the development of a boundary layer over a super-hydrophobic surface : experimental and numerical coupled approach

Marco Castagna

Centre Val de Loire UNIVERSITÉ Spirit of the Loire Valley

UNIVERSITÉ D'ORLÉANS

UNIVERSITE D'ORLEANS

ÉCOLE DOCTORALE ÉNERGIE, MATÉRIAUX, SCIENCES DE LA TERRE ET DE L'UNIVERS

LABORATOIRE PRISME

Thèse présentée par :

Marco CASTAGNA

soutenue le : **15 Novembre 2019**

pour obtenir le grade de : **Docteur de l'Université d'Orléans**

Discipline : **Mécanique des Fluides**

Contribution à l'étude et à la modélisation du développement d'une couche limite sur paroi super-hydrophobe : approche couplée expérimentale et numérique

Contribution to the study and the modelling of the development of a boundary layer over a super-hydrophobic surface: experimental and numerical coupled approach

THÈSE DIRIGÉE PAR :

Azeddine	**KOURTA**	Professeur, Université d'Orléans, PRISME

RAPPORTEURS :

Jacques	**MAGNAUDET**	Directeur de Recherche, CNRS, IMFT
Nicolas	**MORDANT**	Professeur, Université Grenoble Alpes, LEGI

JURY :

Jean-Christophe	**ROBINET**	Professeur, Arts et Métiers ParisTech, DYNFLUID Président du jury
Johannes	**BERNDT**	Chercheur HDR, Université d'Orléans, GREMI
Azeddine	**KOURTA**	Professeur, Université d'Orléans, PRISME
Jacques	**MAGNAUDET**	Directeur de Recherche, CNRS, IMFT
Nicolas	**MAZELLIER**	Maître de Conférences, Université d'Orléans, PRISME
Nicolas	**MORDANT**	Professeur, Université Grenoble Alpes, LEGI

A Giulia,
Mamma e Papà

First, inevitably, the idea, the fantasy, the fairy tale.
Then, scientific calculation.
Ultimately, fulfillment crowns the dream.

K. E. Tsiolkovskii

Contents

List of Figures

List of Tables

Nomenclature

ACRONYMS AND ABBREVIATIONS

2D	Two-Dimensional
3D	Three-Dimensional
AR	Aspect Ratio
BE	Backward Euler
BiCG	Bi-Conjugate Gradient
CAD	Computer-Aided Design
CDD	Charge Coupled Device
CFL	Courant-Friedrichs-Lewy
CG	Conjugate Gradient
CM	Conjugate Method
CMOS	Complementary Metal-Oxide Semiconductor
CN	Crank-Nicolson
DIC	Diagonal Incomplete Cholesky
DILU	Diagonal Incomplete LU
DNS	Direct Numerical Simulation
FE	Forward Euler
FFT	Fast Fourier Transform
FOST	Force Océanique Stratégique
FVM	Finite Volume Method
FWHM	Full Width at Half Maximum intensity
ISO	International Organization for Standardization
LED	Light-Emitting Diode

LES	Large-Eddy Simulation
MARPOL	Maritime Pollution
NC	Reference, No Coating
OF	OpenFOAM®
OMI	Organisation Maritime Internationale
PISO	Pressure Implicit with Splitting of Operators
PIV	Particle Image Velocimetry
PMMA	Poly(Methyl MethAcrylate)
PTFE	Polytetrafluoroethylene
PTV	Particle Tracking Velocimetry
PW	Pointwise®
RANS	Reynolds-Averaged Navier-Stokes
RSP	Reflectional Symmetry Preserving
SEM	Scanning Electron Microscopy
SH	Super-Hydrophobic
SK	Skewness
SLA	Stereolithography
SM	Smoothness
SNA	Sous-marin Nucléaire d'Attaque

GREEK SYMBOLS

χ	Aspect Ratio
δ	Boundary Layer Thickness, [m] (Ch. 6), Wave Amplitude, [m] (Ch. 7)
κ	Permeability, [m^2]
Λ	Wavelength, [m]
λ	Surface roughness size, [m]
μ	Dynamic Viscosity, [$kg\,m^{-1}\,s^{-1}$]
ν	Kinematic Viscosity, [$m^2\,s^{-1}$]
Ω	Rotation Rate, [$rad\,s^{-1}$]
ϕ	Porosity
ψ	Streamfunction

ρ	Density, [$\mathrm{kg\,m^{-3}}$]
Θ	Tortuosity
ϑ	Angle, [°]
ζ	Density Ratio

LATIN SYMBOLS

C_D	Drag Coefficient
Co	Courant Number
d	Diameter, [m]
f	Friction Coefficient (Ch. 7) or Frequency, [Hz] (Ch. 2)
G	Galileo Number
g	Acceleration due to Gravity, [$\mathrm{m\,s^{-2}}$]
L	Length, [m]
m	Mass, [kg]
$N_\perp$	Non-Orthogonality
p	Pressure, [Pa]
Re	Reynolds Number
Sc	Schmidt Number
St	Strouhal Number
T	Temperature, [°C] or [K]
t	Time, [s] (unless otherwise stated)
u	Velocity, [$\mathrm{m\,s^{-1}}$]
r	Radius, [m]
V	Volume, [$\mathrm{m^3}$]

SUBSCRIPTS AND SUPERSCRIPTS

∞	Terminal Conditions
A	Air
a	Advancing
b	Buoyancy
c	Capillary
cb	Cassie-Baxter

cr	Critical
err	Error
fl	Flat
h	Hysteresis
IP	Integration Point
L	Liquid
r	Receding
ref	Reference
ro	Roll-Off
S	Solid
s	Static
sl	Slip
tr	Transversal
w	Wall or Wenzel (Ch. 3)
wv	Wavy
x	Vector Field Component, x-direction
y	Vector Field Component, y-direction
z	Vector Field Component, z-direction

Résumé du Manuscrit

Ce travail de thèse présente des travaux originaux sur l'étude et la modélisation physique des surfaces dites super-hydrophobes que nous désignerons par le sigle SH dans toute la suite du mémoire. Grâce à leurs propriétés physico-chimiques, ces surfaces ont la capacité de piéger une fine pellicule d'air dans les rugosités créant ainsi un effet de glissement pariétal assimilable à un phénomène de lubrification. L'avènement de ces surfaces a été possible grâce aux formidables progrès technologiques réalisés depuis les années 1990 dans le domaine des sciences de matériaux. Les premières études portant sur l'influence des revêtements SH sur les écoulements fluides et les performances hydrodynamiques ont abouti à des résultats prometteurs qui ont largement contribué à la popularité de ces surfaces dans la communauté scientifique comme en témoigne le taux de croissance de publications sur ce sujet sur les vingts dernières années. Bien que de nombreux travaux aient été dédiés à l'interaction entre les revêtements SH et l'écoulement, plusieurs zones d'ombres restent encore à lever afin de proposer des modèles pertinents pour dimensionner et concevoir les surfaces SH optimales pour les futures applications à l'échelle industrielle. C'est tout l'enjeu de cette thèse de doctorat dont l'objectif principal est de contribuer à la description, la compréhension et enfin la modélisation des effets du développement d'une couche limite sur une paroi SH. Pour cela, le cœur de ce travail s'appuie sur une démarche expérimentale qui a ensuite été complétée par une approche numérique. La combinaison de ces outils nous a permis de proposer des modèles physiques originaux permettant d'expliquer les phénomènes que nous avons observés. Afin de faciliter la lecture du mémoire, celui-ci a été décomposé en huit chapitres, chacun abordant une problématique particulière. En complément, plusieurs annexes sont également fournies afin de traiter des points de détail. Dans la suite de ce résumé étendu, les principaux résultats et/ou sujets de chacun des chapitres sont décrits de manière générale. Les détails complets sont disponibles dans les chapitres rédigés en langue anglaise.

Le **Chapitre 1** est une introduction générale qui replace le contexte dans lequel ce travail de thèse a été réalisé. À l'origine, cette étude a été sélectionnée par la *Direction Générale de l'Armement* (DGA) dans la section thématique *Fluides et Structures*. L'intérêt de l'approche proposée trouve une application directe dans le domaine militaire sous-marin où la qualité des performances hydrodynamiques des bâtiments est un élément essentiel pour la furtivité, la manœuvrabilité et l'efficacité. Certaines de ces spécifications sont également applicables au domaine civil dans le transport de passagers, de fret ou de fluides, pour lesquels les normes environnementales deviennent de plus en plus contraignantes. En lien avec ces problématiques plus larges, nous avons obtenu un soutien financier complémentaire de la part du *Labex CAPRYSSES* de l'Université d'Orléans dont une des thématiques phares est dédiées au contrôle des écoulements pour la propulsion efficace et propre. L'amélioration des technologies dans le secteur des transports est donc un point fondamental pour répondre à ces problématiques d'actualité. En fait, l'interaction entre le véhicule et le fluide ambiant se traduit par l'apparition du phénomène de *couche limite* qui induit une force de *traînée* hydrodynamique opposée au mouvement. La compréhension du

mécanisme pilotant cette force et son intensité est à la base du développement de technologies visant son contrôle. Deux contributions à la traînée totale sont identifiées : une composante de *pression*, liée aux différentes propriétés de l'écoulement dans la partie avant et arrière du corps, et le *frottement*, lié aux efforts visqueux se développant tout au long de la surface mouillée du corps. Vue que la composante visqueuse peut représenter la partie dominante de la traînée totale dans des conditions opérationnelles réelles, sa réduction pourrait aboutir à une diminution de la consommation du combustible voir une augmentation de la vitesse du vaisseau. Parmi les méthodes de contrôle employées, nous nous intéressons ici à l'approche dite *bio-mimétique* qui consiste à s'inspirer et à reproduire à l'échelle humaine des techniques peaufinées par l'espèce animale et/ou végétale. Plus particulièrement, la modification de l'état de la surface du corps est une manière attractive pour contrôler l'interaction liquide-solide. L'enjeu est d'introduire un phénomène dit de *glissement* pariétal pour modifier profondément les propriétés de la couche limite. La nature regorge d'exemples où ce phénomène peut être observé. L'un des plus célèbres est la feuille de *Lotus* qui a développé des propriétés hydrophobes lui permettant de maintenir son état de propreté dans un milieu marécageux. Des analyses au microscope électronique ont montré que cette capacité dérive d'un couplage entre rugosité de surface et propriétés chimiques. En pratique, la reproduction artificielle des propriétés identifiées sur les feuilles de Lotus a été au centre du développement des revêtements SH. La facilité de glissement de l'eau sur cette surface pourrait conduire à des avantages non seulement en termes de réduction de frottement, mais aussi de ralentissement du bio-encrassement, du givrage et de la condensation du brouillard. Par ailleurs, une modification appropriée des propriétés de la couche limite par le biais de l'état de surface pourrait avoir des conséquences importantes sur le bruit hydrodynamique rayonné. Ces problématiques ont toutes en commun le taux de production de vorticité, élément central qui sera mis en avant tout au long du manuscrit.

Le **Chapitre 2** présente une vision globale de l'état de l'art dans le contexte spécifique de ce manuscrit. Notre travail se positionnant dans une démarche fondamentale, nous avons fait le choix d'utiliser un obstacle géométrique simple. La géométrie sphérique a été choisie comme prototype de corps non profilé représentatif d'un vaisseau se déplaçant dans un liquide. Pour démarrer la description de l'interaction entre sphère et écoulement, la section §2.1 est dédiée à la discussion du développement du sillage en aval d'une sphère fixe soumise à un écoulement uniforme. Les régimes caractéristiques de cette interaction sont classés en fonction du nombre de Reynolds (basé sur la vitesse de l'écoulement et sur le diamètre de la sphère), qui décrit l'importance relative entre effets inertiels et visqueux. La solution analytique de Stokes est présentée, à partir de laquelle une augmentation du nombre de Reynolds se traduit par la perte de la symétrie du sillage et de sa stationnarité. L'influence de la rugosité de surface est aussi discutée. Ensuite, le lien entre les transitions du sillage d'une sphère fixe et les instabilités de trajectoire d'une sphère en chute ou ascension libre est commenté dans la section §2.2. Le rapport entre les masses volumiques du corps solide et du liquide (indiqué par ζ) est identifié comme un paramètre fondamental gérant le comportement de la sphère. Tout cela permet d'introduire les équations généralisées de Kirchhoff dans la section §2.2.1 qui lient le mouvement du corps aux efforts hydrodynamiques instantanés agissants sur la sphère. Une fois rappelées ces notions de base, le chapitre se poursuit avec la section §2.3 en répertoriant les méthodes existantes pour le contrôle de l'écoulement autour d'un corps non profilé et de son sillage. Les efforts déployés dans les dernières décennies pour modifier favorablement l'état de la surface du corps sont présentés. Ensuite, l'attention est tournée dans la section §2.3.1 vers les techniques basées sur la création d'une couche d'air entre la paroi solide et le liquide. Les méthodes basées sur le phénomène de cavitation, l'injection de bulles d'air ou encore l'effet Leidenfrost sont introduites. Enfin, la description des études sur les surfaces SH disponibles dans la littérature permet de souligner les très gros efforts encore nécessaires pour pouvoir extrapoler les résultats prometteurs

à l'échelle du laboratoire vers les applications pratiques. De plus, nous montrons que les rares études expérimentales dédiées aux sillages de sphères SH mènent à des résultats qui peuvent sembler contradictoires. Quant aux approches numériques, elles sont pour la plupart basées sur des modèles simplistes loin d'être représentatifs de l'interaction entre l'écoulement et la paroi. Pour cette raison, le chapitre débouche sur une série de questions ouvertes auxquelles nous tentons de formuler une réponse à travers ce manuscrit.

Le **Chapitre 3** décrit les différents types de revêtements surfaciques en les classifiant vis à vis de leur capacité à être mouillés. Parmi ces revêtements, on trouve les surfaces SH basées sur l'instauration d'une couche d'air entre paroi solide et liquide. La section §3.1 présente les notions fondamentales pour la caractérisation de l'état d'une surface qui rentre en contact avec un liquide. Le concept macroscopique d'angle de contact statique est introduit pour distinguer les surfaces *hydrophiles* des surfaces *hydrophobes*. De plus, les modèles développés par Wenzel puis par Cassie et Baxter sont discutés pour clarifier les concepts d'états SH. L'approche macroscopique est ultérieurement suivie pour introduire les angles de roulement et d'hystérésis, qui permettent de quantifier la motricité d'une goutte d'eau déposée sur la surface. L'attention est ensuite portée dans la section §3.2 vers les techniques existantes pour produire les revêtements SH. Dans cette thèse, une approche basée sur la création d'un substrat avec une rugosité souhaitée, qui est ensuite recouvert par un revêtement SH, est implémentée. La procédure de fabrication développée est basée sur une méthode de dépôt par spray qui est bien adaptée à des surfaces courbes de grandes dimensions (voir la section §3.2.1). Enfin, la section §3.3 constitue une partie importante de la caractérisation des revêtements produits, qui permet de quantifier certaines propriétés des surfaces qui seront utiles dans la discussion des performances hydrodynamiques. Ces essais ont été réalisés en partenariat étroit avec le Laboratoire GREMI de l'Université d'Orléans. La section débute par la description des essais au microscope digital. Des indications sur la gestion des différentes phases, allant des opérations préliminaires jusqu'au post-traitement, son fournies. La principale quantité identifiée est la taille caractéristique des éléments rugueux λ, présentée dans le Tab. 3.1. Dans cette étude, trois types de revêtements SH (SH-NAR, SH-220, SH-80) ont été utilisés et classifiés en fonction de la taille des particules des poudres employées pendant la procédure de fabrication. Ensuite, les essais au goniomètre digital sont présentés dans la section §3.3.2. Comme dans le cas des essais au microscope, les opérations préliminaires, la phase de test et le post-traitement des données sont discutés. Les difficultés à surmonter afin de parvenir à des résultats fiables sont détaillées. En règle générale, les vidéos enregistrées pendant les essais au goniomètre ont été analysées *a posteriori* avec des codes développés en MATLAB®. Les résultats principaux en termes d'angles de contact macroscopiques sont résumés dans le Tab. 3.3. Ils révèlent une diminution de l'effet SH suite à une augmentation de λ, ainsi qu'une faible dépendance au type de fluides employés pendant les essais, à savoir, de l'eau distillée et de la glycérine.

Le **Chapitre 4** décrit le montage expérimental conçu et construit pour exécuter les essais de sphère en chute libre. La section §4.1 présente les différents éléments qui ont orienté le choix des dimensions du réservoir ainsi que les configurations optiques. Ce choix résulte d'un compromis entre la hauteur de chute, la résolution spatiale et les coûts de fabrication et de fonctionnement. La procédure expérimentale qui a été adoptée est décrite dans la section §4.1.2. De nombreux tests ont été réalisés afin d'optimiser la qualité des résultats. Les équations fondamentales utilisées pour prédire le mouvement de la sphère en chute libre sont détaillées dans la section §4.2. Le montage expérimental que nous avons développé permet d'accéder au mouvement tridimensionnel (3D) résolu dans le temps de la sphère. Le lien entre ce mouvement et les forces hydrodynamiques qui s'exercent à chaque instant sur la sphère est obtenu au travers des équations généralisées de Kirchhoff comme décrit dans la section §4.2.1. Les hypothèses utilisées

pour simplifier les équations du mouvement ont été validées par confrontation avec les essais expérimentaux. La description de la chute verticale d'une sphère nécessite toutefois l'introduction d'une loi du coefficient de traînée C_D en fonction du nombre de Reynolds, dont le choix est discuté dans la section §4.2.2. Ensuite, la section §4.2.3 introduit deux outils utilisés tout au long du manuscrit : *(i)* un modèle de type exponentiel permettant d'approximer le profil temporel de vitesse verticale u_z, *(ii)* le temps et la vitesse caractéristiques de la chute, t_D et u_D, qui seront utilisés pour normaliser les résultats. Toutes ces notions permettent de justifier dans la section §4.3 le choix des propriétés des sphères et liquides analysés. La Fig. 4.14 présente une vue d'ensemble de la très large gamme de nombre de Reynolds étudiée dans le cadre de ces travaux et qui à notre connaissance est unique au vu de la littérature disponible. Ceci a été possible grâce à l'utilisation d'une large gamme de diamètre d des sphères ainsi qu'à l'emploi de plusieurs mélanges eau-glycérine. Pour ces derniers, une procédure spécifique de fabrication a été développée. Les propriétés des mélanges obtenus en fonction de paramètres tels que la température ou les fractions volumiques sont résumées. En particulier, une discussion concernant le temps de repos entre deux essais consécutifs est proposée sur la base des propriétés physiques des mélanges ainsi que du régime d'écoulement. Ce point important nous assure la reproductibilité des essais.

Le **Chapitre 5** discute les techniques implémentées dans MATLAB® pour post-traiter les vidéos enregistrées pendant les essais de sphère en chute libre, qui se résument à une séquence d'images à partir desquelles le mouvement de la particule peut être déduit. Dans le cadre de ces travaux, nous avons développé un code de calcul capable d'estimer le déplacement de la sphère entre deux images consécutives, afin d'obtenir la reconstruction de la trajectoire 3D résolue dans le temps. Cet outil s'inspire très largement des méthodes de type *Particle Image Velocimetry* (PIV). Les principales étapes de calcul sont résumées dans la section §5.1. Le code est basé sur une technique d'inter-corrélation, implémentée dans MATLAB® à travers une approche du type *Fast Fourier Transform* (FFT). Le pre-traitement des images permet de supprimer de l'analyse tous les objets fixes tout en réduisant le bruit. Cette étape est suivie par la détection préliminaire de la position de la sphère dans l'image, qui permet de définir une fenêtre de corrélation de taille réduite par rapport à l'image originale. Il est à noter qu'une technique dite de *padding* est implémentée dans le cas où la fenêtre de corrélation dépasserait les limites de l'image analysée. L'inter-corrélation est ensuite réalisée entre deux fenêtres sur deux images consécutives. Le pic de corrélation permet d'identifier le déplacement instantané de la sphère. Afin d'obtenir une précision spatiale sous-pixel, une fonction bidimensionnelle Gaussienne est ajustée sur le pic de corrélation au sens des moindres carrés. La section §5.2 traite de la validation du code au moyen d'images synthétiques reproduisant artificiellement le mouvement vertical d'une sphère en chute libre. La comparaison entre le mouvement imposé et le mouvement estimé révèle des erreurs relatives sur la position instantanée inférieures à 0.3 %. De plus, une robustesse satisfaisante eu égard à l'augmentation du bruit dans les images analysées est évaluée. À partir de l'estimation du déplacement de la sphère, sa vitesse et son accélération peuvent être calculées comme décrit dans la section §5.3. Ces quantités dérivées sont fondamentales pour la comparaison des performances hydrodynamiques des sphères. Toutefois, l'opération de dérivation s'accompagne d'une augmentation du bruit qui peut pénaliser l'analyse physique. Il était donc nécessaire de proposer une voire des méthodes de filtrage afin de réduire l'influence de ce bruit. La première technique testée est une dérivation basée sur un schéma centré de différences finies. Cela donne lieu à une estimation fiable des vitesses mais à une valeur excessive du bruit de mesure sur les accélérations. La solution identifiée est un filtrage *a posteriori* des profils d'accélération afin de réduire l'effet du bruit de mesure. Toutefois, le défaut principal de cette approche repose sur l'utilisation de réglages du filtre définis par l'utilisateur et donc perfectibles. Pour pallier à ce défaut, nous avons porté notre choix sur une technique plus robuste basée sur l'estimation d'une *spline* optimale pour représenter la position instantanée de la sphère. Le compromis entre précision et *rugosité*

de la spline permet d'identifier les conditions optimales. Le processus de dérivation temporelle est donc effectué directement sur la spline identifiée, limitant ainsi l'amplification du bruit de mesure. Grâce à cette technique implémentée, l'incertitude relative sur la vitesse terminale reste inférieure à 1 %.

Le **Chapitre 6** constitue le cœur des résultats expérimentaux de ce manuscrit, qui sont organisés en fonction du régime de chute étudié. La section §6.1 est dédiée à l'analyse des résultats dans le régime des faibles Reynolds, obtenus en utilisant de la glycérine pure. Les limites du montage expérimental quand un liquide à viscosité dynamique élevée est utilisé sont soulignés, ainsi que les méthodes utilisées pour comprendre leur influence sur les résultats présentés. De manière surprenante, la Fig. 6.7 montre que, dans ce régime, les revêtements SH ne conduisent pas à un effet notable sur la traînée en conditions terminales par rapport aux sphères de référence. Ceci contredit les prédictions théoriques et numériques disponibles dans la littérature et pour lesquelles la présence de la couche d'air devrait donner une réduction significative de la traînée. Fort de ce constat, nous avons proposé une analyse détaillée des mécanismes physiques pouvant être à l'origine de ce phénomène (voir Annexe D). Sur cette base, le mécanisme le plus probable se révèle être lié à la résistance visqueuse induite par l'écoulement d'air au sein des rugosités de la surface SH. Afin de le quantifier, la section §6.1.2 présente le développement d'un modèle de type milieux poreux isotrope dont l'élément original est l'introduction de la tortuosité comme paramètre clé. Ce modèle est ensuite validé grâce à une confrontation avec les quelques données expérimentales disponibles dans la littérature. Cette comparaison se révèle prometteuse et nous encourage à poursuivre dans cette direction dans le futur.
La section §6.2 est ensuite dédiée à la discussion des résultats obtenus pour une gamme de Reynolds intermédiaires (mélanges eau-glycérine). L'élément central de cette partie est l'étude de la transition du sillage de la sphère. En effet, alors que dans les conditions terminales les revêtements SH ne produisent pas des modifications significatives de la traînée, ils semblent avoir un impact important sur le déclenchement des instabilités du sillage. Ces dernières sont identifiables dans la phase transitoire à travers l'étude du mouvement transversal de la sphère. Là encore, nos résultats sont très surprenants puisqu'ils vont à l'encontre des études numériques basées sur une hypothèse d'interface air-liquide non-déformable. L'observation expérimentale du *plastron*, dont un exemple typique est fourni sur la Fig. 6.18, montre très clairement que cette hypothèse n'est pas valide pour des nombres de Reynolds suffisamment élevés. À partir de nos essais, nous avons introduit un autre paramètre sans dimension, le nombre de Weber, afin de quantifier la réceptivité de la couche d'air aux perturbations hydrodynamiques caractérisées par le nombre de Reynolds. Au final, nous observons un couplage potentiel entre ces deux phénomènes qui se traduit par un déclenchement des instabilités à des nombres de Reynolds critiques plus faibles que dans le cas de référence. Ce processus est en accord, au moins qualitativement, avec des résultats très récents de la littérature.
Enfin, la section §6.3 discute les résultats à nombre de Reynolds élevés, obtenus avec des essais dans l'eau. Dans ce régime, les phénomènes détectés avec les essais à nombres de Reynolds intermédiaires sont amplifiés. Une déformation macroscopique de la couche d'air est mise en évidence dans les séquences d'images en Figs. 6.26 et 6.27. Des indications préliminaires pour approfondir l'étude de cette déformation sont discutées. La section §6.3.2 montre que les performances hydrodynamiques dépendent étroitement de la déformation relative de la couche d'air par rapport à la dimension de la sphère. La Fig. 6.38 souligne que les revêtements SH favorisent les instabilités de trajectoire, mais avec une intensité différente en fonction de la déformation relative de la couche d'air. Ces résultats sont ensuite liés en Fig. 6.39 aux effets sur la traînée à conditions terminales. Une grande déformation relative se traduit par une augmentation de traînée, alors qu'une déformation relative plus faible conduit à une réduction de traînée. Nous avons proposé un modèle original reliant le nombre de Weber et la déformation relative du plastron (voir Eq. 6.56). Comme

le montre la Fig. 6.43, cette approche permet d'unifier les résultats disponibles dans la littérature et qui jusque là étaient en désaccord.
Le chapitre est terminé avec une discussion globale dans la section §6.4, où un processus de boucle fermée est présenté afin d'expliquer l'interaction entre la perturbation hydrodynamique due au sillage et la réceptivité de la couche d'air à cette perturbation. La déformation de la couche d'air pourrait alors induire une modification de la production de vorticité à la paroi, conduisant à une variation de la vorticité évacuée par le sillage et donc à une modification des propriétés de ce dernier. On fait ici un lien direct avec le concept de rayonnement du bruit généré par l'interaction de l'écoulement avec un obstacle solide.

Le **Chapitre 7** présente les résultats d'une approche numérique utilisée pour compléter les essais expérimentaux décrits dans le chapitre précédent. L'objectif principal de cette approche est de pallier aux difficultés expérimentales dans l'analyse fine des phénomènes de proche paroi. La description du comportement d'un revêtement SH peut être menée par le biais de deux approches diamétralement opposées basées soit sur une description microscopique soit sur une description macroscopique. À l'échelle microscopique, on se focalise sur le comportement du système solide-air-liquide en considérant par exemple une seule rugosité sur la paroi SH. Cela implique la résolution d'un problème multiphasique, où la position instantanée de l'interface air-liquide doit être détectée en fonction des contraintes pariétales. Cette approche devient exigeante quand la description d'une surface SH de grandes dimensions est recherchée, en raison de l'ampleur de la gamme d'échelles à résoudre. C'est pour cette raison que nous avons fait le choix d'adopter une approche macroscopique (voir la section §7.1), avec le but final de parvenir à un modèle de longueur de glissement effective capable de prendre en compte les phénomènes qui peuvent influencer le glissement à la paroi. La section §7.2 est dédiée à la description du problème considéré, c'est-à-dire l'écoulement incompressible et laminaire dans un canal où la paroi inférieure est modélisée par une paroi SH. De plus, pour représenter la déformation de la couche d'air identifiée grâce aux essais expérimentaux, cette paroi présente une forme ondulée. Il est à noter que dans cette première approche le problème est traité dans un cas stationnaire (ondulation fixe), ce qui bien entendu ne reflète pas les observations expérimentales. Sur la paroi ondulée SH, le glissement est imposé à travers une condition aux limites de Navier, qui relie la vitesse de glissement au taux de cisaillement à travers la longueur de glissement. La Fig. 7.2 souligne que la gamme de variation de la déformation de la paroi dérive directement des résultats expérimentaux. De plus, les valeurs de la longueur de glissement sont choisies de façon à être représentatives d'applications macroscopiques réelles. La section §7.2.1 présente le développement de la solution analytique de l'écoulement de Poiseuille, qui est utilisée pour valider les résultats des simulations laminaires. Une vue d'ensemble des paramètres de contrôle des simulations exécutées est donnée dans la section §7.2.2 et résumée dans le Tab. 7.2. D'autres détails de l'approche numérique sont disponibles dans l'Annexe G. Ensuite, la section §7.3 montre que la formulation d'une longueur de glissement effective peut s'exprimer sous la forme d'une perte de charge équivalente. Cette dernière est obtenue au travers d'une approche intégrale, comme illustré dans la section §7.3.1. La perte de charge équivalente le long du volume de contrôle est estimée à travers l'évaluation du terme lié au taux de dissipation dans le bilan d'énergie cinétique. La section §7.4 présente les résultats des simulations effectuées. La Fig. 7.11 met en évidence que l'augmentation de l'ondulation de la paroi provoque une réduction de la longueur de glissement effective par rapport à la longueur de glissement imposée. Les variations entre les différentes valeurs de longueur de glissement analysées deviennent significatives quand une zone de recirculation apparaît dans les vallées de l'ondulation. Les effets de la déformation et du glissement sont ensuite étudiés séparément dans la section §7.4.2. En fonction de la déformation relative de la paroi par rapport à la hauteur du canal, des effets soit positifs soit négatifs sur la perte de charge sont obtenus. Au contraire, une augmentation de la longueur de glissement, à iso-déformation, est toujours

bénéfique en terme de réduction de perte de charge. L'analyse est ensuite ultérieurement affinée dans la section §7.4.3 en étudiant le poids relatif des différents termes qui apparaissent dans le bilan intégral de quantité de mouvement. L'augmentation de l'amplitude de l'ondulation accroît le poids du terme de pression au niveau de la paroi déformée. De plus, une influence de la paroi déformée sur la paroi opposée est détectée. Pour terminer l'analyse des résultats, une approche locale est décrite dans la section §7.4.4, en se focalisant sur les phénomènes qui se produisent dans les vallées de la paroi ondulée. En détail, l'augmentation de l'amplitude de la déformation favorise l'apparition d'une zone de recirculation. Le chapitre s'achève par une discussion globale des résultats présentés (voir la section §7.5).

Le **Chapitre 8** conclut ce manuscrit et propose des perspectives pour la poursuite future du travail. Rappelons que l'objectif principal de cette thèse était d'apporter une meilleure compréhension des effets du développement d'une couche limite sur une paroi SH, avec un intérêt particulier pour des applications macroscopiques sous-marines. Une première étape de production et caractérisation des revêtements SH a permis d'introduire et d'estimer les grandeurs fondamentales utilisées ensuite pour la discussion des performances hydrodynamiques. Les essais expérimentaux se sont concentrés sur la chute libre d'une sphère dans un liquide au repos. Les principaux résultats peuvent être résumés en fonction du régime de chute :

- à faible Reynolds, le mouvement transversal de la sphère en chute est négligeable et les revêtements SH ne montrent pas d'effets significatifs sur la traînée en conditions terminales. Un modèle en milieux poreux isotrope a été développé pour prendre en compte l'importance relative entre l'effet bénéfique dû à la présence de la couche d'air et l'effet négatif dû à l'interaction entre le mouvement de l'air et les éléments rugueux de la surface ;
- à Reynolds intermédiaire, les effets des revêtements SH sur la traînée terminale sont toujours négligeables. Au contraire, une apparition précoce du mouvement transversal est identifiée quand le sillage de la sphère perd son axisymétrie. Les instabilités hydrodynamiques sont susceptibles d'induire et d'interagir avec le mouvement et la déformation de la couche d'air initialement piégée dans les éléments rugueux. Deux nombres sans dimension sont identifiés pour décrire ce scénario : le nombre de Reynolds, qui quantifie l'importance de la perturbation hydrodynamique du sillage, et le nombre de Weber, qui décrit la réceptivité de la couche d'air à la perturbation ;
- à Reynolds élevé, un renforcement des phénomènes détectés à Reynolds intermédiaire est observé. L'apparition du mouvement transversal est favorisée par les revêtements SH. Cela se traduit soit par une augmentation soit par une réduction de traînée en fonction de la déformation relative de la couche d'air par rapport à la dimension macroscopique de la sphère.

En synthèse, nous avons proposé un scénario permettant de décrire l'interaction entre la couche d'air et l'écoulement. Quand la perturbation hydrodynamique due au sillage est significative, la réceptivité de la couche d'air peut conduire à sa déformation et son mouvement autour de la partie arrière de la sphère en chute libre. La variation de production de vorticité à la paroi peut donc influencer la vorticité évacuée par le sillage, avec un effet possible sur les propriétés du sillage lui-même.
Les essais expérimentaux ont été complétés par une approche numérique examinant un écoulement laminaire, incompressible dans un canal. Une description macroscopique de la paroi SH a été adoptée, avec une modélisation du glissement via une condition aux limites de type Navier et de la déformation de la couche d'air via une ondulation fixe de la paroi. L'objectif principal étant la formulation d'un modèle de longueur de glissement effective, un indicateur de performance basé sur le taux de dissipation à l'intérieur du volume de contrôle a été défini à travers

une approche intégrale. L'augmentation de la déformation de la paroi génère une réduction de la longueur de glissement effective. Pour approfondir l'analyse, une description séparée des effets du glissement et de la déformation a été proposée. En fonction de l'importance relative de la déformation de la paroi par rapport à la hauteur du canal, des effets soit positifs soit négatifs sur la perte de charge ont été observés. L'analyse a été enrichie en se focalisant ultérieurement sur le poids relatif des termes intégraux figurant dans le bilan de quantité de mouvement. Le terme de pression à la paroi ondulée gagne progressivement en importance suite à l'augmentation de l'amplitude de l'ondulation. Enfin, une approche locale a permis de souligner le rôle de l'apparition du décollement dans les vallées de l'ondulation sur les résultats présentés.
Plusieurs activités de recherche futures pourraient tirer avantage des résultats ici discutés.

- en premier lieu, une caractérisation plus exhaustive de la couche d'air en fonction des propriétés de la paroi SH semble nécessaire. Pour cela, une approche basée sur une méthode Schlieren pourrait être exploitée, comme fait d'habitude pour la détection de la surface dans des écoulements à surface libre. Pour ce faire, des images à haute résolution spatiale de revêtements SH non-opaques avec et sans couche d'air pourraient être utilisées pour estimer l'épaisseur de la couche d'air ;

- en second lieu, le modèle de tortuosité proposé en régime d'écoulements rampants pourrait être validé et étendu par des tests complémentaires en utilisant des moyens de fabrication adaptés (e.g. impression 3D) en suivant les essais préliminaires que nous avons réalisés (voir l'Annexe E) ;

- en troisième lieu, puisque les essais expérimentaux ont montré l'importance relative entre nombres de Reynolds et de Weber, la réalisation de tests dans un tunnel hydrodynamique pourrait faciliter le contrôle de ces deux paramètres de manière indépendante. L'analyse du sillage via PIV pourrait donner des informations intéressantes sur les effets SH, en complément des résultats discutés ici ;

- enfin, la modélisation présentée dans l'approche numérique pourrait être étendue vers des conditions opérationnelles plus réalistes, i.e. écoulement turbulent. Les lois d'échelle éventuellement obtenues pourraient aider au développement de modèles de surface SH pertinents, évitant ainsi une résolution complète du problème, qui implique la description d'un écoulement multiphasique avec des échelles allant de la texture microscopique jusqu'à la géométrie macroscopique du domaine de calcul.

Chapter 1

Introduction

A fleet of *Sous-marins Nucléaires d'Attaque* (SNA) is today essential to protect and support the French *Force Océanique Stratégique* (FOST) and the ensemble of land, naval and air forces (Ministère des Armées 2019). The current six SNA of *Rubis* class were designed during the 1970s and entered into service in the decade $1983 - 1993$, reaching or approaching today the end of their lifespan, initially set to 35 years of active service. For this reason, France launched in 1998 the design of a new SNA generation named *Barracuda*, which is going to progressively replace the Rubis class in the decade $2020 - 2030$. In fact, the *Suffren*, first submarine of the series, was recently unveiled in Cherbourg and is expected to undergo sea tests during 2020. The expected lifespan longer than 30 years, which engages the actors involved in the program at least until 2060, can be reached only via a continuous evolution and amelioration of the current state of the art technology. In detail, some of the key points raised during the design and development of a new submarines generation are (Joubert 2004):

- low vulnerability, which is connected to the ability of increasing both the maximum velocity for silent operations and the target detection;
- large manoeuvrability, which is someway linked to the control and the amelioration of hydrodynamic performance;
- costs containment, which, among others, is promoted by a longer permanence at sea with a reduced amount of necessary maintenance, still assuring an optimal efficiency until the end of the mission.

Interestingly, these points are strongly coupled with the interaction between the vessel and the surrounding flow, which is schematically shown in Fig. 1.1. The *boundary layer* is a thin region close to the body surface where strong velocity variations occur across a limited height in the direction normal to the surface, thus resulting into a dominance of viscous forces. This is physically due to the fact that a discontinuity between the local freestream and body velocities cannot exist: in the case of a standard surface, the relative velocity between flow and body must be zero at the wall. In the very first portion of the body nose the boundary layer is typically *laminar*, i.e. one layer of fluid slides smoothly over another at different velocity (Joubert 2004). However, this smooth configuration can usually be maintained only for a small portion of the body length, since *transition* to *turbulent* conditions occurs. Moreover, depending on the body shape, the flow can face a region of adverse pressure gradient (i.e. rising pressure in the direction of the flow), which could slow down the fluid inside the boundary layer until reverse flow is eventually reached. This is the so-called flow *separation*, which therefore impacts the characteristics of the

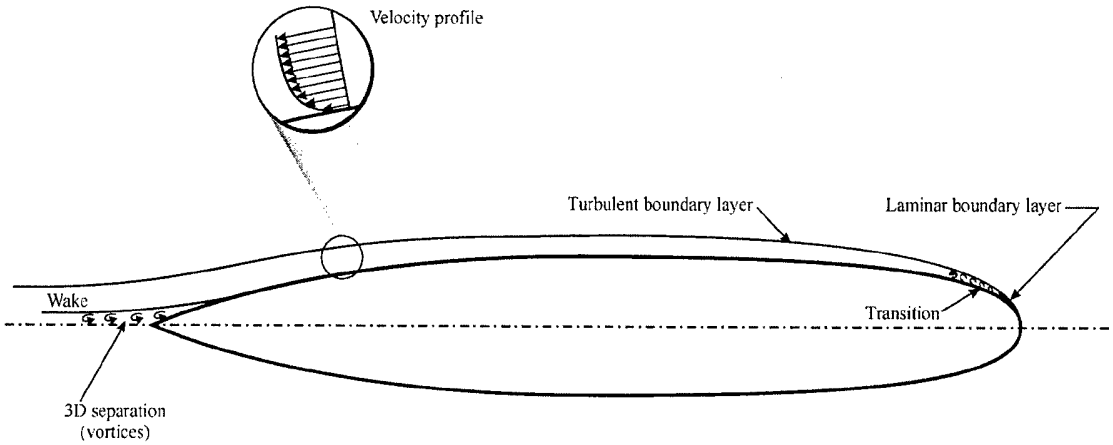

Figure 1.1 – Illustration of the boundary layer growth around a submarine shape (adapted from Joubert 2004). The flow goes from right to left (equivalently, the submarine moves from left to right.)

wake developing behind the body, thus affecting the hydrodynamic and acoustic fields. The evolution of the described scenario is affected by the *regime* of motion, which depends on the properties of both body and fluid, as well as on their relative velocity. This fact is exploited in the experimental campaigns of this study to analyse regimes characterised by different phenomena occurring in the near-wall region and in the body wake.

In the framework of acoustic supremacy, which implies acquiring information without being detected, the described body-flow interaction plays a key role in the capability to reduce the produced hydrodynamic noise. Every modification of the external surface state must therefore demonstrate to be efficient from this point of view, i.e. a possible new coating implementation has to demonstrate to be non-detrimental with respect to the noise generated by current adopted solutions. In this perspective, the description of the general hydro-acoustic problem of the noise generated by the interaction of a solid body with a turbulent flow is extremely challenging, due to the different length and energy scales of the hydrodynamic and acoustic problems (Khalighi *et al.* 2010). The commonly implemented numerical method consists in a hybrid approach where the two phenomena are described separately. To achieve that, a convenient technique in low Mach number flows (a non-dimensional number describing the magnitude of the flow velocity with respect to the local speed of sound), where the assumption of the absence of any acoustic field influence on the flow is made, relies on the Lighthill's analogy, which allows to represent a flow as an equivalent acoustic source term (Lighthill 1952). However, the relaxation of the cited assumption can be overcome by considering the *vorticity* as a convenient quantity to describe a low Mach number flow, which can be exploited to reach a *vortex sound* description of the problematic (Rienstra & Hirschberg 2019, Chapter 2). This formulation connects the modification of the total enthalpy of the flow with the vorticity variations, thus identifying the latter as the responsible of sound generation (Howe 2002, Chapter 5). No attempt is performed in this manuscript to provide a thorough discussion of the acoustic problematic. However, the exposed considerations clearly suggest that in a hydrodynamic problem any observation on the vorticity quantity, which will be continuously recalled along the manuscript, is intimately connected to the noise generation.

Furthermore, the detailed body-flow interaction affects the hydrodynamic performance of the vessel. The *drag* is commonly perceived as a force acting in the direction opposed to

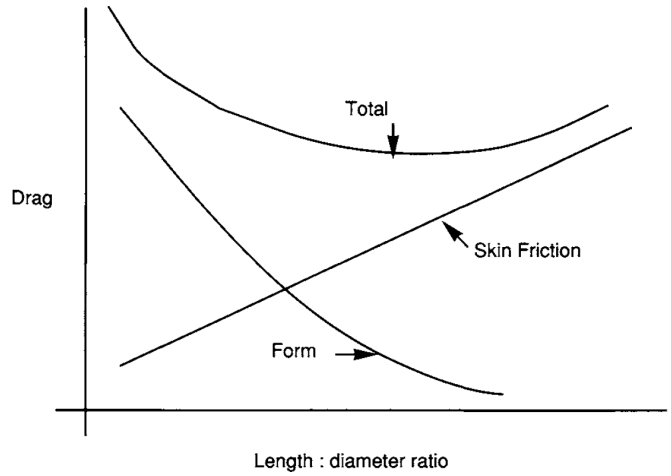

Figure 1.2 – Evolution of the total drag, together with the pressure and viscous contributions, as a function of the body length over diameter ratio (adapted from Burcher & Rydill 1994, Chapter 6). A constant body volume is considered.

motion. For flows such as that described in Fig. 1.1, drag can be decomposed as the sum of two contributions different in nature. The first is connected to the pressure difference between front and rear sides of the body, i.e. it is mainly due to the wake developing behind the body. This *pressure* drag contribution (also called *form* drag) is thus enhanced by bluff-bodies generating a large wake behind them. Conversely, it is minimised by streamlined shapes, such as the airfoils on aircraft wings at low angles of attack. The second contribution is instead connected to the interaction of the boundary layer with the surface all along the body length, and therefore takes the name of *skin friction*. A long slender body can increase the wetted surface with respect to a short fat one, thus augmenting the skin friction contribution (Joubert 2004). The concept is well resumed by the schematic in Fig. 1.2, where the pressure and viscous contributions on the total drag are depicted as a function of the body aspect ratio (length over diameter of a submarine shape). The region of total drag minimum is almost flat and occurs at an aspect ratio around $6-7$ (Joubert 2004), which is someway lower than the values of built submarines due to practical constraints (Burcher & Rydill 1994, Chapter 6). As an example, the Suffren shows an aspect ratio slightly larger than 11. The pressure and viscous contributions to the total drag depend not only on body characteristics but also on operating conditions. In fact, airfoils operated at high angles of attack may behave as bluff-bodies once significant flow separation occurs. The same concept is true for slender submarine configurations during manoeuvring, e.g. diving, or because of the presence of appendages, e.g. masts, on the main body. This fact clearly influences the percentage contribution to the total drag of pressure and viscous effects. However, a preliminary order of magnitude extrapolation to real world applications of the qualitative schematic shown in Fig. 1.2 is proposed. In the Suffren submarine case, considering a diameter of 8.8 m, an underwater velocity of 23 kn ($\approx 12\,\mathrm{m\,s^{-1}}$), and a drag coefficient equal to 0.05 (no detailed information is available, the value being guessed from technical reports (Granville 1976; Joubert 2004)), a gross estimation of the power required to advance the vessel at zero angle of attack leads to ≈ 2.63 MW. In the analysed configuration, the large aspect ratio implies a dominance of the skin friction component, let's say 90 % of the total drag, based on the qualitative diagram in Fig. 1.2. This implies that, if a new external hull coating is developed able to reduce skin friction of around 10 %, a total saving of ≈ 0.24 MW on the required power would be achieved.

The possibility of affecting drag is thus interesting both from a military and a civil perspective. In fact, while the Barracuda program, besides increasing performance, also engaged in respecting the environmental directives of the MARPOL Convention of the *International Maritime Organisation* (IMO 2019), the civil transport sector is strongly impacted by the ambitious objectives of recent conferences on climate, e.g. the *Paris Agreement* signed in occasion of the *United Nations Climate Change Conference* (COP21) (Paris Agreement 2015, Article 2). According to the *International Energy Agency*, in 2018 about one fourth of CO_2 emissions deriving from fuel combustion were due to transportation (IEA 2019). Approximately 75 % of this contribution is due to passenger and freight road vehicles, whereas aviation and maritime shipping count $\approx$ 10 % each, the percentage descending below 3 % for pipeline transport. Overall, the global transport emissions continuously increased over the years, even if the new technological developments significantly decreased the rate with respect to the previous decade ($\approx$ 0.6 % in 2018). This shows that efforts towards a more sustainable development of the transport sector may lead to significant effects on the global greenhouse gas emissions. In practice, what does *sustainable development* imply? How substantially ameliorate current transport vehicles? The schematic in Fig. 1.2 highlighted that in practical configurations the skin friction may constitute a significant portion of the total drag. In fact, in real-life operating conditions, the skin friction contribution reaches $\approx$ 50 % of the total drag for a long range aircraft at cruise conditions (Reneaux 2004), increases up to $\approx$ 85 % for low-speed cargo ships (Lackenby 1962; Manen & Oossanen 1988) and is almost the totality of drag in oil transport in pipelines. It seems thus convenient to develop methods able to directly act on skin friction, with an eventual side influence on the pressure contribution. Since the power required to move a vessel can be interpreted as the total drag multiplied by the vehicle velocity, a significant reduction of drag could translate in practice to vehicle speed increase at constant power, or required power decrease at constant speed. Among the possibilities, this manuscript is focused on techniques inspired by nature, which take the name of *biomimetics* (Vincent *et al.* 2006). The idea is well known by scientists from centuries, it is enough to think about the *Ornithopter* drawing by Leonardo da Vinci in the 15^{th} century, which was inspired by an intensive analysis of birds flight. If that design was probably never created at that time, today nature often leads to possible real-life practical implementations. This is testified e.g. by the flapping wing-tips of the *AlbatrossOne* aircraft that recently underwent flight test (Airbus 2019*a*), or by the futuristic conceptual design of the airliner *Bird of Prey* (Airbus 2019*b*). Focusing on methods to influence skin friction, one possibility is a relaxation of the requirement discussed above of zero relative velocity between flow and body at its surface. This can be achieved in practice by acting on the body surface state, as is the case of the *Lotus* leaf (see Fig. 1.3(a)), which inspired the development of *super-hydrophobic* (indicated by SH hereinafter) coatings (Rothstein 2010; Bhushan & Jung 2011). The Lotus plant exploits the water-repellent properties of its leaves to enhance the mobility of droplets on the surface, which are therefore able to trap dust particles while rolling, thus leading to self-cleaning properties (see Fig. 1.3(b)) (Samaha *et al.* 2012). In practice, how the Lotus leaf attains these properties? To understand the mechanism, scientists performed electron microscopy tests (Barthlott & Neinhuis 1997), which highlighted the rough nature of the leaf surface (see Fig. 1.4(a)), which is covered by micron-sized bumps (see Fig. 1.4(b)) that host wax nano-structures with a tubular shape (see Fig. 1.4(c)). This configuration thus results into a hierarchical structure with multiple length-scales, where the elements are randomly distributed on the surface. When in contact with water, this coupling of suitable surface texture and chemical properties allows air to be enclosed among the surface asperities. This results into an increase of the air-liquid contact area at the expense of the solid-liquid counterpart, leading to the evidenced inability of water to spread over the surface and the corresponding easy droplet roll-off. The presence of an air-liquid interface promotes the appearance of slip, i.e. the liquid velocity does not accommodate to the solid motion, with the

(a)

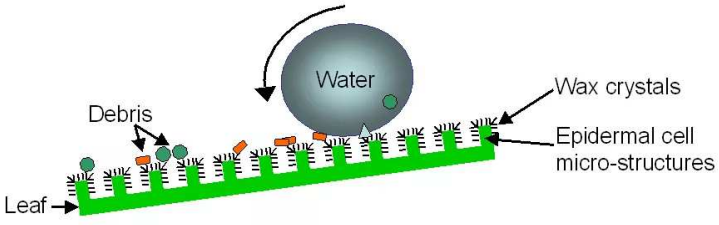

(b)

Figure 1.3 – Interaction between a Lotus leaf and water droplets. (a), macroscopic water droplets are not able to wet the leaf surface, highlighting its water-repellent property (Flickr Gallery 2019). (b), schematic of the self-cleaning mechanism: the rain drop traps dust particles while rolling off the leaf surface (The Naked Scientists 2019).

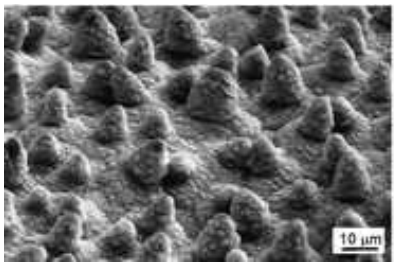

(a)

(b)

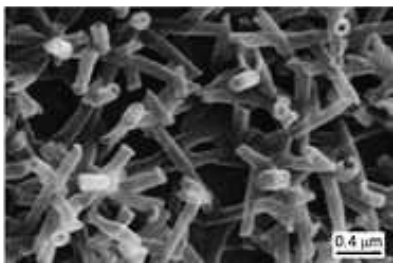

(c)

Figure 1.4 – Scanning Electron Microscopy (SEM) images of the Lotus leaf surface, at progressively higher magnification from (a) to (c) (adapted from Koch *et al.* 2009). The leaf surface is constituted by micron-sized papillose epidermal cells covered with wax nano-sized tubules.

subsequent possible influence on skin friction via a reduction of the shear stress at the wall.

However, the possible practical advantages in terms of drag reduction are not limited to the identified mechanism. In fact, marine vessels performance is strongly influenced by bio-fouling, which is the formation of a bio-film on the underwater hull due to the colonisation by micro-organisms (Townsin 2003), the solution being typically represented by paints containing biocides, whose usage is more and more restricted (Schultz & Swain 2000). For instance, because of bio-fouling, Burcher & Rydill (1994, Appendix 5) proposed an increase of the skin friction coefficient of a submarine of $\approx 0.13\,\%$ per each day of mission in temperate water, with a limit of 180 days, which translates into an $\approx 23\,\%$ friction coefficient augmentation at the end of the period. This explains the interest towards a limitation of the phenomenon, with beneficial retarding effects deriving by the use of SH coatings (Genzer & Efimenko 2006). The same typology of beneficial retarding effect was demonstrated facing freezing conditions (Tourkine *et al.* 2009) and fog condensation (Mouterde *et al.* 2017). Moreover, also food industry could be positively affected by the SH coatings introduction in real-life. The participation to the conference *CFM2017* (Castagna *et al.* 2017) introduced our team to the use of SH coatings in dairy processing (Zouaghi *et al.* 2017). In fact, the pasteurisation procedure results into significant minerals and proteins fouling on the stainless steel surfaces of the used heat exchangers (Barish & Goddard 2013). Increased environmental impact and operating costs thus derive by the necessity of bio-film removal, which otherwise could result into decreased heat transfer rate and product quality, with possible bacteria development. Good SH coatings performance was generally demonstrated (Zouaghi *et al.* 2019).

In order to enter into the details of the topics discussed from a general perspective in this introduction, the manuscript is organised in height chapters, as presented in the next section.

1.1 Plan of Presentation

The plan of the manuscript can be summarised as follows:

- **Chapter 1**: a general introduction to the topic is provided, underlying the interest in the real-life implementation of SH coatings;
- **Chapter 2**: the state of the art of wake analysis of fixed and free-moving bluff-bodies is discussed, together with methods to influence the hydrodynamic loads acting on the body;
- **Chapter 3**: a characterisation of the manufactured SH coatings is performed to acquire knowledge on the properties that may influence the hydrodynamic performance;
- **Chapter 4**: describes the experimental set-up designed for the execution of the falling sphere tests;
- **Chapter 5**: discusses the post-processing techniques implemented to analyse the falling sphere tests;
- **Chapter 6**: constitutes the core of the experimental results of falling sphere tests;
- **Chapter 7**: introduces the implemented numerical method and the reasons that have led to the necessity of a numerical investigation, together with a presentation of the results of the numerical campaign;
- **Chapter 8**: concludes the manuscript and provides some perspectives deriving from the realised study.

Chapter 2

Wakes and Control Strategies

The introduction highlighted the focus put in this manuscript on the potential role played by SH coatings over macroscopic surfaces in naval and submarine transport systems. In detail, the complex real-life issues need to be translated into an equivalent problem manageable at laboratory scale. To resume, the main points raised in Chapter 1 and that need to be properly addressed in the laboratory analysis are:

- a laminar boundary layer that develops along the body wall and eventually undergoes transition and separation;

- a boundary layer evolution influenced by a favourable or adverse pressure gradient, depending on the local body geometry;

- the possibility to influence the total drag by properly acting on the pressure or viscous contributions (or both), which could attain a different relative magnitude (thus resembling to a streamlined shape or a bluff-body) depending on body shape, presence of appendages and manoeuvring.

In this manuscript, the spherical geometry was chosen as prototype of bluff-body able to take into account all the raised issues. In fact, a large amount of studies characterising its interaction with the flow is available in literature. The next section is therefore dedicated to a brief resume of the development of the wake behind a fixed sphere. Depending on the considered flow regime, the laminar boundary layer evolution and the eventual transition to turbulent conditions and separation are described. The latter are strongly influenced by the favourable or adverse pressure gradient in the front and rear-side of the sphere. Similarly, depending on the flow regime the bluff-body configuration implies a dominance of the viscous or the pressure drag contribution. However, a strong coupling between the two contributions will be shown all along the chapter, rising the possibility to achieve a net total drag modification. In the following section, the modifications of the scenario due to the movement of a free falling or rising sphere in a fluid are described, underlying the connection between the flow around the sphere, its trajectory and the instantaneous hydrodynamic loads. This interconnection is finally exploited to introduce different flow control strategies, whose objective could be interpreted as the control of the loads underwent by the body via a modification of the flow around the sphere and thus its wake.

2.1 Wake Development of a Fixed Sphere

The study of flows and of their interactions with bodies has attracted attention of scientists for centuries. However, a real mathematical formalisation of the concepts only appeared during the 19^{th} century. In detail, Reynolds (1883) was the first to understand the importance of the relative magnitude of convection and diffusion in the motion of a liquid. The concept was formalised by the introduction of a non-dimensional number referenced today in literature as Reynolds number:

$$Re = \frac{\rho_l u L}{\mu_l}, \tag{2.1}$$

where u represents a velocity, L a length-scale and ρ_l, μ_l the liquid density and dynamic viscosity, respectively. In the case of a fixed sphere, the incoming flow velocity u_∞ and the sphere diameter d are usually taken as reference velocity and length. The flow regimes around a fixed sphere are then usually described as a function of the Re value, since it physically describes the relative significance of inertia effects and diffusion. Therefore, in the following a brief description of each identified regime with the corresponding Re thresholds is provided. For exhaustive reviews on the topic, the interested reader is referred to available literature (see e.g. Clift *et al.* 1978; Ern *et al.* 2012, and references therein).

***Re* → 0.** In the limit of vanishing Reynolds number (*creeping flow regime*), Stokes (1851) analytically developed a solution for the axisymmetric viscous flow around a fixed sphere due to an incoming flow at velocity u_∞ infinitely far from the rigid body. The following expressions for the streamfunction ψ, the radial u_r and tangential u_ϑ velocity components well resume the cited development:

$$\psi = \frac{1}{2} u_\infty \sin^2\vartheta \left(r^2 + \frac{\left(\frac{d}{2}\right)^3}{2r} - \frac{3\left(\frac{d}{2}\right) r}{2} \right), \tag{2.2a}$$

$$u_r = u_\infty \cos\vartheta \left(1 + \frac{\left(\frac{d}{2}\right)^3}{2r^3} - \frac{3\left(\frac{d}{2}\right)}{2r} \right), \tag{2.2b}$$

$$u_\vartheta = -u_\infty \sin\vartheta \left(1 - \frac{\left(\frac{d}{2}\right)^3}{4r^3} - \frac{3\left(\frac{d}{2}\right)}{4r} \right), \tag{2.2c}$$

where (r, ϑ) represents the two-dimensional (2D) spherical coordinate system centred on the sphere. The contour lines of the streamfunction ψ are reported in Fig. 2.1 for illustration purposes, underlying the symmetry of the analysed flow with respect to the central axis passing through the sphere.

***Re* < 212.** By progressively increasing the Reynolds number inertia effects gain importance with respect to diffusion, thus modifying the flow around the rigid sphere with respect to the Stokes' solution. However, the steadiness is preserved and the axisymmetry is maintained up to the occurrence of the first wake transition at $Re_{cr,1} \approx 212$. In detail, the wake visualisations sampled from Taneda (1956) and reported in Fig. 2.2 show that at Re sufficiently low (< 20) no vortex ring is clearly detectable in the wake of the sphere, with streamlines qualitatively similar to the Stokes' solution (see Fig. 2.2(a)). No complete agreement is found in literature concerning the Re which determines the appearance of the recirculation region, i.e. flow separation. However, Clift *et al.* (1978, Chapter 5) identify $Re \approx 20$ as the best estimate, based on the comparison of several numerical and experimental studies. Further increasing Re, the strength of the vortex ring grows, as shown in Fig. 2.2(b).

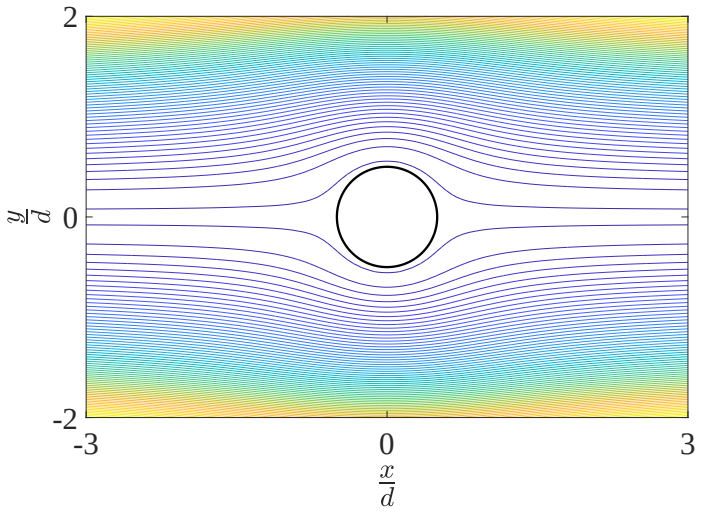

Figure 2.1 – Contour lines of the streamfunction ψ of the Stokes's solution of a uniform flow over a fixed sphere at vanishing Re (see Eqs. 2.2). The sphere (——) is centred on the origin $(0, 0)$ of the (x, y) Cartesian coordinate system, whereas for simplicity Eqs. 2.2 are written in the corresponding polar coordinate system (r, ϑ).

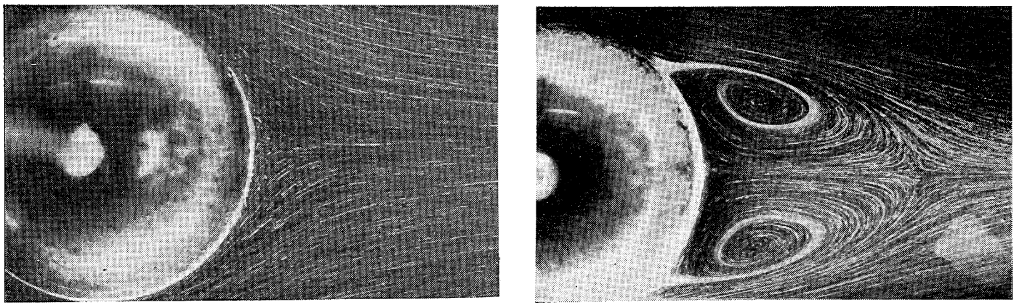

(a) (b)

Figure 2.2 – Qualitative visualisations of the wake region immediately behind a fixed sphere at Re lower than the occurrence of the first transition (adapted from Taneda 1956). (a), $Re \approx 9$ showing the absence of a detectable vortex ring. (b), $Re \approx 74$ highlighting the presence of an axisymmetric vortex ring, whose strength progressively increases with Re. The flow is from left to right.

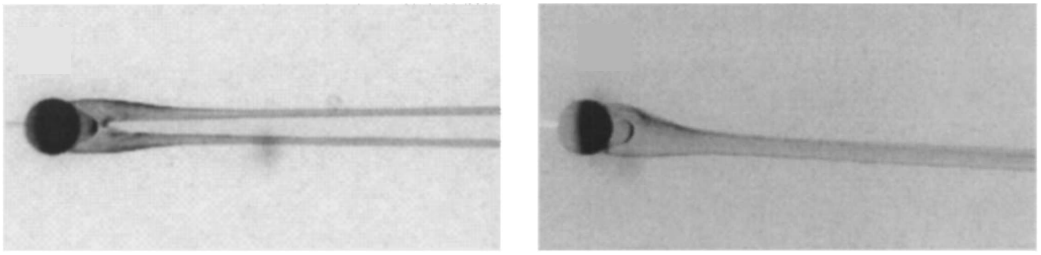

(a) (b)

Figure 2.3 – Qualitative visualisations of the stationary wake of a fixed sphere in a uniform flow at $Re \approx 270$, i.e. in between the first and second transition (adapted from Schouveiler & Provansal 2002). (a), top view that highlights the shedding of two stationary counter-rotating vortical structures from the recirculation region. (b), side view that underlines the planar symmetry on a plane inclined with respect to the incoming flow, which is from left to right.

$212 < Re < 275$. A first transition of the sphere wake is usually identified at $Re_{cr,1} \approx 212$, which determines the loss of the axisymmetry towards a planar reflectional symmetry with respect to a longitudinal plane passing through the sphere centre (Ern *et al.* 2012). However, the steadiness is preserved across the first transition. The indicated $Re_{cr,1}$ is the best estimate based on multiple numerical (Natarajan & Acrivos 1993; Johnson & Patel 1999; Mittal 1999*a*; Ghidersa & Dušek 2000; Tomboulides & Orszag 2000; Thompson *et al.* 2001) and experimental (Ormières & Provansal 1999; Schouveiler & Provansal 2002) investigations, which slightly differ on the evaluated critical value. However, the mechanism that physically drives the wake transition was shown to be based on a competition between the vorticity produced at the sphere wall and the amount evacuated in the wake (Leal 1989). When a critical vorticity amount is reached, the nature of the wake is forced to change in order to still be able to evacuate the larger amount of generated vorticity (Magnaudet & Mougin 2007). Moreover, Magnaudet & Mougin (2007) also showed that the achievement of a critical amount of vorticity is a transition criterion valid independently of the nature of the body surface, thus being meaningful at the same time for solid spheres and shear-free bubbles. A qualitative visualisation of the stationary wake in the discussed regime adapted from Schouveiler & Provansal (2002) is provided in Fig. 2.3. It makes evident the shedding of two vortical structures from the recirculation region and the planar symmetry of the wake. The analysis of the streamwise component of vorticity reveals that the two vortices are steady and counter-rotating (Ern *et al.* 2012). The symmetry on a plane inclined with respect to the incoming flow implies that the sphere undergoes a steady transverse force, i.e. lift.

$275 < Re < 300$. A second wake transition is identified at $Re_{cr,2} \approx 275$, even if, as in the previous case, the actual value slightly differs from study to study. The $Re_{cr,2}$ achievement results into a Hopf bifurcation, implying a transition from a stationary to a periodic wake, still preserving the planar symmetry. For that reason, this periodic state has been named Reflectional Symmetry Preserving (RSP) by Fabre *et al.* (2008). From experimental visualisations, the approach to the second transition is detected by peristaltic oscillations of the longitudinal vortices (see Fig. 2.4(a) adapted from Gumowski *et al.* (2008)), which finally grow in intensity leading to the periodic shedding of alternated-sign vortices (see Fig. 2.4(b) adapted from Przadka *et al.* (2008)). Accordingly, the lift force oscillates in magnitude around a zero-mean, while maintaining a constant direction (Ern *et al.* 2012). This regime allows the clear identification of the frequency f of the vortex shedding in the wake, thus enabling the evaluation of the corresponding Strouhal

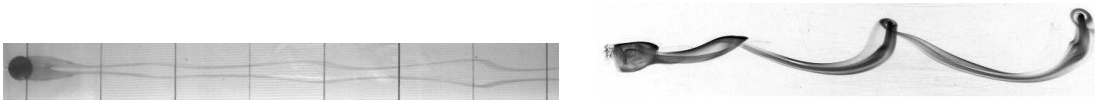

(a) (b)

Figure 2.4 – Qualitative visualisations of the wake of a fixed sphere in the proximity of the second transition at $Re_{cr,2} \approx 275$. (a), $Re \approx 271$ before the second transition occurrence, showing the oscillation of the longitudinal vortices (adapted from Gumowski *et al.* 2008). (b), $Re \approx 300$ after the second transition occurrence, showing the periodic shedding of alternated-sign vortices (adapted from Przadka *et al.* 2008). The flow is from left to right.

number:

$$St = \frac{fd}{u_\infty}, \tag{2.3}$$

This non-dimensional number allows the connection between the length-scale of the studied geometry and the temporal scale of the detected phenomenon.

$300 < Re \lesssim \mathcal{O}(10^2)$. A further Reynolds number increase progressively determines a loss of the wake planarity and periodicity (Mittal 1999*a*; Ormières & Provansal 1999; Tomboulides & Orszag 2000). Qualitative agreement is found between numerical simulations and experiments, however a clear detection of the threshold Re values is non-trivial. While planarity is maintained up to $Re \approx 355$ (Ern *et al.* 2012), the wake was shown to become completely 3D at $Re \geq 375$ (Mittal 1999*b*) and the detection of an unambiguous frequency of the vortex shedding is no more easily feasible. The so-called *chaotic* regime is thus entered for increasing Re.

$Re \gtrsim \mathcal{O}(10^2)$. Interestingly, all the discussed transition scenarios occur in a limited low Re range. Once reached the chaotic wake configuration, no additional modification of the wake nature occurs over a Re range that spans several orders of magnitude. The scenario is well resumed by the qualitative evolution of the drag coefficient C_D as a function of Re adapted from Achenbach (1972) and reported in Fig. 2.5. The C_D can be evaluated by dividing the measured drag on the sphere by the quantity $\frac{1}{2}\rho_l u_\infty^2 \pi \frac{d^2}{4}$, as is discussed in detail in Chapter 4. For Re in the range $\mathcal{O}(10^3 - 10^5)$ the *sub-critical* regime is characterised by $C_D \approx 0.5$. A reference direction aligned with the incoming flow can be considered to define a corresponding angle ϑ. A laminar boundary layer develops along the front-side of the sphere and then undergoes separation before reaching the sphere equator, i.e. $\vartheta = 90°$. Achenbach (1972) evaluated laminar boundary layer separation at $\vartheta \approx 82°$ for $Re \approx 1.6 \times 10^5$ in the case of smooth fixed spheres hold from the rear. The scenario is well depicted by the visualisation reported in Fig. 2.6(a) at $Re \approx 1.5 \times 10^4$. The separated boundary layer remains laminar for a significant length after the sphere equator and then undergoes transition to turbulence in the rear-side of the sphere. A Re increase of one order of magnitude progressively determines a shift of the separation point of the laminar boundary layer toward the rear-side of the sphere. Achenbach (1972) evaluated laminar boundary layer separation at $\vartheta \approx 95°$ for $Re \approx 2.8 \times 10^5$. A sudden C_D decrease occurs by further increasing Re, thus entering the *critical* regime around $Re \approx 3.5 \times 10^5$. In fact, intermediate separation of the laminar boundary layer occurs, which is followed by transition to turbulence. The turbulent boundary layer is then able to reattach to the wall down to a significant length in the rear-side of the sphere. Consequently, the size of the wake is considerably reduced, as shown in Fig. 2.6(b), with the highlighted effect on drag. For this reason, the phenomenon is known in literature as *drag crisis*. Achenbach (1972) estimated a minimum C_D occurring at $Re \approx 3.7 \times 10^5$, which is indicated as critical Reynolds number in Fig. 2.5. A further Re increase determines a

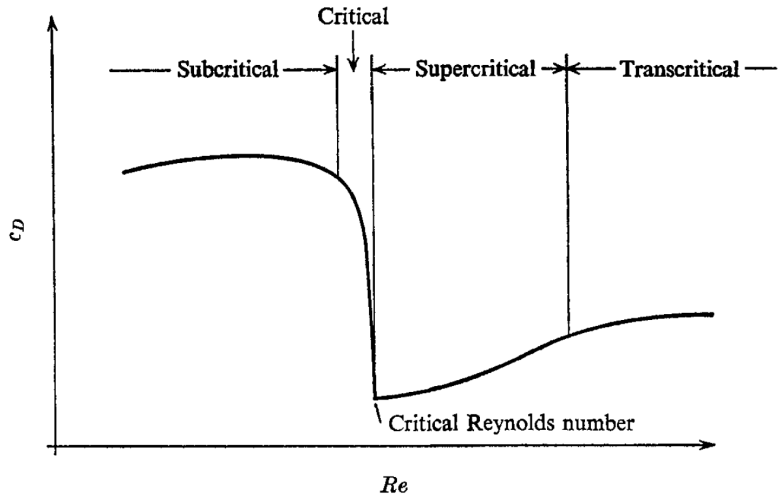

Figure 2.5 – Qualitative evolution of the drag coefficient C_D of a fixed sphere as a function of the Reynolds number Re (adapted from Achenbach 1972).

slow C_D increase in the *super-critical* regime, which is characterised by a direct transition of the boundary layer from laminar to turbulent without the formation of the separation bubble, occurring downstream of the equator. A Re increase above $\approx 1.5 \times 10^6$ implies a shift of the transition location in the front-side of the sphere, thus entering the *trans-critical* regime.

The discussed drag crisis scenario and the corresponding indicated Re values are valid for smooth spheres. However, Achenbach (1974) studied the effect of an augmentation of the roughness of the sphere surface on the onset of the critical regime, as shown in Fig. 2.7. It is evident that an increase of the height of the roughness elements λ determines a decrease of the critical Re at which drag crisis occurs. Moreover, the minimum C_D increases for increasing λ, and the super-critical regime is entered at progressively lower Re. The highest λ analysed by Achenbach (1974) corresponds approximately to 1.3×10^{-2} times the sphere diameter d, and determines a shift of the critical Re down to $\approx 8.0 \times 10^4$.

Finally, Fig. 2.8 shows the contribution of friction drag with respect to the total C_D along a Re range spanning the regimes introduced in Fig. 2.5 (Achenbach 1972). The analytical Stoke's development can be shown to result in the well-known Stokes' drag law:

$$C_D = \frac{24}{Re}, \tag{2.4}$$

where two-thirds of the drag are due to friction, and the remainder is pressure drag (see e.g. Clift *et al.* 1978, Chapter 3). In the sub-critical regime the friction contribution scales as $\sim Re^{-0.5}$, while reaches a maximum of $\approx 12.5\,\%$ in critical conditions. Then, the friction contribution decreases again in the super-critical and trans-critical regimes (Achenbach 1972).

2.2 Moving Sphere

As indicated by Ern *et al.* (2012), visualisations of falling spheres and drops at terminal velocity reveal that the discussed transition scenarios valid for fixed spheres are retrieved also in the case of a free body, at least qualitatively (see e.g. Magarvey & Bishop 1961*a*,*b*; Magarvey &

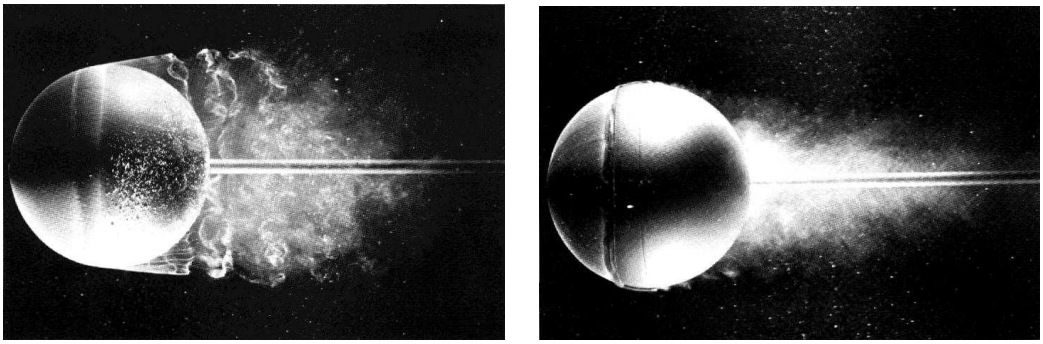

(a) (b)

Figure 2.6 – Dye visualisation of the boundary layer behaviour over a fixed sphere hold from the rear (adapted from Werlé 1980). (a), separation of the laminar boundary layer before reaching the sphere equator and transition to turbulence in the rear-side of the sphere at $Re \approx 1.5 \times 10^4$. (b), artificial trip of the laminar boundary layer via a wire placed ahead of the equator at $Re \approx 3.0 \times 10^4$ to reproduce what naturally occurs at $Re \approx 3.5 \times 10^5$. The laminar boundary layer undergoes intermediate separation followed by transition to turbulence. The turbulent boundary layer is able to reattach to the wall and finally separates in the rear-side of the sphere.

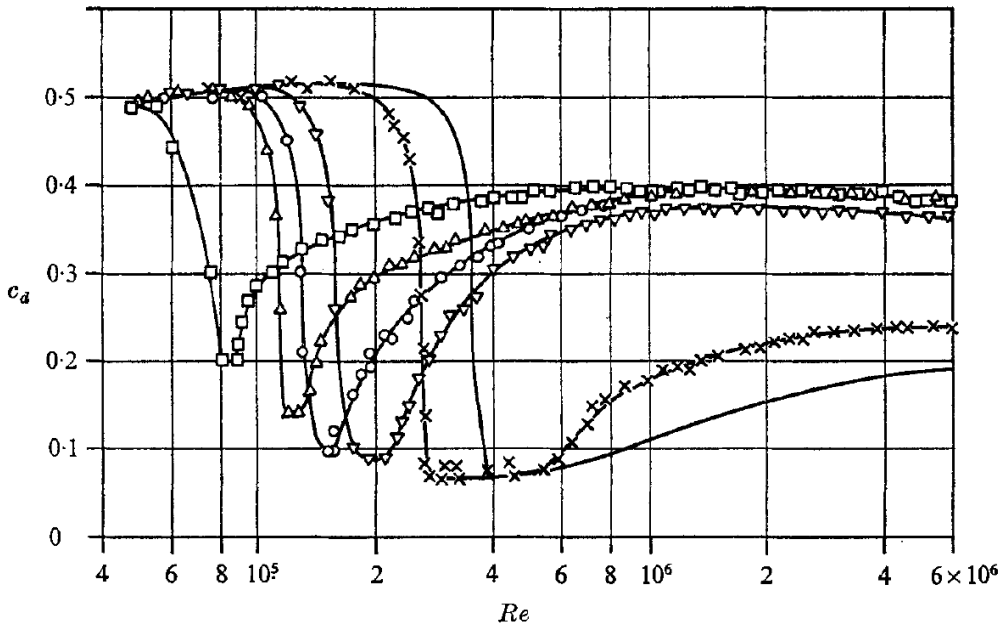

Figure 2.7 – Influence of the sphere surface roughness λ on the onset of drag crisis (adapted from Achenbach 1974). (—), smooth sphere. $\times$, $\frac{\lambda}{d} = 2.5 \times 10^{-4}$. $\triangledown$, $\frac{\lambda}{d} = 1.5 \times 10^{-3}$. $\circ$, $\frac{\lambda}{d} = 2.5 \times 10^{-3}$. $\triangle$, $\frac{\lambda}{d} = 5.0 \times 10^{-3}$. $\square$, $\frac{\lambda}{d} = 1.3 \times 10^{-2}$.

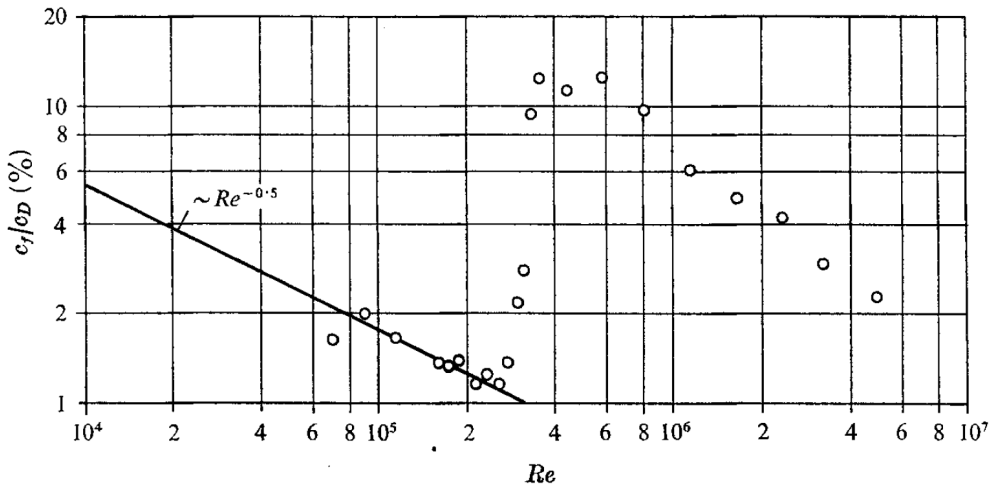

Figure 2.8 – Friction percentage contribution with respect to the total drag over the Re range characterising the regimes introduced in Fig. 2.5 (adapted from Achenbach 1972).

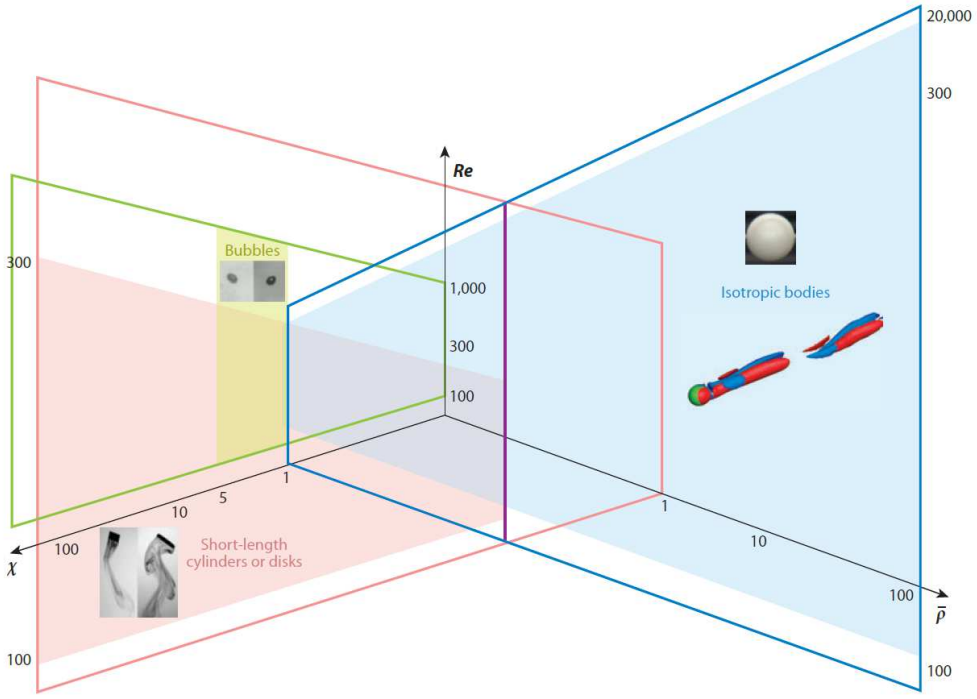

Figure 2.9 – Map of the 3D space determined by the parameters influencing the free motion of bluff-bodies (adapted from Ern *et al.* 2012). Following the notation of the original article, $\overline{\rho}$ represents the density ratio between body and fluid (indicated by ζ in this manuscript), Re the Reynolds number and χ the geometric aspect ratio of the body describing its anisotropy.

MacLatchy 1965; Goldburg & Florsheim 1966). However, the scheme in Fig. 2.9 (adapted from Ern *et al.* 2012) clearly shows that additional parameters other than Re come into play when describing the free motion of a body, as was also discussed by Jenny *et al.* (2004). The body-to-liquid density ratio $\zeta = \frac{\rho_s}{\rho_l}$ (ρ_s indicating the body density) controls the rising or falling behaviour of the body, thus vanishing towards a zero value in the case of bubbles. The aspect ratio χ can be defined via some characteristic dimensions of the body (e.g. the two axes of an ellipse) and thus describes the anisotropy of the body, being equal to the unitary value for perfect spheres. Moreover, Jenny *et al.* (2004) introduced the Galileo number:

$$G = \frac{\sqrt{|\zeta - 1| g d^3}}{\nu_l}, \tag{2.5}$$

which is a rephrasing of Re based on a buoyancy/gravitational velocity scale. In the above expression, ν_l is the liquid kinematic viscosity and g denotes the acceleration due to gravity. In the case of an ideal perfect sphere, the axisymmetry around its centre implies that the only mechanism that can generate path oscillations from the initial vertical trajectory is the onset of wake instabilities. Interestingly, Jenny *et al.* (2004) proposed, via a joint numerical and experimental work, a parallel scenario with the fixed sphere case (later partially verified by Veldhuis & Biesheuvel (2007); Horowitz & Williamson (2010*a*)), whose results are well resumed by the chart in Fig. 2.10. A strong ζ influence on the critical G (equivalently Re) was observed. For $G < 156$ a vertical straight path is found independently of ζ, which corresponds to the axisymmetric wake regime in the fixed sphere case for $Re < 212$. The axisymmetric regime then undergoes transition for a critical G that slightly depends on ζ (Jenny *et al.* 2003), thus entering a steady oblique regime. This path transition corresponds to the first wake transition identified at $Re_{cr,1} \approx 212$ for the fixed sphere, where axisymmetry is lost. Conversely, the path modification corresponding to the second transition at $Re_{cr,2} \approx 275$ strongly depends on ζ. A detailed discussion of rising spheres ($\zeta < 1$), which implies the occurrence of oscillatory and then zigzagging regimes is available in Jenny *et al.* (2004), Ern *et al.* (2012). For falling spheres ($\zeta > 1$), which represent the main focus of this work, the frequency f of the periodic oscillating oblique regime is influenced by the ζ value, with a f increase for increasing ζ. Finally, as in the fixed sphere case, the chaotic regime is entered, where a dominant frequency cannot be identified. Interestingly, a ζ increase determines an increase of the critical G (or Re) in all the transition processes, with values that finally converge toward the fixed sphere values for high enough ζ. Jenny *et al.* (2004) evaluated a difference on $Re_{cr,2}$ of $\approx 1\,\%$ for falling spheres with $\zeta = 5$ with respect to the fixed sphere case. This finding somehow agrees with the more simple scenario of transition process on the cylindrical geometry which, conversely to the sphere, is characterised by a simultaneous loss of wake steadiness and symmetry at $Re \approx 47$ in the fixed body case. In fact, Cossu & Morino (2000) experimentally showed with spring-mounted cylinders that the critical Re of the occurrence of vortex shedding was similar to the fixed cylinder case for high enough ζ, whereas it dropped to less than half the value for low enough ζ. Overall, this implies that the fixed sphere wake transition scenario depicted in §2.1 is well representative of the path transition mechanism of solid heavy spheres ($\zeta \gg 1$), e.g. the stainless steel spheres considered in this study, both from a qualitative and a quantitative point of view.

The shown results are valid for a perfectly spherical geometry with a centre of mass coincident with the geometrical centre. The effect of a varying aspect ratio χ on a falling solid body was investigated for example by Fernandes *et al.* (2007) via the analysis of short cylinders where the ratio between the diameter and the thickness varied in the range $2 - 20$. A χ increase was found to induce a diminution of the critical Re values describing both the path transition processes identified for the sphere case. Moreover, Jenny *et al.* (2004) also tested the influence of a non-perfectly symmetric mass distribution on rising spheres, showing that non-homogeneous

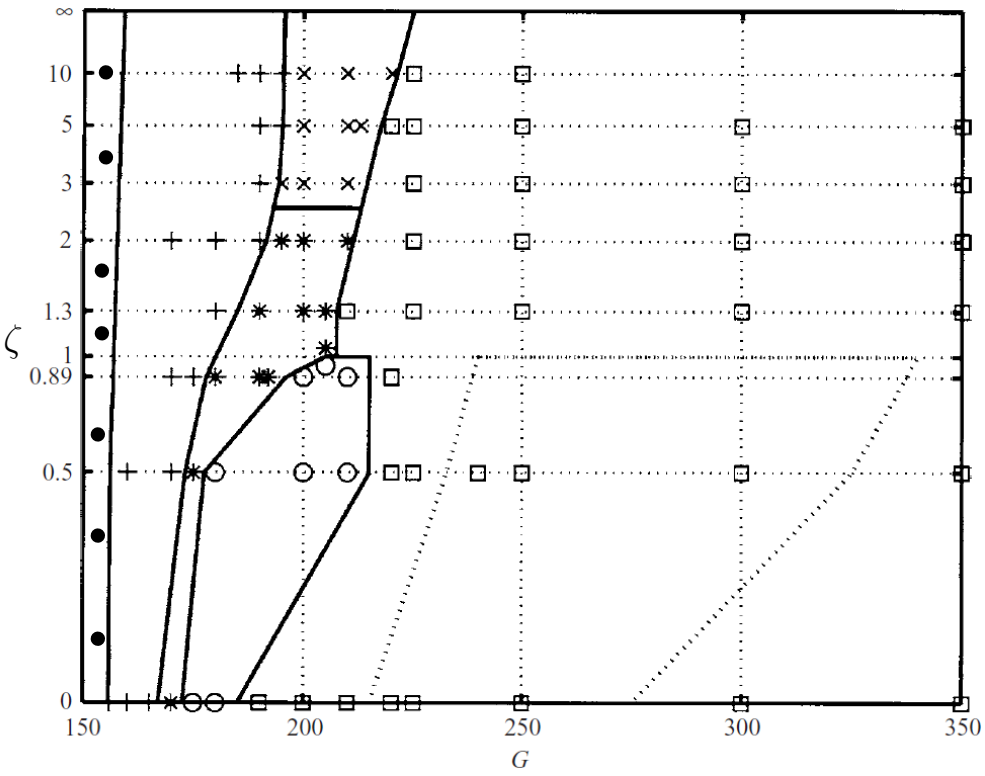

Figure 2.10 – Diagram of the path states of free moving spheres as a function of the density ratio ζ and the Galileo number G (or equivalently the Reynolds number Re) (adapted from Jenny *et al.* 2004). •, axisymmetric regime. +, steady oblique regime. ×, oscillating oblique regime with high frequency. ∗, oscillating oblique regime with low frequency. ○, zigzagging periodic regime. □, chaotic regime. (- - -), region of coexistence of chaotic and periodic regime for rising spheres.

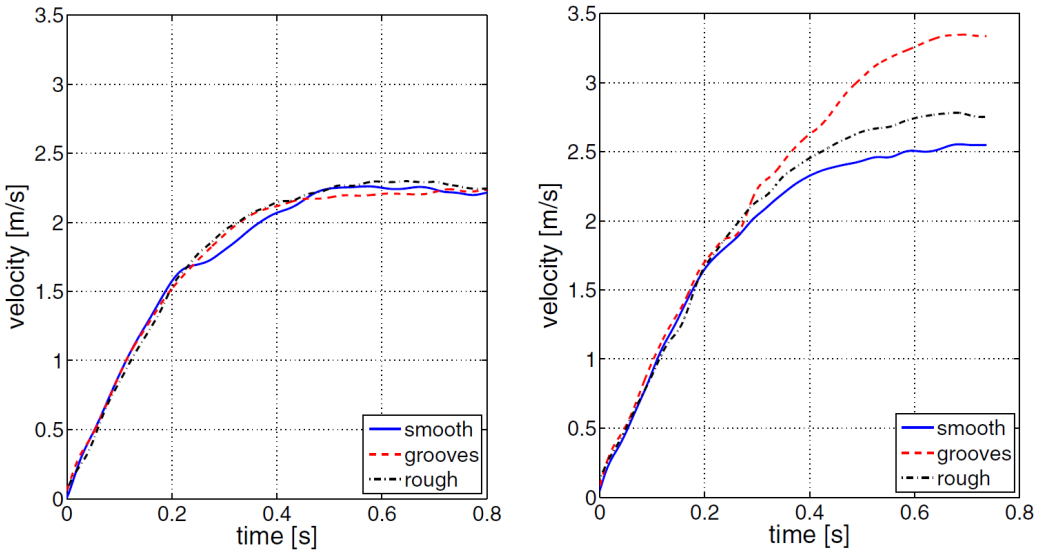

Figure 2.11 – Effect of the surface roughness on the onset of drag crisis for steel spheres falling in water (adapted from Lyotard *et al.* 2007). (a), $d = 30\,\mathrm{mm}$. (b), $d = 40\,\mathrm{mm}$.

spheres undergo transitions more rapidly than the ideal case. Even if no proof was provided for the falling sphere case, large ζ values should mitigate the effects of a slight asymmetry of both the mass distribution and of the geometry.

Focusing attention on the high Re regimes introduced in Fig. 2.5, an interesting study on the effect of surface roughness on the onset of drag crisis was performed by Lyotard *et al.* (2007), whose results in the case of falling spheres in pure water are reported in Fig. 2.11. These authors modified the surface state by creating a *groove* texture, 0.5 mm deep and 1 mm wide, and a *rough* texture by gluing a single layer of glass beads ($d \approx 0.7\,\mathrm{mm}$) on the surface. The $d = 30\,\mathrm{mm}$ spheres results in Fig. 2.11(a) show no appreciable difference due to the different investigated surface roughness. This implies that at sufficiently low Re ($\approx 6.8 \times 10^4$ estimated from Fig. 2.11(a)), a roughness with typical size as large as $\approx 3\,\%$ of the sphere diameter is not large enough to promote an early onset of the drag crisis. Conversely, the $d = 40\,\mathrm{mm}$ reference spheres in Fig. 2.11(b) reach at terminal conditions $Re \approx 1.0 \times 10^5$, which is closer to the critical range identified in Fig. 2.5. The augmentation of the surface roughness clearly determines a modification of the sphere vertical acceleration while reaching terminal conditions, at which a larger terminal velocity is achieved. These results qualitatively agree with the highest roughness case analysed by Achenbach (1974) in the fixed sphere case and previously reported in Fig. 2.7. Moreover, the largest Re reached in the experiments performed in this manuscript (see Chapter 6) was below the reported range valid for the onset of drag crisis, and the corresponding non-dimensional surface roughness $\frac{\lambda}{d}$ was one order of magnitude lower than the maximum value analysed by Achenbach (1974), thus excluding a possible entry in the critical regime.

2.2.1 Loads Estimation

The main difference between the fixed and the falling/rising sphere scenarios relies on the coupling between the body and the fluid motions occurring in the latter case. The most practical description of the issue thus reduces to the evaluation of forces and torques exerted by the fluid flow on the body (Ern *et al.* 2012). In numerical studies, the loads are practically estimated by a resolution of the Navier-Stokes equations governing the fluid flow, being then injected into the Kirchhoff equations governing the body motion from a Lagrangian perspective (Mougin & Magnaudet 2002*a*). The evaluated velocity and rotation rate of the body can then be re-injected as boundary conditions on the Navier-Stokes equations to perform calculations at the next time-step.

In the following, a brief introduction to the topic is provided. For full details and for the mathematical developments, see e.g. the elegant introduction provided by Mougin & Magnaudet (2002*a*). As discussed by Lamb (1945, Chapter 5), Lord Kelvin with Tait and later Kirchhoff were the first to understand that solids moving into a fluid can be treated as forming one single dynamic system. In detail, Kirchhoff developed equations (named after him) describing the motion of a rigid body in an inviscid, incompressible and unbounded fluid at rest at infinity, which were later extended to steady, converging streams by Taylor (1928). Other authors more recently further extended the development to unsteady, inviscid, irrotational flows, including also the body deformation (Landweber & Miloh 1980; Galper & Miloh 1995). However, it is only thanks to the work of Howe (1995) that the discussion could be extended to viscous flows. In that case, the loads acting on the body depend on added mass effects, viscous skin friction at the wall and stresses induced by the vorticity in the fluid. However, the review by Magnaudet & Eames (2000, and references therein) showed that added mass contributions can still be defined in viscous flows and are independent on the nature of the body surface, i.e. they do not depend on the vorticity generated at the body wall and on the vorticity eventually present in the fluid (Ern *et al.* 2012). A separation of the added mass terms from the hydrodynamic contributions depending on vorticity can thus be performed (Howe 1995), which allows for the direct extension of the Kirchhoff equations to viscous flows. The generalised Kirchhoff equations are thus reported in the following in the case of a rigid body of arbitrary shape with three mutually orthogonal symmetry planes and written in a coordinate system fixed with respect to the laboratory frame but rotating with the body. By considering a rigid body of mass m, volume $\mathcal{V}$, velocity $\boldsymbol{u}$ and rotation rate $\boldsymbol{\Omega}$, its motion can be described by:

$$(m\boldsymbol{I} + \boldsymbol{\Lambda}) \frac{d\boldsymbol{u}}{dt} + \boldsymbol{\Omega} \times ((m\boldsymbol{I} + \boldsymbol{\Lambda})\, \boldsymbol{u}) = \boldsymbol{F} + \boldsymbol{F}_b, \tag{2.6a}$$

$$(\boldsymbol{J} + \boldsymbol{D}) \frac{d\boldsymbol{\Omega}}{dt} + \boldsymbol{\Omega} \times ((\boldsymbol{J} + \boldsymbol{D})\, \boldsymbol{\Omega}) + \boldsymbol{u} \times (\boldsymbol{\Lambda} \boldsymbol{u}) = \boldsymbol{\Gamma}, \tag{2.6b}$$

where $\boldsymbol{I}$ is the unity tensor, $\boldsymbol{J}$ is the inertia tensor of the body, $\boldsymbol{\Lambda}$ is the added mass tensor and $\boldsymbol{D}$ is the added rotational inertia tensor. On the right-hand side of the above equations $\boldsymbol{F}$ and $\boldsymbol{\Gamma}$ are the hydrodynamic forces (lift and drag) and torques respectively, while $\boldsymbol{F}_b$ is the gravity/buoyancy force. As discussed above, $\boldsymbol{\Lambda}$ and $\boldsymbol{D}$ depend only on the body geometry and can be determined via irrotational flow theory (Mougin & Magnaudet 2002*a*), thus describing the instantaneous reaction of the fluid to the body linear and rotational acceleration. Conversely, $\boldsymbol{F}$ and $\boldsymbol{\Gamma}$ derive from the existence of a non-zero vorticity in the flow, and generally depend on the history of the fluid motion (Ern *et al.* 2012). The direct connection between path and wake instabilities previously introduced is now evident in Eqs. 2.6. In fact, wake transitions determine a modification of the nature of the flow in the proximity of the body, with consequent modification of the loads $\boldsymbol{F}$ and $\boldsymbol{\Gamma}$. The modification of the right hand side of Eqs. 2.6 thus demands the body motion variation for the system to be again satisfied.

Interestingly, the approach described above can still be exploited from an experimental perspective, where the vorticity-dependent loads $\boldsymbol{F}$ and $\boldsymbol{\Gamma}$ are not available from numerical resolution. In fact, they can be readily estimated from the temporal evolutions of the trajectory, velocity and acceleration. This approach is described by Shew *et al.* (2006), Fernandes *et al.* (2008) for loads measurements on rising bubbles and disks, respectively, and is discussed in detail in Chapters 4 - 6, being one of the outputs of the performed experimental tests where large transversal motion was detected.

2.3 Control Methods

Sections §2.1 and §2.2 overall highlighted the interconnection between path oscillations, wake instabilities and hydrodynamic loads acting on a bluff-body freely moving in a fluid. Therefore, it is straightforward to infer that someway modifying the flow in the proximity of the object wall could be an effective method to act on the hydrodynamic loads experienced by the body. This is exactly the perspective of the brief flow control methods discussion provided in the following. For an introduction to flow control and a review of existing techniques see e.g. Gad-El-Hak (2000), whose map of the available control strategies is reported in an adapted form in Fig. 2.12. In fact, one common classification scheme is based on the requirement of an external energy supply, which results into *active* methods. This strategy can be further divided into *predetermined* and *reactive* techniques, depending on the absence (or presence, respectively) of sensors to acquire information of the flow. If this information is sensed at an upstream location and is used to trigger an actuator at a downstream position, without further interaction between the two, the technique is called *feedforward* control. If instead a control variable is measured and compared to a reference input in order to establish the magnitude of the actuator action, the technique is called *feedback* control. The main advantage of these techniques is their adaptability to flow conditions, with the drawback of continuously assuring that the achieved gain is larger than the consumed energy.

Conversely, *passive* methods do not require an external energy input. However, the main drawback of these techniques that is typically mentioned in literature is their limited robustness to varying flow conditions. Strategies to mitigate this disadvantage exist, such as compliant passive methods able to adapt to the flow (see e.g. Pavlov 2006; Venkataraman & Bottaro 2012).

The classification discussed via Fig. 2.12 is one of the possible schemes to map the available control strategies. Depending on the chosen classification parameter, many approaches that interconnect the identified areas can exist. In this manuscript, focus is given to methods originated from the effort to artificially reproduce natural features in order to solve complex problems. This is known in literature as *biomimetics* (see e.g. Vincent *et al.* 2006). The interest of the *ESA* team (*Écoulements et Systèmes Aérodynamiques*) of the PRISME Laboratory on bio-inspired control methods can be traced back to the last decade. As an example, Feuvrier (2015) studied a self-adaptive method to passively control the turbulent wake of a square-section cylinder. Two flaps were mounted on the sides of the cylinder and left free to adapt their angular position to the flow (see Fig. 2.13), mimicking the action of the feathers on the wings of birds during landing. The author experimentally showed the possibility to influence the length of the recirculation region behind the bluff-body and the wake width, with effects on the lateral flow entrainment in the wake of the cylinder. The proposed control strategy was therefore at the borderline between passive and active methods, with the ability to adapt to the flow and the absence of an external energy input.

In the following, focus is given to methods developed to influence the interaction between the flow and the solid body via a modification of the state of the body wall. Due to the extent of

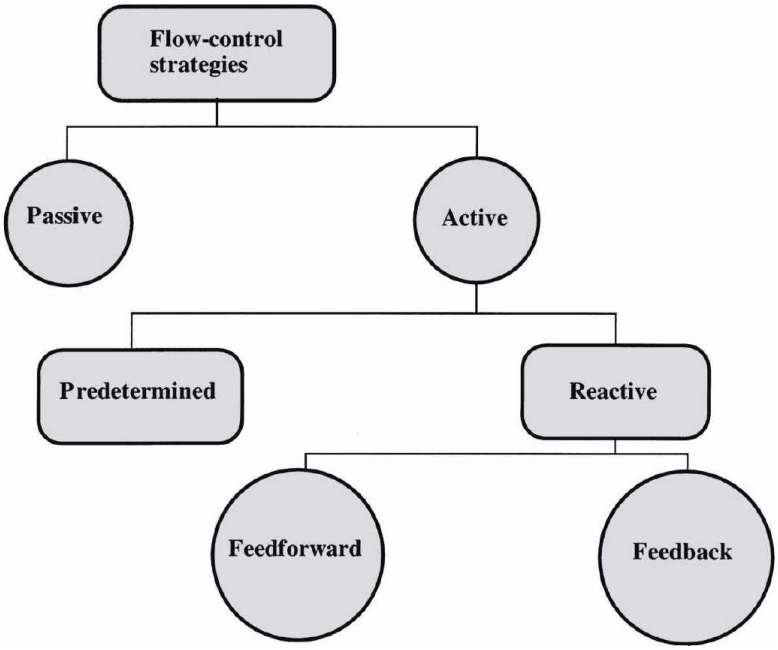

Figure 2.12 – Schematic of the implemented control strategies (adapted from Gad-El-Hak 2000).

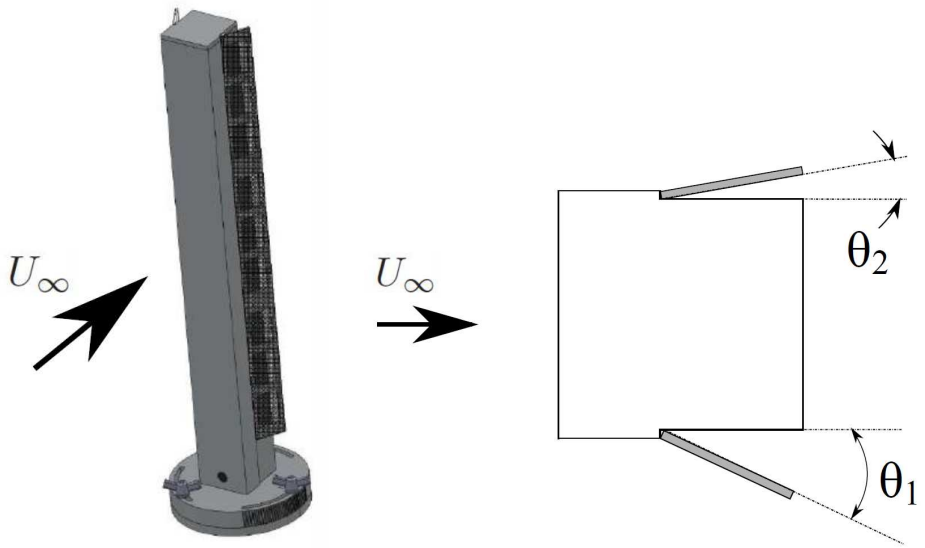

(a) (b)

Figure 2.13 – Schematic of the experimental set-up with freely moving flaps mounted on the sides of a square-section cylinder (adapted from Feuvrier 2015). (a), 3D view. (b), 2D detail with the flap rotation activated by the flow. Following the notation of the original work, the symbol U_∞ indicates the incoming flow velocity and θ the angular position of the flaps.

available literature, no attempt is here made to fully describe the developed strategies. Attention is given to methods that are someway related to the peculiarities of SH coatings, which are the focus of this manuscript.

One interesting strategy is based on the passive manipulation of the boundary layer in a turbulent flow, which can be obtained by the use of riblets. The latter are surface protrusions, e.g. v-shaped, aligned with the direction of the main flow. Fundamental studies oriented towards the understanding of the physical mechanism responsible of the evidenced drag reduction were executed both from an experimental and a numerical perspective (Walsh & Weinstein 1978; García-Mayoral & Jiménez 2011). Modification of the velocity gradients in the near-wall region due to the peak-valley sequence, break down of the longitudinal vortices, prevention of the transversal motion of streamwise vortices were identified as the main effects on the flow (see e.g. Szodruch 1991; Dean & Brushan 2010). The latter study also provides an exhaustive review of riblets applications and their derivation from the shark skin properties in a biomimetics perspective. Moreover, since for a long range aircraft about half of the total drag is due to skin friction (Reneaux 2004), the aeronautical industry revealed a strong interest in the attempt to reduce detrimental viscous effects. The possible advantages being fuel saving and therefore cost reduction, extended flight range, increased payload and environmental impact reduction. Performed studies ranged from wind tunnel tests on scaled models up to real scale flight tests (see Fig. 2.14) (Walsh *et al.* 1989; Coustols & Schmitt 1990; Szodruch 1991). Overall, the significant drag reduction obtained during flight tests confirmed the indications provided by wind tunnel investigations. However, the technology had to face the non-negligible aircraft weight increase coupled with the high erosion and pollution of the texture under operational conditions, which slowed down the general application to aircrafts.

The SH coatings studied in this manuscript belong to the same category of cited technologies, where a control of the interaction with the flow is achieved via a modification of the wall texture and of its chemistry. The resulting main peculiarity is the establishment of an air layer between the liquid flowing over the solid wall and the body. Therefore, the next paragraph is dedicated to a brief introduction to the main features of technologies based on the creation of an air layer between the liquid and the wall. Then, Chapter 3 is entirely dedicated to the characterisation of the manufactured SH coatings.

2.3.1 Air Layer Methods

When a relative velocity is set between a liquid and a solid body, the flow in the near-wall region can be strongly affected by the establishment of an air layer between the liquid and the solid, with the potential achievement of skin friction drag reduction (Ceccio 2010). If the objective of all air layer based techniques is common, the methods to achieve the establishment of a stable air or bubbles layer are multiple.

Cavitation Methods

Cavitation is an effective technique developed along the 20^{th} century (Brennen 2014), which consists in the formation of a gas cavity, e.g. behind an axisymmetric body. As shown in Fig. 2.15, the main body could be completely immersed in the wake generated by the front bluff-body, named *cavitator*. This way, the solid surface of the main body would interact with the gaseous flow in the wake rather than with the liquid main flow. If the pressure in the cavity decreases below the liquid vapour pressure, the cavity is filled with vapour and is named *natural* or *vapour* cavity. If instead non-condensable gas is injected, the cavity is named *ventilated*. The cavity length can be shorter than the body length (*partial cavity*) or longer (*super-cavity*). As shown by

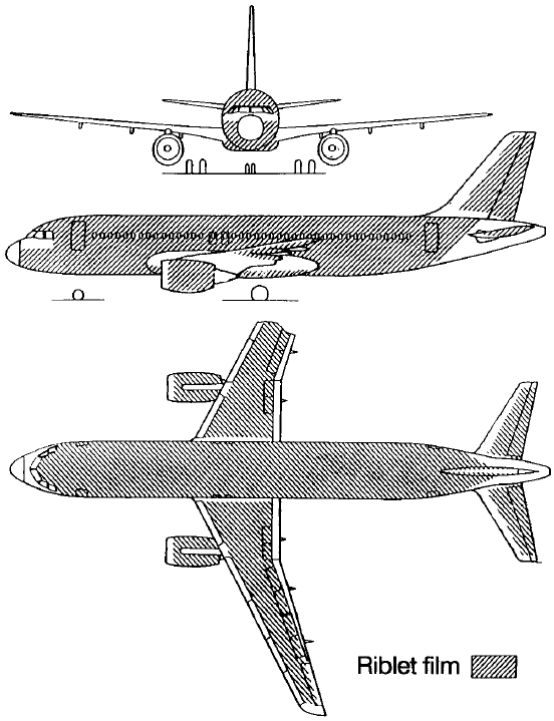

Figure 2.14 – Schematic of an A320 covered by a riblet film (adapted from Szodruch 1991). Approximately 70 % of the surface is coated, with a consequent 80 kg weight increase.

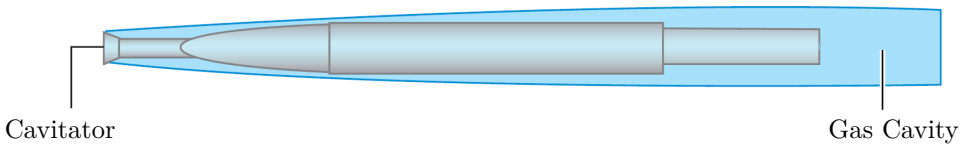

Figure 2.15 – Schematic of a cavity flow over an axisymmetric object (adapted from Ceccio 2010). The cavitator generates a wake that can incorporate the whole body. The cavity can be filled by vapour or by injected gas. The reported configuration illustrates the super-cavity case, with a cavity length longer than the main body length. The flow is from left to right.

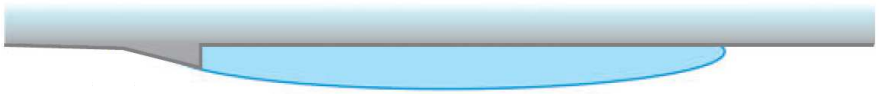

Figure 2.16 – Schematic of a partial cavity flow over an non-axisymmetric object (adapted from Ceccio 2010). The cavitator protrudes into the flow generating a cavity that downstream reattaches to the surface. The flow is from left to right.

Ceccio (2010), a ventilated super-cavity is the configuration typically encountered in the framework of drag reduction and speed increase of fast moving underwater vehicles. If drag reductions up to 90 % are potentially demonstrated, significant control problems are observed. The main body must be assured to remain inside the cavity during speed changes and maneuvering, while the cavitator reduces the directional stability of the vessel since it displaces the centre of pressure of the vehicle in the front-side, far from the centre of gravity. A similar technique could be also applied to non-axisymmetric bodies, e.g. ships hulls (see Fig. 2.16). In that case, both natural and ventilated cavities can be considered, which are formed e.g. by a cavitator protruding into the flow. However, the potential friction reduction deriving from the cavity presence may be counterbalanced by a drag penalty due to unsteadiness of the cavity dynamics. Suitably shaped hydrofoils able to adjust the pressure gradient in the cavity reattachment region are shown to mitigate unsteadiness, leading to lift-to-drag ratio increase (Amromin *et al.* 2006).

Bubbles Injection

The momentum transport in a turbulent boundary layer can be influenced by the injection of bubbles, which under suitable conditions could also coalesce forming a continuous air layer (Ceccio 2010). Historically, the first studies on flat plates were performed since the 1970s in the Soviet Union (see e.g. Bogdevich *et al.* 1980), reporting drag reductions up to 80 % (Ceccio 2010). Subsequent studies on the same geometry by Madavan *et al.* (1985) showed the beneficial influence of decreasing flow velocity, increasing bubble injection rate and favourable buoyancy on the obtained drag reduction. Experimental investigation on a more practical axisymmetric geometry mimicking an underwater vessel was performed by Deutsch & Castano (1986), who showed an increasing friction reduction for increasing flow rate, explained by the capability of high speed flows to maintain bubbles closer to the wall. The investigation was further deepened by Clark III & Deutsch (1991), who applied on the same geometry favourable and adverse pressure gradients. Interestingly, the former resulted into an inhibition of the drag reducing ability, while the latter promoted separation even at low bubbles injection rates, resulting into increased friction reduction. Beside the influence on the turbulent momentum transport, which could be also due to bubbles merging and splitting, another mechanism could explain the evidenced friction variations. In fact, the local viscosity of the liquid-bubbles mixture could increase with respect to the liquid value, with subsequent reduction of the local turbulent Reynolds number and increase of the boundary layer thickness. Since bubbles are effective when lying in the near-wall region, this could result into increased effectiveness in reducing friction (Clark III & Deutsch 1991).

One interesting evolution of the proposed bubble injection method arises for large enough injection rate, which can determine bubbles coalescence into a continuous air layer (Ceccio 2010). The phenomenon is exploited by Elbing *et al.* (2008) in a flat plate geometry, showing that once the continuous air layer is established, drag reductions up to 80 % can be achieved. The same typology of test with a discontinuous bed of bubbles determined a drag reduction of $\approx 25\,\%$, spatially limited to the region close to the injection. The same concept was previously exploited

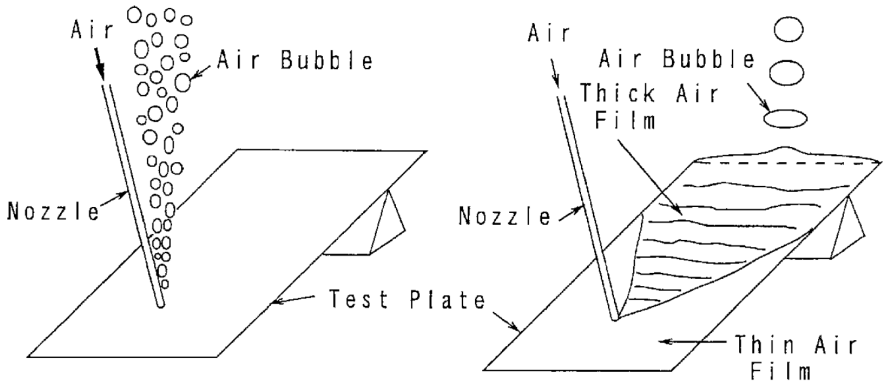

Figure 2.17 – Working principle of the air injection method on (left) reference and (right) hydrophobic surfaces (adapted from Fukuda *et al.* 2000). The hydrophobic coating promotes the establishment of a continuous air layer on the wall and the formation of macroscopic bubbles.

by Fukuda *et al.* (2000), who tried to promote the persistence of the bubbles into the near-wall region by covering a flat plate with a hydrophobic coating. The method, which resulted into the formation of an air layer pinned to the wall and the formation of macroscopic bubbles (see Fig. 2.17), resulted into friction reduction up to 80 % depending on the considered configuration.

Leidenfrost Effect

The discussed methods typically require the injection of air, thus implying an external energy supply to be provided. An air layer can be also sustained by a reverse approach, where energy is supplied directly to the body under the form of heat. This is known in literature as Leidenfrost effect (Leidenfrost 1756), which requires the body to be heated above the boiling temperature of the surrounding liquid. An example of the Leidenfrost effects on the flow around a falling sphere is available in Vakarelski *et al.* (2011), with additional results provided by other publications by the same team in the last decade. The sampled results reported in Fig. 2.18 highlight the influence of the sustained air layer on the onset of the drag crisis. In fact, the results reported in Fig. 2.18(a) for reference spheres lie below the critical Reynolds number range for drag crisis occurrence (see §2.1). Conversely, an air layer sustained by Leidenfrost effect is shown to promote an early onset of drag crisis, with the corresponding abrupt drag coefficient decrease. The phenomenon is confirmed by the detected motion of the separation angle, which progressively moves in the rear-side of the falling sphere. Qualitative confirmation of the analysed phenomenon is provided by the visualisations in Fig. 2.18(b). A sphere heated to a temperature below the Leidenfrost limit shows the typical configuration of the sub-critical regime at terminal velocity, with a separation occurring approximately at the equator (see Fig. 2.18(b)1). The effects of a sustained air layer are already perceptible prior to the achievement of terminal conditions (see Fig. 2.18(b)2). However, the configuration typical of drag crisis is evident once a sphere heated above the Leidenfrost limit reaches terminal velocity, with a separation on the rear-side of the sphere and a narrower wake (see Fig. 2.18(b)3). Some practical drawbacks that limit the applicability of the method are noticed. Since to reach the beneficial drag reduction qualitatively evidenced in Fig. 2.18(b)3 the body has to be heated above the liquid boiling point, typically water cannot be used as working fluid. An an example, Vakarelski *et al.* (2011) used a perfluorinated compound with a

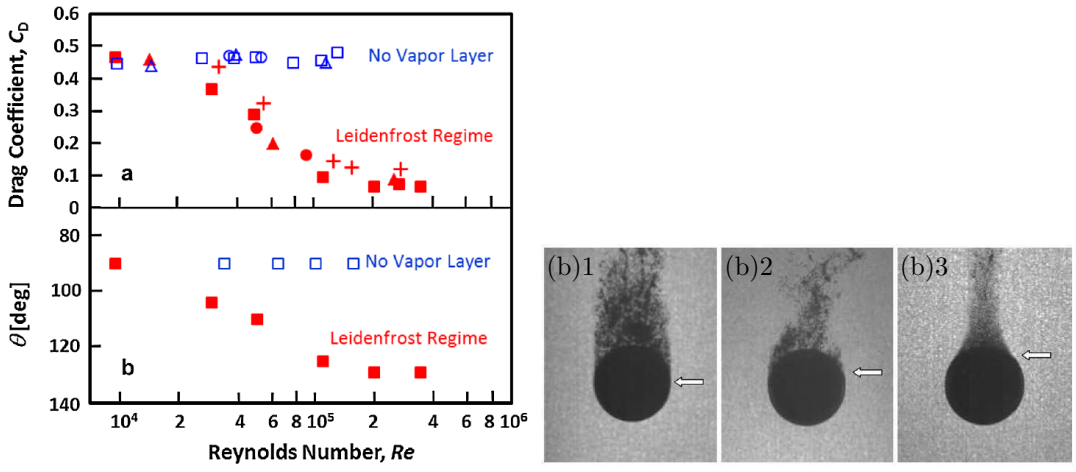

(a) (b)

Figure 2.18 – Influence of an air layer sustained by Leidenfrost effect on free falling spheres (adapted from Vakarelski *et al.* 2011). (a), evolution of the drag coefficient C_D and of the separation angle θ as a function of the Reynolds number Re. (b), wake visualisations: (b)1, terminal velocity and temperature below the Leidenfrost limit, (b)2, velocity lower than the terminal value and temperature above the Leidenfrost limit, (b)3, terminal velocity and temperature above the Leidenfrost limit. The white arrows indicate the position where separation is estimated.

boiling point and a vaporisation heat capacity significantly lower than water. Moreover, even if the point is not discussed by the authors, the sphere heating at $T \sim 10^2$ °C could imply significant local liquid density and viscosity variations, with effects on the estimated Reynolds number. Furthermore, the bubble release evidenced in Fig. 2.18(b) implies that the sustained air layer is progressively carried away by the flow, while simultaneously the sphere temperature drops. A possible solution towards the stabilisation of the air layer was proposed by the same authors (Vakarelski *et al.* 2012, 2013, 2014) by coupling the Leidenfrost effect with a textured SH coating. Promising results in terms of air layer stability with respect to progressively decreasing temperature are shown in the cited articles.

Super-Hydrophobic Surfaces

The common feature of the largest part of the control strategies discussed so far in this section is the requirement of an external energy supply to establish or maintain the air layer, thus classifying them as active methods (see Fig. 2.12). In this case, the obtained gain should always be compared to the energy expended to achieve the desired effect. It appears therefore attractive the possibility to create an air layer between a solid wall and a liquid via a passive method that does not require *a priori* any external energy input. In the following, a brief review of the use of SH coatings towards friction reduction is provided. This allows the introduction of some results available in literature that are used all along the manuscript for comparison purposes. Moreover, some practical issues that need to be elucidated and understood if a practical real-life implementation is sought are introduced. A detailed description of SH coatings is then provided in Chapter 3.

Theoretical, numerical and experimental studies towards the application of SH surfaces for friction reduction in flat wall configurations spread in the last twenty years, at least at lab-

oratory scale (see e.g. Rothstein 2010, and references therein). Numerical works on laminar and turbulent channel configurations typically simulated SH coatings via a Navier partial slip boundary condition (Min & Kim 2004) or by alternating free shear/no-slip regions (Philip 1972; Lauga & Stone 2003; Martell *et al.* 2009). From an experimental point of view, drag reductions up to $\approx 50\,\%$ were evaluated in turbulent channel flow at $Re \sim 10^3$ (based on the channel height) (Daniello *et al.* 2009), additionally underlying the connection between the SH roughness elements size and the viscous sub-layer thickness. However, turbulent flow over flat SH plates at much higher Re ($\sim 10^7$, based on the plate length) was shown to result into drag increase due to the partial or complete depletion of the air layer by the flow (Aljallis *et al.* 2013). The same decrease of drag reducing ability with increasing Re from laminar to turbulent conditions on flat SH plates was experimentally evidenced by Henoch *et al.* (2006). Some techniques effective at laboratory scale were proposed to restore the air layer on SH surfaces once being depleted by the flow. For shallow-water applications, simple control of gas concentration in the liquid or mechanical connection between the SH surface and the ambient air were shown to be effective in the re-establishment of the air layer (Lee & Kim 2012). However, such methods appear impractical in real-life environments. Thermal generation requires a simple electrical heater to locally increase temperature above the liquid boiling point, however it was shown to be energetically disadvantageous and the generated vapour bubbles were shown to be strongly unstable with regard to local temperature decrease (Meng *et al.* 2005). More interesting results were obtained via electrolysis, where bubbles can be generated at a cathode embedded in the solid wall, when a corresponding anode, e.g. a metallic wire, is in contact with the liquid (Stephani & Goldstein 2010). Lee & Kim (2011) developed a self-controlled electrolysis system, where the gas generation automatically activated once the liquid touched the cathode at the bottom of the cavity, i.e. air layer depletion occurred. The power consumption was shown to be order of magnitudes lower than thermal systems.

Overall, this discussion shows that the extrapolation of these results to real-life applications, where flow conditions are more demanding, still needs more efforts (Samaha *et al.* 2012). Preliminary estimations of the air layer stability with respect to external perturbations recently appeared. Piao & Park (2015) analytically investigated the compliance of the air-liquid interface on a single cavity of a SH surface to external pressure fluctuations and air diffusivity into water. The authors performed a description of the interface dynamics via a simplified non-linear oscillator (see Fig. 2.19(a)), finding out that small grooves ($\mathcal{O}(10^0)$ µm) are more robust to interface collapse than larger size elements ($\mathcal{O}(10^1)$ µm). The leading-order pressure fluctuations effect was then shown to be further worsened by air diffusion into the liquid. The same team recently experimentally extended their findings via interference microscopy to analyse the shape of the interface and its evolution towards collapse in a channel flow (Kim & Park 2019). The interface deformation effect was also one of the main results of the experimental investigation by Song *et al.* (2018), which showed how convex interfaces (protruding into the flow) maximised the flow velocity in the proximity of the cavity with respect to concave interfaces (bent inside the groove). The same authors experimentally analysed the effects of the presence of surfactants in the working fluid. In fact, numerical simulations (Cuenot *et al.* 1997; Palaparthi *et al.* 2006) showed that a sufficient amount of contaminants build-up could result into a complete reversal of a free-shear interface to the no-slip counterpart (see Fig. 2.19(b)). Song *et al.* (2018) experimentally showed that the interfacial stresses due to the presence of surfactants (associated with the Marangoni flow) are significant in closed cavities geometries, whereas open cavities prevented surfactants build-up, thus limiting the adverse influence of the surface tension gradient. Similar results on a rectangular closed cavity were numerically and experimentally retrieved by Peaudecerf *et al.* (2017).

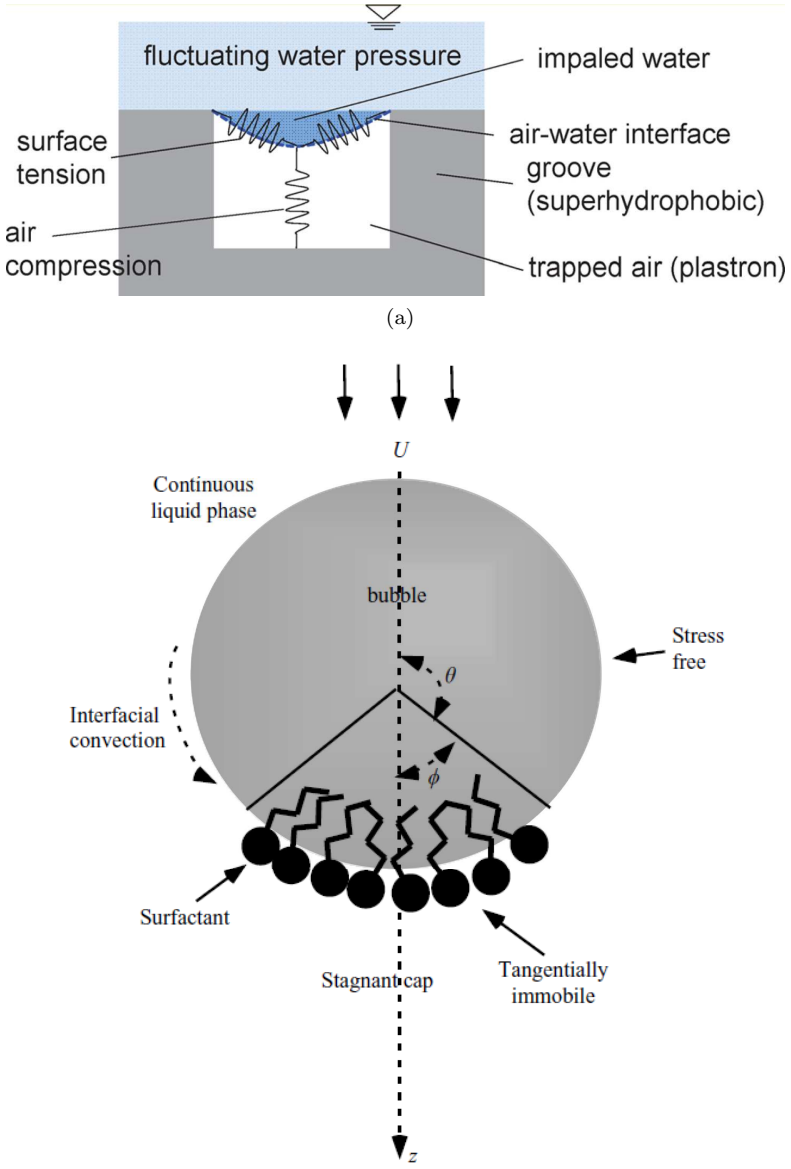

Figure 2.19 – Examples of some practical issues connected to the establishment of an air-liquid interface. (a), 2D oscillator model to describe the compliance of the interface to external pressure perturbations (adapted from Piao & Park 2015). (b), stagnant cap model on the rear-side of a bubble due to surfactants build-up, which could set to zero the tangential velocity on the originally free-shear interface (adapted from Palaparthi *et al.* 2006).

Conversely to internal flows and flat wall geometries, very few works concerning SH coatings effects on external flows over bluff-bodies are available. Moreover, the works identified in literature dealing with the SH coatings effects on spheres typically focused on terminal drag, that is the drag evaluated once the falling sphere reached terminal velocity u_∞ after the initial transient. The corresponding terminal Reynolds number will be indicated hereinafter as $Re_\infty = \frac{u_\infty d}{\nu_l}$. Byon *et al.* (2010) experimentally reported an $\approx 2\,\%$ terminal velocity increase with respect to the reference for SH spheres falling in glycerine in the Stokes' regime ($Re_\infty < 10^{-1}$). The authors analysed SH copper spheres where nano-sized surface roughness elements were created via chemical oxidation. The same regime was studied by Modak & Bhaumik (2017) via SH spheres falling in golden syrup and honey. Similarly to Byon *et al.* (2010), a chemical etching procedure resulted into nano-sized surface roughness elements. Drag of SH spheres was found to vary between the reference value down to $\approx 8\,\%$ decrease. Conversely, the results at $Re_\infty \approx 2 \times 10^{-1}$ reported by Ahmmed *et al.* (2016) on SH nano-laser-textured PTFE (Polytetrafluoroethylene) spheres falling in glycerine showed no drag variations with respect to the reference spheres. Overall, experimental results at low Reynolds number show that a clear trend of SH coatings in terms of terminal drag is not identifiable. This appears even more interesting considering that the corresponding analytical and numerical predictions estimate significant beneficial SH effects. McHale *et al.* (2011) analytically predicted drag reductions up to $30\,\%$ via a simplified model of SH sphere in Stokes' flow made of a solid body encapsulated by a uniform and non-deformable air layer (see Fig. 2.20(a)). An optimal air layer thickness able to maximise the beneficial effect of the air layer presence with respect to the increased form drag was found. The mechanism leading to drag reduction was identified in the ability of the external flow to transfer momentum across the air-liquid interface, thus generating an internal circulation in the ideal air layer. This first step towards the modelling of SH surfaces clearly showed the necessity of models more representative of reality, such as the work proposed by Gruncell *et al.* (2013). The authors performed numerical simulations up to $Re_\infty = 10^2$ using the model introduced by McHale *et al.* (2011) and further refining it via the introduction of baffles in the transverse direction with respect to the flow (see Fig. 2.20(b)). The presence of the solid obstacles resulted into a decrease of the drag reducing ability down to potential drag augmentation, depending on the fraction of solid with respect to the total air layer volume. No data are available in literature in the Re_∞ range $10^2 - 10^3$, which includes the region where wake instabilities are encountered (see §2.1). In fact, the next available results by Ahmmed *et al.* (2016) lie at $Re_\infty \approx 2 \times 10^3$ and $Re_\infty \approx 5 \times 10^3$, showing an $\approx 10\,\%$ u_∞ decrease for SH spheres. Conversely, McHale *et al.* (2009) reported drag decrease up to $\approx 15\,\%$ at Re_∞ in the range $1 \times 10^4 - 3 \times 10^4$, testing SH acrylic spheres with micron-sized surface roughness.

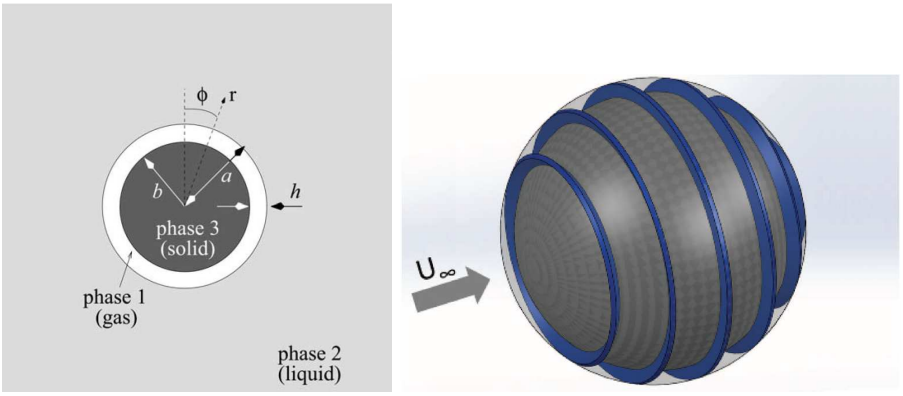

(a) (b)

Figure 2.20 – Models of SH spheres. (a), analytical model with a solid sphere encapsulated by a uniform and non-deformable air layer (adapted from McHale *et al.* 2011). (b), refined model with baffles transverse to the flow direction (adapted from Gruncell *et al.* 2013).

2.3.2 Open Issues

To resume, the reported results clearly evidence that:

1. no experimental work spanning a large Reynolds number range exists at the moment of the redaction of this manuscript in the available literature. This prevents a clear comparison of the effects of the same typology of SH coating in different falling sphere regimes. Does the influence of increasing Re on the nature of the wake discussed is §2.1 and §2.2 result into different interactions with the SH wall? A first attempt to answer to this question is performed via the experimental campaign described in Chapters 4 - 6 for Re spanning five orders of magnitude;

2. being directly connected to the previous point, a clear description of SH effects at least on terminal drag cannot be achieved. Reported experimental results show someway contradictory results, underlying that a full comprehension of SH coatings over bluff-bodies is still missing. How to explain the discordant results on terminal drag? Is it adequate to limit the analysis to terminal conditions? The experimental results in Chapter 6 will show the importance to analyse the available hydrodynamic loads along the whole sphere drop;

3. in addition to the previous raised point, current analytical and numerical models of SH coatings seem to be only able to partially describe the real complex SH surface interaction with the flow. Can we rely on partial/approximated models to numerically describe the SH wall behaviour at challenging realistic conditions? The numerical approach in Chapter 7 can be viewed as a first simple step towards the achievement of a robust modelling of the SH surface behaviour.

Considering the issues listed above as starting point, the following of the manuscript can therefore be interpreted as a contribution to help clarify, at least partially, the identified open questions.

Chapter 3

Super-hydrophobic Coatings

After the general picture on control methods provided in Chapter 2, the discussion is continued by introducing some basic definitions concerning SH coatings. Then, a brief overview of the existing manufacturing techniques is followed by a step-by-step description of the implemented manufacturing procedure. Finally, the coatings characterisation performed in the clean room of the GREMI Laboratory, CNRS-Université d'Orléans, is presented. An innovative optical technique to estimate the thickness of the air layer is reported in Appendix A, showing the preliminary promising raw results.

3.1 Fundamentals

In this section the basic definitions used to characterise the wettability of a solid surface are provided.

The most frequently used parameter to characterise wetting of a solid substrate is the macroscopic static contact angle ϑ_s, which is defined in Fig. 3.1 as the angle that a liquid drop makes with the solid surface. The latter is considered smooth in the general case analysed in Fig. 3.1. As discussed in Bhushan & Jung (2011), a surface is considered *hydrophilic* if $0° \leqslant \vartheta_s \leqslant 90°$, that is the water easily wets the solid (see Fig. 3.1(a)). A typical example is the spreading of water, a highly polar molecule, on non-noble metals (not covered by an oxide layer). As a general rule, hydrophilic materials represent the largest part of the materials existing in nature (Drelich *et al.* 2011). Conversely, when $90° < \vartheta_s \leqslant 180°$, the solid surface is considered *hydrophobic* (see Fig. 3.1(b)). The upper theoretical limit of 180° corresponds to a perfectly spherical drop in contact with the solid surface. Non-polar molecules based on hydrocarbon bonds such as Polyethylene and Polypropylene are examples of the available low-surface energy, hydrophobic materials. Two more refined definitions directly derive from the ϑ_s ranges discussed above. When $\vartheta_s \leqslant 10°$, the strong affinity between the solid material and water is highlighted by calling the material *super-hydrophilic*. Conversely, when $150° \leqslant \vartheta_s \leqslant 180°$, the material is called *super-hydrophobic* (indicated by SH, as was introduced in Chapters 1 and 2). However, these definitions only derive from empirical practice and do not represent absolute thresholds.

In order to reach the high ϑ_s values characterising SH materials, the chemical repellency is not sufficient all alone. The latter has to be coupled with a suitable surface texturing, which means enhancement of the surface roughness. The three situations of interest in this work are resumed in Fig. 3.2. The static contact angle of an ideally smooth reference solid substrate (indicated by the subscript *ref* in Fig. 3.2(a)) can be expressed via the Young equation, which

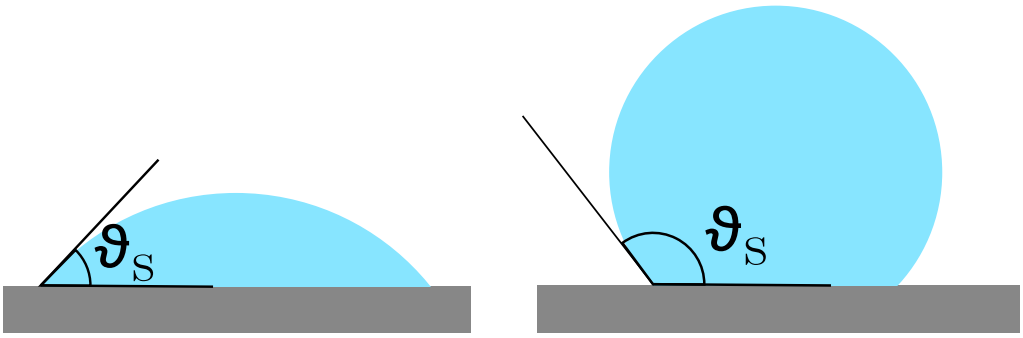

(a) (b)

Figure 3.1 – Definition of the macroscopic static contact angle ϑ_s on a smooth flat surface. (a) hydrophilic surface, $\vartheta_s < 90°$ (b) hydrophobic surface, $\vartheta_s > 90°$.

is retrieved by minimising the net free surface energy of the air (A), liquid (L), solid (S) system:

$$cos\left(\vartheta_{s,ref}\right) = \frac{\gamma_{SA} - \gamma_{SL}}{\gamma_{LA}}, \tag{3.1}$$

where γ indicates the surface tension or free surface energy, and the subscripts represent the two considered phases. Wenzel (1936) experimentally studied the effect of an increase of the surface roughness (a uniform roughness in all directions is considered) on the static contact angle (see Fig. 3.2(b), where it is indicated by the subscript w), achieving the following expression:

$$cos\left(\vartheta_{s,w}\right) = r cos\left(\vartheta_{s,ref}\right), \tag{3.2}$$

where r is the ratio between the actual area of the rough surface and its projection on a horizontal flat surface. The Wenzel model thus predicts an increase of the hydrophobic behaviour for increasing r, in the case of hydrophobic materials ($\vartheta_{s,ref} > 90°$). However, the Wenzel model only considers a uniform liquid-solid interface, where the liquid completely wets the solid material. The case of a heterogeneous interface, where air is trapped between the liquid and the rough solid (see Fig. 3.2(c), where it is indicated by the subscript cb), was analysed by Cassie & Baxter (1944), who determined the following expression:

$$cos\left(\vartheta_{s,cb}\right) = r f_{SL} cos\left(\vartheta_{s,ref}\right) - 1 + f_{SL} = r cos\left(\vartheta_{s,ref}\right) - f_{LA}\left(r cos\left(\vartheta_{s,ref}\right) + 1\right), \tag{3.3}$$

where f_{SL} represents the solid-liquid fraction and $f_{LA} = 1 - f_{SL}$ indicates the liquid-air fraction. An increase of the liquid-air fraction thus results into an increase of the hydrophobic behaviour, in the case of hydrophobic materials ($\vartheta_{s,ref} > 90°$). It is important to underline that the expressions reported in Eqs. 3.2 and 3.3 represent a macro-scale parameter often called *apparent* contact angle (Bhushan & Jung 2011), since it is a convenient macroscopic description of a phenomenon governed by interactions at the micro- and nano-scale. The actual contact angle, often referred to as *microscopic* contact angle, can be different descending down to the nano-scale (Nosonovsky & Bhushan 2008).

A second indication of the degree of hydrophobicity of a material is the force required to remove a drop from the surface. This force is usually provided by the own weight (or a fraction of it) of a drop deposited over the solid surface (Ras & Marmur 2017). The easiest way to implement this test, and the one used in this work, is by tilting the solid plate over which the drop was

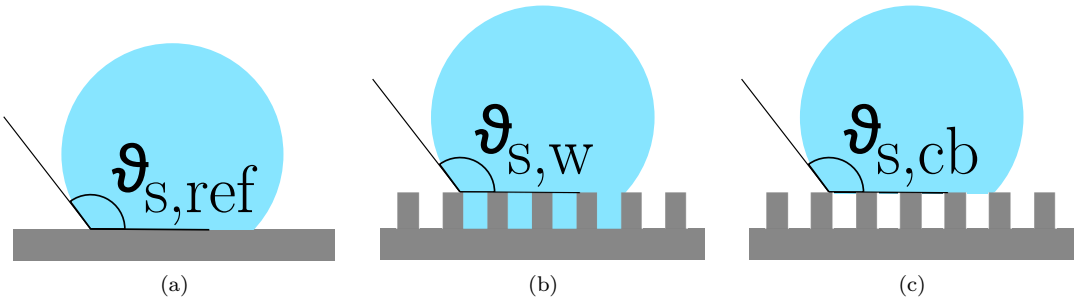

Figure 3.2 – Definition of the macroscopic static contact angle ϑ_s on flat and textured surfaces. (a) reference smooth flat surface, (b) textured fully wetted surface, firstly analysed by Wenzel (1936), (c) textured surface with trapped air among the roughness elements, firstly analysed by Cassie & Baxter (1944).

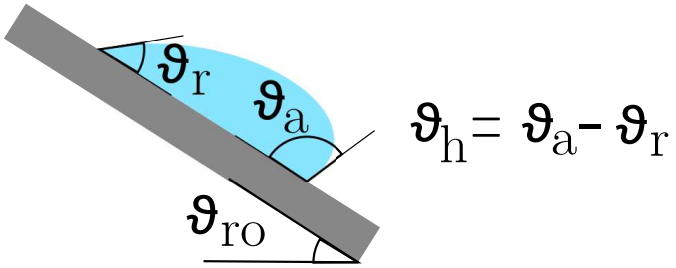

Figure 3.3 – Definition of roll-off angle ϑ_{ro} as the lowest tilt angle that forces the drop to be removed from the solid surface. In the case of SH materials, the drop tends to roll-off rather than slide. The hysteresis angle ϑ_h is defined as the difference of the advancing ϑ_a and receding ϑ_r angles.

deposited until the drop starts to move (see Fig. 3.3). Since in the case of SH materials the drop tends to roll-off rather than sliding, the corresponding tilting angle will be called roll-off angle ϑ_{ro} hereinafter. Values close to 0° are an indication of easiness of removal of the drop from the solid surface. At the roll-off angle, the contact angle at the front of the drop (advancing contact angle ϑ_a) becomes larger than the corresponding angle at the back of the drop (receding contact angle ϑ_r). The difference between the two angles ($\vartheta_h = \vartheta_a - \vartheta_r$, see Fig. 3.3) is called *hysteresis* and is a measure of the energy dissipation in the process of the movement of a drop along a solid surface. In the framework of self-cleaning and drag reducing surfaces, values of ϑ_{ro} and ϑ_h angles as close as possible to 0° coupled with high static contact angles should be achieved. From a macroscopic point of view, even if high $\vartheta_{s,w}$ could result from the homogeneous condition described by Fig. 3.2(b) and Eq. 3.2, the corresponding ϑ_{ro} and ϑ_h angles would be large enough to produce a sticky surface, since the liquid would be strongly pinned at the roughness elements peaks. Conversely, the Cassie-Baxter state described by Fig. 3.2(c) and Eq. 3.3 would result into a slippery surface due to the low ϑ_{ro} and ϑ_h values coupled with the high static contact angle values. As an example, the Lotus leaf exhibits the values $\vartheta_{s,cb} = 164°$ and $\vartheta_h = 3°$ (Bhushan & Jung 2011), which explain the self-cleaning properties of this plant. A brief overview of the manufacturing techniques implemented in the attempt to artificially reproduce the properties of the Lotus leaf is provided in the next section.

3.2 Manufacturing Techniques

In this section, a brief overview of the techniques developed to produce SH coatings is provided, followed by the step-by-step description of the spray coating method implemented in the present study. For further details about the existing manufacturing techniques, the interested reader is referred to the exhaustive reviews by Bhushan & Jung (2011), Zhang *et al.* (2008) and the chapters dedicated to the fabrication techniques in Ras & Marmur (2017). The information provided in the following lines is taken from the cited works and references therein. As discussed in §3.1, a SH surface is the result of the coupling between surface texturing and chemical properties. Since water is characterised by a polar molecule, the suitable hydrophobic material should show a lower surface energy than water and should be constituted of non-polar molecules. Two main approaches can thus be followed to produce a SH coating:

1. increase the roughness of low surface energy materials;
2. create a substrate of a material (no matter its surface energy) with the desired roughness and then coat it with a low surface energy material or modify its surface chemistry.

Since SH surfaces can be obtained even from a moderately hydrophobic material, the critical role on the manufacturing technique is played by the surface roughness. Therefore, Fig. 3.4 (adapted from Bhushan & Jung (2011), p. 37) resumes the main techniques available to modify the surface roughness of a raw smooth material.

Lithography is a method invented at the end of the 18^{th} century to print text or artwork. The modern micro- and nano-lithography techniques are able to generate a pattern of periodic elements down to the nano-scale. The method can be based on a pre-fabricated mask from which the final pattern is derived, as in the case of photo- and soft-lithography, or on a beam of electrons or X-rays controlled by a computer. As a general rule, the process is very accurate, can produce macroscopic surfaces (depending on the specific technique) but at high cost and large processing time.

Etching is a common alternative to make a rough surface and can be based on plasma, laser, chemical or electrochemical techniques. It can produce both anisotropic and isotropic roughness, the former being more limited in the type of geometry produced. A practical etch rate of $5\,\mu\mathrm{m\,min}^{-1}$ of a plasma etching to produce sparse pillars is reported in Ras & Marmur (2017). The etching technique generally allows a less accurate control of the produced elements with respect to lithography.

The deformation of an existing material, e.g. by stretching, is a simple and cheap technique to modify the surface roughness. However, the accuracy of the produced elements is poor.

The deposition of materials by multiple available techniques, casting, imprinting are all cheap and flexible procedures but assuring a lower control of the final roughness. However, the deposition techniques can be also used to coat a suitable layer of a low surface energy material over a substrate. An interesting opportunity is the dispersion of micro- or nano-particles in a polymer matrix, which can then be sprayed on a substrate and reach the desired properties via a curing process (see Ras & Marmur (2017), Chap. 4). The surface chemistry of the produced SH surfaces can be further modified by exposing the material to ultra-violet light or plasma (see Ras & Marmur (2017), Chap. 7). This technique is interesting to locally pattern the surface, for practical applications such as water collection from the humid air, or the movement of liquids by surface tension gradients in micro-devices. The complementary approach of removing material from a low surface energy substrate to create surface roughness was demonstrated to be effective by Nilsson *et al.* (2010) applying sandpaper with different grain size over Polytetrafluoroethylene (PTFE). The deposition and abrasion techniques may be suitable to produce randomly distributed surface roughness over large macroscopic surfaces. Since the former is the kind of

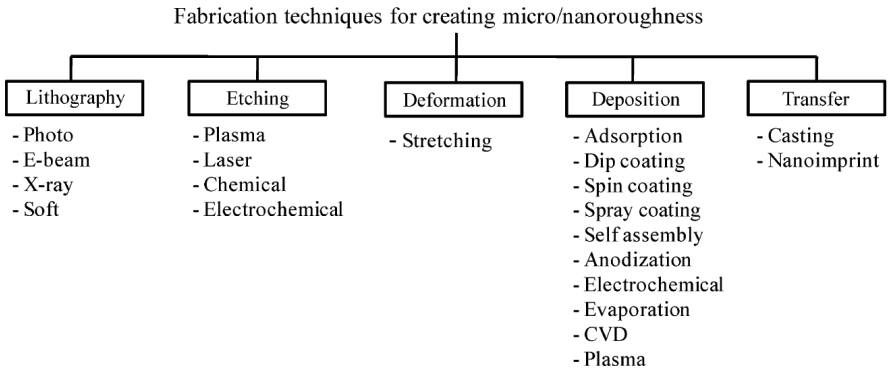

Figure 3.4 – Techniques to modify the surface roughness of a material (adapted from Bhushan & Jung 2011).

applications investigated in this study, a spray coating method was implemented, as described in the following paragraph.

3.2.1 Spray Coating Method

The wide range of manufacturing procedures briefly discussed above shows that, depending on the selected technique, either regular or random patterns of micron-sized and/or nano-sized structures can be produced at the surface. In most cases, the samples studied are flat surfaces with typical dimensions suitable for laboratory analysis. However, a large number of techniques mentioned above are not suited as far as curved and large size surfaces are concerned. This is the reason why a spray coating method (McHale *et al.* 2009; Aljallis *et al.* 2013; Kim *et al.* 2015) was used to produce the SH coatings in this study. The SH properties were obtained by depositing a commercially available product, Ultra-Ever Dry® (UltraTech International, Inc. 2019). The latter consists in two layers (*bottom* and *top*) to be successively applied to the surface. It is presented on the form of a polymer (proprietary, no information available) diluted into a mixture of solvents (i.e. xylene, acetone, butyl acetate). Once sprayed, the solvents exposed to ambient air evaporate, thus leaving the cured polymer on the surface. To provide the reader an idea of the characteristics of the described method, at the moment of the redaction of this manuscript 1 l of bottom and top coatings cost around 200€, with a coverage of $\approx 6\,\mathrm{m}^2$. Several attempts, often unsuccessful, were made at the beginning of the thesis to adapt the described working principle of the coating to the curved spherical geometry here considered. The main difficulties arose from the necessity of assuring a uniform coating around the whole sphere surface. The final configuration thus required the deposition of the sphere over a mechanical holder made of three needles in order to limit the contact area with the surface and assure satisfactory sphere stability during manufacturing. The holder was turned during spraying and the sphere was flipped upside down to cover all the portions of the surface. The implemented manufacturing procedure, valid both for spheres and flat plates, was therefore designed as follows:

1. the reference material surface (indicated as NC, No Coating) was first cleaned with a suitable solvent, that is acetone in the case of stainless steel and ethanol-based alcohol in the case of transparent optical glass. The surface was then rinsed with double-distilled water and finally air dried;

2. an etch primer (Ultra-Ever Dry® bottom coating) was uniformly sprayed over the surface;

(a) (b) (c)

Figure 3.5 – Images taken during the manufacturing procedure of a $d = 10\,\text{mm}$, SH-220 sphere. (a), reference stainless steel sphere after cleaning (step 1 of the procedure), (b) intermediate layer made of the P220 powder (step 3 of the procedure), (c) qualitative evidence of the presence of the air layer around the SH sphere once immersed in pure water.

3. an intermediate layer made of a carbon-based powder was deposited onto the surface in order to control the surface texture. To facilitate the embedding, this point was performed when the bottom coating was still sticky, that is right after the execution of the previous step;

4. the etch primer was sprayed again over the intermediate layer and then air dried for at least 1 hour with a double purpose: firmly stick the powder to the surface and provide a consistent material for the SH coating to bond;

5. the SH properties were obtained by spraying the Ultra-Ever Dry® top coating over the surface and letting it air dry. The dry time required to reach the desired SH properties was at least 2 hours. Typically, one whole night dry time was imposed.

Two different carbon-based powders with grade P220 and P80 (ISO, International Organization for Standardization nomenclature) were employed as intermediate layers in this study. The nominal particle diameter was $\approx 70\,\mu\text{m}$ and $\approx 200\,\mu\text{m}$, respectively. The resulting coatings are therefore labelled SH-220 and SH-80 hereinafter. In addition, SH spheres without intermediate powder layer were produced by skipping steps 3 and 4 of the above procedure. This coating will be referred to as SH-NAR (No Additional Roughness) in the following. The sequence of images in Fig. 3.5 resumes some of the steps discussed in the above manufacturing procedure. The reference stainless steel sphere after cleaning (see Fig. 3.5(a)) is covered by a carbon-based powder (P220 in Fig. 3.5(b)) and after achieving the SH properties shows an air layer around the surface when immersed in water (see Fig. 3.5(c)). The shiny appearance can derive from light reflection and refraction at the air-water interface. The properties of the produced coatings are discussed in the next section.

3.3 Coatings Characterisation

This paragraph resumes the techniques used to characterise the manufactured SH coatings. Due to the difficulty of testing curved surfaces, transparent flat plates covered by the different SH coatings were used. The goal of this section is to provide useful information about the main quantities that influence the hydrodynamic performance of the SH coatings, which are discussed in Chapter 6. Initially, the evaluation of the typical length scale of the surface roughness elements is shown via 3D digital microscopy measurements. Then, the description of the SH behaviour via the angles introduced in §3.1 is discussed via digital goniometer tests. These tests were executed in the clean room of the GREMI Laboratory, CNRS - Université d'Orléans.

3.3.1 Digital Microscopy

The results shown in this section were obtained by using a *Keyence VHX-5000* digital microscope. This instrument was chosen because it allowed the acquisition of 3D models of the analysed surface with a very large depth of field ($\sim 10^2$ µm) and a very high spatial resolution in the normal direction to the surface (down to 5 µm). The objective *VH-Z500T* that allowed a magnification up to 5000x at an observation distance of 4.4 mm was used. Blank tests were performed in order to find the most suited lightning configuration. The results shown here were obtained by combining the light coming from the objective itself and the transmission light coming from the holder where the sample was placed. Both light sources were of LED (Light-Emitting Diode) type.

Preliminary Operations

Once entered the clean room having followed all the instructions concerning the clothing, the first operation to do was the switching on of the microscope and of the objective in order to launch the starting procedure. Since transmission light was also used, the sample holder used was the transparent one. The latter was manually shifted up to the highest height (closest position to the objective) and the objective cap was removed. The *autofocus* procedure was launched in order to let the microscope software make its self-calibration.

Test Phase

The flat plate sample was put in position on the transparent holder. The horizontal position on the holder could be varied manually for macroscopic shifts (e.g. to cover different zones of the sample) or by the joystick controller for refined displacements. The results shown here were obtained by performing at least three different scans over different areas of the analysed sample. This number was chosen as a compromise between statistical relevance, total time required by the tests and total size of the generated files. Before using the 3D reconstruction tool, the area around the centre of the image was examined in order to check the focus, which could be set manually or automatically by the software. The key point of the 3D reconstruction tool is the manual inspection of the limits of the depth of field required to accurately detect all the rough elements inside the image. For that, the focus was manually varied between the farthest and the closest element to the objective (see Fig. 3.6(a)). The two corresponding heights were entered into the software as the limits to be used for the 3D reconstruction in the wall-normal direction. The scanning method rotating around the centre of the image was then selected: the holder automatically shifted around the centre adding at each step one new image (of the same size than the first one) to the whole model (see Fig. 3.6(b)). At each step, a scan in the wall-normal direction was performed to reconstruct the roughness elements. The scan was stopped when a 3D model covering an $\approx 1.5 \times 1.0$ mm^2 portion of the sample was obtained. This size guaranteed a statistical relevance to be achieved (sample size at least one order of magnitude larger than the roughness elements) and was a good compromise with respect to the total file size. The latter could then be saved and downloaded to an external device.

Post-Processing

Even if the *Keyence VHX-5000* software allows for some post-processing to be performed directly on the microscope (e.g. profiles sampling), the approach followed in this work consisted in saving the recorded 3D models and process them later via a home-built code in MATLAB®. An example of the reconstructed 3D models is shown in Fig. 3.7 for the three produced coatings. It

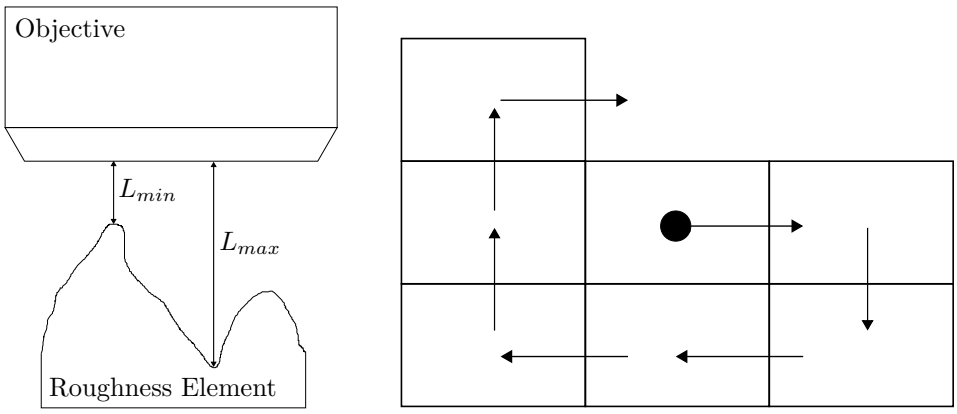

Figure 3.6 – 3D digital microscopy scanning details. (a), the shortest (L_{min}) and longest (L_{max}) distance from the objective were set in order to define the limits of the 3D reconstruction in the wall-normal direction. (b), the complete sample was constructed by shifting around the first central image, indicated by the black circle.

clearly emerges that the inclusion of powders determines an increase of the roughness size. The maximum peak height increased from $\approx 50\,\mu m$ in the case of the SH-NAR coating (Fig. 3.7(a)) up to $\approx 370\,\mu m$ for the SH-80 coating (Fig. 3.7(c)). In all cases, the manufactured coatings resulted into a random distribution of the surface roughness.

A quantitative characterisation of the surface texture was obtained by evaluating the root-mean-square surface roughness:

$$\lambda = \sqrt{\frac{1}{N}\sum_{i=1}^{N} z_i^2}, \tag{3.4}$$

where z_i represents the local roughness height and N the total amount of pixels in the image. In practice, the 3D model in Fig. 3.7 was converted into the corresponding 2D wall-normal projected grayscale image (see Fig. 3.8), where each pixel stored information on the local z_i, thus enabling the λ estimation. This analysis was repeated on different areas of the same sample and on different produced samples, thus providing the statistically relevant values reported in Tab. 3.1. The λ values increase from $\approx 25\,\mu m$ in the SH-NAR case up to $\approx 142\,\mu m$ for the SH-80 coating.

Moreover, a profilometer approach was followed to analyse the height/width ratio of the roughness elements in order to estimate an eventual significant anisotropy. This was of fundamental importance in the following of the manuscript where a characteristic length of the surface roughness had to be chosen to scale the obtained results. An example of a profile extracted from the 3D model shown in Fig. 3.7 is reported in Fig. 3.9 for all analysed SH coatings. As appears from the sampled profiles, the λ value introduced in Tab. 3.1 can be considered representative of both the horizontal and vertical sizes of the roughness elements. Even if the horizontal width of the elements was found to be sometimes larger than the corresponding height, both kept on average the same order of magnitude. This was due to the completely random nature of the implemented coating procedure. A further confirmation of the meaningfulness of choosing λ as the characteristic dimension of the randomly distributed roughness is provided in Fig. 3.10, where a schematic of the approach followed to estimate the horizontal size of the roughness

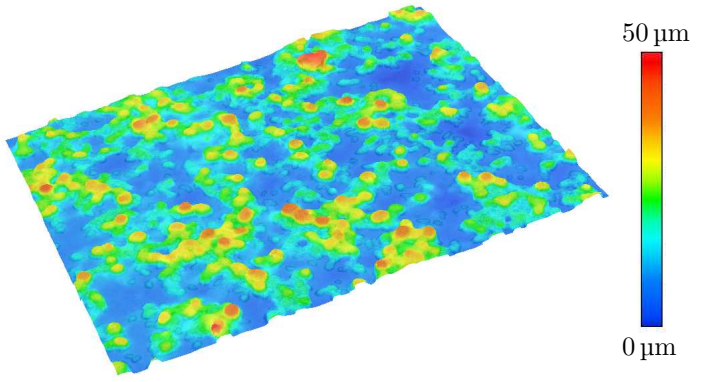

(a)

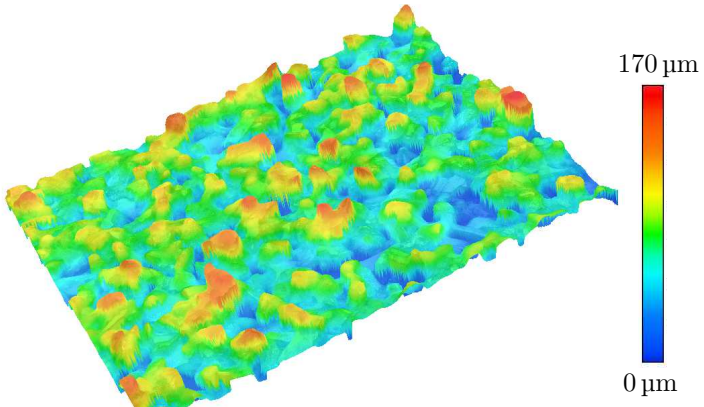

(b)

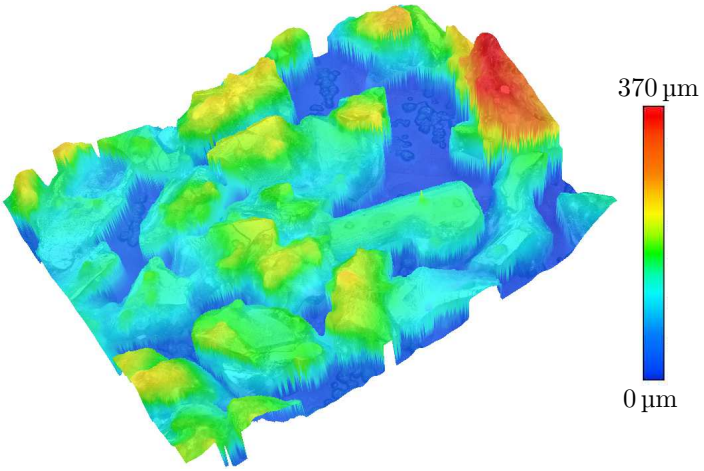

(c)

Figure 3.7 – 3D digital microscopy images of a portion ($\approx 1.5 \times 1.0$ mm^2) of a flat plate covered with a SH coating. (a), SH-NAR. (b), SH-220. (c), SH-80. The color scales indicate the range of surface roughness. All the coatings resulted into a random spatial distribution of the roughness elements.

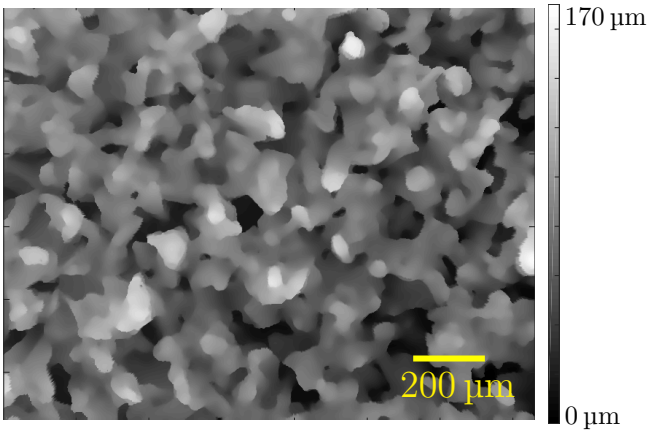

Figure 3.8 – 2D grayscale image obtained from the 3D digital microscopy model. The case of the SH-220 coating shown in Fig. 3.7(b) is reported.

	SH-NAR	SH-220	SH-80
λ, [µm]	25 ± 4	74 ± 12	142 ± 23
h_r, [µm]	-	77 ± 22	183 ± 96
h_s, [µm]	-	116 ± 48	209 ± 99
ϕ_{LA}	0.59 ± 0.06	0.54 ± 0.06	0.55 ± 0.05

Table 3.1 – Quantitative results of the 3D digital microscopy analysis over the manufactured SH coatings. λ, root-mean-square surface roughness. h_r, horizontal size of the roughness elements. h_s, horizontal spacing of the roughness elements. ϕ_{LA}, gas fraction. The reported uncertainties represent the 95% confidence level. The missing values in the SH-NAR coating are not reported since considered not reliable, due to limitations of the adopted technique.

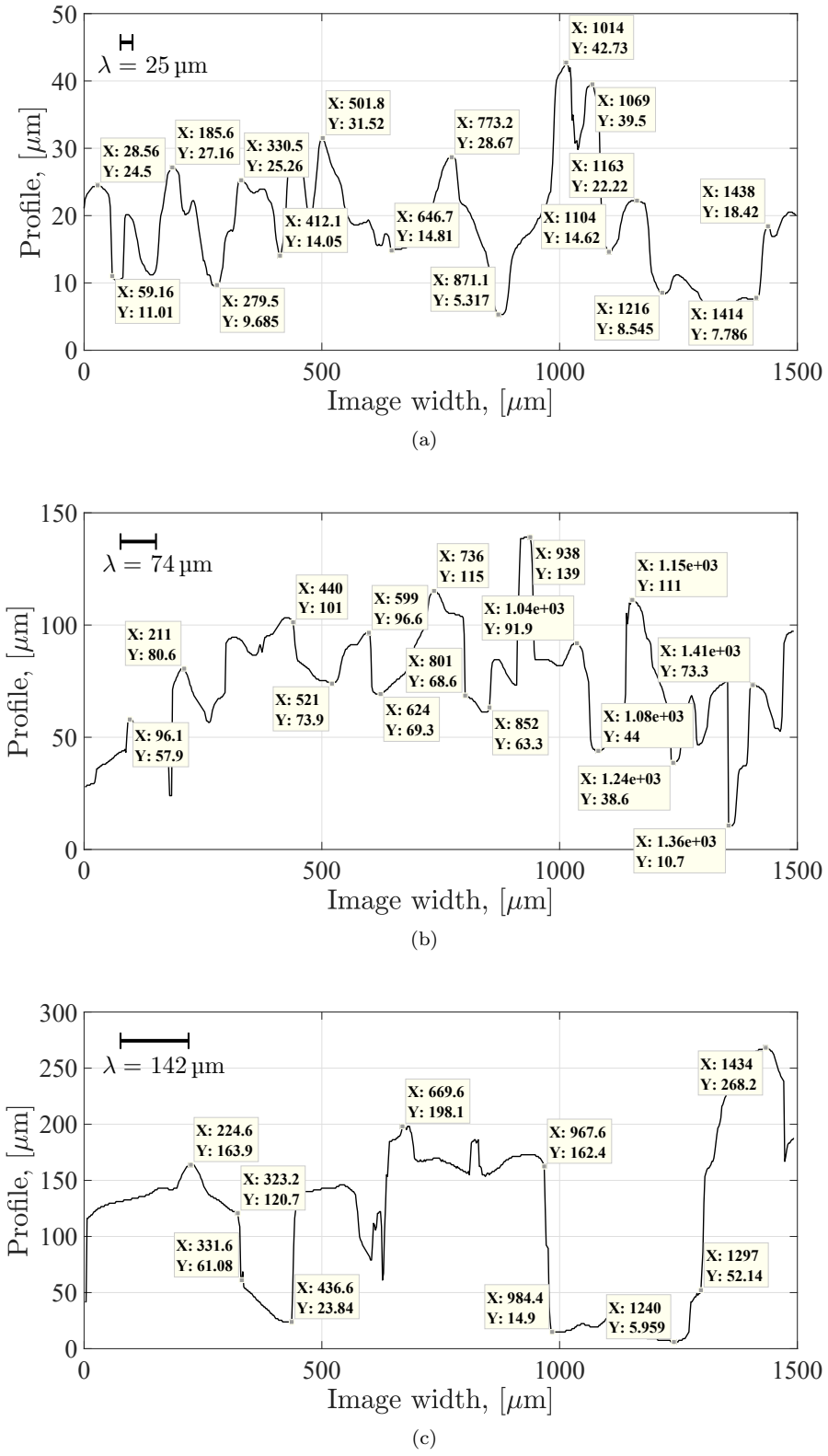

Figure 3.9 – Profilometer approach on 3D digital microscopy images. (a), SH-NAR. (b), SH-220. (c), SH-80. The black bars indicate the corresponding surface roughness λ. The same behaviour is retrieved by multiple profiles along the length of the available images.

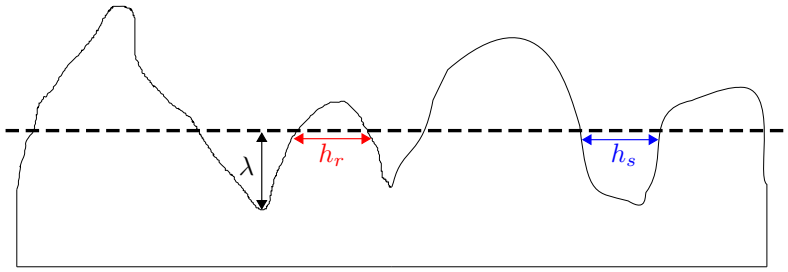

Figure 3.10 – Schematic of the characteristic dimensions of the randomly distributed surface roughness. λ, root-mean-square surface roughness evaluated via Eq. 3.4. h_r, horizontal size of the roughness elements. h_s, horizontal spacing of the roughness elements.

elements h_r and the corresponding spacing h_s is shown. The two parameters were evaluated by progressively sampling the roughness profiles on the available images and then calculating the root-mean-square of the obtained values. The corresponding values reported in Tab. 3.1 indicate that both h_r and h_s show the same order of magnitude than λ. However, the limits of the present analysis are also evident. Setting the height at which h_r and h_s are evaluated equal to λ always results into larger estimated values than the corresponding λ. This could be at least qualitatively in agreement with the images previously shown in Fig. 3.7. However, a limited motion of the imposed threshold was found to result into significant variations of the h_r and h_s values. Moreover, the large uncertainties associated to the estimated h_r and h_s values indicate that the proposed technique is extremely sensitive to local roughness modifications with respect to the average behaviour. The large h_s values are also due to the fact that the available 2D images where sampled along the image width and height, whereas the roughness elements could be aligned along transversal directions. The resulting evaluated spacing could thus be overestimated. That was the case of the SH-NAR coating, where the limited λ value resulted in to a non-significant h_r and h_s estimation. Overall, these considerations imply that, if interest is focused on a complete characterisation of the produced coatings texture, more adapted experimental techniques (e.g. Atomic Force Microscopy) should be implemented.

One final exploitation of the microscopy images can be derived by making an assumption on the position of an ideally flat air-liquid interface. In fact, the position of the pinning of the interface could theoretically vary from the maximum valley depth (fully wetted wall, see §3.1) up to the maximum peak height. While the first case corresponds to the Wenzel state, which is not of interest for SH coatings with an existing air layer, the latter is an upper limit. As a first guess, the assumption that the interface lies at the height λ can be made. Following this path, the grayscale images used for the λ evaluation (see Fig. 3.8) were further processed by executing a binarisation with the threshold set exactly equal to the λ value of each coating. An estimation of the solid fraction ϕ_{SL} could thus be achieved by evaluating the ratio between the surface lying above the λ threshold and the total projected surface. Therefore, the gas fraction ϕ_{LA} could be evaluated as:

$$\phi_{LA} = 1 - \phi_{SL}. \tag{3.5}$$

The average values reported in Tab. 3.1 indicate an approximately constant ϕ_{LA} for varying λ: the variations of the mean values of the different coatings lie inside the uncertainties of each measurement.

3.3.2 Digital Goniometer

In this section, the results obtained using a *MCAT Digidrop* digital goniometer are discussed. This instrument allowed the characterisation of the hydrophobic nature of a material by depositing a small liquid droplet on a solid surface. The basic components of the apparatus are an holder where the sample was placed, a syringe and a needle used to create and deposit the droplet and a camera to visualise and record the test. The available low-speed camera was able to record videos up to 50 fps and the installed objective could assure a maximum magnification of 20x. The range of measurable static contact angles went from 0° for super-hydrophilic surfaces up to the limit of 180° in the case of a SH surface.

Preliminary Operations

As in the case of the microscopy measurements, all the instructions to enter the clean room and correctly clothing had to be followed. First, the correct syringe, depending on the tested liquid, had to be chosen. To avoid any possible contamination, the protocol of the clean room involved the complete emptying of the syringe, whose liquid had to be dismissed in the proper vessel. A cleaning of the syringe with isopropyl alcohol was followed by rinsing with distilled water for three times. The syringe could then be filled with the desired liquid and mounted on its support. Power could then be given to the camera, its light and the computer. A calibration was executed by taking as reference size the needle diameter, which had to be previously measured with a calibre. Before starting the tests execution, it is advised to start the emission of the liquid from the needle to assure that eventual air is removed from the interior of the syringe. Since the deposition of a small volume droplet on a SH surface via a standard steel needle could be problematic (the liquid interacts more easily with the needle tip than with the SH surface), the use of a PTFE needle or a coating of the tip with paraffin (Drelich 2013) could facilitate the tests implementation.

Test phase

The required elements for a proper execution of the tests are resumed in Fig. 3.11. First, the position of the sample holder was adjusted in order to slightly enter on the bottom side of the image. Second, the needle was displaced inside the field of view of the camera by the controller on the software. Both these elements were used to adjust the camera focus. Then, the ejection/injection controller was activated in order to produce a droplet of the desired volume. The flow rate should be low enough (typically $\mathcal{O}(10^{-1})$ µl s^{-1}) to assure the control of the drop total volume, which was estimated via the software thanks to the previous calibration. In case of overshoot of the desired volume, the injection mode could be set to aspirate the exceeding quantity. The required droplet volume should be large enough to assure the drop to be larger than the surface roughness elements and small enough to assure gravity not to dominate over surface tension. To this end, the capillary length ℓ_c can be estimated as follows:

$$\ell_c = \sqrt{\frac{\gamma}{\Delta\rho g}}, \tag{3.6}$$

where γ is the surface tension of the fluid interface and $\Delta\rho$ is the density difference of the two fluids. As an example, considering distilled water and air at 20 °C, the value $\ell_c \approx 2.7$ mm is obtained. If this value is considered as the largest tolerable diameter, the corresponding drop volume would be $V \approx 10$ µl. For this reason, a droplet of $V \approx 6$ µl was used in this study, as shown in Fig. 3.11. Finally, the needle was lowered until the droplet touched the surface (see Fig. 3.11). Once the interaction was established, the needle could be raised and the drop

should keep in position on the surface. The macroscopic static contact angle ϑ_s could be directly evaluated via the software or equivalently an image could be recorded and later post-processed. For the roll-off ϑ_{ro} and hysteresis ϑ_h angles a video was recorded at 50 fps while tilting the holder of the flat plate at a controlled rate of 8.7×10^{-3} rad s^{-1}. The resulting images sequence was post-processed in MATLAB®. An example of frames sampled from a recorded sequence over a SH-220 flat plate is shown in Fig. 3.12. Starting from the horizontal position in Fig. 3.12(a), the holder is tilted in the clockwise direction until the drop starts to roll-off (see Fig. 3.12(b)). Once the drop starts to move, the low recording rate of the camera quickly results into blurred images (see Figs. 3.12(c) and 3.12(d)).

Post-processing

As discussed by Zhang *et al.* (2008), different types of post-processing applied to the same image would lead to different absolute values of the static contact angle ϑ_s. This is due to the fact that the latter is usually evaluated as the angle between the tangent to the drop and the solid substrate (see Fig. 3.1). The question of what type of shape should be used for the fitting of the drop arises. In detail, Zhang *et al.* (2008) showed that a Young-Laplace fitting generally led to higher ϑ_s values than elliptical and circular fitting. When comparing results of different studies, it is therefore important to underline the used technique. Moreover, once the same technique is applied to all the available images, the relative ϑ_s variation among the different coatings is more meaningful than the absolute value. Since no detailed information was available about the *polynomial* fitting executed on the *MCAT Digidrop* software, the results obtained directly on the digital goniometer were compared with a built-in script developed in MATLAB® where a circular fitting on each side of the drop in contact with the solid surface was performed (see Fig. 3.13). The main steps of the implemented code are the following:

1. load the recorded image and convert it to grayscale;
2. identify the edges of the image: detect the local points where the gradient in the image is maximum, by using a Sobel algorithm for the spatial derivative approximation;
3. perform a least-mean squares circular fit of the bottom-left side of the drop by using the algebraic fit algorithm developed by Pratt (1987). This code was chosen since it performed well even by providing as input data only a small portion of a circle;
4. follow the same approach of the previous step for the bottom-right side of the drop;
5. perform a least-mean squares linear fit of the points constituting the solid surface edge to generate an horizontal line describing the SH surface;
6. find the intersections between the two circles and the horizontal line;
7. find the tangent line to the circle that passes through the intersection point, for both the left and right sides;
8. evaluate the angles between the tangent lines to the circles and the horizontal line.

The ϑ_s was evaluated as the average of the left and right contact angles, which typically differed by less than 1% for tests over non-tilted flat plates. The approach based on fitting a circle for both the left and right sides of the drop was chosen to take into account the drop deformation induced by gravity, which was not completely eliminated even considering drop volumes below the threshold identified via Eq. 3.6. The results of the implemented algorithm are compared in Tab. 3.2 with the values evaluated via the *MCAT Digidrop* in the case of distilled water as

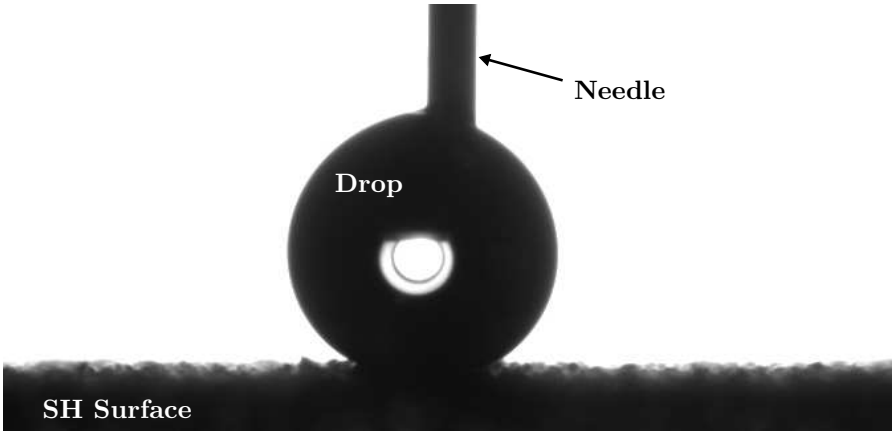

Figure 3.11 – Image taken during the tests at the digital goniometer over a SH-220 flat plate. The incoming light from the camera illuminates the SH surface at the bottom of the image, the drop ($V \approx 6\,\mu l$) and the needle.

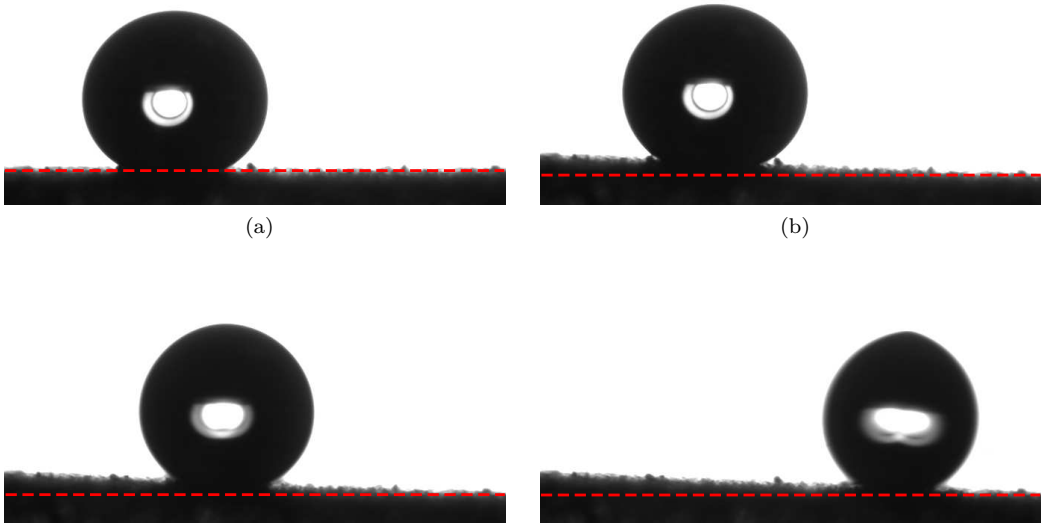

Figure 3.12 – Frames sampled from a sequence recorded at the digital goniometer to estimate the roll-off and hysteresis angles of a water droplet over a SH-220 flat plate. (a), holder in the horizontal position at the beginning of the test. (b), onset of droplet motion, where the angles are estimated. (c) and (d), once the droplet accelerates, the image quickly becomes blurred due to the limited camera recording rate. (- - -), indication of the horizontal direction.

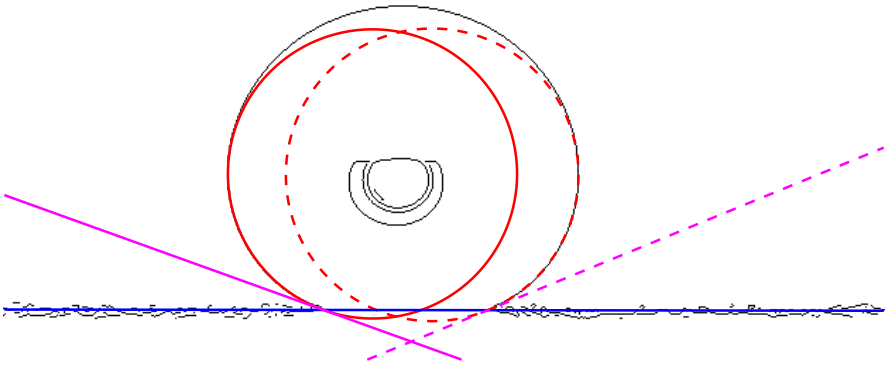

Figure 3.13 – Post-processing of one image taken during the tests at the digital goniometer over a SH-NAR flat plate. ——, edges detection of the drop and of the SH solid surface in the original image. The lines at the drop centre are related to the reflection of the incoming light from the camera, see Fig. 3.11. ——, least-mean squares fit of the SH surface edges. ——, least-mean squares fit of the drop bottom-left side. - - -, least-mean squares fit of the drop bottom-right side. ——, tangent line to the fitted circle on the drop bottom-left side passing through the intersection with the horizontal SH surface. - - -, tangent line to the fitted circle on the drop bottom-right side passing through the intersection with the horizontal SH surface.

	SH-NAR	SH-220	SH-80
MCAT Digidrop	160.7 ± 2.8	150.1 ± 3.0	145.7 ± 2.0
MATLAB®	162.2 ± 2.9	152.2 ± 2.9	144.8 ± 1.5

Table 3.2 – Comparison of the static contact angle (ϑ_s, [°]) values evaluated via the *MCAT Digidrop* software and the home-built code developed in MATLAB®. The reported uncertainties represent the 95% confidence level.

testing liquid. A good agreement between the two methods is noticed, since the differences among the average values lie inside the evaluated uncertainties. Moreover, an influence of the surface roughness on the code performance was noticed. As shown in Fig. 3.14, the larger surface roughness of the SH-80 coating might influence the detection of the intersections between the lines shown in Fig. 3.13. Since the drop was deposited at each performed test on a different location over the plate, local surface roughness variations should be overall averaged, thus mitigating the possible effects of the identified issue.

This algorithm was further exploited to evaluate the tilting angle that caused the drop to roll-off (ϑ_{ro}) and the corresponding hysteresis angle ϑ_h. The image used to evaluate these two angles was the last available frame before the drop rolled-off (see Fig. 3.12(b)). In fact, due to the relatively low frame rate achievable by the camera, the drop resulted blurred when accelerated toward the lower part of the image (see Figs. 3.12(c) and 3.12(d)). The least-mean squares linear fit in step 5 of the above code was used to evaluate the tilt angle ϑ_{ro} of the SH flat plate. Then, the difference between the advancing and receding angles retrieved in step 8 was evaluated to calculate ϑ_h. The ensemble of the evaluated angles is resumed in Tab. 3.3 for the cases of distilled water and glycerine as working liquids, which are the two baseline liquids used in pure or mixed form to test the SH spheres (see Chapter 4). The ϑ_s values for distilled

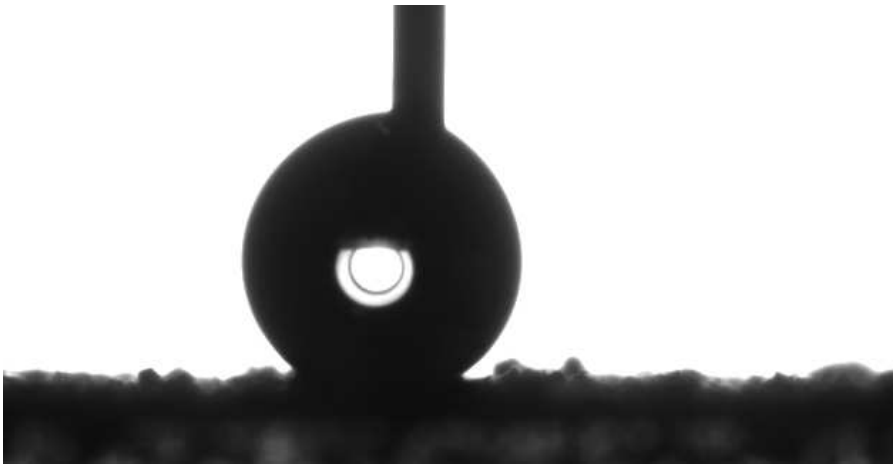

Figure 3.14 – Image taken during the tests at the digital goniometer over a SH-80 flat plate. The large surface roughness might influence the estimation of the contact angles with respect to the less challenging configuration of the SH-NAR coating shown in Fig. 3.11. To mitigate the effects of local surface roughness variations, the drop was deposited on several locations over the flat plate.

		SH-NAR	SH-220	SH-80
Water	ϑ_s, [°]	160.7 ± 2.8	150.1 ± 3.0	145.7 ± 2.0
	ϑ_{ro}, [°]	1.6 ± 0.2	2.4 ± 1.0	5.4 ± 3.2
	ϑ_h, [°]	2.3 ± 0.5	4.3 ± 2.0	11.9 ± 3.6
Glycerine	ϑ_s, [°]	156.4 ± 5.8	147.3 ± 7.6	136.7 ± 12.0
	ϑ_{ro}, [°]	2.6 ± 0.8	2.3 ± 0.8	5.4 ± 2.6
	ϑ_h, [°]	2.7 ± 0.7	4.1 ± 2.3	13.2 ± 4.7

Table 3.3 – Quantitative results of the digital goniometer tests on the manufactured SH coatings. ϑ_s, static contact angle. ϑ_{ro}, roll-off angle. ϑ_h, hysteresis angle. The reported uncertainties represent the 95% confidence level. The values are reported for the two cases of distilled water and pure glycerol.

water show that a λ increase resulted into a static contact angle reduction, down to $\vartheta_s \approx 146°$ in the case of the SH-80 coating. Similarly, a λ increase determined an increase of both ϑ_{ro} and ϑ_h. This can be explained by the fact that a larger λ may cause the liquid to be more strongly pinned at the roughness elements peaks. The slight ϑ_s diminution in the case of glycerine with respect to water testifies that the produced coatings were able to preserve the SH behaviour. The average ϑ_{ro} and ϑ_h for glycerine agree with the corresponding water values, the difference lying within the evaluated uncertainties.

Chapter 4

Experimental Set-up

This chapter describes the experimental set-up designed to perform the falling sphere experimental campaigns in PRISME Laboratory. First, details about the experimental rig, the recording technique and the test execution are provided. The main output of these procedures, which is an image sequence storing the 3D motion of the falling body, allows the discussion of some basic notions describing the free fall of spheres, which will be useful in the following of the manuscript. Finally, the performed discussion justifies the choice of the properties of the tested spheres and liquid mixtures.

4.1 Experimental Rig

The falling sphere experiments were performed in a transparent Poly(methyl methacrylate) (PMMA) tank. The scheme of the experimental rig is shown in Fig. 4.1. The PMMA was chosen as a compromise between suitable mechanical and optical properties. The tank is characterised by a square cross-section whose width measures 100 mm and by a height of 650 mm. The square shape was preferred to cylindrical walls in order to avoid optical distortion. The sphere position at the beginning of the test was remotely controlled by an electromagnetic holder that was used to gently dip the sphere beneath the liquid surface. This choice was made possible thanks to the use of ferromagnetic reference spheres. Blank tests were performed to exclude any significant influence of the electromagnetic field and of the holder sting on the sphere drop. The temperature of the liquid was monitored by a thermocouple, whose position could be shifted from right below the liquid surface down the bottom of the tank, in order to detect eventual temperature gradients along the channel height. The average temperature of the liquid was $\approx 20\,^{\circ}\mathrm{C}$, with vertical gradients along the tank height $< 2\,^{\circ}\mathrm{C\,m^{-1}}$. The beginning of the test was controlled by cutting off the power of the electromagnetic holder, thus assuring an initial zero velocity. An auto-trigger functionality on the employed high-speed Phantom V341 camera allowed the recording of the whole sphere drop, by detecting the initial movement of the sphere inside a user-defined control region on the image. Some basic characteristics of the camera are resumed in Tab. 4.1. A mirror placed at 45° with respect to the tank side wall enabled the simultaneous recording of the front and the side views with a single camera (see Fig. 4.1(b)). Back-lights were placed behind the front and the side recording planes to provide sufficient contrast. This last point was of fundamental importance to guarantee a reliable result of the cross-correlation algorithm (see §5.1) developed to estimate the sphere motion. Since the accuracy of the presented results relied on the recording of high-quality images, the camera settings are briefly described in the next paragraph.

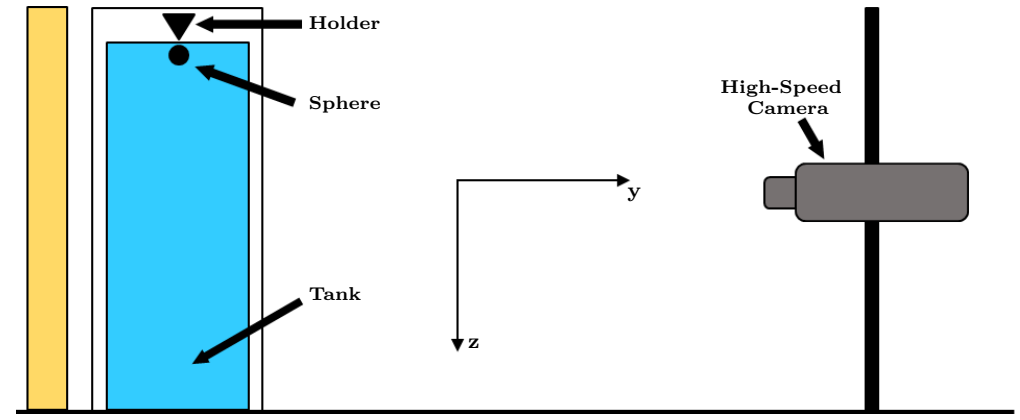

(a)

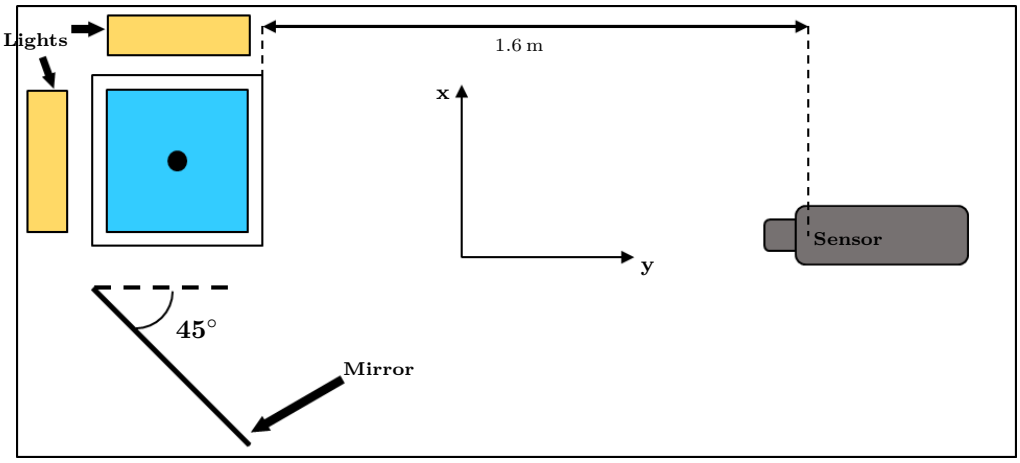

(b)

Figure 4.1 – Schematic of the falling sphere experimental rig. (a), side view. (b), top view. The camera position refers to the configuration used to record the sphere motion along the whole tank height.

Sensor	CMOS
Full resolution, [px^2]	2560×1600
Maximum frame rate, [fps]	129 500 (at 256×8 px^2)
Minimum frame rate, [fps]	10
Maximum frame rate at full resolution, [fps]	800
Minimum shutter speed, [µs]	1
Memory Size, [GB]	8
Pixel depth, [bit]	8 and 12

Table 4.1 – Technical specifications of the Phantom V341 high-speed digital camera.

4.1.1 Camera Settings

Two camera configurations were considered depending on the objective of the test. The configuration in Fig. 4.1 refers to tests whose goal was the recording of the sphere motion along the whole tank height. When details of the sphere near-wall region were sought, the camera was moved closer to the tank and a macro lens was used. The two configurations are discussed in the following.

Trajectory Configuration

The two main features that influenced the quality of the recorded videos were the spatial and the temporal resolutions.

As discussed above, the field of view had to be large enough to include both the front and the side planes. The size of the field of view was also influenced by the choice of the lens and by the absolute distance of the camera sensor from the measurement plane. The best configuration was found by mounting a Zeiss Makro-Planar T* 2/50 mm ZF lens, placing the camera sensor at 1.6 m from the tank (see Fig. 4.1(b)) and using a recording window of 2560×1100 px^2, which resulted into a spatial resolution of 0.3 mm px^{-1}.

Secondly, the high-speed camera was exploited to assure the recorded videos to be time-resolved. An upper and lower limit of the used frame rate had thus to be defined depending on the sphere falling velocity. The latter was influenced by both the sphere and liquid properties. The problem is qualitatively sketched in Fig. 4.2, where the inter-frame vertical displacement Δz is defined as the distance travelled by the falling sphere between two consecutive frames. A too low frame rate would result into a Δz much larger than the sphere diameter d, thus preventing the estimation of actual instantaneous displacement, velocity and acceleration values. Typically, the frame rates employed in this work assured Δz to be a fraction of the sphere diameter, thus indicating that the strongest constraint was the upper frame rate limit. The latter was established by considering two different factors. First, a $\Delta z > 0$ had to subsist between two consecutive frames, meaning that a too high recording rate could determine the sphere to be approximately in the same position (the minimum detectable displacement being limited by the pixel size). This problem could be circumvented in the post-processing phase by analysing only a fraction of the available images, separated by a larger Δt than the one used during the recording. However, since the latter solution would not have been efficient, the frame rate that assured a sphere displacement of at least 1 px was selected for each combination of sphere and liquid. The second motivation was linked to the total time required by the sphere drop. The camera memory being of finite size (8 GB), a too high frame rate would result into a video cut when the sphere still had to reach the bottom part of the tank.

Altogether, these considerations underline that every time the properties of sphere and liquid were modified, a new suitable configuration in terms of recording parameters had to be identified. For this reason, a resume of the details of the recording parameters is reported in Tabs. C.1 and C.2 in Appendix C. Moreover, this discussion clearly shows that the size of the designed rig was a compromise between opposing constraints. A large tank height might be suitable to provide sufficient distance for the sphere acceleration towards terminal conditions. Similarly, a large cross-section could limit the effects of the walls on the falling sphere. However, larger measurements planes would oblige a different camera configuration to be set, with a consequent detrimental effect on the spatial resolution. Moreover, a larger available volume inside the tank could represent an issue when high cost liquids are used. As an example, one litre of glycerine with a $\geq 99.5\,\%$ purity cost around 23€ at the moment of redaction of this manuscript, which could rapidly increase the total cost of the experimental set-up.

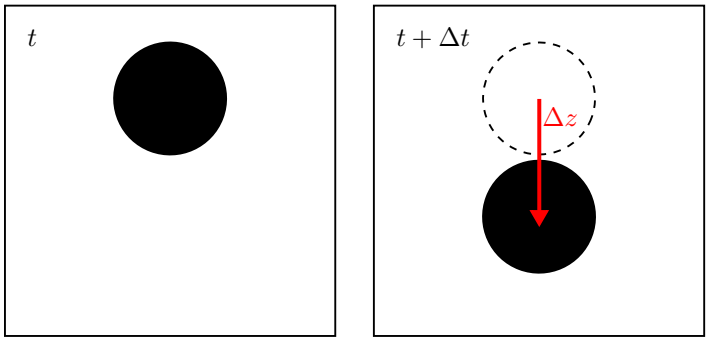

Figure 4.2 – Schematic of the sphere inter-frame vertical displacement Δz definition between two consecutive frames. (a), time t. (b), time $t + \Delta t$. The Δz length is magnified for illustration purposes only, the actual value being a fraction of the sphere diameter (see Tab. C.1 in Appendix C).

High-Magnification Configuration

A high-magnification configuration was set-up in order to analyse the details of the phenomena occurring in the near-wall region of the falling sphere. In this case, only the front plane was recorded and the camera was horizontally centred accordingly. A Sigma 180 mm F2.8 APO Macro EX DG OS lens was used and the distance of the camera sensor to the tank front plane was reduced down to 0.8 m to assure a conversion factor up to 0.05 mm px^{-1}. This configuration did not represent the best achievable spatial resolution, the minimal focus distance of the objective being 0.47 m. This choice was made because the presence of the sphere inside the recording window for a sufficiently high number of images represented an additional constraint. Moreover, the sphere transversal motion determined a quick departure outside the image for too small recording window width. The used configuration (recording window 2048×1152 px^2) thus represented a compromise between these constraints. The temporal resolution was increased up to 1300 fps in order to describe the motion and deformation of the air layer around the SH sphere surface (see Chapter 6).

4.1.2 Falling Sphere Test

A short description of checks and activities to be performed before, during and after the test is here provided. These are basic rules to be followed in order to assure the achievement of reliable results and the preservation of the SH coatings.

Preliminary Operations

The falling spheres tests were performed at least one day after the production of the SH coatings via the manufacturing procedure described in §3.2.1, to assure satisfactory SH properties of the surfaces and prevent coatings damage. Before the execution of the calibration, the alignment between camera and tank wall was verified via a laser beam (see Fig. 4.3): a mirror placed on the tank vertical wall assured the collimation between the ray incoming from the laser source mounted on the camera and the reflected ray. A calibration target was then mounted on a moving support able to cover the whole tank height. This was made to further verify the alignment and

check the focus status. When the satisfactory recording parameters were met, the calibration snapshots were taken. An example is shown in Fig. 4.4 for both the front and the side planes. These snapshots were used to evaluate the mm to px conversion factor, which varied between front and side views but did not vary along the channel height due to the satisfactory obtained alignment and to the relatively large distance from the camera sensor to the recording plane (dozens of times the lens focal length). Finally, the back-lights were turned on right before the test execution to avoid significant heating of the working fluid.

Test Phase

The auto-trigger functionality of the Phantom camera was exploited to assure the recording of the whole drop (see Fig. 4.5). The method consists in triggering the camera from a motion detected inside the image. It is based on four parameters that had to be properly set:

- an area that specifies the region of interest inside the whole image. The area around the sphere hold by the electromagnet was selected (see Fig. 4.5);
- a threshold that specifies the amount a pixel has to change to be considered active. In the case of 8 bits images, a $0 - 255$ gray levels range is available. A threshold of 10 levels was thus set in the performed tests;
- an area percentage that specifies the amount of the selected area to be active to trigger the recording. This parameter was set to 10 %;
- a check interval that specifies the frequency to be used to scan the region of interest. Typically this parameter was set equal to 1 ms.

The recording mode of the camera was set as follows: once the *Capture* command was given, the Phantom V341 camera continuously recorded new frames, overwriting the existing frames once the memory was full. A sufficient number of frames was set to be kept in memory before the detected trigger to assure the presence of the whole drop sequence in the available images. Once the trigger was detected, the camera recorded new frames until the memory was filled, then the recording automatically stopped. Practically, the sphere was placed inside the auto-trigger region by the remotely controlled electromagnetic holder and the test start was given by the cut-off of the output of the power generator. Frames sampled from the complete drop of a $d = 10$ mm reference stainless steel sphere are shown in Fig. 4.6. Once the sphere hit the bottom of the tank (a soft foam avoided coating damage) the lights were promptly turned off to limit the working liquid heating. The images sequence was then downloaded from the camera memory to the controlling computer. The sphere was recovered by a system of two valves at the bottom of the tank. This recovery method was chosen because the disadvantage of the (limited) liquid loss from the bottom of the tank was counterbalanced by the advantage of a negligible perturbation of the liquid in the measurement section of the tank. Finally, the initial liquid free-surface level could be restored at the end of the day by adding the proper amount of liquid into the tank.

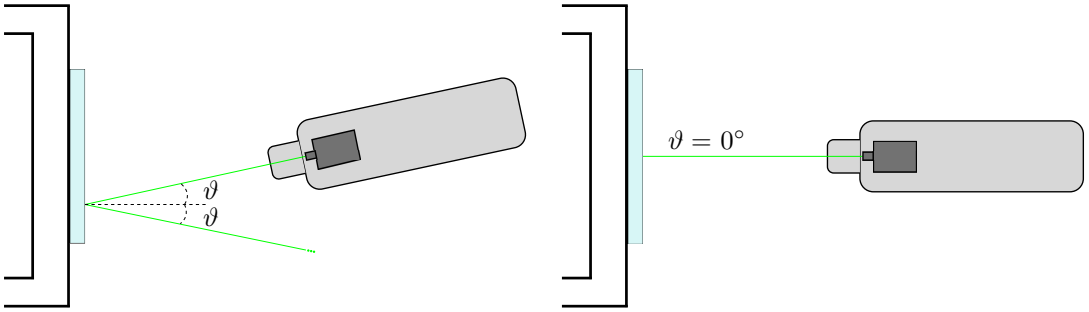

Figure 4.3 – Schematic of the laser alignment procedure between camera and tank wall. A laser source is mounted and aligned on the camera body, while a mirror is fixed on the tank wall. The ensemble of camera and laser source is tilted until collimation between incoming and reflected ray is reached. The procedure is executed in both horizontal and vertical planes. (a) non-aligned configuration with an angle $\vartheta > 0°$. (b) collimated configuration.

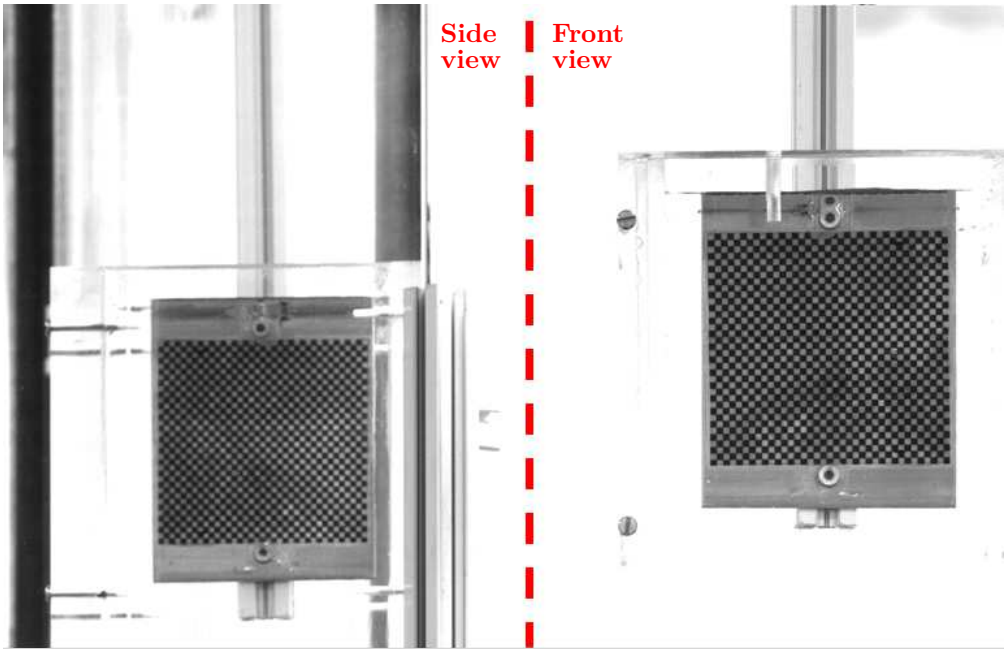

Figure 4.4 – Calibration frames for the falling sphere tests. The red dashed line separates the side view (left) from the front view (right). The region close to the liquid free surface is shown in these snapshot. The height difference between front and side views is due to the projection on the mirror. The calibration target was displaced along the whole tank height by the holder visible on the top of the images. The chessboard texture consists of 2 mm size squares. The back-lights are discernible on the background of the images in both side and front views.

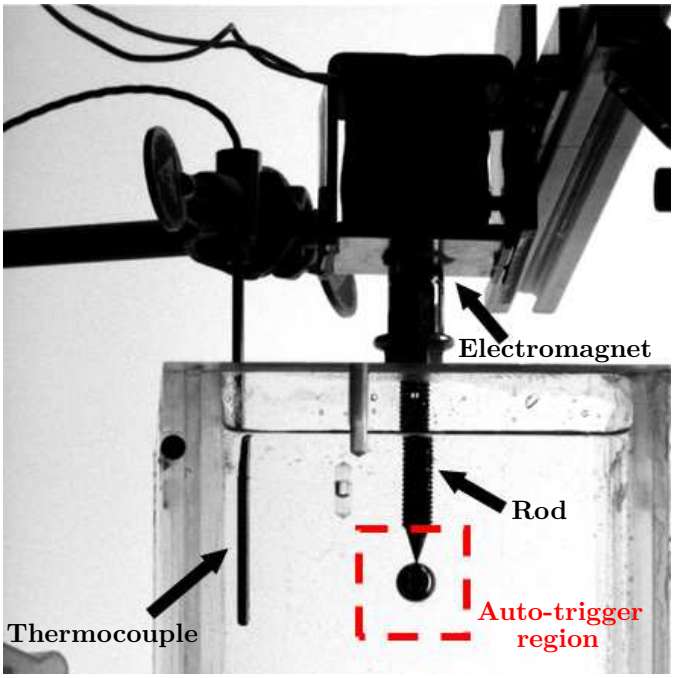

Figure 4.5 – Definition of the region to be checked by the camera to trigger the recording at the beginning of the drop. In the Phantom software the motion of the sphere ($d = 10\,\text{mm}$ reference stainless steel in the image) was detected by scanning (check interval equal to 1 ms) the pixels gray level variation (threshold equal to 10 levels) over the whole auto-trigger region. The trigger of the recording occurred when a percentage of the total number of pixels inside the region was reached (threshold equal to 10 %). The black arrows indicate the thermocouple close to the liquid free surface, the electromagnet and the rod connecting the sphere to the electromagnet. Notice the sharp tip of the rod to limit the contact area with the sphere surface.

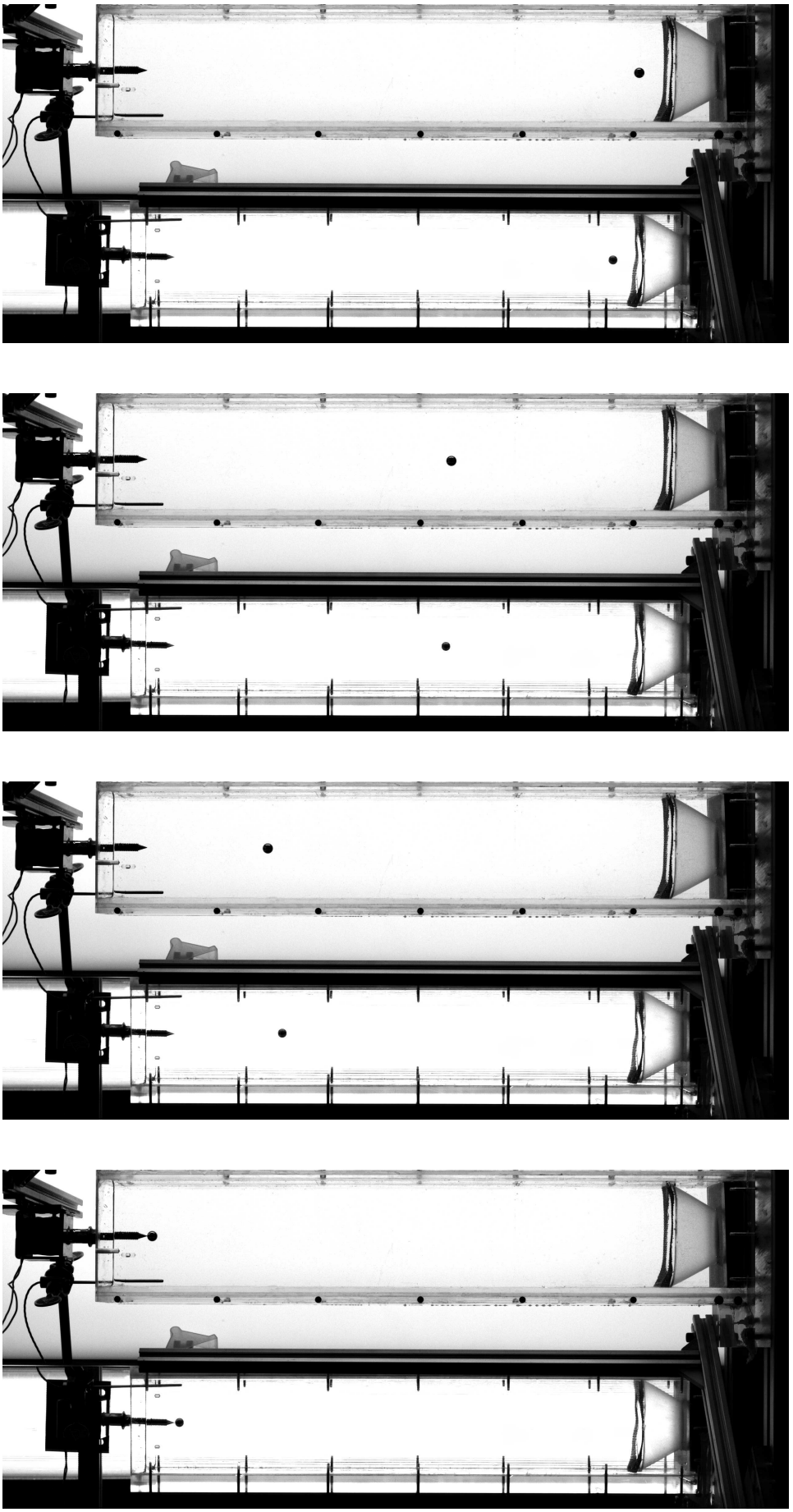

(a) $t = t_0$ (b) $t = t_0 + 220\,\mathrm{ms}$ (c) $t = t_0 + 440\,\mathrm{ms}$ (d) $t = t_0 + 660\,\mathrm{ms}$

Figure 4.6 – Frames sampled from a drop of a d =10 mm stainless steel reference sphere, recorded at 1000 fps. (a)-(d), increasing falling time, starting from the beginning of the drop (indicated by t_0 in (a)) until when the sphere reached the bottom of the tank (d). The left side of each image shows the side view, while the right side shows the front view. The bottom of the tank was made of a cone shaped outlet covered by a soft foam to avoid coating damage.

4.2 Basic Notions on Free Falling Spheres

4.2.1 Equation of Motion

The main information stored in the recorded image sequence as the one shown in Fig. 4.6 is the 3D motion of the falling sphere, which is reported in Fig. 4.7 in the case of a $d = 5\,\mathrm{mm}$ reference stainless steel sphere. The technique implemented to reconstruct the 3D trajectory, together with the corresponding velocity and acceleration, is the main topic of Chapter 5. Here focus is put on the physical description of the illustrated phenomenon. The sphere is shown in Fig. 4.7 to accelerate from the initial zero velocity value at the top of the tank up to the terminal velocity u_∞ in the lower part of the tank. The analysis of this behaviour, initially introduced in §2.2.1 via the generalised Kirchhoff equations in the case of a rigid body of arbitrary shape, is further developed in this paragraph in the case of a rigid spherical geometry. In fact, Mordant & Pinton (2000) showed that, starting from the analysis of the motion of a particle at vanishing Re (Maxey & Riley 1983), developments on the expression of each relevant term in the description of the motion of a solid sphere under gravity (Auton *et al.* 1988; Lovalenti & Brady 1993; Chang & Maxey 1995) led to the following general vector form:

$$\left(m_s + \frac{1}{2}m_l\right)\frac{d\mathbf{u}}{dt} = (m_s - m_l)\,\mathbf{g} + \frac{3}{2}m_l\frac{D\mathbf{u}_l}{Dt} + \frac{1}{2}\rho_l\|\mathbf{u}_l - \mathbf{u}\|\,(\mathbf{u}_l - \mathbf{u})\,\pi\left(\frac{d}{2}\right)^2 C_D + \mathbf{F}_{Hist}, \tag{4.1}$$

where $m_s = \rho_s\frac{4}{3}\pi\left(\frac{d}{2}\right)^3$ is the mass of a sphere moving at velocity $\mathbf{u} = (u_x, u_y, u_z)$ in a Cartesian coordinate system (x, y, z), $m_l = \rho_l\frac{4}{3}\pi\left(\frac{d}{2}\right)^3$ is the liquid mass displaced by the sphere and $\mathbf{u}_l$ is the undisturbed liquid velocity field. In Eq. 4.1 the term $\frac{D\mathbf{u}_l}{Dt} = \left(\frac{\partial}{\partial t} + \mathbf{u}_l\cdot\nabla\right)\mathbf{u}_l$ denotes the total derivative of $\mathbf{u}_l$, $\nabla = \left(\frac{\partial}{\partial x}, \frac{\partial}{\partial y}, \frac{\partial}{\partial z}\right)$ being the *nabla* operator. The expression in Eq. 4.1 is therefore a form of the generalised Kirchhoff equations describing the translational degrees of freedom previously reported in Eq. 2.6(a), where each term is explicitly written in the case of a rigid sphere undergoing negligible rotation. The last term in Eq. 4.1 ($\mathbf{F}_{Hist}$) is the Boussinesq-Basset memory integral (Boussinesq 1885; Basset 1888) and describes the modification of the liquid state due to the sphere motion, thus requiring the whole *history* of the effect of wake development on the body motion to be known. Conversely to the other terms in Eq. 4.1, an explicit expression of $\mathbf{F}_{Hist}$ is not straightforward. While numerical works provided information of the $\mathbf{F}_{Hist}$ behaviour (Lawrence & Mei 1995; Chang & Maxey 1995; Kim *et al.* 1998), Mordant & Pinton (2000) experimentally analysed its relevance on free-falling sphere tests. The experimental velocity profiles at $Re_\infty \sim 10^2$ were found to always lie between two numerically simulated curves obtained considering and neglecting the history term. Moreover, the spheres were found to experience the memory term at the very early stage of the drop, until a fraction (between $\frac{1}{3}$ and $\frac{1}{2}$) of u_∞ was reached. In the highest analysed Reynolds number region ($Re_\infty \sim 10^3$), Mordant & Pinton (2000) pointed out an initial experimental acceleration without the memory term followed by an abrupt change of the sphere acceleration, the sphere finally reaching the predicted u_∞. This phenomenon, which was guessed to be related to a modification of the sphere wake, was qualitatively retrieved in this study and constitutes one of the main subject of discussion in Chapter 6. In the same chapter, it is demonstrated that in this study the experimental velocity data satisfactorily follow the predicted profiles calculated without the memory term, the agreement on u_∞ being particularly good. For all these reasons, in the following of the manuscript the history term will be neglected and, since in this study the liquid in the tank is at rest, $\mathbf{u}_l = \mathbf{0}$.

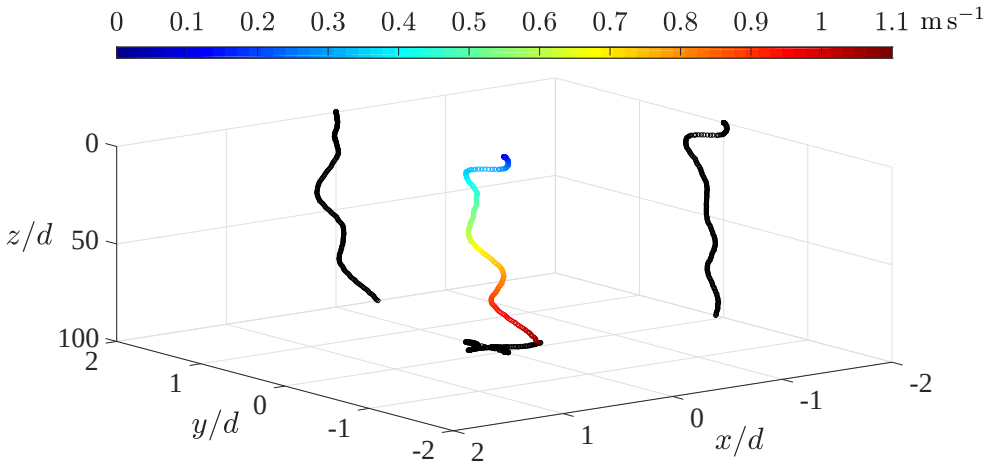

Figure 4.7 – Example of a 3D trajectory of a free-falling $d = 5\,\mathrm{mm}$ reference sphere. The color scale indicates the sphere velocity in $\mathrm{m\,s^{-1}}$, which increases from the zero value at departure up to the terminal value in the lower portion of the tank. The three black curves represent the projections of the 3D trajectory on vertical and horizontal planes.

Interestingly, the 3D trajectory shown in Fig. 4.7 qualitatively introduces the departure of the falling sphere from a purely vertical fall, which will be one of the main subject of discussion in Chapter 6. Moreover, the scales of the horizontal (x, y) and vertical (z) axes in Fig. 4.7 are an indication of the relative magnitude of the transversal and vertical motions. Since in this study the density ratio $\zeta = \frac{\rho_s}{\rho_l}$ introduced in §2.2 assumed a value much larger than unity, the transversal motion was always found to be at least one order of magnitude lower than the vertical counterpart. This finding allows to further simplify the expression in Eq. 4.1 to the following scalar form valid along the vertical z direction (Mordant & Pinton 2000):

$$\left(m_s + \frac{1}{2}m_l\right)\frac{du_z}{dt} = (m_s - m_l)\,g - \frac{1}{2}\rho_l u_z^2 \pi \left(\frac{d}{2}\right)^2 C_D. \tag{4.2}$$

On the above expression, $m_s \frac{du_z}{dt}$ indicates the sphere acceleration, while the term $\frac{1}{2}m_l \frac{du_z}{dt}$ represents the so-called *added mass*, that is the resistance to acceleration of the liquid surrounding the sphere. The nature of the added mass term was discussed in several works (see e.g. Auton *et al.* 1988; Magnaudet & Eames 2000) and also numerically verified (Chang & Maxey 1995), pointing out a $\frac{1}{2}$ coefficient valid for the spherical geometry. On the right hand side of Eq. 4.2, the first term describes the net gravity/buoyancy effect, whereas the second term indicates the drag contribution. Finally, the expression in Eq. 4.2 can be conveniently re-written exploiting the ζ definition, which gives:

$$\left(\zeta + \frac{1}{2}\right)\frac{du_z}{dt} = (\zeta - 1)\,g - \frac{3}{4}\frac{u_z^2}{d}C_D. \tag{4.3}$$

The above expression clearly shows that, once the properties of the sphere and of the liquid are known, the vertical motion can be estimated if a suitable $C_D(Re)$ law is available. The latter constitutes the focus of the next section.

4.2.2 Drag Coefficient Evolution

A large number of works that analysed the evolution of the drag coefficient of reference spheres over several Reynolds number regimes is available in literature. The scenario is resumed by the data reported in Fig. 4.8, which approximately cover all the regimes discussed in §2.1 in the fixed sphere case. The largest C_D values are reached in the creeping flow regime (left side of Fig. 4.8), then progressively decrease for increasing Re. Interestingly, a $C_D \approx 0.5$ constant value is retrieved in the range $10^3 < Re < 10^5$, which corresponds to the discussed sub-critical regime. Finally, the modification of the separation-transition scenario evidenced in Fig. 2.6(b) determines an abrupt C_D drop, which corresponds to the drag crisis.

The development of an analytical solution in the limit of vanishing Re, under the hypotheses of steady state and infinite medium (Stokes 1851) (see §2.1), has inspired the developments of methods to investigate the relative interaction between a solid body and a liquid. A falling-ball viscometer (see e.g. Sutterby 1973*a*) is an experimental set-up designed to accurately evaluate the dynamic viscosity μ_l of a liquid of density ρ_l via a drop of a sphere of known diameter d and density ρ_s. In fact, at terminal conditions (see Fig. 4.9) the balance between gravity/buoyancy and drag, coupled with the Stokes' drag law introduced in Eq. 2.4, allows to retrieve the following expression from Eq. 4.2 (or equivalently Eq. 4.3):

$$\mu_l = \frac{d^2}{18u_\infty}\left(\rho_s - \rho_l\right) g = \frac{d^2}{18u_\infty}\left(\zeta - 1\right)\rho_l g. \tag{4.4}$$

It is evident from Eq. 4.4 that the accuracy of the implemented method depends on the measurement uncertainties of several quantities. In detail, Brizard *et al.* (2005) demonstrated that two operations revealed to be crucial to obtain a satisfactory method accuracy: the measurement of the sphere diameter d and the estimation of the terminal velocity u_∞. The d measurement is usually quite straightforward, with instruments that reach accuracies $\mathcal{O}(10^0)$ µm, which for $d \sim 10^{-3}$ m represent relative uncertainties lower than 1 %. Conversely, the accurate estimation of the sphere falling velocity revealed more tricky. This is related to the fact that generally information not only on u_∞ but also on the instantaneous sphere vertical velocity $u_z(t)$ (t indicating the time) is sought, with good enough spatial and temporal resolutions. Therefore, many techniques based on Laser Doppler (Flude & Daborn 1982), Doppler effect of an ultrasonic wave (Mordant & Pinton 2000), and cameras (Lommatzsch *et al.* 2001; Brizard *et al.* 2005) have been employed.

This simple experimental set-up and the connected issues on measurement accuracy can thus be considered as preliminary indications of the problems that had to be faced during the experimental work performed in this study.

Moreover, a Re increase determines a progressively appearance and strengthening of inertial effects. As a consequence, the experimental data (see e.g. data from Lapple & Sheperd (1940) in Fig. 4.8) gradually deviate from the Stokes's drag law. A significant departure of experimental data from theory is noticed for $Re > 1$. Corrections to the Stokes' expression were proposed (see e.g. Clift *et al.* 1978, and references therein), which progressively added higher order terms in the form $c_i Re^i$ (c_i being a constant) and/or $ln(Re)$ in order to expand the Re range of validity. However, for Re much larger than unity the above analytical expressions lose the ability to describe experimental data, the best strategy being represented by the use of empirical formulas obtained by fitting experimental results. In this work, the empirical formula proposed by Cheng (2009) was used, which writes as follows:

$$C_D = \frac{24}{Re}\left(1 + 0.27Re\right)^{0.43} + 0.47\left[1 - \exp(-0.04Re^{0.38})\right]. \tag{4.5}$$

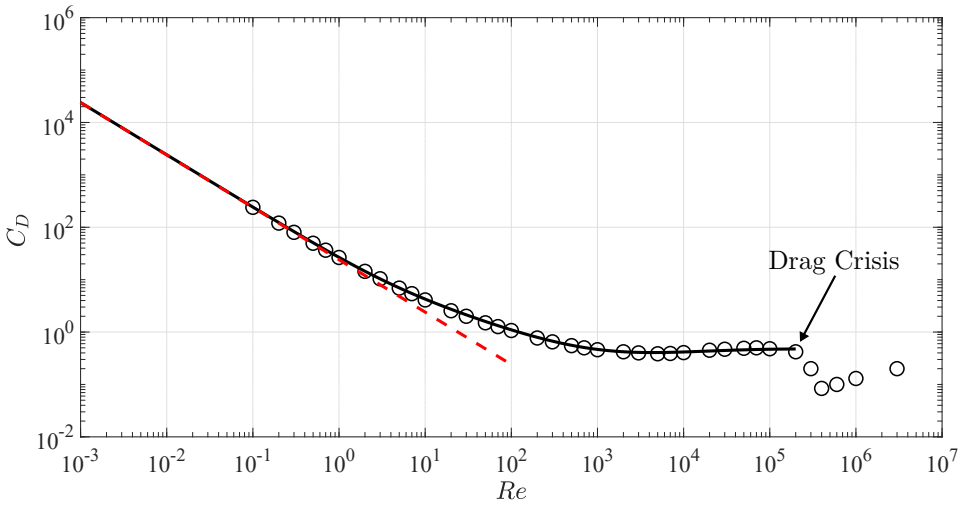

Figure 4.8 – Evolution of the drag coefficient C_D as a function of the Reynolds number Re for reference spheres. ∘, experimental data by Lapple & Sheperd (1940). ——, empirical law by Cheng (2009). - - -, Stokes' law.

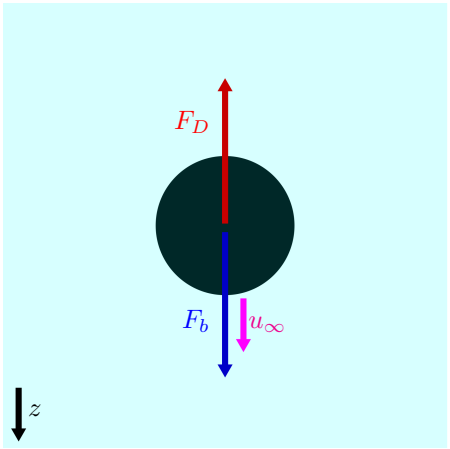

Figure 4.9 – Schematic of the force balance in the gravity direction (z, indicated by the black arrow) on a sphere falling in the creeping flow regime (vanishing Re) at terminal velocity u_∞ (indicated by the magenta arrow) in an infinite medium. The drag F_D balances the net gravity/buoyancy force F_b.

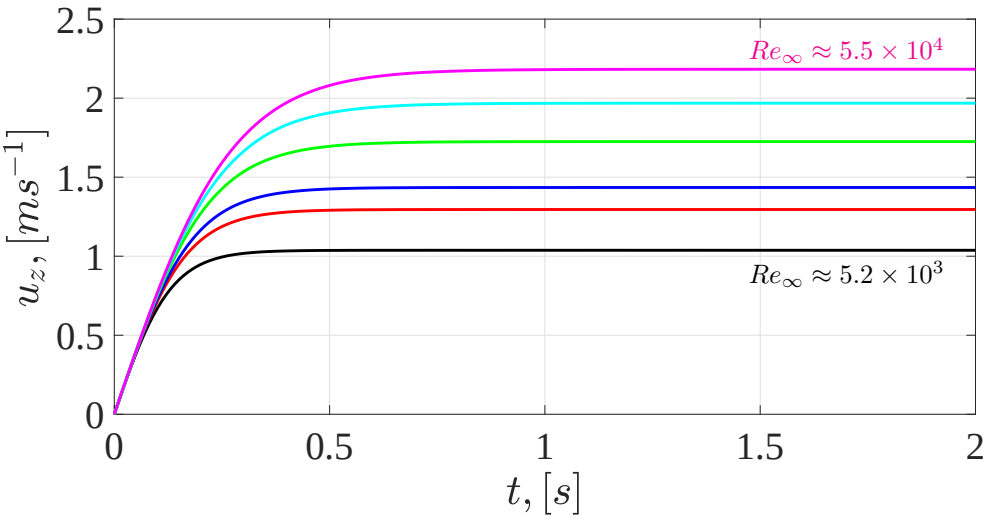

Figure 4.10 – Time evolution of the vertical velocity of reference spheres as predicted by Eq. 4.3. (—), $d = 5\,\text{mm}$. (—), $d = 8\,\text{mm}$. (—), $d = 10\,\text{mm}$. (—), $d = 15\,\text{mm}$. (—), $d = 20\,\text{mm}$. (—), $d = 25\,\text{mm}$. The terminal Reynolds number Re_∞ varies in the range $5.2 \times 10^3 - 5.5 \times 10^4$.

The choice to use the expression in Eq. 4.5 was made since, beside its simplicity, Cheng (2009) compared the proposed relation with several formulas previously published in literature and multiple experimental data sets, demonstrating its reliability up to $Re = 2 \times 10^5$, that is before the appearance of the drag crisis phenomenon (see §2.1). The whole Reynolds number range analysed in this study (see §4.3) is thus covered by the presented formula. The comparison between the expression in Eq. 4.5 and the experimental data by Lapple & Sheperd (1940) in Fig. 4.8 demonstrates the satisfactory agreement with available literature. Please note that the experimental data by Lapple & Sheperd (1940) were not used by Cheng (2009) to derive the empirical formula reported in Eq. 4.5, thus representing a further validation.

4.2.3 Vertical Motion Description

The availability of an equation describing the vertical motion of a falling sphere (see §4.2.1) and of a suitable drag coefficient law (see §4.2.2) allows for an estimation of the vertical velocity evolution, once the sphere and liquid properties are known. An example of the estimated curves for stainless steel spheres falling in pure water is reported in Fig. 4.10 for the diameter range 5 mm to 25 mm. The spheres are shown to accelerate from initial zero velocity towards the corresponding u_∞ at terminal conditions. The corresponding Re_∞ range based on the estimated u_∞ values increases from $\approx 5.2 \times 10^3$ for $d = 5\,\text{mm}$ up to $\approx 5.5 \times 10^4$ for $d = 25\,\text{mm}$. In detail, an increase of the sphere diameter (at fixed ζ) determines an augmentation of the reached u_∞ and of the initial transient time required to reach terminal conditions. The latter can be estimated by detecting the time required to reach the 95 % of the corresponding u_∞ value, thus being indicated by the symbol t_{95}. The parameter t_{95} was shown by Mordant & Pinton (2000) to be significant towards the modelling of the motion of a particle. In fact, the authors found out that the velocity profiles of falling spheres normalised by the respective terminal velocities collapsed

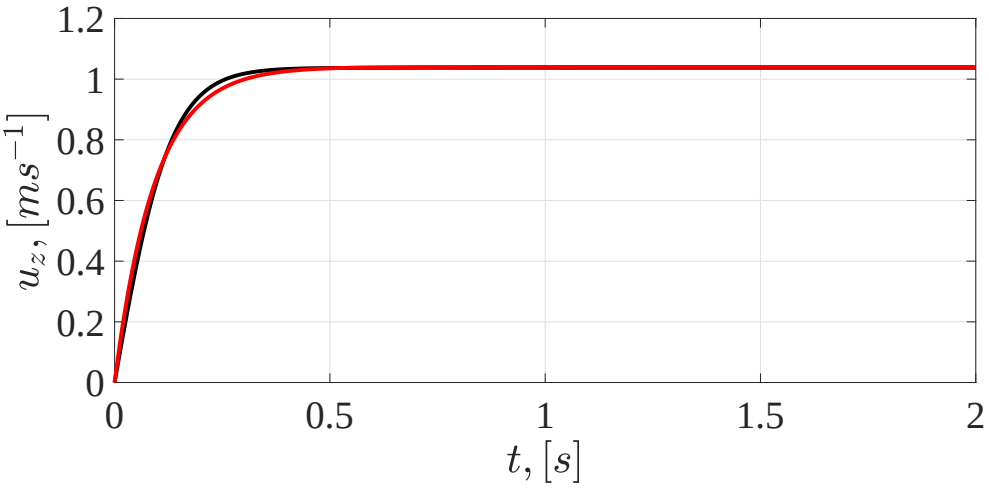

Figure 4.11 – Time evolution of the vertical velocity u_z of a $d = 5\,\text{mm}$ reference sphere in water. (——), prediction via the semi-empirical law described by Eq. 4.3. (——), exponential model described by Eq. 4.6 fitted on the data predicted via Eq. 4.3.

onto a curve that could be well represented by the following exponential law:

$$\frac{u_z\,(t)}{u_\infty} = 1 - \exp\left(-\beta t\right), \tag{4.6}$$

where the relation $\beta = \frac{3}{t_{95}}$ was proposed. By fitting, in the least-mean squares sense, the expression in Eq. 4.6 to available data describing the vertical velocity profile of a falling sphere, the u_∞ could be estimated. This approach reveals interesting when, due to limitations on the tank height, the falling sphere is not enabled to reach terminal conditions. Details on the latter case are provided in Appendix B. The validity of the presented method is demonstrated in Fig. 4.11 by comparing the profile predicted via Eq. 4.3 and the fitted model described by Eq. 4.6 in the case of a $d = 5\,\text{mm}$ reference sphere falling in pure water. While the exponential law in Eq. 4.6 shows some limitations in correctly catching the transient phenomena occurring in the accelerating region ($t \leq 0.5\,\text{s}$), the approximation reaches a satisfactory level approaching terminal conditions. In fact, the u_∞ estimation differs only of 0.3 % from the value predicted by the semi-empirical law in Eq. 4.3.

One step further in the analysis of the velocity profiles shown in Fig. 4.10 can be performed by introducing two scaling parameters that will be used all along the manuscript to take into account gravity/buoyancy effects (Jenny *et al.* 2004), that is the characteristic time t_D and velocity u_D, defined as follows:

$$t_D = \sqrt{\frac{d}{(\zeta - 1)\,g}}, \tag{4.7a}$$

$$u_D = \sqrt{(\zeta - 1)\,gd}. \tag{4.7b}$$

The SH coatings manufacturing procedure described in §3.2.1 consisted into two polymeric layers successively sprayed on the reference surface. Therefore, the density ρ_s of the SH sphere is expected to slightly vary with respect to the reference stainless steel value. Accordingly, the

relevance of the introduced parameters is testified in Fig. 4.12 in the case of a $d = 5\,\mathrm{mm}$ reference sphere, whose density is varied with respect to the nominal value. As shown in Fig. 4.12(a), the two velocity profiles depart from each other when a 10 % ρ_s decrease is imposed, especially in the terminal conditions region where a u_∞ decrease of approximately 6 % is retrieved. Conversely, the scaling by t_D and u_D in Fig. 4.12(b) demonstrates that the two non-dimensional profiles are almost perfectly collapsed, a slight difference being visible only at the end of the accelerating phase. This property will be exploited during the results discussion for comparison purposes between SH and reference spheres. For the remainder of the manuscript, the symbol (*) denotes variables scaled by t_D and u_D.

Moreover, the $u^\star_\infty = \frac{u_\infty}{u_D}$ and $t^\star_{95} = \frac{t_{95}}{t_D}$ behaviour for all the spheres previously shown in Fig. 4.10 is reported in Fig. 4.13. It is found that over a Re_∞ variation of one order of magnitude in the sub-critical regime both parameters are approximately constant, thus validating the scaling choice proposed in this chapter. This finding, which someway agrees with the experimental findings reported by Mordant & Pinton (2000), further validates the assumption of considering $C_{D\infty} \approx 0.5$ over the sub-critical regime. In fact, as shown in Fig. 4.13(a), a good agreement is found between the evaluated $u^\star_\infty$ points and the value estimated by imposing $C_{D\infty} = 0.5$ in Eq. 4.3 at terminal conditions and normalised by u_D. This fact will be exploited in Chapter 6 to discuss the results of falling spheres at high Re_∞.

Finally, one practical difference between experiments and theory is the effect of the tank walls on the falling sphere. In fact, when a free falling/rising body moves into a finite-size cross-section tank filled with a liquid, a counter motion of the latter occurs, which balances the motion of the solid body and of the liquid dragged by it. An increasing ratio between the solid body and tank characteristic dimensions results into a larger retarding effect of the tank walls on the body motion. This issue is widely studied in literature and is usually handled by a correction of the estimated velocity values. The technique implemented in this work is available, for the interested reader, in Appendix B.

4.3 Spheres and Mixtures Choice

The strategy followed in the choice of the spheres/liquids combinations was based on the purpose of analysing multiple regimes characterised by different phenomena occurring on the flow around the falling body (see the discussion in §2.1). Since a prediction of the terminal velocity was available for reference spheres via Eq. 4.3, the falling regime could be a priori estimated before the manufacturing of the SH spheres and of the mixtures. An overview of all the performed falling sphere experimental campaigns is shown in Fig. 4.14, where the $C_D - Re$ behaviour discussed in §4.2.2 is reported. In detail, the three gray-shaded rectangles show the extent of the Re_∞ range investigated. All the executed tests lie below the appearance of the drag crisis phenomenon. This is due to the fact that in this study the main goal was to show the effects of SH coatings without triggering the boundary layer evolution modifications that cause the drag crisis.

The two main parameters that influenced the Re_∞ range were the sphere and the liquid properties. Stainless steel spheres ($\rho_s \approx 7700\,\mathrm{kg\,m^{-3}}$) for ball bearings applications were chosen as reference (as introduced in §3.2.1, the acronym NC, which stands for No Coating, is used). Following the ISO 3290-1 norm, the selected grade of precision was G10, which assured a variation of the sphere diameter $\pm$ 0.25 µm, a surface roughness of 0.02 µm and a variation of diameter on the available lot of 0.50 µm. These values were considered satisfactory in terms of precision with respect to the spheres typical dimensions (for the sake of completeness, all the measured sphere properties are reported in Appendix C). As an example, the diameter variation on the lot represented only 0.01 % of the smallest analysed $d = 5\,\mathrm{mm}$. The high ρ_s value was selected to

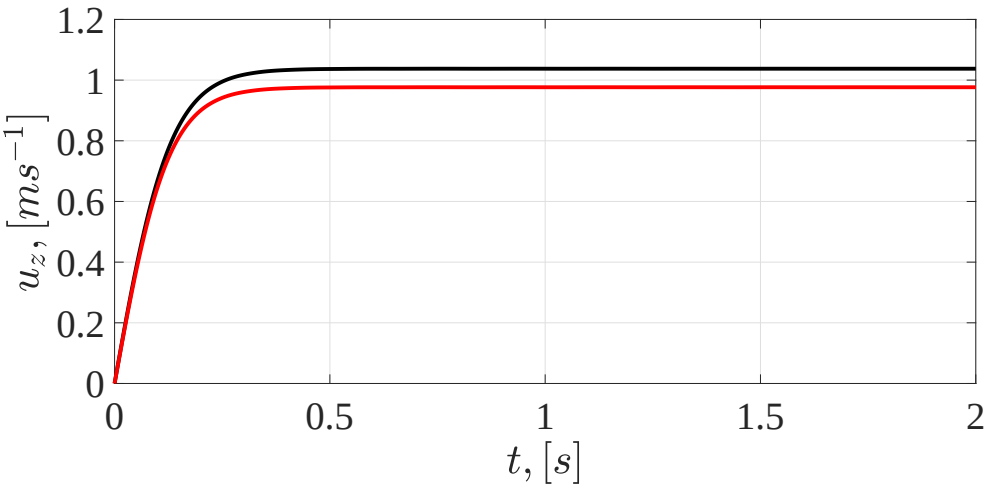

(a)

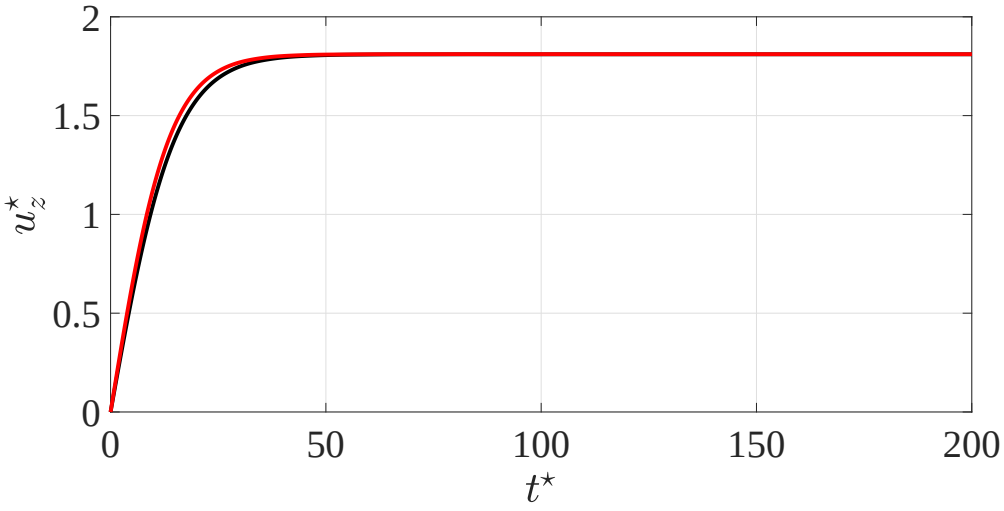

(b)

Figure 4.12 – Vertical velocity time evolution of a $d = 5\,\mathrm{mm}$ sphere in water. (——), $\rho_s = 7700\,\mathrm{kg\,m^{-3}}$. (——), $\rho_s = 6930\,\mathrm{kg\,m^{-3}}$. (a) dimensional profiles. (b) non-dimensional profiles (indicated by the symbol ($\star$)) using t_D and u_D as scaling parameters.

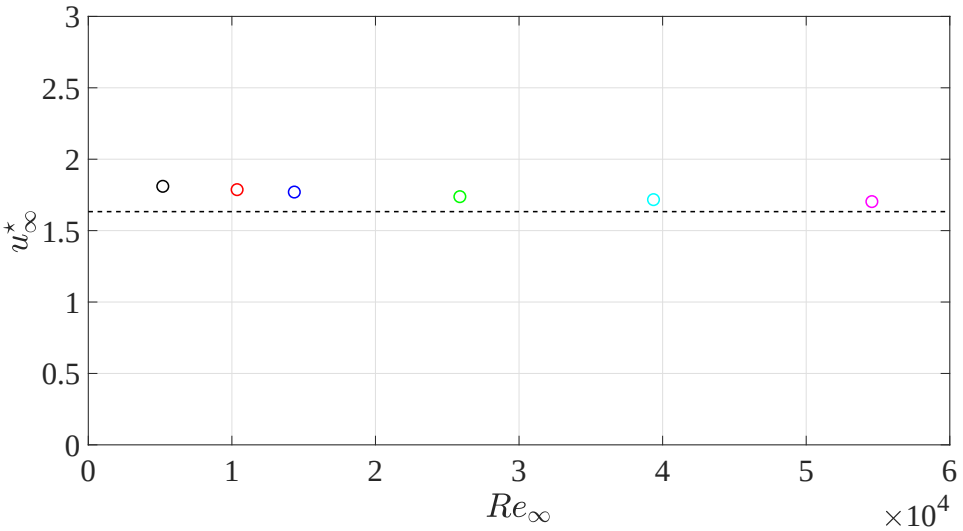

(a)

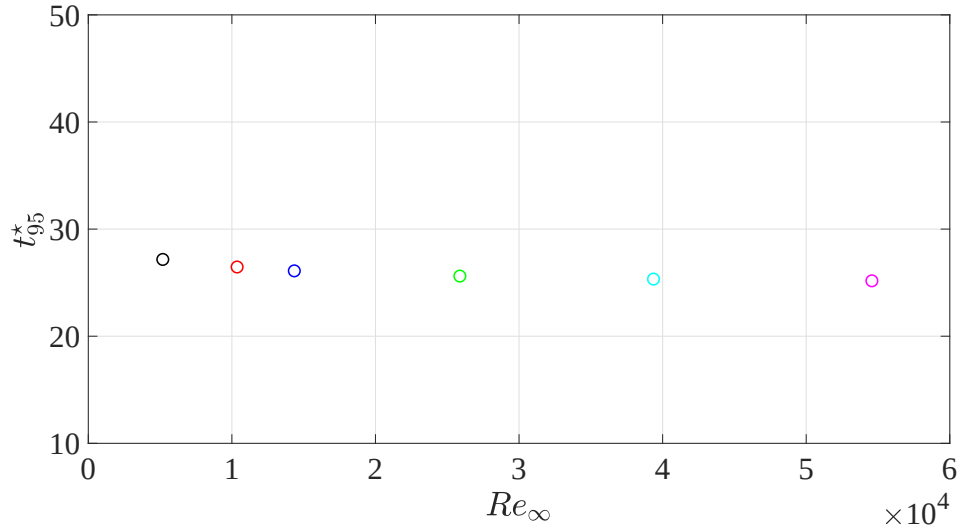

(b)

Figure 4.13 – Evolution of the non-dimensional characteristic parameters of the drop over a Reynolds number variation of one order of magnitude. (a), terminal velocity $u^\star_\infty = \frac{u_\infty}{u_D}$. (- - -), prediction of the $u^\star_\infty$ value via evaluation of Eq. 4.3 at terminal conditions and considering $C_{D\infty} = 0.5$, which is the typical value indicated in the analysed sub-critical regime. (b), transient time $t^\star_{95} = \frac{t_{95}}{t_D}$. Same color code as in Fig. 4.10.

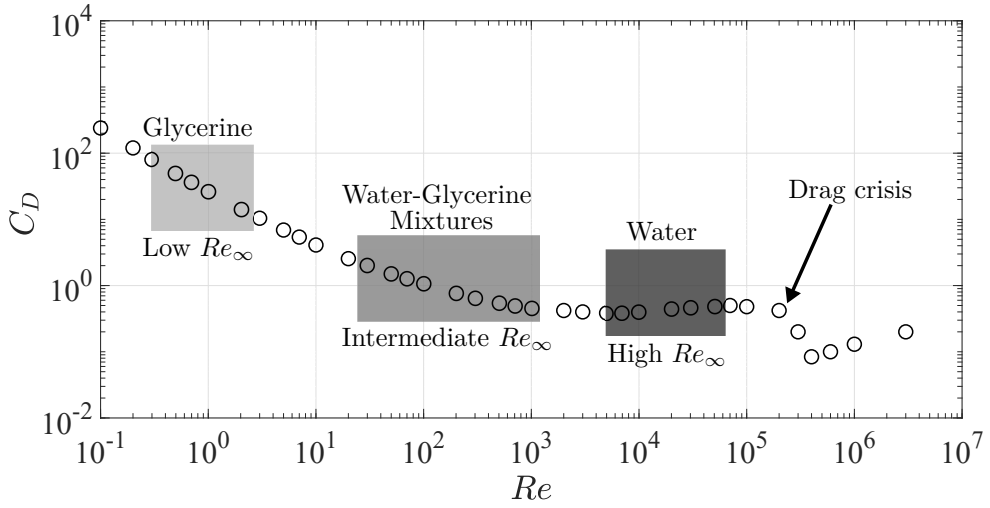

Figure 4.14 – Drag coefficient C_D as a function of the Reynolds number Re for reference spheres. ∘, experimental data from Lapple & Sheperd (1940). The gray-shaded rectangles indicate the whole Re_∞ ranges analysed with the falling sphere experimental campaigns. All the shown results lie below the appearance of the drag crisis phenomenon, indicated by the black arrow.

assure the reaching of the high Re_∞ range (see Fig. 4.14) and to move sufficiently away from the critical case $\rho_s \approx \rho_l$, that was shown to determine the appearance of different phenomena on the wake/path influencing the resultant sphere hydrodynamic loads (Jenny *et al.* 2004; Horowitz & Williamson 2010*a*). While the largest d was chosen to limit the maximum blockage factor δ (see §B.2 in Appendix B) as a function on the falling regime, the smallest d was imposed by handling constraints during the manufacturing and testing phases. In fact, a diameter smaller than 5 mm was found to be particularly difficult to handle during the manufacturing procedure (see §3.2.1), resulting into a reduction of the quality of the SH coatings.

Once established the spheres properties, the only way left to vary Re_∞ was a modification of the liquid properties. In order to reach the high Re_∞ region in Fig. 4.14, double-distilled water was employed. This choice was preferred to tap water in order to minimise the possible effects of surfactants on SH coatings behaviour (Peaudecerf *et al.* 2017) and to minimise the proliferation of micro-organisms. The double-distilled water was characterised by a density $\rho_l = 998\,\mathrm{kg\,m^{-3}}$, a kinematic viscosity $\nu_l = 1.0 \times 10^{-6}\ \mathrm{m^2\,s^{-1}}$ and a surface tension $\gamma \approx 72\,\mathrm{mN\,m^{-1}}$ (with respect to air) at a temperature $T = 20\,^\circ\mathrm{C}$. The research of a liquid soluble in water, with a similar density, surface tension and a much higher viscosity in order to attain the low Re_∞ regime ended on the use of *glycerol*. In fact, pure glycerol shows a density $\rho_l = 1264\,\mathrm{kg\,m^{-3}}$, a kinematic viscosity $\nu_l = 1.1 \times 10^{-3}\ \mathrm{m^2\,s^{-1}}$ and a surface tension $\gamma \approx 62\,\mathrm{mN\,m^{-1}}$ (with respect to air) at a temperature $T = 20\,^\circ\mathrm{C}$. The liquid used in this work will be indicated as *glycerine*, being constituted of glycerol with a purity $\geq 99.5\,\%$. The intermediate Re_∞ regime was attained by properly mixing the desired amounts of the two liquids. A dedicated mixing procedure was thus developed, whose main objectives were the minimisation of the amount of air embedded inside the mixture and the volumetric fractions of the two liquids to be as accurate as possible. Instead of producing at once the whole required volume of mixture, a smaller amount (typically half a litre) was considered and the procedure was then repeated. This was made to facilitate the mixture handling, and the volumes of the two liquids were calculated accordingly. The main

steps of the procedure are the following:

1. a graduated glass beaker was installed on an electromagnetic stirrer and a magnetic bar was deposed on the beaker lower wall;
2. the desired quantity of water was gently added into the glass beaker. Attention was put to avoid air bubbles to form;
3. the stirrer was turned on at minimum power in order to assure the magnetic bar to start turning. Due to the low water viscosity, a too high rotational speed would have caused the liquid to exit the beaker;
4. the desired quantity of glycerine could then be progressively added into the beaker. The glycerine had to slowly slip on the beaker wall in order to minimise the quantity of embedded air bubbles. The instantaneous injection of the total required amount of glycerine resulted into a worsening of the mixing process quality, and it was therefore avoided. This is due to the large increase of the mixture viscosity with respect to pure water;
5. while waiting for glycerine to slip down along the beaker wall, the rotational speed of the magnetic bar was progressively increased to balance the augmentation of the mixture viscosity;
6. once the total volume of glycerine was embedded inside water, the mixing was continued for 15 min. The transparency of the obtained mixture was an indication of the goodness of the mixing process;
7. the mixture was then put under void for at least 1 h to further eliminate all the possible air inclusions;
8. once the total volume of mixture was produced, the tank could be filled. As in the previous steps, the mixture had to gently slip on the tank wall to minimise air inclusions;
9. at least one night was assured between the tank filling and the execution of the first test to assure the mixture to be uniform and quiescent.

Some of the relevant properties of the analysed water-glycerine mixtures are resumed in Tab. 4.2. The mixtures will be indicated hereinafter with the following nomenclature:

$$Waaa\_Gbbb,$$

where *aaa* and *bbb* indicate the volumetric fractions of water (W) and glycerine (G), respectively. The full range of available diameters was investigated in the pure water case (W100_G000), while diameters up to 10 mm were analysed in all the other mixtures. This choice was made to limit the wall factor influence that becomes stronger for decreasing Re_∞ (see §B.2 in Appendix B). In fact, considering the range of analysed d (see Tab. 4.2) and a tank equivalent diameter $D_{eq} = 0.11$ m, the experimental blockage factor δ range is $0.04 - 0.22$. However, in order to limit blockage effects, in the low Re_∞ region where the retarding effect is stronger (see Fig. B.4 in Appendix B) the highest analysed value was $\delta = 0.09$. The largest diameter spheres ($d \geq 15$ mm) were tested only in the pure water case ($W100\_G000$), characterised by the highest Re_∞ region where the blockage effects mitigate (see Fig. B.4 in Appendix B). The actual sphere diameter d was measured along at least five different directions, with a resolution of 10 µm. The uncertainties on d (95 % confidence level) kept lower than 2 % of the respective average value in all cases, testifying the satisfactory sphericity of the coated spheres. All the SH coatings determined a d increase

Mixture Name	Water Fraction, [%]	Glycerine Fraction, [%]	Settling Time, [min]	Number of Tests	Diameter Range, [mm]
$W100\_G000$	100	0	15	10	5 - 25
$W040\_G060$	40	60	30	10	5 - 10
$W030\_G070$	30	70	30	10	5 - 10
$W020\_G080$	20	80	30	10	5 - 10
$W000\_G100$	0	100	60	5	5 - 10

Table 4.2 – Nomenclature and properties of the water-glycerine mixtures investigated in the falling spheres tests, from pure water to pure glycerine. The water and glycerine percentages represent the volumetric fractions. The last column indicates the sphere diameter range investigated in each mixture.

with respect to the corresponding reference sphere, with a maximum +10 % in the SH-80 coating case. Masses were evaluated by a single measurement with a Mettler Toledo AB104-S analytical balance, with an accuracy of 0.1 mg. The largest mass augmentation (+5 %) with respect to the corresponding reference sphere was reached with the SH-80 coating. The deposition of the SH coatings resulted in a decrease of the sphere density with respect to the reference stainless steel sphere (down to −20 %). The largest uncertainties of the sphere densities (95 % confidence level) were approximately 4 % of the respective average value.

In order to *a priori* estimate the attained Re_∞ range, the density ρ_l and dynamic viscosity μ_l of the mixtures were calculated by following the work of Cheng (2008), who proposed empirical formulas based on comparison with several sets of experimental data. The approach is here briefly discussed. The objective being the evaluation of the water-glycerine mixture properties at a temperature T expressed in Celsius degrees, the densities of the glycerine and water fractions could be estimated as follows:

$$\rho_G = 1277 - 0.654T, \tag{4.8a}$$

$$\rho_W = 1000\left(1 - \left|\frac{T-4}{622}\right|^{1.7}\right). \tag{4.8b}$$

From these density values, the glycerine mass (subscript m) concentration $C_{G,m}$ could be calculated as follows:

$$C_{G,m} = \frac{\rho_G V_G}{\rho_G V_G + \rho_W V_W}, \tag{4.9}$$

where the volumes of glycerine V_G and water V_W were the experimentally controlled quantities. The mixture density was then calculated as:

$$\rho_l = \rho_G C_{G,m} + \rho_W \left(1 - C_{G,m}\right). \tag{4.10}$$

An estimation of the dynamic viscosities of the two fractions was obtained as:

$$\mu_G = 12100 \exp\left(\frac{(T-1233)\,T}{70T + 9900}\right), \tag{4.11a}$$

$$\mu_W = 1.790 \exp\left(\frac{(-T-1230)\,T}{360T + 36100}\right). \tag{4.11b}$$

These two viscosity values were then used to evaluate the mixture dynamic viscosity via the following power law:

$$\mu_l = \mu_W^\alpha \mu_G^{1-\alpha}, \tag{4.12}$$

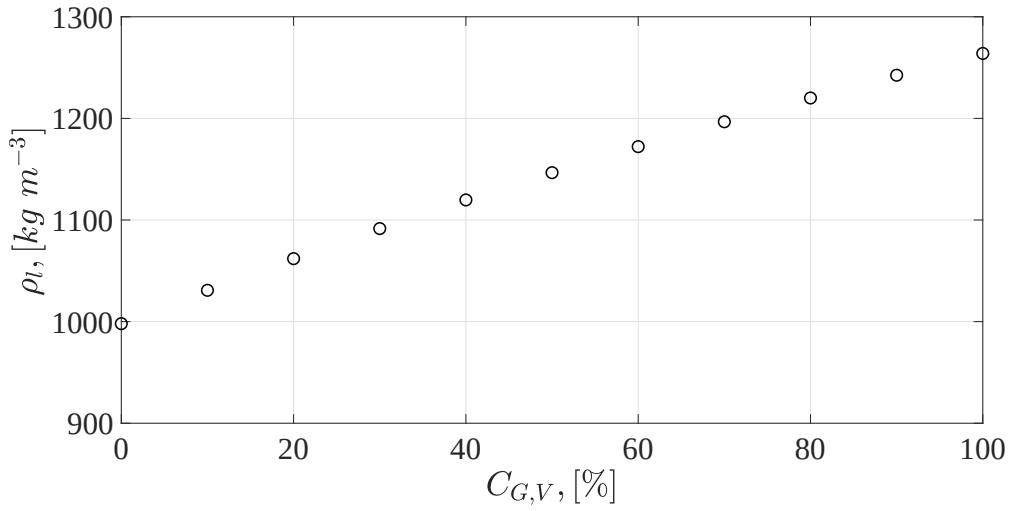

Figure 4.15 – Evolution of the mixture density ρ_l for increasing glycerine volumetric fraction $C_{G,V}$. Data are evaluated from Eq. 4.10 at a temperature $T = 20\,°\text{C}$. Modifications due to limited T variations ($\pm\ 1\,°\text{C}$) would be overlapped to the reported symbols, and were therefore not reported.

where the exponent α was computed as:

$$\alpha = 1 - C_{G,m} + \frac{c_1 c_2 C_{G,m}\,(1 - C_{G,m})}{c_1 C_{G,m} + c_2\,(1 - C_{G,m})}, \tag{4.13a}$$

$$c_1 = 0.705 - 0.0017T, \tag{4.13b}$$

$$c_2 = (4.9 + 0.036T)\,c_1^{2.5}. \tag{4.13c}$$

The evolution of the mixture density as a function of the volumetric glycerine fraction $C_{G,V} = \frac{V_G}{V_G + V_W}$ is shown in Fig. 4.15, highlighting the augmentation of the mixture density up to $\approx +25\,\%$ with respect to water when the glycerine case is reached. However, T variations of $\pm 1\,°\text{C}$ with respect to the reported data at $T = 20\,°\text{C}$ determined little effect ($\ll 1\,\%$) on ρ_l even in the glycerine case ($C_{G,V} = 100\,\%$). The evolution of the mixture dynamic viscosity as a function of $C_{G,V}$ is reported in Fig. 4.16 at $T = 20\,°\text{C}$ and shows that augmentations of three order of magnitudes are obtained for glycerine with respect to water. Conversely to the mixture density, the T effects on μ_l were more relevant at the highest glycerine percentages. This is testified by Fig. 4.17, where the non-dimensional dynamic viscosity $\frac{\mu_l}{\mu_l^{T=20°C}}$ evolution is reported for T variations in the range $19\,°\text{C}$ to $21\,°\text{C}$. The normalisation was performed with respect to data evaluated at $T = 20\,°\text{C}$. While small differences ($\approx 3\,\%$) are appreciable at low $C_{G,V}$, $1\,°\text{C}$ variation in the glycerine case determines a μ_l decrease or increase up to $\approx 10\,\%$. All together, these properties evolutions underline the importance of executing the experimental campaigns under controlled temperature T, especially when high glycerine percentages are considered. In the case of pure water or low glycerine percentages, small T variations result into less relevant mixture properties modifications. Finally, the μ_l predicted values were experimentally verified with a Fungilab$^{\text{TM}}$ viscometer.

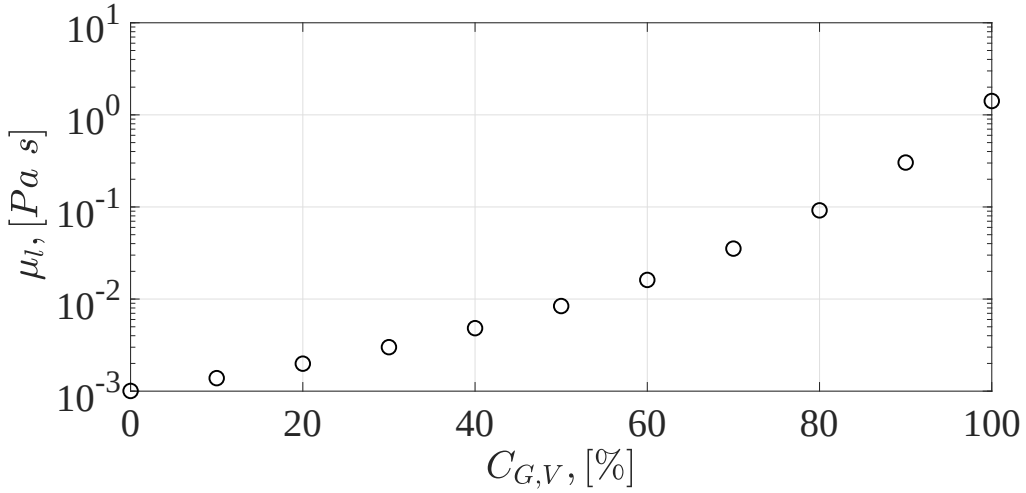

Figure 4.16 – Evolution of the mixture dynamic viscosity μ_l for increasing glycerine volumetric fraction $C_{G,V}$. Data are evaluated from Eq. 4.12 at a temperature $T = 20\,°\text{C}$.

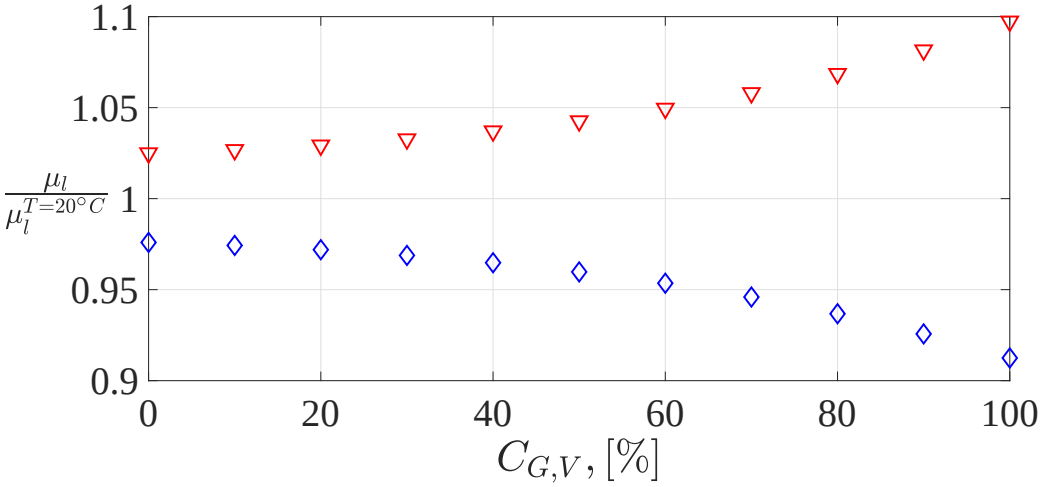

Figure 4.17 – Effect of the temperature on the evolution of the non-dimensional mixture dynamic viscosity $\frac{\mu_l}{\mu_l^{T=20°C}}$ for increasing glycerine volumetric fraction $C_{G,V}$. Data are evaluated from Eq. 4.12 and normalised with respect to the corresponding value at a temperature $T = 20\,°\text{C}$. ▽, $T = 19\,°\text{C}$. ◇, $T = 21\,°\text{C}$.

Settling Time

In order to assure the liquid to be quiescent before the execution of each drop, a settling time had to be imposed between two consecutive tests. However, due to the large number of executed tests ($\mathcal{O}(10^2)$), the minimum acceptable settling time for quiescence had to be established. Notwithstanding the importance of this parameter, agreement on the proposed values does not exist in available literature, and imposed settling times are sometimes not even reported. For this reason, a scaling analysis is developed in the following to achieve a gross estimation of the relative modification that had to be imposed on the settling time for the considered mixtures. Then, the imposed settling time, partially based on the few available works in literature, is discussed.

A scaling analysis based on the characteristic time of the dissipation phenomena in the wake of a sphere was performed to estimate the relative order of magnitude of the settling time of the different employed liquids. In the case of a turbulent wake of a fixed sphere subjected to an incoming non-turbulent uniform flow u_∞ in the x direction (y indicating the transversal direction), Tennekes & Lumley (1972) showed that the wake velocity deficit u_w and the associated transversal length-scale l_w scale as:

$$\frac{u_w}{u_\infty} = \left(\frac{x}{d}\right)^{-\frac{2}{3}}, \tag{4.14a}$$

$$\frac{l_w}{d} = \left(\frac{x}{d}\right)^{\frac{1}{3}}. \tag{4.14b}$$

By coupling Eqs. 4.14 with the scaling of the turbulent viscosity $\nu_t \sim u_w l_w$ (Pope 2000), it can be shown that:

$$\nu_t \sim u_\infty \left(\frac{x}{d}\right)^{-\frac{2}{3}} d \left(\frac{x}{d}\right)^{\frac{1}{3}} \sim u_\infty d \left(\frac{x}{d}\right)^{-\frac{1}{3}}. \tag{4.15}$$

Finally, a balance between the rate of dissipation of turbulent kinetic energy ε and the kinetic energy injected into the wake E_k leads to:

$$\varepsilon \sim \nu_t \left(\frac{\partial u}{\partial y}\right)^2 \sim \frac{E_k}{\tau_t} \sim \frac{u^2}{\tau_t}, \tag{4.16}$$

where u is the characteristic velocity in the sphere wake. The expression in Eq. 4.16 enables to achieve a scaling of the characteristic time associated with the dissipation of turbulent kinetic energy in the wake:

$$\tau_t \sim \frac{u^2}{\nu_t \left(\frac{\partial u}{\partial y}\right)^2} \sim \frac{u^2}{\nu_t \frac{u^2}{l_w^2}} \sim \frac{l_w^2}{\nu_t}. \tag{4.17}$$

With the help of Eqs. 4.14(b) and 4.15, the following expression can be retrieved:

$$\tau_t \sim \left(\frac{l_w}{d}\right)^2 \frac{d^2}{\nu_t} \sim \frac{x}{u_\infty} \sim \frac{x}{k d^{1/2}}, \tag{4.18}$$

where the last scaling was performed exploiting Eq. 4.3, which at terminal conditions states $u_\infty \sim k d^{1/2}$, with $k \sim 10^1$. In order to maximise the quantity in Eq. 4.18, the longest possible streamwise length compatible with the experimental tests is considered, that is the tank height $H \approx 0.6\,\mathrm{m}$, together with the smallest analysed diameter $d = 5\,\mathrm{mm}$, which provides:

$$\tau_t \sim 10^0 s. \tag{4.19}$$

The scenario changes by focusing attention on the low Re_∞ limit. Assuming as a first approximation that the creeping flow hypotheses are valid in the considered regime, the Stokes'

analytical solution showed in §2.1 can be interpreted as a perturbation on the uniform flow at u_∞ induced by the presence of the rigid sphere. A first indication of the effect of the presence of the body can thus be retrieved by evaluating the distance from the body at which the velocity field tends towards the uniform value u_∞. A first order approximation of the radial velocity u_r (see Eq. 2.2(b)) along the sphere streamwise axis ($\vartheta = 0°$) is considered:

$$u_r \approx u_\infty \left(1 - \frac{3}{4}\frac{d}{r}\right), \tag{4.20}$$

where the third order term was neglected since it is expected $r \gg d$. The search of the radial distance which assures $\frac{u_r}{u_\infty} \approx 0.99$ (a 1 % gap is considered) provides:

$$r \approx \frac{300}{4} d. \tag{4.21}$$

Considering the largest diameter investigated in the glycerine tests ($d = 10\,\mathrm{mm}$), the corresponding streamwise distance results $r \approx 0.75\,\mathrm{m}$. Finally, the characteristic laminar time evaluated considering a terminal velocity $u_\infty \sim 0.1\,\mathrm{m\,s^{-1}}$ (representative of the glycerine tests values) is:

$$\tau_l = \frac{r}{u_\infty} \sim 10^1 s. \tag{4.22}$$

One order of magnitude of difference on the characteristic times was thus retrieved between turbulent wake and laminar solution, which could be a gross indication of the necessity to vary the settling time in the two extreme cases of pure water and glycerine.

By looking at available literature on the subject, a brief discussion on the topic was made by Horowitz & Williamson (2010*a*), who imposed a two hours settling time for falling/rising spheres in pure water, showing how residual disturbances in the fluid may lead to the appearance of random transverse motion. However, their results concerned rising ($\zeta = \rho_s/\rho_l < 1$) and falling spheres with a maximum $\zeta = 1.4$, that is very close to the borderline case $\zeta = 1$. Truscott *et al.* (2016) performed tests on rising spheres and estimated the required settling time by performing Particle Image Velocimetry (PIV) measurements of the flow field following an experimental run. The measured disturbances velocity after 30 min was found to be of the same order of the settling velocity of the tracer particles. Intuitively, a significant ζ increase ($\zeta \approx 7$ in this study) should determine a lower sensitivity of falling spheres to residual disturbances. For this reason, a 15 min settling time was imposed in the $W100\_G000$ mixture case (see Tab. 4.2). The validity of this value was verified by comparing the results of tests executed with a virtually infinite settling time (one night) with the same test executed after 15 min from the previous drop. As an example, the transversal velocity $u_{tr} = \sqrt{u_x^2 + u_y^2}$ (the reference coordinate system was introduced in Fig. 4.1) of a $d = 10\,\mathrm{mm}$ stainless steel reference sphere in water is shown in Fig. 4.18 in the region corresponding to the onset of the transversal motion (details are provided in Chapter 6). As shown in Fig. 4.18, no significant modification of the onset time for transversal motion is retrieved, neither a substantial magnification or reduction of the transversal velocity magnitude is noticed. A 15 min settling time in pure water was therefore considered appropriate to reduce residual disturbances to a level sufficiently low not to affect the high ζ spheres analysed in this study. This value corresponded to $\sim 10^3$ time units, when normalised with respect to the τ_t value in Eq. 4.19.

In the glycerine case, following the previous discussion on the characteristic time τ_l, the settling time was increased up to at least 1 h, thus achieving $\sim 10^2$ non-dimensional time units (with respect to τ_l in Eq. 4.22). This choice was performed as a compromise between the quiescence requirement and the high number of performed tests.

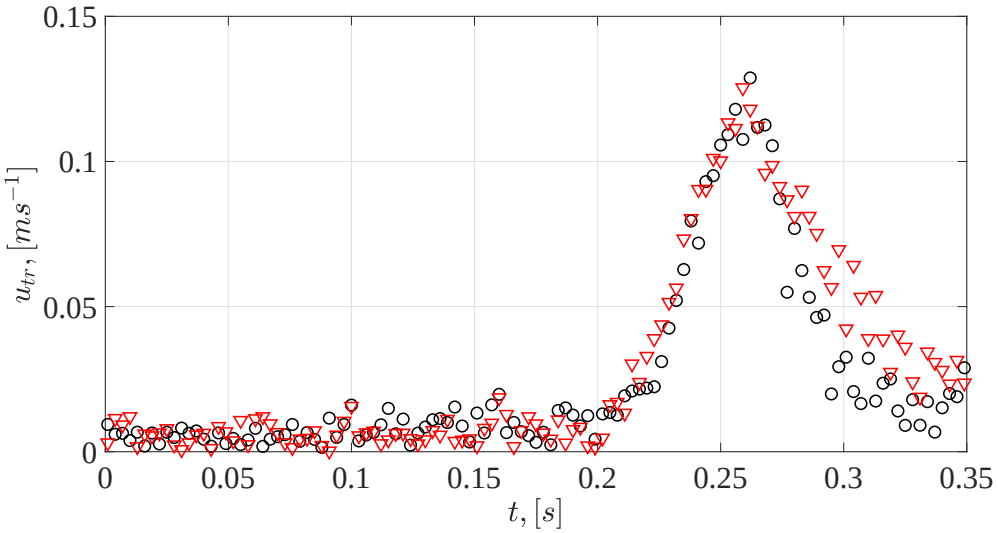

Figure 4.18 – Transversal velocity u_{tr} of a $d = 10\,\text{mm}$ stainless steel reference sphere in water in the region corresponding to the onset of transversal motion. ○, one night settling time. ▽, 15 min settling time. For the sake of clarity, one point out of three is reported. Non-significant differences between the two settling times are noticed.

In the intermediate mixtures case, no direct expression of the characteristic times could be achieved. The settling times were therefore imposed as intermediate values between the two extreme cases of pure water and glycerine (see Tab. 4.2).

Chapter 5

Post-Processing Techniques

The main output of the experimental set-up described in Chapter 4 is a sequence of images storing the 3D motion of the falling sphere. The first objective of the post-processing phase was thus the implementation of a code able to estimate the displacement of the sphere between two consecutive images, therefore reconstructing the 3D time-resolved trajectory (see the example previously provided in Fig. 4.7). In §5.1 the description of the implemented code to estimate the instantaneous sphere displacement is provided. The code is based on a standard cross-correlation technique which was practically implemented in MATLAB® using a Fast Fourier Transform (FFT) approach. Then, §5.2 is dedicated to the validation of the implemented code via the use of synthetic images describing the vertical motion of a free falling sphere. Moreover, the robustness of the code to experimental noise is assessed.

Once reconstructed the sphere temporal displacement and position, a technique able to estimate the velocity and acceleration profiles had to be implemented. The latter revealed of fundamental importance to compare the relative hydrodynamic performance of the tested spheres. The most straightforward method, which was the first to be implemented in this work, was the calculation of velocity and acceleration via a time derivative on position data $p_z(t)$ using a central finite difference scheme. However, in §5.3 it will be shown that for time-resolved data the experimental noise ϵ may be amplified to non-acceptable levels, even if very accurate measurements are performed ($\epsilon \to 0$). For this reason, a second technique based on a spline fitting method on position data is described, and the relative performance of the two approaches is discussed.

5.1 Sphere Displacement Estimation

In order to process the recorded images sequences, a code was developed in MATLAB®, which was founded on the basic principles of the techniques available in literature to estimate the displacement of particles. Since the 3D trajectory was reconstructed from two 2D analyses in the planes $z - x$ and $z - y$ (the coordinate system was previously introduced in Fig. 4.1), in the following a generic plane described by the two orthogonal directions $\mathbf{e}_1$ and $\mathbf{e}_2$ is considered (see Fig. 5.1). The common aspect of all these kind of techniques is that, knowing the imposed time-step Δt between two consecutive frames, if the displacement $\mathbf{s} = s_1\mathbf{e}_1 + s_2\mathbf{e}_2$ of a particle from point A to point B can be estimated, the corresponding velocity can be simply evaluated as:

$$\mathbf{u} = \frac{1}{\Delta t}\mathbf{s}. \tag{5.1}$$

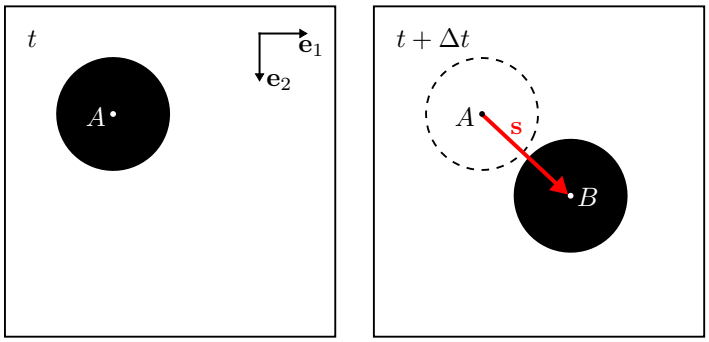

(a) (b)

Figure 5.1 – Schematic of the sphere displacement **s** between two consecutive frames. (a), time t. (b), time $t + \Delta t$. The generic plane $\mathbf{e}_1 - \mathbf{e}_2$ is representative of the front and side views of the experimental set-up (see Figs. 4.1 and 4.7). The **s** magnitude is enlarged for illustration purposes only, the actual value being a fraction of the sphere diameter.

As a general rule, a first order approximation of the particle displacement, which cannot detect effects of acceleration and curvature, can be retrieved (Raffel *et al.* 2007).

Focusing on the application of this approach on the images sequences of this study, in §5.3 it will be introduced a technique to estimate the velocity **u** from position data that resulted more robust with respect to the simple expression in Eq. 5.1. Attention in the following of the present section §5.1 is therefore put on the estimation of the displacement **s**. In fact, in the framework of the detection of a single particle (the falling sphere) displacement between two consecutive frames, a step-by-step description of the implemented code, which exploited both the features of PIV (Particle Image Velocimetry) and PTV (Particle Tracking Velocimetry) techniques, is provided in the next paragraphs. The followed approach consisted in detecting the position of the individual particle within the images and then match the images by a pairing algorithm (Ohmi & Li 2000). The following list resumes the main steps of the procedure:

1. the recorded images were pre-processed to define the analysis regions and reduce the background noise (see §5.1.1);
2. a preliminary gross detection of the sphere position was performed, which let define the position and size of the interrogation window (see §5.1.2);
3. a padding of the interrogation window was performed when needed, as in the case of the first frames where the sphere was close to the image top border (see §5.1.3);
4. a cross-correlation between the identified region on each pair of consecutive images was executed (see §5.1.4);
5. a Gaussian fit of the correlation peak was implemented to reach sub-pixel accuracy (see §5.1.5).

5.1.1 Image Pre-Processing

The starting point of the procedure was a recorded video constituted by a sequence of images as the one shown in Fig 4.6. Inside each image, the limits defining the drop region of the front and

side views were manually checked by inspecting one of the available images (see Fig. 5.2). This operation had to be performed only once, since no movement of the instruments was carried out during the experimental campaign. The top limit of the analysis region (l_t) was based on the initial position of the sphere kept fixed by the electromagnetic holder. On the lower part of the tank, the analysis region was cut (l_b) at approximately one D_{eq} from the tank bottom wall in order to exclude significant end effects (see the discussion in §B.1 in Appendix B). Similarly, at least one sphere d was imposed between the analysis region lateral borders (l_l on the side view, l_r on the front view) and the tank walls in order to exclude solid walls from the following analysis. The front and side views were finally separated by properly selecting the left (l_l on the front view) and right (l_r on the side view) limits, respectively. The recovered pixel values were used to crop each image into the corresponding front and side views (F and S in Fig. 5.2). Moreover, approximately one hundred images were recorded after the drop end at t_{end} (the sphere being in the cone at the bottom of the tank, outside the identified drop region) and were used to evaluate an average background for both planes. This average noise (small and random variations of the pixels gray-levels) was subtracted to each extracted image ($F_{A,raw}$ and $F_{B,raw}$ in Fig. 5.2, considering the couple of images at time t_n and $t_n + \Delta t$) in order to reduce the influence of the experimental noise on the detected sphere displacement. This operation was also useful to suppress from the analysed region all the fixed objects that could lie inside the image, such as the thermocouple, the tip of the electromagnetic holder or imperfections on the tank transparent walls (see Fig. 5.3). The gray-scale in Fig. 5.3(c) highlights a bright sphere (large gray level) over a darker background (low gray level), which is a necessary condition for the cross-correlation code (see §5.1.4) to properly work. Starting from the next section, the described operations were performed on every couple of two consecutive cropped images where the background was already subtracted (F_A and F_B in Fig. 5.2).

5.1.2 Preliminary Sphere Detection

The images resulting from the operations on the previous section (F_A and F_B) usually had sizes of the same order of magnitude than the tank, that is much larger than the sphere d. The goal of this section of code was thus the preliminary gross detection of the sphere position inside the whole image in order to define an interrogation window approximately centred on the sphere. The computational cost of these operations was more than balanced by the savings in performing the cross-correlation operations on a small region of the whole image. The pre-processed images from the previous section were thus converted to an intensity image where each pixel original value in the range $0-255$ was transformed in an intensity equivalent value in the range $0-1$. This operation allowed for the binarisation of the images (see Fig. 5.3(d), where the binarised image is indicated as $F_{A,b}$) using a threshold computed via the Otsu' method (Otsu 1979). This method required the knowledge of the image intensity histogram to evaluate an optimal threshold, which was defined as the one maximising the between-class variance (a cumulative parameter describing the separability of the two classes, that is background and object on the original image). Other local-based statistics could be used as segmentation alternatives (see e.g. Bradley & Roth 2007), but were not considered here since the goal was a raw preliminary detection of the sphere position. The binarisation allowed for the separation of the background (black in Fig. 5.3(d)) from the detected object (the white sphere in Fig. 5.3(d)), whose properties (centroid position $C = (x_1, x_2)$ and equivalent diameter d_{eq}) could be evaluated via the MATLAB® *regionprops* tool. The latter simply detected the identified object pixels and calculated the desired properties based on the known pixels coordinates. As an example, the equivalent diameter was calculated as $2\sqrt{S/\pi}$, where S was the surface of the detected object obtained by summing all the pixels being part of it.

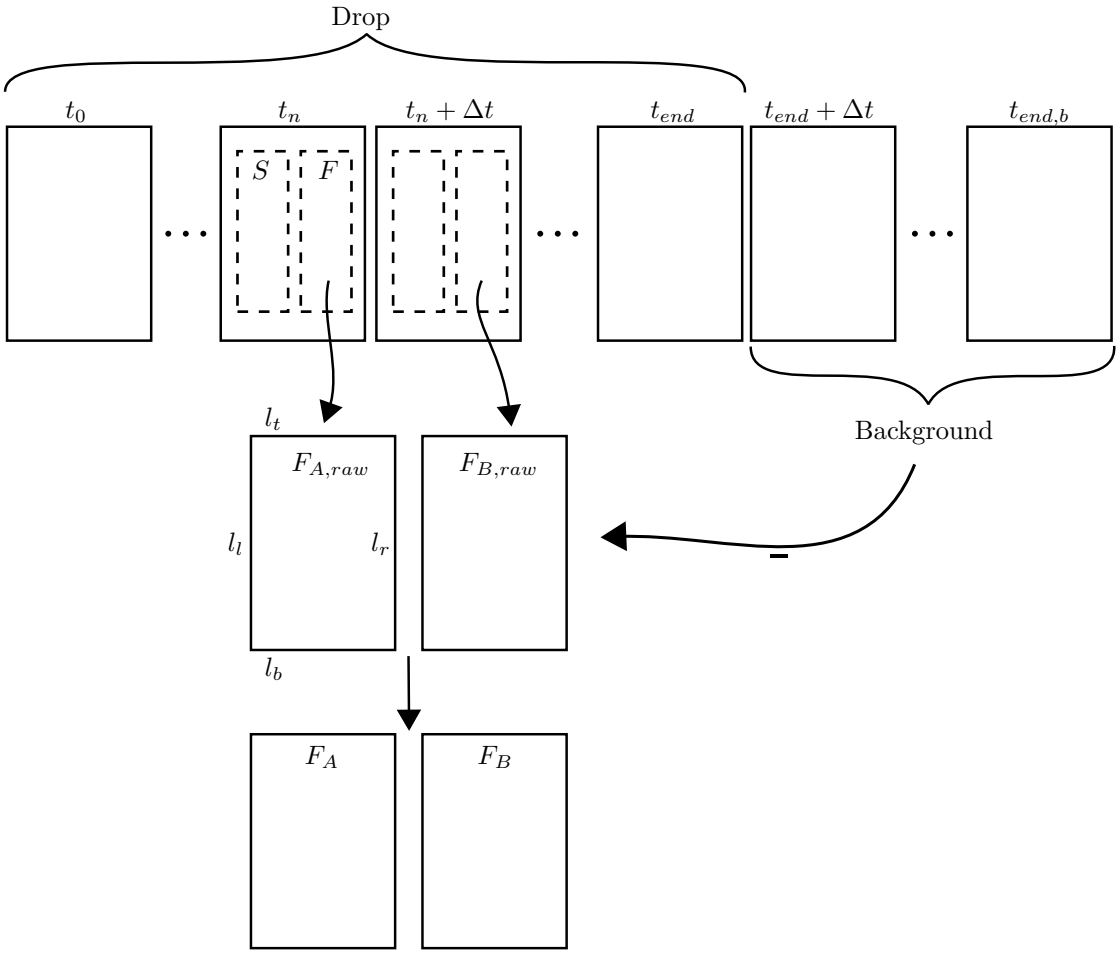

Figure 5.2 – Schematic of the pre-processing phase in the code to estimate the sphere displacement between each image separated by a time-step Δt. The sphere drop begins at t_0 and finishes at t_{end}. The last frames ($\mathcal{O}(10^2)$, from $t_{end}+\Delta t$ to $t_{end,b}$) were used to define an average background. The left (l_l), right (l_r), top (l_t), bottom (l_b) limits were defined to crop the front (F) and side (S) views on the original images and extract the raw portions ($F_{A,raw}$ and $F_{B,raw}$) on each couple at times t_n and $t_n + \Delta t$. The subtraction of the background generated the images F_A and F_B per each considered couple.

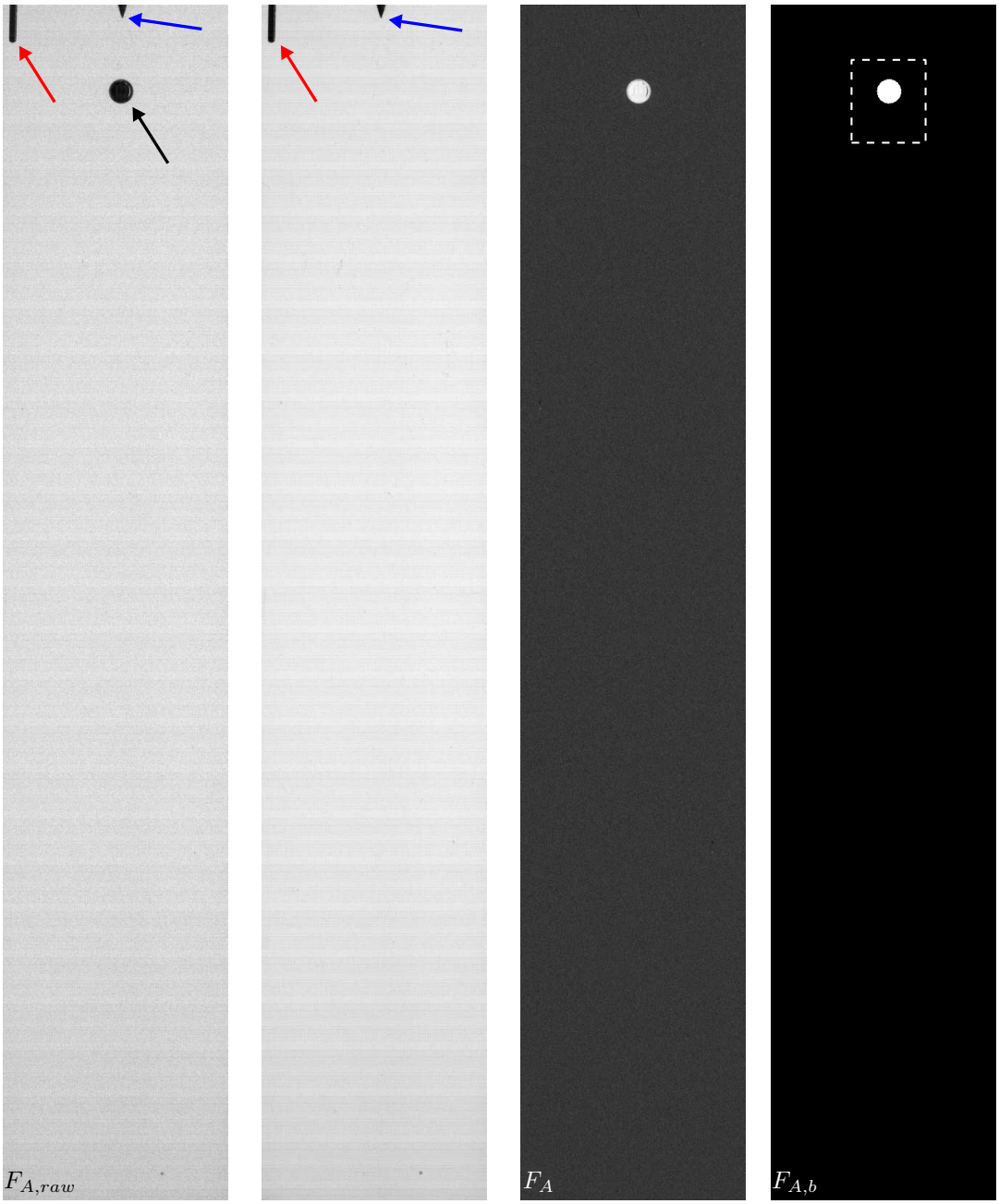

Figure 5.3 – Example of the front view extracted from an image inside a falling sphere sequence ($d = 10\,\text{mm}$ reference sphere, mixture $W000\_G100$). (a), raw image. (b), background. (c), background subtracted from the raw image. (d), binarised image. The black arrow indicates the sphere, the red arrow the thermocouple and the blue arrow the electromagnetic holder tip. The residual noise in (c) is shown to be sufficiently low (see §5.1.4) to assure a satisfactory detection of the sphere displacement. The nomenclature in (a) and (c) follows the identifiers introduced in Fig. 5.2. The dashed rectangle in (d) indicates the interrogation window identification, whose position and size is discussed in §5.1.2.

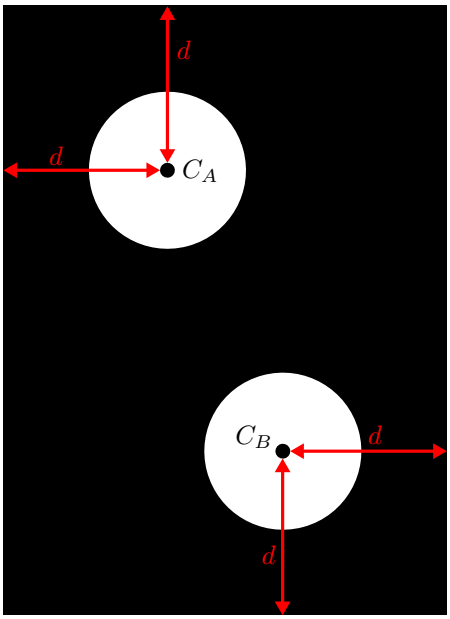

Figure 5.4 – Schematic of the definition of the position and of the dimensions of the interrogation window. The latter is centred on the average position of the sphere that displaced from point A in $F_{A,b}$ to point B in $F_{B,b}$. The size in each direction is estimated by adding one d to the coordinates of the centroids $C_A = (x_{1A}, x_{2A})$ and $C_B = (x_{1B}, x_{2B})$. The next power of two larger than the estimated dimensions along both directions $\mathbf{e}_1$ and $\mathbf{e}_2$ was selected as the interrogation window size.

An interrogation window centred on the sphere average position (between the centroids $C_A = (x_{1A}, x_{2A})$ and $C_B = (x_{1B}, x_{2B})$ of the two images of the couple) could then be generated exploiting the properties evaluated on images $F_{A,b}$ and $F_{B,b}$. The followed approach is shown in Fig. 5.4, where the sphere that displaced from point A in image $F_{A,b}$ to point B in image $F_{B,b}$ is shown. Please note that in Fig. 5.4 the sphere displacement was magnified for illustration purposes only. Knowing the position of the sphere in the two consecutive frames, the minimum size in each direction that assured one sphere d to exist between the sphere centres and the interrogation window borders was calculated. This way the sphere was assured to be inside the interrogation window in both the analysed frames. Then, the lowest possible power of two larger than the identified dimensions along both directions $\mathbf{e}_1$ and $\mathbf{e}_2$ was selected as the interrogation window size ($2K$ along $\mathbf{e}_1$ and $2L$ along $\mathbf{e}_2$). This requirement derives from the practical implementation of the FFT approach introduced at the beginning of this chapter and discussed in detail in §5.1.4. Since the aspect ratio of the interrogation window was not *a priori* imposed, if the vertical motion resulted much larger than the transversal one, the resulting interrogation window could be rectangular ($2K \neq 2L$). Otherwise, a square interrogation window was considered ($2K = 2L$). While assuring the sphere to be included in the analysis region, this approach also had the advantage to reduce the computational effort, since the cross-correlation operations were executed only on a small portion of the original images.

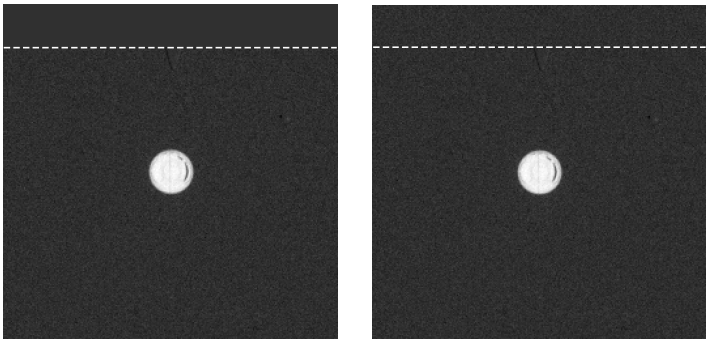

(a) (b)

Figure 5.5 – Padding techniques used to fill the interrogation window in order to achieve a size multiple of a power of two in each direction. The white dashed line indicates the discontinuity between the sample and the region artificially filled. (a) zero-padding (the region above the dashed line is completely black). (b), padding with the average noise (the region above the dashed line is filled with random noisy pixels).

5.1.3 Padding

In some of the recorded images, the sphere could be so close to the borders of the analysed region in the front and side views (F and S in Fig. 5.2) that the interrogation window defined in §5.1.2 would exceed the F and S limits. The snapshots already reported in Fig. 5.3 could be taken as an example, since they are representative of the situation encountered at the beginning of the test, where the sphere was close to the F and S top borders. The approach implemented to fix this issue consisted in a padding procedure, which typically consists in adding a sample around the analysed data in order to make the final dimension equal to a power of two (Raffel *et al.* 2007). Filling the extended sample with zeroes (zero-padding, subscript $0-p$) is the most straightforward technique but generally introduces high frequency noise when applied to noisy PIV experimental images, due to the sharp discontinuity between the noisy background and the zero values (Raffel *et al.* 2007). One common alternative is the filling of the sample to be correlated by the average background noise (noise-padding, subscript $n-p$): this technique should limit the discontinuity at the border between the sample and the artificially filled part. The comparison between the two techniques is shown in Fig. 5.5. However, in the present work the correlation procedure was applied to images where the average background noise was already subtracted, with a negligible effect of the choice of the values used for the padding. Due to its simplicity, the latter was thus executed by adding zeros until the next power of two size was encountered. The goodness of the proposed choice under the investigated conditions of this study is testified by Fig. 5.6(a) where the displacement estimation with a zero-padding and a padding with the average background noise are compared. At the beginning of the drop, that is the region where artificial padding had to be performed, the two instantaneous vertical displacements profiles $s_1(t)$ are superposed. In fact, the difference:

$$\Delta s_1 = \frac{|s_{1,0-p} - s_{1,n-p}|}{s_{1,\infty}}, \tag{5.2}$$

reported in Fig. 5.6(b) keeps lower than 0.4 % with respect to the average displacement at terminal conditions $s_{1,\infty}$.

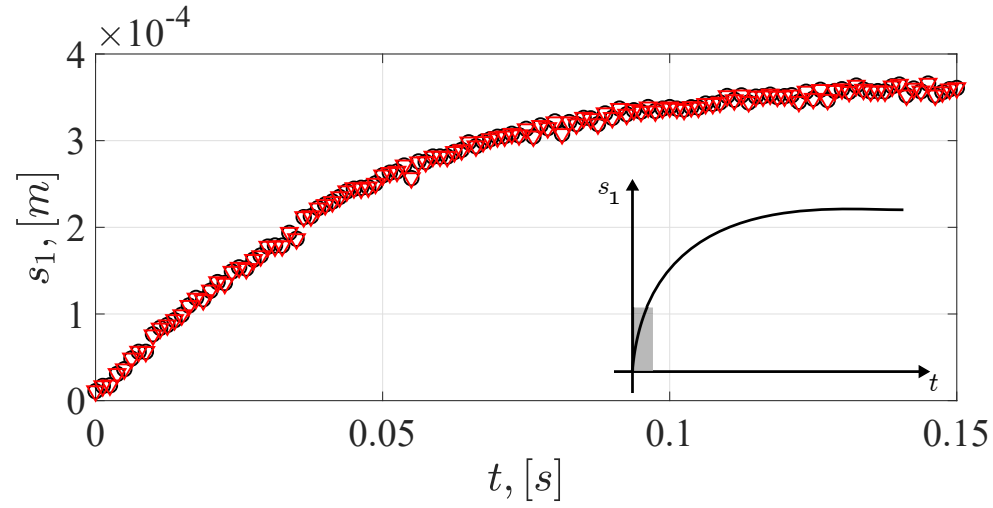

(a)

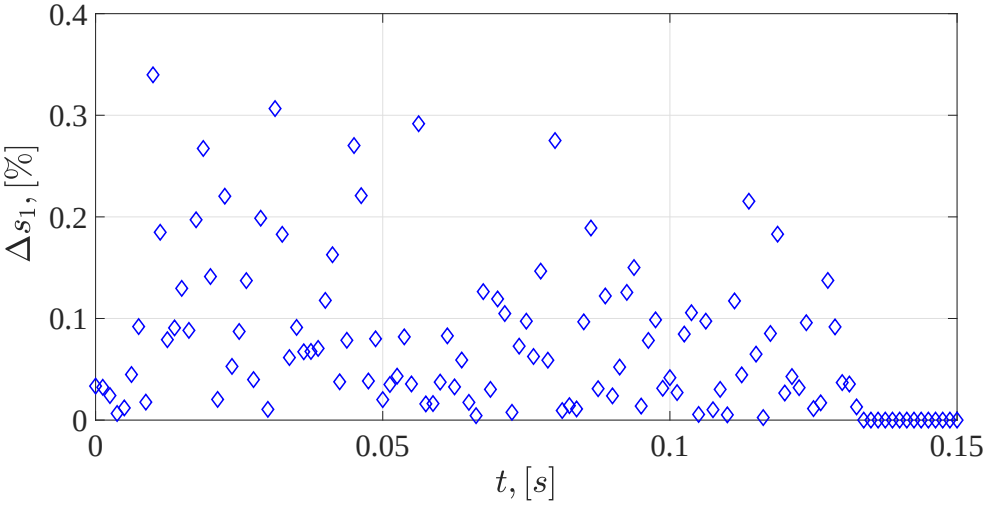

(b)

Figure 5.6 – Comparison of the zero-padding technique and of the padding with the average noise at the beginning of the drop. (a), instantaneous vertical displacement s_1 profiles of ∘, zero-padding and ▽, noise-padding. The insert with the gray rectangle qualitatively highlights the focus on the very beginning of the drop. (b), difference Δs_1 (see Eq. 5.2) on the instantaneous vertical displacement profiles between the two techniques. The difference Δs_1 reduced to zero towards high t when the padding was no more performed.

5.1.4 Cross-Correlation

The key-point of the PIV/PTV algorithms is a reliable estimation of the displacement $\mathbf{s}$ introduced in Eq. 5.1. One of the most common methods is the local search of the best match between the two images of the analysed couple in a statistical sense (Raffel *et al.* 2007). Let I_A and I_B refer to the intensity fields on the interrogation window on the first (F_A) and second (F_B) images on the couple retrieved by the procedure discussed in the previous sections. Their discrete cross-correlation can be formulated as follows (Raffel *et al.* 2007):

$$R_{I_A I_B}\left(\Delta x_1 \mathbf{e}_1 + \Delta x_2 \mathbf{e}_2\right) = \sum_{i=-K}^{K} \sum_{j=-L}^{L} I_A\left(i,j\right) I_B\left(i+\Delta x_1, j+\Delta x_2\right), \tag{5.3}$$

where $2K$ and $2L$ correspond to the interrogation window size in the $\mathbf{e}_1$ and $\mathbf{e}_2$ directions evaluated in §5.1.2. For each possible shift $\Delta\mathbf{x} = \Delta x_1 \mathbf{e}_1 + \Delta x_2 \mathbf{e}_2$ the sum of the products of the overlapping pixels of I_A and I_B is evaluated, yielding the so-called cross-correlation map, an example of which is shown in Fig. 5.7. Since the cross-correlation function measures the degree of match of the two intensities fields, the largest $R_{I_A I_B}$ value (the peak in Fig. 5.7) is obtained when the shift $\Delta\mathbf{x} = \Delta x_1 \mathbf{e}_1 + \Delta x_2 \mathbf{e}_2$ best matches the particle displacement $\mathbf{s} = s_1 \mathbf{e}_1 + s_2 \mathbf{e}_2$. In the general case of a PIV code, $\mathbf{s}$ corresponds to the mean motion of the particles inside the analysed interrogation window. The procedure thus has to be repeated for each window in order to cover the whole analysed field, with an effect of the window size on the signal over noise ratio. In the case of interest of our study, a single interrogation window for each couple of analysed frames is considered, yielding the displacement of the single particle (the sphere) inside the image.

Please note that the cross-correlation operations were executed on the gray-scale images F_A and F_B (see Fig. 5.3(c)) and not on the corresponding binarised images $F_{A,b}$ and $F_{B,b}$ (see Fig. 5.3(d)). This is due to the fact that the binarisation process affected the segmentation procedure (see Fig. 5.8), that is the identification of the sphere boundaries, by imposing one pixel at the sphere edge to be either part of the sphere or of the background. The advantage of completely removing the background noise was thus more than balanced by a gross estimation of the sphere edges (and thus its position), whose accuracy was limited by the pixel size. This was shown to possibly result into an increase of the measurement uncertainty (see e.g. Raffel *et al.* 2007, Chapter 5), especially in the tracking of single particles in PTV applications. While the preliminary estimation of the sphere position based on the binarised images revealed satisfactory for the definition of the interrogation window (see §5.1.2), the accuracy on the sphere displacement could be affected. An example ($d = 5\,\mathrm{mm}$ reference sphere falling in the mixture $W030\_G070$) is shown in Fig. 5.9, where the instantaneous displacement evaluated by the cross-correlation code applied on binarised and gray-scale images was compared. As expected, the instantaneous displacement evaluated on the binarised images resulted more noisy, thus highlighting an augmentation of the measurement uncertainty.

Since the number of multiplications to execute in the right hand side of Eq. 5.3 increases with the size of the interrogation window, and the operations have to be repeated for all the interrogation windows, the computational effort of a direct evaluation of the correlation function usually becomes prohibitive in a practical case. A more efficient method relies on the correlation theorem that states the equivalence between the cross-correlation of two intensities functions and the complex conjugate ($(\cdot)^*$ symbol) product of their Fourier transforms (indicated by the $\widehat{(\cdot)}$ symbol):

$$R_{I_A I_B} \leftrightarrow \widehat{I}_A \cdot \widehat{I}_B^*. \tag{5.4}$$

The practical implementation of this theorem used in this work consists on the Fast Fourier Transform (FFT) approach. Instead of directly evaluating the cross-correlation function via

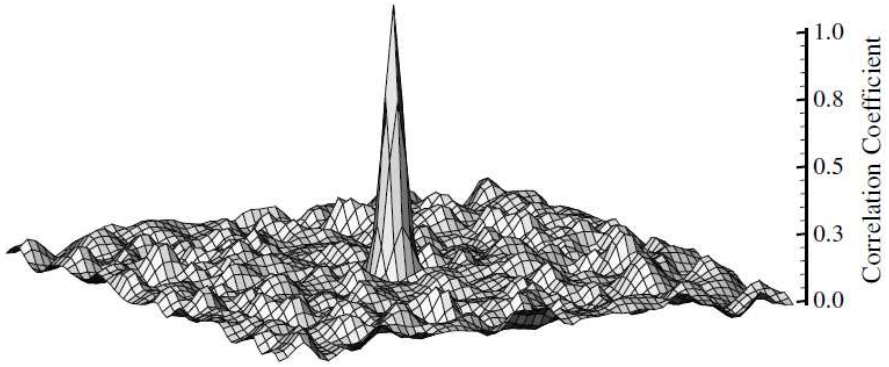

Figure 5.7 – Representation of a cross-correlation map, adapted from Raffel *et al.* (2007). A single symmetric peak of the correlation coefficient (a normalised expression of the correlation function in Eq. 5.3) is visible at the origin (the centre) of the correlation map.

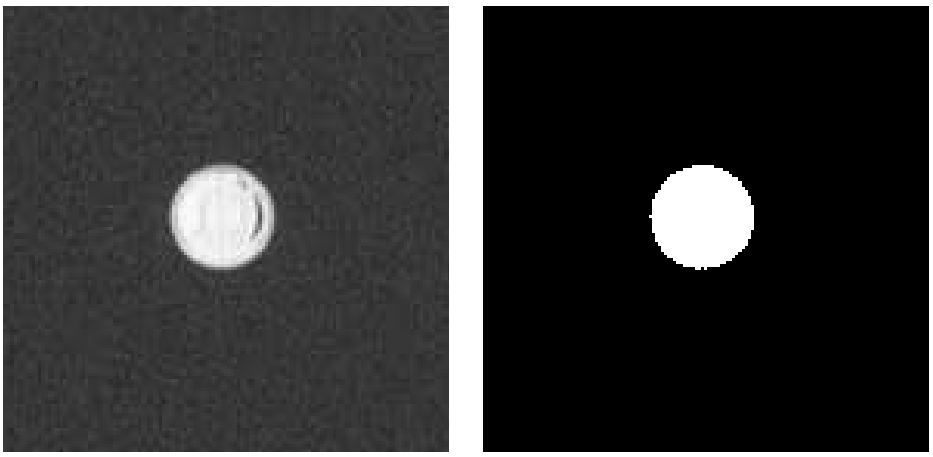

(a) (b)

Figure 5.8 – Magnified view of the region close to the falling sphere ($d = 10\,\text{mm}$ reference sphere, mixture $W000\_G100$). (a) gray-scale image. (b), binarised image. The binarisation procedure completely removes the background noise but affects the identification of the sphere edges.

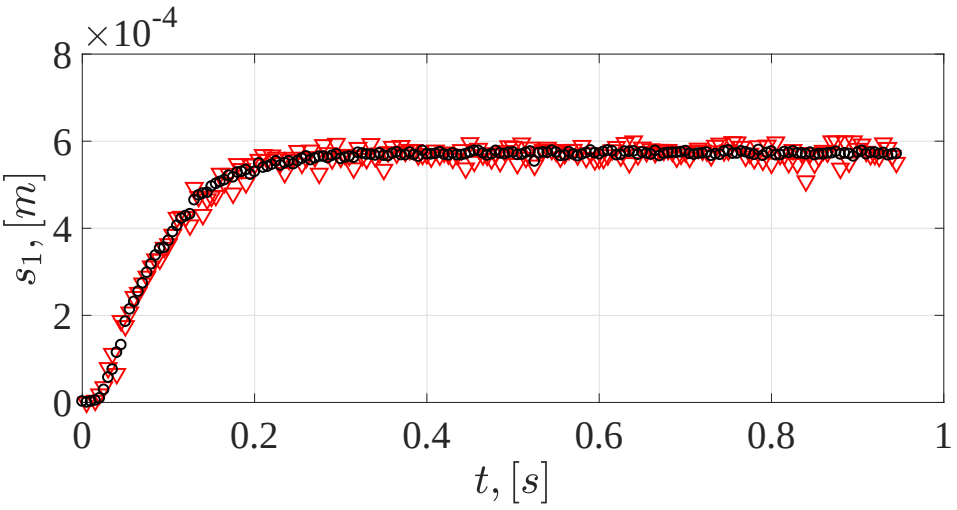

Figure 5.9 – Instantaneous vertical displacement s_1 of a $d = 5\,\text{mm}$ reference sphere falling in the mixture $W030\_G070$ evaluated by the proposed cross-correlation code applied on: ∘, original gray-scale images with background subtracted and ▽, *a priori* binarised images. The binarisation resulted into an amplification of the noise on the displacement estimation. For the sake of clarity, one point out of five is reported.

Eq. 5.3, which demands $\mathcal{O}(N^4)$ operations for a interrogation window of size N, two 2D FFTs are calculated, the complex conjugate product of their coefficients is executed and finally an inverse Fourier transform is calculated to retrieve the cross-correlation value. This procedure results in a computational effort decrease, with operations of the order $\mathcal{O}(N^2 \log_2 N)$. Moreover, a further decrease of the number of operations is achieved by exploiting the symmetry properties of the Fourier transform coefficients. Finally, as anticipated in the previous sections, the classical implementation of this efficient FFT approach requires the window size to be a power of two value, justifying the performed choice of the correlation window.

5.1.5 Sub-Pixel Accuracy

The limit of the spatial resolution of the procedure in §5.1.4 was dictated by the fact that the shifts in the definition of the cross-correlation function in Eq. 5.3 could only be represented by integer pixel values. The corresponding uncertainty on the location of the correlation peak was therefore $\pm\frac{1}{2}$ pixel (Raffel *et al.* 2007). Among the methods developed to increase the spatial resolution (see the examples reported in Fig. 5.10), the one selected in this study relied on a fit of the correlation data to a 2D Gaussian function f, which in its general elliptical form can be written as (Nobach & Honkanen 2005):

$$f\left(\Delta x_1, \Delta x_2\right) = A \exp\left[-\frac{\left(\Delta x_1 - \Delta\overline{x}_1\right)^2}{B} - \frac{\left(\Delta x_2 - \Delta\overline{x}_2\right)^2}{C} - \frac{\left(\Delta x_1 - \Delta\overline{x}_1\right)\left(\Delta x_2 - \Delta\overline{x}_2\right)}{D}\right], \tag{5.5}$$

where $\Delta\overline{\mathbf{x}} = \Delta\overline{x}_1\mathbf{e}_1 + \Delta\overline{x}_2\mathbf{e}_2$ is the identified location of the maximum peak, A describes the maximum peak height, B and C the peak widths along $\mathbf{e}_1$ and $\mathbf{e}_2$ respectively, and D is the coefficient of the peak's ellipticity term (Raffel *et al.* 2007). The latter term was in general the

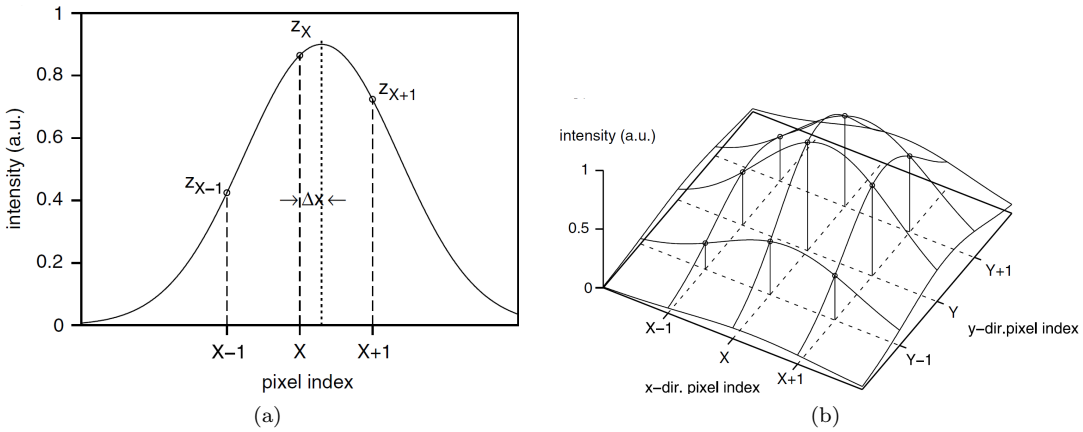

Figure 5.10 – Qualitative representation of the interpolation methods to achieve sub-pixel accuracy, adapted from Nobach & Honkanen (2005). (a), one-dimensional three-points method. (b), two-dimensional Gaussian regression. The example in (a) shows that the best estimation of the peak location achieved via a cross-correlation without sub-pixel interpolation would be at the integer pixel position X, while the actual peak was located at a distance ΔX from X.

less important in the present study due to the correlation algorithm being executed to track a single large spherical particle, resulting into a symmetric peak around its centre. The fit of the Gaussian function on the correlation data was executed in a least-mean squares sense, using three points around the peak in each direction.

5.2 Code Validation

In this section, the reliability of the presented tracking code for displacement estimation is assessed via multiple approaches.

First, synthetic images (noise free) describing the vertical free fall of a sphere were generated and the imposed motion was compared to the one retrieved by the developed algorithm. This case was representative of the situation where the subtraction of the average background to the analysed images resulted into a negligible background noise. However, since it was not possible to completely remove the random background noise (without further actions on the available images, e.g. filtering, which could negatively affect the sphere identification process) a Gaussian noise was added to the synthetic images to assess the robustness of the algorithm to residual experimental noise.

5.2.1 Synthetic Images

The synthetic images describing the vertical free fall under gravity of a solid sphere in a fluid at rest were generated by integrating in time (via a Runge-Kutta method) the expression previously reported in Eq. 4.3 in §4.2.1. The drag coefficient evolution $C_D(Re)$ proposed by Cheng (2009) and reported in Eq. 4.5 was injected into Eq. 4.3. Once retrieved the instantaneous vertical velocity $u_z^{law}(t)$ (in this section the superscript law indicates data obtained via Eq. 4.3), the corresponding instantaneous vertical position $p_z^{law}(t)$ was evaluated with a time integration via a trapezoidal rule.

A $d = 5\,\text{mm}$ reference stainless steel sphere falling in pure water ($W100\_G000$) was chosen as test case since, combining small diameter and high falling velocity, represented the most demanding conditions for the analysis. The synthetic images simulated experimental sequences recorded at 1000 fps, with a 8 bits pixel depth and a spatial resolution similar to the experimental value. A sufficient number of images ($\mathcal{O}(10^3)$) was generated to allow the drop to proceed from initial zero velocity to terminal conditions. The generated images were then analysed with the cross-correlation code following the procedure detailed in §5.1, whose main output was the instantaneous vertical displacement $s_1(t)$. The latter is shown in Fig. 5.11(a) to be superposed to the synthetic profile. The sphere accelerated up to $t \approx 0.25\,\text{s}$ and then reached terminal conditions. The error on the instantaneous displacement estimation introduced in §5.1.3 is here re-defined for convenience as follows:

$$\Delta s_1 = \frac{\left|s_1(t) - s_1^{law}(t)\right|}{s_{1,\infty}}, \tag{5.6}$$

and in reported in Fig. 5.11(b). In the transient accelerating phase a Δs_1 up to $\approx 1\,\%$ is noticed, which then progressively decreases towards terminal conditions. A cumulative sum of s_1 allowed for the estimation of the instantaneous vertical position $p_z(t)$, which is shown in Fig. 5.12(a) to be similarly superposed to the imposed synthetic profile. The error on the sphere position estimation:

$$\Delta p_z = \frac{\left|p_z(t) - p_z^{law}(t)\right|}{p_{z,\infty}}, \tag{5.7}$$

is reported in Fig. 5.12(b), showing a largest value up to $\approx 0.1\,\%$ in the accelerating phase. After terminal conditions are reached, the t increase determines an increase of the error on the position estimation up to $\approx 0.25\,\%$. This increasing trend is coherent with available experimental works on tracking of falling spheres (see e.g. Truscott *et al.* 2012). The analysis was stopped at $t_{end} = 1\,\text{s}$ since this value was representative of the time duration of the experimentally executed drops in pure water. The source of uncertainty that could influence the position estimation error were originated not only by the cross-correlation analysis but also by the generated artificial images. In fact, the approach followed in the creation of the artificial sequence consisted in evaluating the instantaneous position of the sphere centroid and then in building the circle around it. The pixels lying inside the circle were then separated from the background by modifying their value as in the case of the binarised image shown in Fig. 5.8(b). This operation was shown to negatively affect both the sphere edges smoothness and the cross-correlation code performance (see Fig. 5.9). The overall accuracy reported in Figs. 5.11 and 5.12, which was representative of all the tested case (e.g. varying frame rate and sphere diameter), was therefore considered satisfactory.

5.2.2 Noise Robustness

From the analysis of the images where the average background was subtracted (see e.g. Fig. 5.3(c)) it clearly appeared that a complete noise removal from the experimental images was unlikely to be reached. For an exhaustive review of the noise sources in CMOS sensors (the typology used in this work, see Tab. 4.1) and their advantages and disadvantages with respect to traditional CDD (Charge Coupled Device) sensors see e.g. Bigas *et al.* (2006). Since the main risks in filtering the images with a denoising algorithm are the creation of artifacts and the loss of finer structures (Buades *et al.* 2005), with possible effects on the sphere edges detection, no further process of the experimental images was performed before the execution of the cross-correlation code.

To test the robustness of the implemented code to increasing background noise, a Gaussian noise with zero mean and increasing variance σ_n was progressively added to the synthetic images discussed in §5.2.1. The same approach introduced in the previous section was followed, which

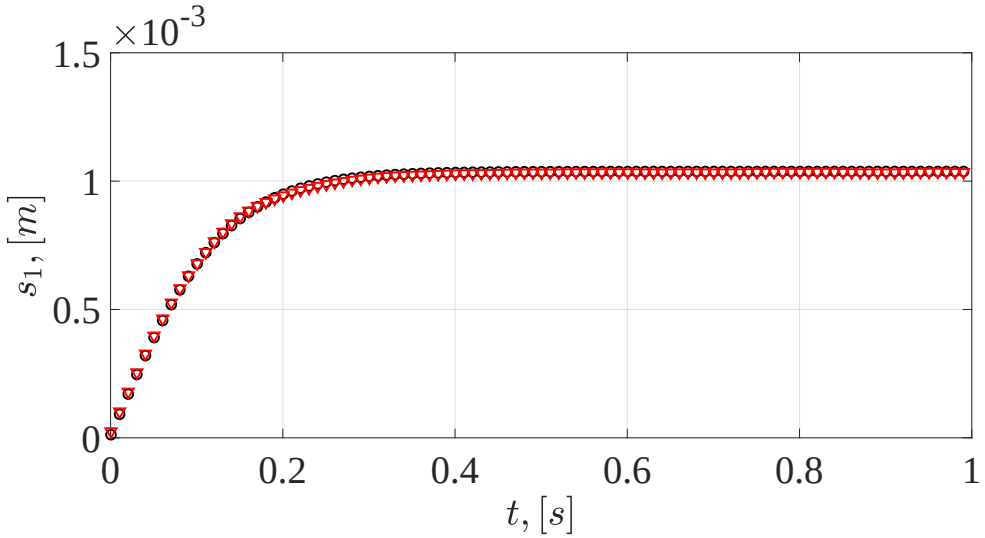

(a)

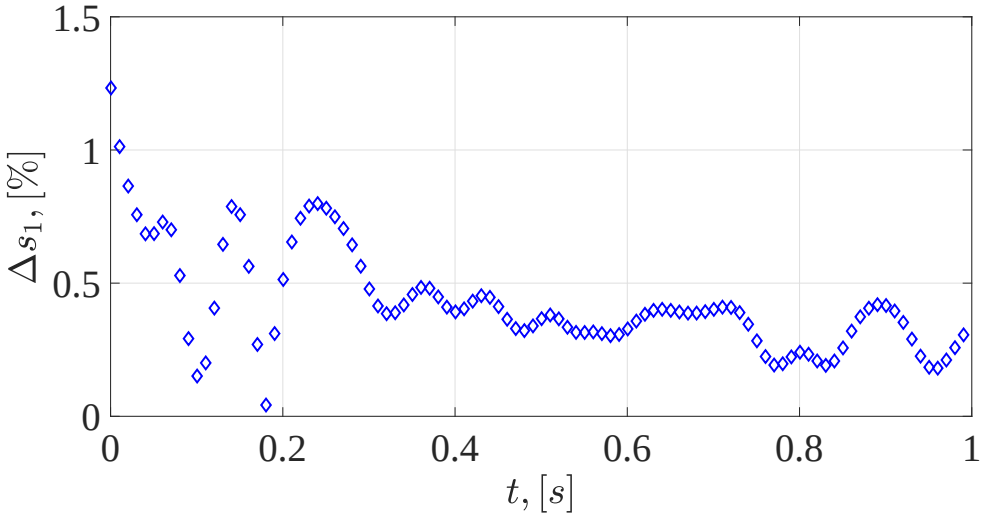

(b)

Figure 5.11 – Estimation of the instantaneous sphere vertical displacement $s_1(t)$ for a $d = 5\,\mathrm{mm}$ reference stainless steel sphere falling in pure water ($W100\_G000$). (a), comparison between: ∘, synthetic profile imposed via Eq. 4.3 and ▽, results of the cross-correlation code. (b), percentage difference (with respect to the displacement maximum value) on the displacement estimation (see Eq. 5.6).

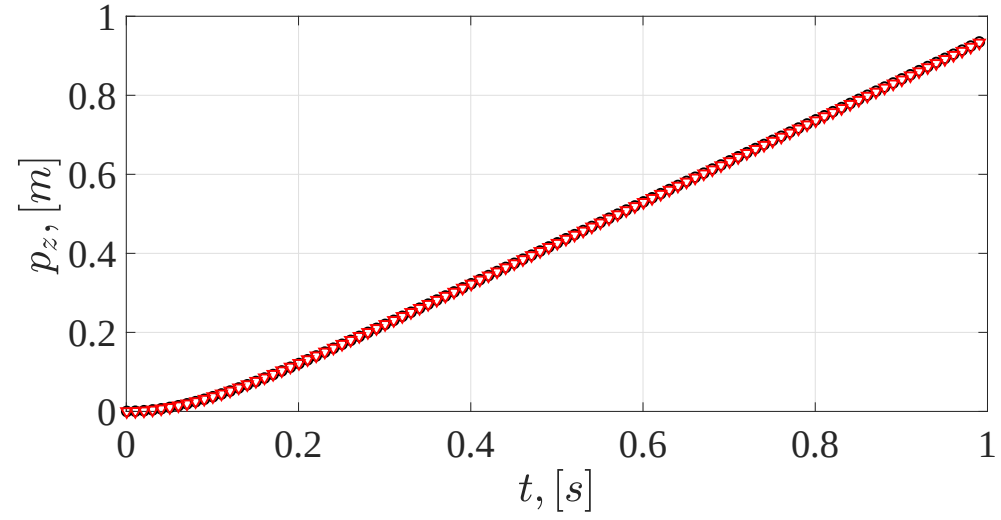

(a)

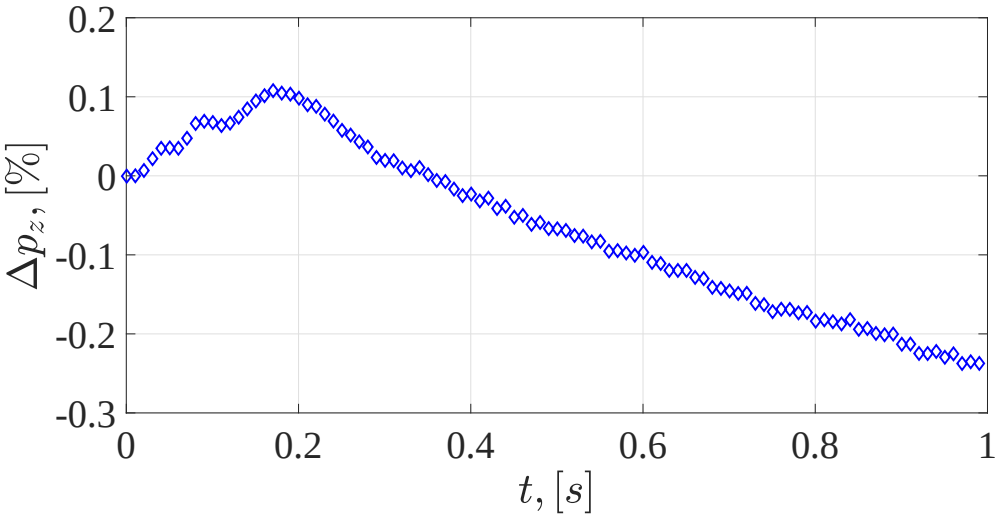

(b)

Figure 5.12 – Estimation of the instantaneous sphere position $p_z(t)$ for a $d = 5\,\text{mm}$ reference stainless steel sphere falling in pure water ($W100\_G000$). (a), comparison between: ∘, synthetic profile imposed via Eq. 4.3 and ▽, results of the cross-correlation code. (b), percentage difference (with respect to the position maximum value) on the position estimation (see Eq. 5.7).

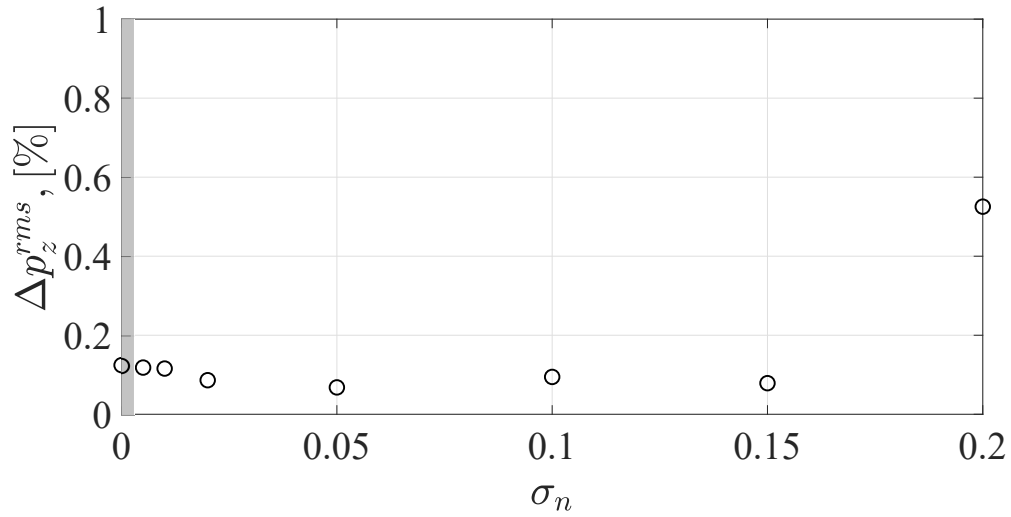

Figure 5.13 – Variation of the root-mean-square error Δp_z^{rms} (see Eq. 5.8) on the estimation of the instantaneous sphere position for increasing variance σ_n of the Gaussian noise applied to the artificially generated images ($d = 10\,\text{mm}$ reference stainless steel sphere falling in pure water ($W100\_G000$)). The accuracy of the method is almost unaffected by the noise for σ_n values typical of the experimentally recorded images ($\approx 2 \times 10^{-3}$, as highlighted by the gray-shaded region).

allowed for the recovering of the instantaneous estimation of the error on the position $\Delta p_z(t)$ introduced in Eq. 5.7. The instantaneous position is here considered, since in the next section it will be shown to be the physical starting point for the evaluation of derived quantities. In order to compare the results for increasing σ_n, the root-mean-square (superscript rms) of each error profile was evaluated as:

$$\Delta p_z^{rms} = \sqrt{\frac{1}{N}\sum_{i=1}^{N} \Delta p_{z,i}^2}, \tag{5.8}$$

and is reported in Fig. 5.13. The tested noise variance was varied in the range $0 - 0.2$ in order to stress the limits of the implemented code. However, the σ_n of the experimental images after background subtraction was estimated via the noise level estimation method proposed by Liu *et al.* (2013), providing values lower than 2×10^{-3}, which correspond to the very left region in Fig. 5.13. The accuracy of the chosen noise estimation method was a priori checked on the synthetic generated noisy images, providing an $\approx 1\,\%$ difference between the imposed and the estimated σ_n. The results in Fig. 5.13 highlight the robustness of the implemented code to background noise, with a Δp_z^{rms} that increases up to $0.6\,\%$ only for extremely high noise levels, much larger than the values characterising the recorded experimental images.

5.3 Velocity and Acceleration Estimation

Once reliable information on the instantaneous displacement and position of the falling sphere was obtained, a robust method to evaluate the vertical velocity $u_z(t)$ and acceleration $a_z(t)$ had to be developed. A rapid analysis of the expression in Eq. 4.3 shows that both $u_z(t)$ and $a_z(t)$

come into play when comparing the vertical motion of free falling spheres. Moreover, a more general perspective provided by the generalised Kirchhoff equations in §2.2.1 highlights that the comparison of the instantaneous hydrodynamic loads acting on the falling sphere requires the knowledge of both $u_z(t)$ and $a_z(t)$.

Initially, the two implemented methods for the $u_z(t)$ and $a_z(t)$ estimation are presented. Experimental data are used all along this section, which allow for a discussion of the achieved accuracy of the method. Then, the relative performance and accuracy with respect to the prediction via Eq. 4.3 is discussed.

The most straightforward method, which was the first to be implemented in this work, was the calculation of velocity and acceleration via a time derivative on position data $p_z(t)$ using a central finite difference scheme (superscript fd). However, considering an experimental measurement error ϵ on a recorded sequence whose images are separated by a time-step Δt, it can be shown that:

$$\frac{d^\alpha p_z}{dt^\alpha} \sim \frac{\epsilon}{\Delta t^\alpha}, \tag{5.9}$$

which states that the error on the estimation of a time derivative of order α of the position $p_z(t)$ scales as $\Delta t^{-\alpha}$. Therefore, for time-resolved data the noise amplification may raise to non-acceptable levels, even if very accurate measurements are performed ($\epsilon \to 0$). In that case, the amplified noise could be reduced by an *a posteriori* filtering of the evaluated profile, as will be shown in the following.

The search of a more robust technique led to the implementation of the second algorithm that was based on a smoothing spline method (superscript spl) originally introduced by Reinsch (1967) and later developed by Epps & Truscott (2010). Instead of directly performing the time derivative on the available position information, a smoothing spline $spl(t)$ constructed from a piecewise polynomial of degree n was fitted on the $p_z(t)$ profile, finally executing the time derivative on the fitted spline. Cubic ($n = 3$) and quintic ($n = 5$) splines were typically implemented. However, since in this work a smooth second derivative (the acceleration $a_z(t)$) was desired, $n = 5$ was considered. The originality of the development proposed by Epps & Truscott (2010) lied in the method to choose the optimal spline to be fitted on data. In fact, considering the time-steps t_i ($i = 1, ..., N$) of a recorded sequence, two parameters could be used to characterise a quintic spline:

$$E(spl) = \sum_{i=1}^{N} |p_z(t_i) - spl(t_i)|^2 \Delta t, \tag{5.10}$$

that is the error describing the accuracy of the approximation of the spline with respect to the available data, and:

$$R(spl) = \int_{t_1}^{t_N} \left| \frac{d^3 spl}{dt^3} \right|^2 dt, \tag{5.11}$$

that is the roughness of the spline. A high roughness value indicates a spline able to follow all the experimental data oscillations, included the noise. The interest is therefore in finding a compromise between accuracy and smoothness. The approach introduced by Epps & Truscott (2010) thus reduced to evaluate for each error tolerance E the spline with the least possible roughness R, provided that $E(spl) \leq E$. The analysis of the generated $R - E$ chart then allowed for the identification of the critical error tolerance E_{cr}, which corresponded to the optimal fit spline. The starting point of the procedure was an experimental $p_z(t)$ profile, as the one reported in Fig. 5.14(a) in the case of a $d = 5\,\text{mm}$ reference stainless steel sphere falling in pure water ($W100\_G000$). Once defined a sufficiently large error tolerance range inside which the acceptable tolerance was searched, the corresponding roughness was evaluated via Eq. 5.11, generating the

chart in Fig. 5.14(b). The latter clearly shows that, starting from the highest E values, the roughness R progressively increased and kept to low values until a critical error tolerance E_{cr} was reached, which made R suddenly increase of several orders of magnitude. The optimal spline was therefore evaluated in correspondence of E_{cr}. The identified $R-E$ trend was representative of all the executed tests. Moreover, the E_{cr} evaluation was interesting from the point of view of the overall method accuracy estimation since Epps & Truscott (2010) showed that:

$$\epsilon \sim \sqrt{\frac{E_{cr}}{N\Delta t}}, \tag{5.12}$$

which for the experimental values of the considered test case ($N \approx 7 \times 10^2$ and $\Delta t = 1 \times 10^{-3}$ s) provided an experimental measurement error $\epsilon \approx 5\,\mu$m, that is 0.1 % of the sphere diameter $d = 5$ mm analysed in the test case here reported. Considering the achieved experimental spatial resolution (0.3 mm px^{-1}), the estimated ϵ value corresponds approximately to ± 0.02 px, confirming the achievement of the sub-pixel accuracy discussed in §5.1.5. Once generated the optimal spline (see Fig. 5.14(a)), two time-derivative steps allowed for the evaluation of the instantaneous vertical velocity and acceleration profiles.

The vertical velocity profiles $u_z(t)$ shown in Fig. 5.15(a) highlight that under the investigated operating conditions no significant differences between the two implemented methods were found, and both techniques agree with the semi-empirical prediction of Eq. 4.3. In detail, the experimental curves well agree with the computed profile at the beginning of the drop ($t < 0.1$ s) and at terminal conditions ($t > 0.4$ s). The difference between the predicted and the experimentally evaluated terminal velocities for reference spheres was always lower than 1 %. The departure of the experimental curves from the semi-empirical prediction will be shown in Chapter 6 to be connected to the onset of transversal motion, which cannot be taken into account by the expression proposed in Eq. 4.3 valid in the gravity direction. The relative variation (with respect to the terminal velocity predicted by Eq. 4.3) of the vertical velocity:

$$\Delta u_z = \frac{u_z^{fd} - u_z^{spl}}{u_\infty^{law}}, \tag{5.13}$$

is reported in Fig. 5.15(b) and shows that the finite difference scheme and the smoothing spline technique provided approximately the same u_z estimation along the whole drop, with differences lower than 1 %. The larger values at the beginning of the drop were due to the low u_z magnitude right after the sphere started to fall. In fact, the difference was estimated lower than 0.5 % approaching terminal conditions. Since no filtering was performed in the finite difference case, Fig. 5.15(b) testifies that the measurement error amplification in the first time derivative step, that is from position data to velocity, was negligible.

Conversely, a second time derivative step from velocity to acceleration amplified the measurement error to a non-satisfactory level in the finite difference case. The marked amplification of the experimental noise is shown in Fig. 5.16(a), where the finite difference-based acceleration is compared to the profile evaluated via the spline technique and the curve predicted via Eq. 4.3. The latter predicted a monotonous decrease of the sphere acceleration magnitude from the beginning of the drop to terminal conditions. The trend is well followed by the spline fitting profile. As in the $u_z(t)$ case, the differences between the predicted and the experimental curves were due to the onset of transversal motion, as will be discussed in Chapter 6. The acceleration estimated by the finite difference scheme thus needed to be filtered to adequately reduce the experimental noise to a satisfactory level. With the objective of reducing the noisy finite difference acceleration information shown in Fig. 5.16(a) to the smooth profile evaluated via the spline technique, a Savitzky-Golay filter (see e.g. Orfanidis 2010, Chapter 8) with a third order polynomial and a

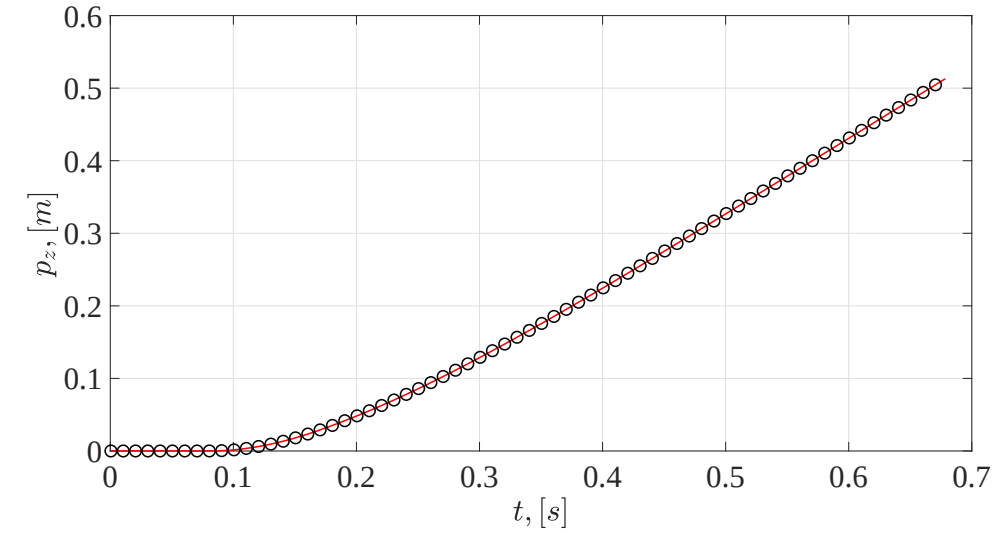

(a)

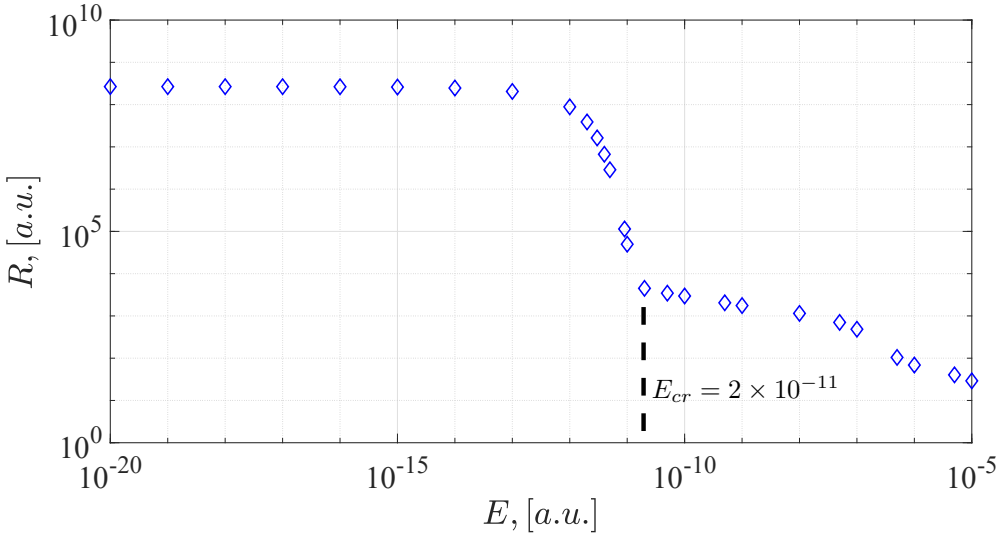

(b)

Figure 5.14 – Smoothing spline method for the fit of the instantaneous sphere position $p_z(t)$ for a $d = 5\,\text{mm}$ reference stainless steel sphere falling in pure water ($W100\_G000$). (a), $p_z(t)$ profile: ∘, cross-correlation code, (—), smoothing spline fitted on the data (selected via the E_{cr} criterion). (b), identification of the critical error tolerance ($E_{cr} = 2 \times 10^{-11}$) as the best compromise between low roughness R and high accuracy (low E). In the reported test case the sphere was kept fixed at the beginning of the test and the drop started at $t_0 \approx 0.1\,\text{s}$.

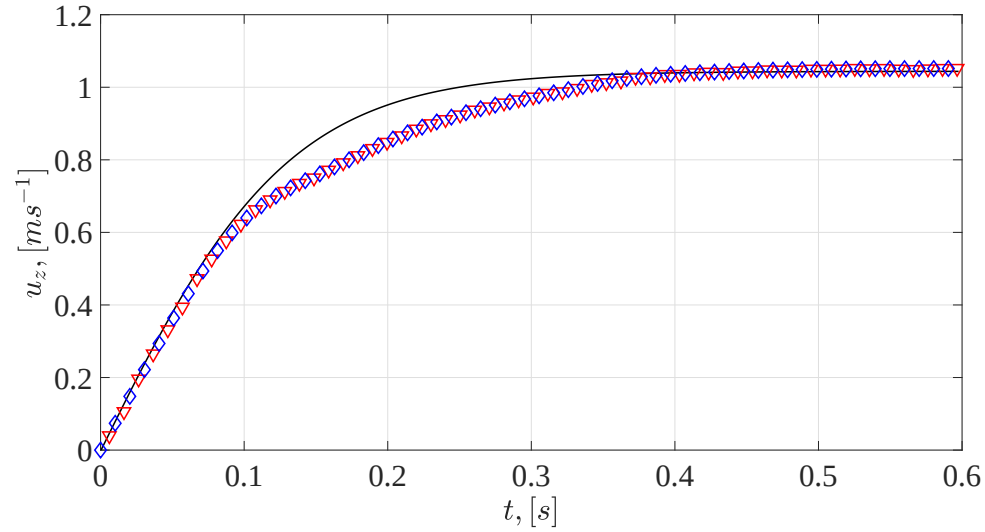

(a)

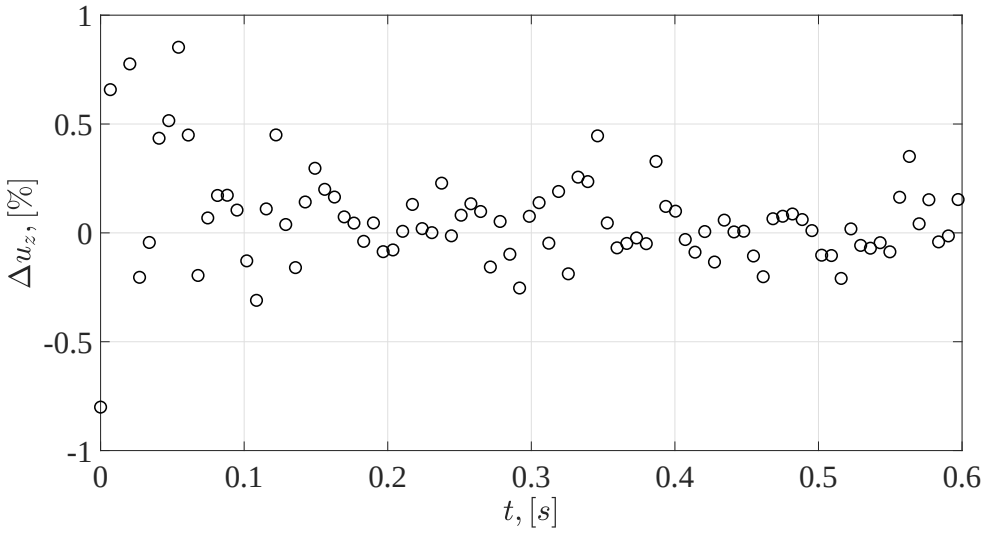

(b)

Figure 5.15 – Vertical velocity evaluation from position data shown in Fig. 5.14 with the finite difference scheme and the smoothing spline fitting technique. (a), vertical velocity profile $u_z(t)$: (—), prediction via Eq. 4.3, ◇, smoothing spline, ▽, finite difference. (b), variation on the evaluated vertical velocity between spline fitting and finite difference scheme (see Eq. 5.13). For the sake of clarity, one point out of fifteen is reported. Please note that the $u_z(t)$ experimental profiles in (a) were reported starting from the initial time of the drop t_0 introduced in Fig. 5.15, in order to be compared with the predicted curve. The detachment of the experimental curves from the prediction is due to the onset of transversal motion, as discussed in Chapter 6.

window length equal to at least 25 experimental points was used. The proposed filter performed particularly well in preserving a part of the high-frequency content of the experimental data, thus avoiding a too strong smooth out of the signal. The corresponding filtered $a_z(t)$ profile then collapsed on the spline technique curve. In fact, the deviation of the vertical acceleration (with respect to the acceleration maximum value predicted by Eq. 4.3) between filtered finite difference and spline technique was defined as:

$$\Delta a_z = \frac{a_z^{fd} - a_z^{spl}}{a_z^{law,max}}, \tag{5.14}$$

and is shown in Fig. 5.16(b) to keep lower than 1 % along the whole drop except for the very beginning of the test ($t < 0.1\,\mathrm{s}$). In that region, the low instantaneous u_z values coupled with the high instantaneous a_z variation could explain the residual larger difference between the proposed techniques. These variations do not influence the region of interest discussed in Chapter 6, where attention will be focused on the onset of wake instability and on terminal conditions, which both occur at larger t. Since the uncertainties discussed above were evaluated in the most severe case (i.e. for $d = 5\,\mathrm{mm}$), their order of magnitude is representative of the uncertainties of all the analysed spheres, characterised by larger diameter and velocity values.

The properties of the two implemented techniques are resumed in Tab. 5.1. The finite difference technique was shown to perform well in the $u_z(t)$ estimation, whereas a poor $a_z(t)$ profile was generated. This required the introduction of a filtering process, whose properties had to be arbitrarily set by the user. Conversely, the spline fitting procedure performed well in all the considered time derivative steps. This less arbitrary method was nevertheless shown to increase the complexity of the procedure with respect to the finite difference. However, due to the robustness of the implemented smoothing spline technique, the latter was preferred in this study. The results shown in the next chapters concerning the vertical velocity and acceleration were therefore evaluated via the smoothing spline technique.

	$u_z(t)$	$a_z(t)$	**Complexity**	**User Input**
fd	OK	Filter	Simple	Filter Properties
spl	OK	OK	More Complex	None

Table 5.1 – Comparison of advantages and disadvantages of the finite difference (fd) and spline fitting (spl) techniques for velocity $u_z(t)$ and acceleration $a_z(t)$ estimation.

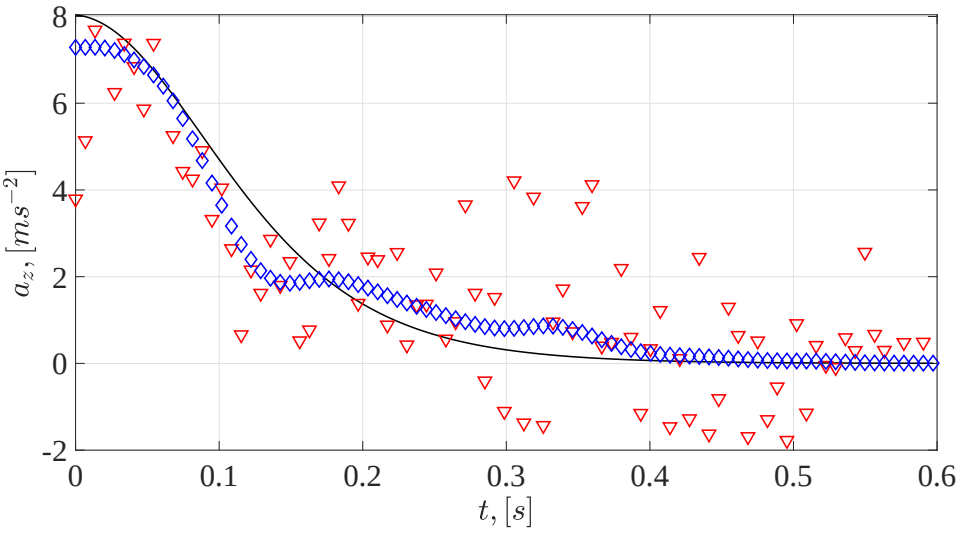

(a)

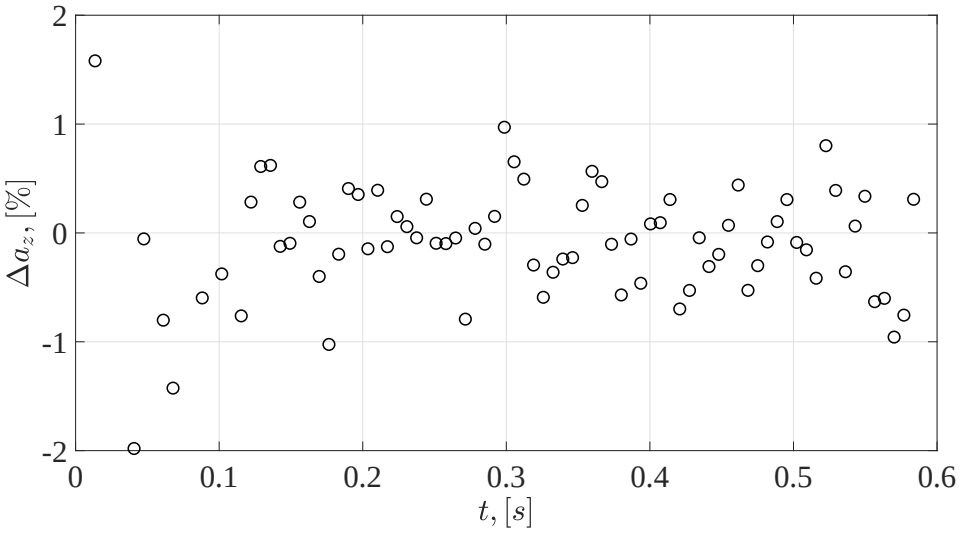

(b)

Figure 5.16 – Vertical acceleration evaluation from velocity data shown in Fig. 5.15 with the finite difference scheme and the smoothing spline fitting technique. (a), vertical acceleration profile $a_z(t)$: (——), prediction via Eq. 4.3, ◇, smoothing spline, ▽, finite difference. (b), variation on the evaluated vertical acceleration between spline fitting and filtered finite difference scheme (see Eq. 5.14). For the sake of clarity, one point out of fifteen is reported. Please note that the $a_z(t)$ experimental profiles in (a) were reported starting from the initial time of the drop t_0 introduced in Fig. 5.15, in order to be compared with the predicted curve. The detachment of the experimental curves from the prediction is due to the onset of transversal motion, as discussed in Chapter 6.

Chapter 6

Experimental Results

This chapter describes the results of the falling sphere experimental campaigns, obtained via the experimental set-up and the post-processing techniques introduced in Chapters 4 and 5. For the sake of clarity, the overview of the performed tests introduced in §4.3 in here reported in Fig. 6.1. In fact, the plan of the present chapter follows naturally from the identified ranges. First, the low Reynolds number limit attained with tests in glycerine is discussed, with the presentation of a porous medium model able to explain the absence of a noteworthy drag reducing ability of SH coatings in the investigated regime. Second, the results in the intermediate Reynolds number regime in water-glycerine mixtures are presented, highlighting the role of SH coatings in a regime where wake instabilities occur. This discussion allows the introduction of the results in the high Reynolds number regime obtained with tests in pure water, where the interaction between the deformation of the air layer around SH spheres, the instantaneous hydrodynamic loads acting on the falling sphere and the development of wake and path instabilities is further analysed.

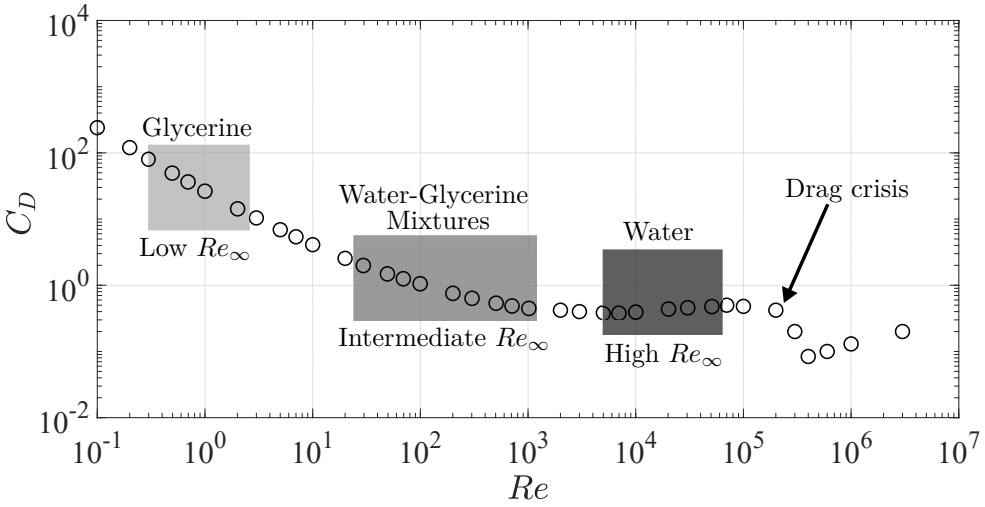

Figure 6.1 – Drag coefficient C_D as a function of the Reynolds number Re for reference spheres. ∘, experimental data from Lapple & Sheperd (1940). The grey-shaded rectangles indicate the whole Re_∞ ranges analysed with the falling sphere experimental campaigns. All the shown results lie below the appearance of the drag crisis phenomenon, indicated by the black arrow.

6.1 Low Reynolds Number

This section discusses the results of the falling sphere tests in glycerine, which were executed to analyse the low terminal Reynolds number regime, $0.3 < Re_\infty < 3$ (see Fig. 6.1). The regime analysed with the glycerine tests resulted not so far from the upper limit of the Stokes's flow (typically $Re_\infty \approx 10^{-1}$ is considered as threshold) and well below the $Re_\infty \sim 10^2$ necessary to enter the region of the transitions of the wake of a fixed sphere (see §2.1 in Chapter 2). In the next paragraph, the experimental results in terms of terminal drag are presented. A scaling analysis is fully presented in Appendix D to show which are the suitable physical mechanisms that could explain the evaluated results. Once identified the leading mechanism, a porous medium model able to justify the absence of a significant SH coating drag reduction is developed and validated with the few data available in literature.

These results constitute the main findings included in an article that, at the moment of the redaction of this manuscript, was under review in *Physical Review Fluids* (Castagna *et al.* 2019*c*).

6.1.1 Hydrodynamic Performance

Before the execution of the falling tests campaign, the behaviour of the produced SH coatings when interacting with glycerine was tested. The quantitative results on flat plates reported in Tab. 3.3 showed a limited variation of the SH behaviour when switching from pure water to glycerine. Moreover, a qualitative assessment of the presence of the air layer was performed directly on the produced SH spheres. The visualisation sequence in Fig. 6.2 testifies the establishment of the air layer once the SH sphere is progressively dipped into glycerine. In fact, the shiny appearance of the near-wall region may be explained by light reflection and refraction at the curved interface between liquid and air. Moreover, the SH spheres recovered from the tank after the drop were always dry, confirming that the air layer was present all along the test execution.

As discussed in §2.1 and §2.2, the low Re_∞ range characterising the tests in glycerine implies that no reason *a priori* exists for the appearance of wake instabilities and therefore relevant transversal motion. This was confirmed by analysing the recorded videos via the techniques discussed in Chapter 5, retrieving a transversal motion within the measurement noise. For this reason, in the following focus is given on the vertical motion only.

The vertical velocity profiles for all the analysed d range are reported in Fig. 6.3. As discussed in §4.3, the largest investigated d was set to 10 mm in order to limit the blockage factor to $\delta = 0.09$. Two limitations of the experimental set-up, which was conceived to operate with water, must be taken into account when working with high μ_l liquids. First, the free surface of the liquid inside the tank was in contact with ambient air. Even if a cap was manufactured to cover the top side of the tank, this could not prevent the interaction between the liquid and the humid air in the room. As a result, ambient air humidity could saturate into the glycerine, determining a non-negligible local μ_l decrease in the region close to the free surface. This fact is guessed to be responsible of the $u_z^\star$ overshoot visible in Fig. 6.3 at the very beginning of the drop. In fact, the overshoot peak corresponds to a distance from the free surface of the order of 1 cm, that is right after the beginning of the sphere vertical motion. In detail, the $u_z^\star$ peak value in Fig. 6.3 can be estimated via the prediction in Eq. 4.3 by considering an $\approx 2\,\%$ (volumetric fraction) water inclusion in the glycerine, which is sufficient to determine a local μ_l decrease of $\approx 30\,\%$. The liquid density is less sensitive to small fractions of water inclusions, with a corresponding ρ_l variation limited to $\approx 0.3\,\%$. The sphere initial acceleration thus occurs in a liquid that locally presents a significantly lower dynamic viscosity, thus explaining the reached velocity higher than the corresponding terminal value. Further descending along the tank height,

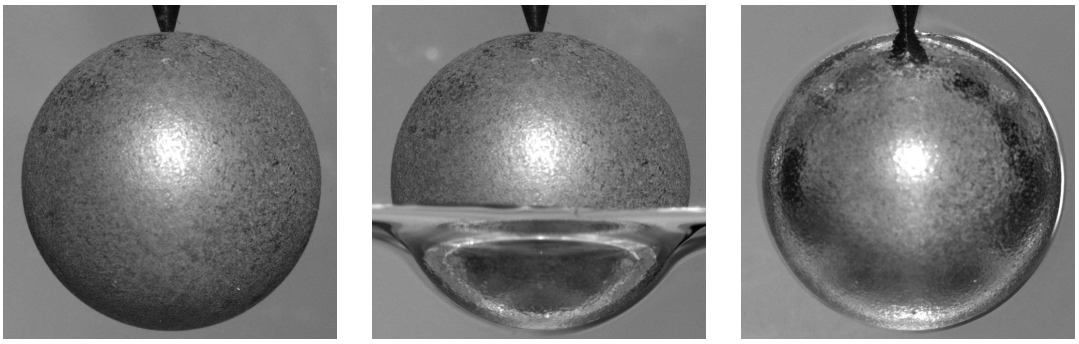

(a) (b) (c)

Figure 6.2 – Visual evidence of the air layer establishment around a $d = 15\,\text{mm}$, SH-NAR sphere progressively dipped in glycerine. (a), air. (b), partially dipped. (c), fully immersed. Image (b) highlights the difference between the area above the glycerine surface and the part of the sphere dipped in the glycerine. The bright appearance in images (b) and (c) testifies the establishment of the air layer.

the effect of the interaction with the ambient air is progressively reduced, due to the difficulty of water molecules to diffuse into quiescent glycerine. In fact, the relative magnitude between the momentum and mass transport can be estimated via the Schmidt number $Sc = \frac{\nu_l}{D}$, where D is the mass diffusivity (see e.g. Mauri 2015, Chapter 14). The high Sc range ($10^5 - 10^6$) valid for the couple water-glycerine (see e.g. Rapp 2017, Chapter 9) testifies the slowdown of transfer processes in glycerine physically due to the inter-molecular hydrogen bonds created by the OH groups present in its molecule (Atanov & Berdenikov 1981). A kinematic viscosity $\nu_l \sim 10^{-3}\ \text{m}^2\,\text{s}^{-1}$ (valid for glycerine at $T = 20\,^\circ\text{C}$) allows to evaluate the order of magnitude of the diffusion coefficient as $D \sim 10^{-8} - 10^{-9}\ \text{m}^2\,\text{s}^{-1}$. By considering a characteristic time τ_{exp} of the experimental campaign duration, the height L of glycerine contaminated by water molecules can be estimated as:

$$L \sim \sqrt{D\tau_{exp}}. \tag{6.1}$$

An upper limit of τ_{exp} equal to ten days clearly shows that L could vary in the range $3 - 10$ cm, depending on the actual considered D value. It can thus be inferred that the effects of the water fraction inclusion could be considered limited to the region close to the free surface, with reduced influence on terminal conditions reached in the lower part of the tank.

Moreover, a second limitation of the experimental set-up was connected to the liquid temperature handling. In fact, the temperature at different heights of the tank could be monitored by a thermocouple, but no active temperature control was available, except for a constant ambient temperature on the room. This implied that the liquid inside the tank was influenced by the contact with the tank walls, which at the same time were in contact with the supporting structures of the experimental rig. While the temperature along the tank height was uniform in the case of pure water, a difference of approximately $1\,^\circ\text{C}$ was observed for glycerine, decreasing from the free surface towards the bottom of the tank. As was shown in Fig. 4.17, this could result into a glycerine μ_l variation up to $10\,\%$. This finding could explain the descending $u_z^\star$ trend observed in Fig. 6.3, which becomes more evident for increasing d. In fact, an increasing μ_l due to the decreasing T is progressively encountered by the falling sphere.

The combined effect of water molecules inclusion from ambient air and temperature variation along the tank height was estimated via Fig. 6.4, where the viscosity variation along the

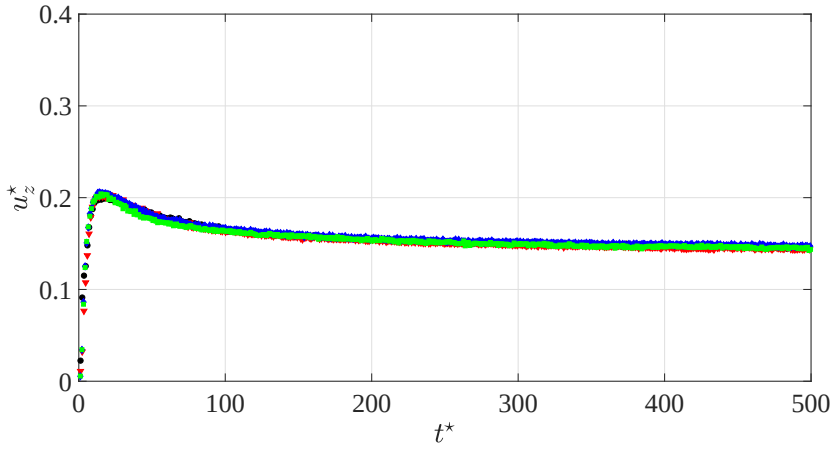

(a)

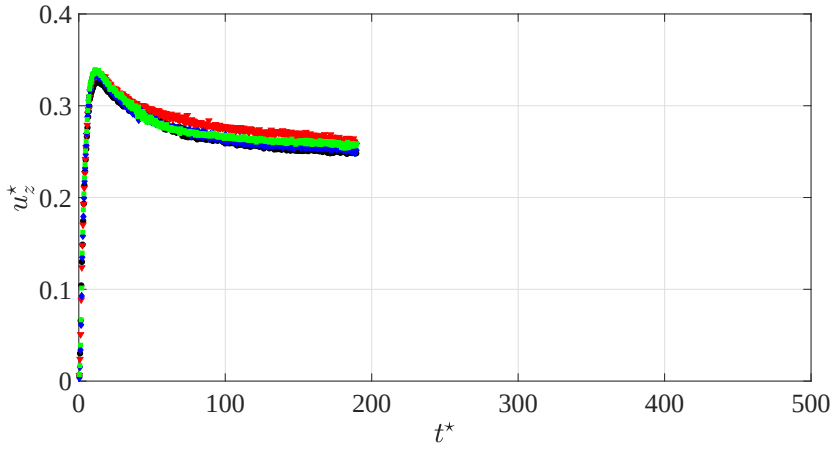

(b)

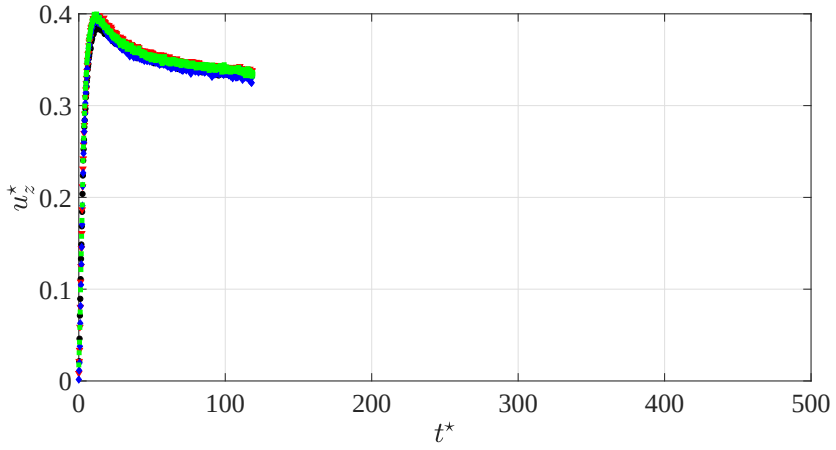

(c)

Figure 6.3 – Instantaneous vertical velocity $u_z^\star$ for all the analysed coatings in the glycerine tests. •, reference. ▼, SH-NAR. ♦, SH-220. ■, SH-80. (a), $d = 5\,\text{mm}$. (b), $d = 8\,\text{mm}$. (c), $d = 10\,\text{mm}$.

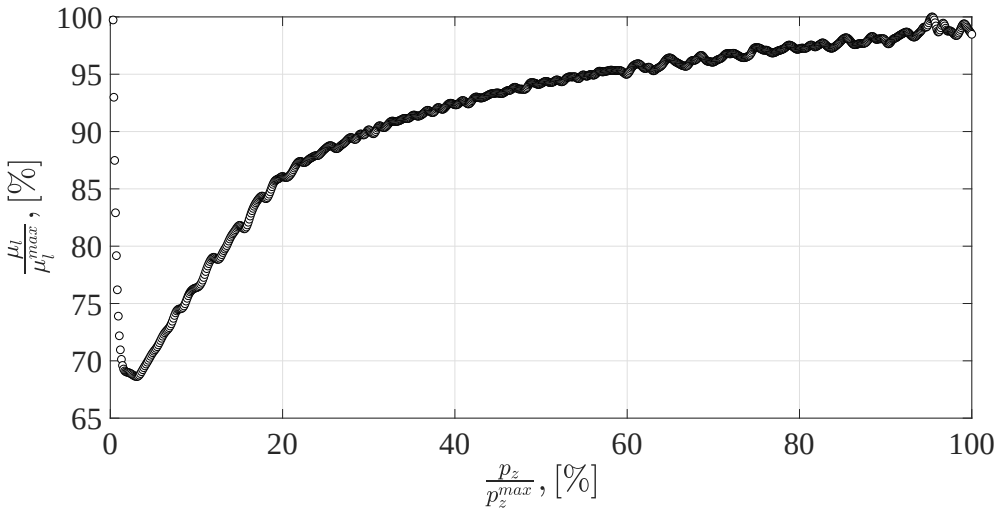

Figure 6.4 – Non-dimensional dynamic viscosity $\frac{\mu_l}{\mu_l^{max}}$ variation as a function of the non-dimensional sphere position $\frac{p_z}{p_z^{max}}$ along the tank height. The minimum value ($\approx 70\,\%$) is reached approximately 1 cm below the free surface. The oscillations are due to the low threshold value set in the spline technique for velocity and acceleration estimation (see §5.3), necessary to correctly catch the identified $u_z^\star$ overshoot, thus determining an increase of the spline roughness.

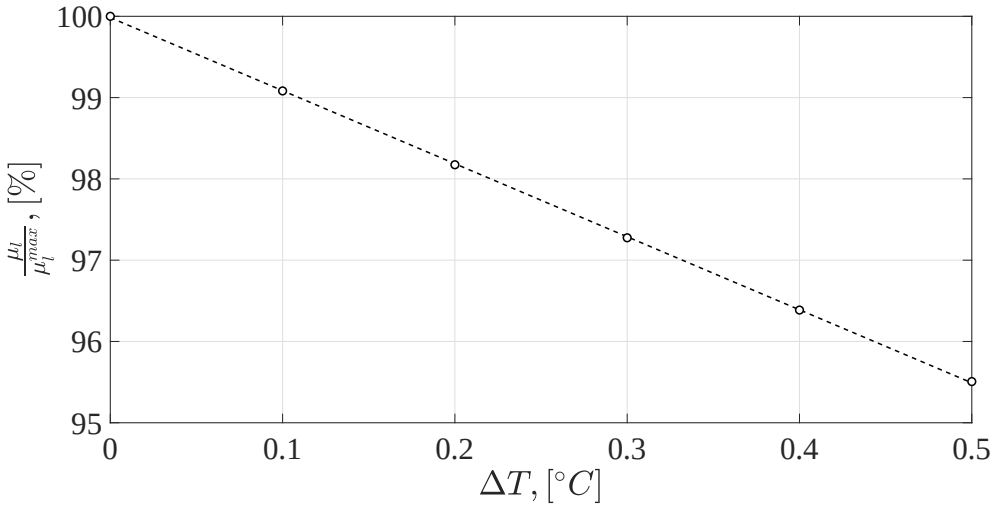

Figure 6.5 – Non-dimensional dynamic viscosity $\frac{\mu_l}{\mu_l^{max}}$ variation as a function of an imposed temperature variation, according to the empirical laws by Cheng (2008) discussed in §4.3. (- - -), fit of the evaluated data to highlight the linear behaviour.

tank height was evaluated for the $d = 5\,\text{mm}$ reference sphere shown in Fig. 6.3(a). Starting from the experimentally reconstructed instantaneous vertical position $p_z(t)$, the vertical velocity and acceleration profiles were estimated via the technique described in §5.3. These values were then injected in Eq. 4.3 to retrieve the instantaneous drag coefficient evolution $C_D(t)$, which allowed for the estimation of the instantaneous $Re(t)$ via the $C_D(Re)$ law introduced in Eq. 4.5. The $Re(t)$ profile thus enabled the estimation of $\mu_l(t)$, finally achieving the $\mu_l(p_z)$ relation shown in Fig. 6.4 (in non-dimensional form) thanks to the known $p_z(t)$ evolution. The minimum μ_l ($\approx 70\,\%$ of the asymptotic value in the bottom part of the tank) is reached approximately 1 cm below the free surface. The μ_l then increases towards the corresponding asymptotic value. Please note that a water inclusion of $\approx 0.5\,\%$ determines a μ_l decrease of $\approx 10\,\%$, which is the value reached at $\approx 30\,\%$ of the tank height. Moreover, the approximately linear μ_l increase in the lower part of the tank ($\frac{p_z}{p_z^{max}} > 50\,\%$) visible in Fig. 6.4 can be well explained by considering a linear temperature decrease from the free-surface to the bottom side of the tank, which results into a $\Delta T \approx 0.5\,^\circ\text{C}$ variation in the lower half of the tank. From the empirical law by Cheng (2008) discussed in §4.3, a linear viscosity variation up to $\approx 5\,\%$ is reported in Fig. 6.5 for the considered ΔT, which is exactly the same order of magnitude evaluated in Fig. 6.4 for $0.5 \leq \frac{p_z}{p_z^{max}} \leq 1$. Even if the effects of the experimental set-up limitations on the liquid properties are significant, the evaluated results are discussed in the following of the paragraph since relative considerations between spheres tested in the same conditions are performed. Obviously, a deeper analysis on the detected phenomena should be performed, with a possible implementation on the experimental rig of an active temperature control and of a mechanism to control the interaction with the ambient air to mitigate the observed issues.

The $u_z^\star$ profiles in Fig. 6.3 show the absence of a significant SH coating influence both in transient and terminal regions. To analyse in detail the terminal drag, $u_\infty^\star$ is estimated for each sphere by averaging the last fifty available points (in order to reduce the influence of the decreasing $u_z^\star$). The estimated $u_\infty^\star$ value is corrected for blockage effects via the technique discussed in §B.2 in Appendix B. The resulting terminal drag coefficient is evaluated exploiting Eq. 4.3, which at terminal conditions and after normalisation via u_D (see Eq. 4.7(b)) gives:

$$C_{D\infty} = \frac{4}{3u_\infty^{\star 2}}. \tag{6.2}$$

The $C_{D\infty}$ values are reported in Fig. 6.6, where a good agreement is found between the reference sphere and the Stokes' law $C_{D\infty} = \frac{24}{Re_\infty}$. In detail, the uncertainty on $C_{D\infty}$ (95% confidence level) is of the same order of the size of the symbols. The corresponding horizontal error bars on Re_∞ were evaluated by following the previous analysis on the μ_l uncertainty. In fact, by looking at Fig. 6.4, a μ_l variation $< 10\,\%$ with respect to the nominal value was estimated at terminal conditions. The identified μ_l uncertainty order of magnitude ($10\,\%$) was thus chosen as a conservative upper limit for the Re_∞ error bar estimation. The *loglog* scale in Fig. 6.6 was chosen to allow the insertion of the few data available in literature dealing with SH sphere tests in glycerine. The absence of a noteworthy drag reducing ability of SH coatings visible on the evaluated experimental data is coherent with the results of Byon *et al.* (2010) and Ahmmed *et al.* (2016). The former focused attention on nano-structured super-hydrophilic spheres in Stokes' regime, providing also results for SH spheres, which determined a limited $\approx 2\,\%$ terminal velocity increase. Ahmmed *et al.* (2016) tested in glycerine polytetrafluoroethylene (PTFE) laser-nano-structured SH spheres, evidencing a negligible variation on the evaluated terminal drag with respect to the reference.

The absence of noteworthy effects on terminal drag is made more evident in Fig. 6.7 where

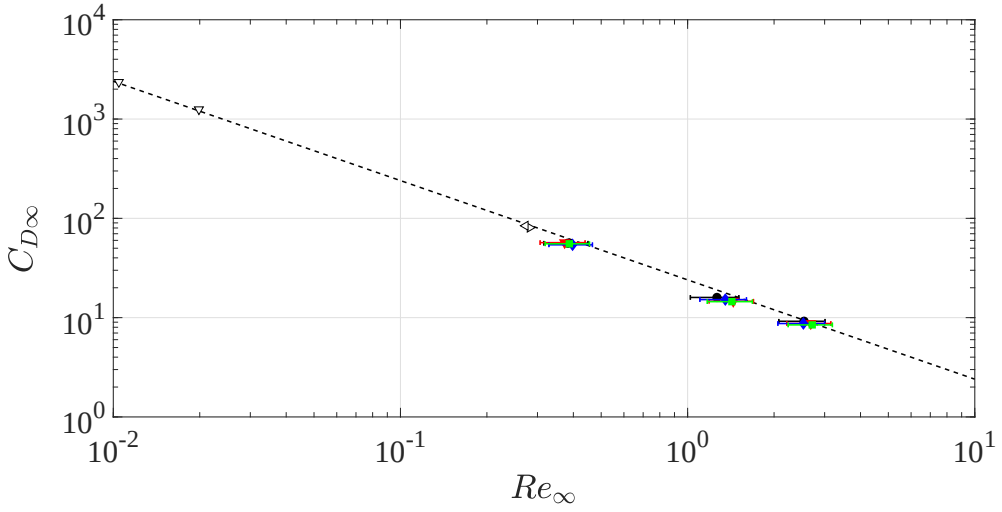

Figure 6.6 – Terminal drag coefficient $C_{D\infty}$ as a function of the terminal Reynolds number Re_∞ for the glycerine tests. ●, reference. ▼, SH-NAR. ♦, SH-220. ■, SH-80. ▽, SH spheres by Byon *et al.* (2010). ▷, reference sphere by Ahmmed *et al.* (2016). ◁, SH sphere by Ahmmed *et al.* (2016). The vertical error bars (95% confidence level) are of the same order of the size of the symbols. The horizontal error bars were estimated via the μ_l uncertainty discussion related to Fig. 6.4. (- - -), Stokes' law $C_{D\infty} = \frac{24}{Re_\infty}$.

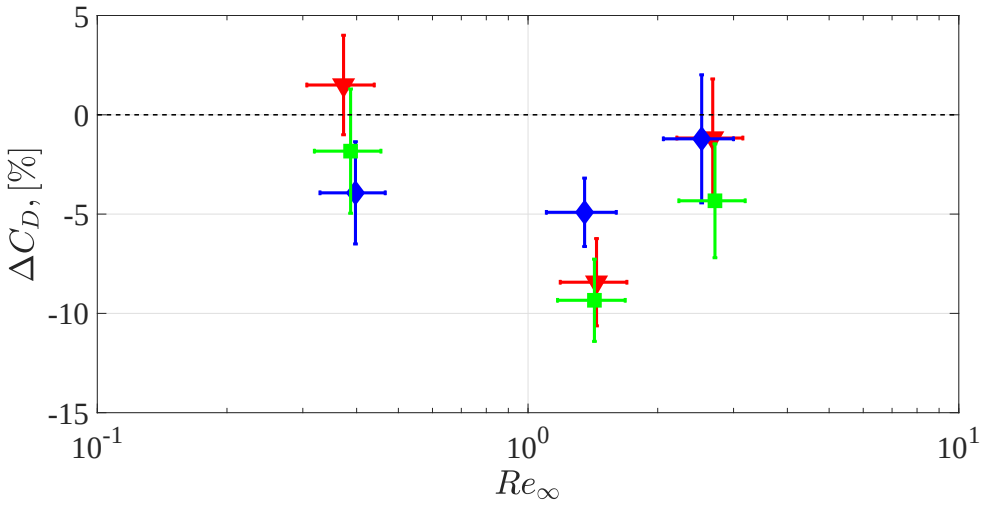

Figure 6.7 – Variation of the terminal drag coefficient as a function of the terminal Reynolds number Re_∞ for the glycerine tests. ▼, SH-NAR. ♦, SH-220. ■, SH-80. The error bars represent the 95% confidence level. (- - -), reference value $\Delta C_D = 0$ indicating the limit between drag increase ($\Delta C_D > 0$) and decrease ($\Delta C_D < 0$) (see the ΔC_D definition in Eq. 6.3).

the drag coefficient variation ΔC_D evaluated as:

$$\Delta C_D = \frac{C_{D\infty}^{SH}}{C_{D\infty}^{NC}} - 1, \tag{6.3}$$

is analysed as a function of Re_∞. The experimental data show that the possible drag reducing ability of the coatings SH-NAR, SH-220 and SH-80 is limited to $< 10\,\%$, in agreement with experimental works available in literature (Byon *et al.* 2010; Ahmmed *et al.* 2016) and in contrast with analytical and numerical predictions, where drag reductions as large as $30\,\%$ are estimated (McHale *et al.* 2011; Gruncell *et al.* 2013). It is also noted that no clear roughness size trend is retrieved. In fact, the vertical errorbars of the coatings differing in the λ magnitude tend to overlap one another.

Overall, the experimental data available in literature and estimated in this work clearly differ from the analytical and numerical predictions in the low Re_∞ regime. The main point that rises by looking at the works by McHale *et al.* (2011), Gruncell *et al.* (2013) is the difficulty in the achievement of an accurate modelling of the SH surface. For this reason, Appendix D is dedicated to an extensive discussion of the possible mechanisms involved in the evidenced drag behaviour. The performed scaling analysis shows that, among the identified physical mechanisms, the only one suitable to significantly affect drag is a laminar diffusion that erodes momentum inside the air layer via the interaction of the moving air with the roughness elements of the SH sphere surface. The interested reader is referred to Appendix D for a discussion on the subject. However, no loss of clarity derives by a direct transition to the next section.

6.1.2 Porous Medium Model

The identified mechanism connected to the motion of the air among the surface roughness elements allows for the adoption of the perspective of a flow across a porous medium to explain the absence of a significant SH drag reducing effect in the results shown in §6.1.1. A schematic of the considered model is depicted in Fig. 6.8, where an elementary volume V of characteristic macroscopic width L and height λ is considered inside the air layer over the surface of a SH sphere. An order-of-magnitude development is performed in the following to show that, if the beneficial lubricating effect due to presence of the air layer (δF_{sl}) can be partially or completely balanced by the resistance induced by the surface roughness (δF_{por}), this may lead to a limited or negligible drag reduction in the case of SH spheres. The total drag force acting on the SH sphere in the Stokes's flow is thus modelled as:

$$F_{SH} = F_{St} - \delta F_{sl} + \delta F_{por}, \tag{6.4}$$

where $F_{St} = 6\pi\mu_l r u_\infty$ ($r = \frac{d}{2}$ being the sphere radius) is the expression of the Stokes' drag force valid for a no-slip sphere under the hypotheses of steady-state, vanishing Reynolds number and infinite medium (see the discussion in §4.2.2). The goal of the following development is therefore the achievement of an estimation of the terms δF_{sl} and δF_{por} in Eq. 6.4.

Concerning the effect of the slip at the wall, Willmott (2009) performed analytical developments on *Janus* spheres in Stokes' flow. A *Janus* sphere can be briefly defined as a partially SH sphere, with a discontinuous transition between a no-slip and a partial slip boundary condition (ℓ_{sl} being the slip length) in a certain position on the sphere surface. By considering the limiting case of a fully SH sphere, a first order approximation of the beneficial lubricating force can be written as:

$$\delta F_{sl} = 6\pi\mu_l \ell_{sl} u_\infty. \tag{6.5}$$

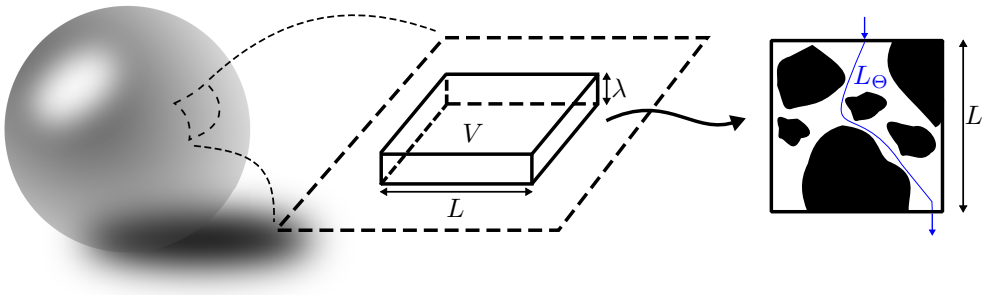

Figure 6.8 – Schematic of a porous medium model over an elementary volume V (width L and height λ) inside the air layer on the surface of a SH sphere. Black regions occupied by the solid are alternated to white regions occupied by the air. The porosity ϕ is defined as the ratio between the volume occupied by the air and the total control volume. The tortuosity Θ is defined as the ratio between the actual path followed by the air L_Θ and the control volume length L.

An expression for the δF_{por} term can then be achieved via the proposed porous medium approach. In fact, the elementary pressure loss across V can be expressed, following a Darcy (or Fanning) formalism, through the friction factor f as follows:

$$\Delta p = f \frac{L}{\lambda} \frac{1}{2} \rho_a u_{sl}^2, \tag{6.6}$$

where the term $f\frac{L}{\lambda}$ can be interpreted as a drag coefficient characterising the elementary volume V. In Eq. 6.6, ρ_a represents the air density and u_{sl} the slip velocity. The discussion in §D.2.1 in Appendix D led to the u_{sl} expression shown in Eq. D.7, which is here reported for completeness:

$$u_{sl} \approx \frac{3}{2} u_\infty \left(\frac{\ell_{sl}}{r} - \left(\frac{\ell_{sl}}{r} \right)^2 - \frac{2\lambda \ell_{sl}}{r^2} \right) \approx \frac{3}{2} \frac{\ell_{sl}}{r} u_\infty. \tag{6.7}$$

Moreover, the Darcy's law (see e.g. Bear 1988, Chapter 5) can be exploited to connect Δp with the volumetric flow rate Q across V:

$$Q = u_{sl} S = \frac{\kappa S}{\mu_a} \frac{\Delta p}{L}, \tag{6.8}$$

where κ is the permeability of the porous medium, μ_a the air dynamic viscosity and $S = L\lambda$ the cross-section of the elementary volume V. By comparing the Δp expression readily retrieved from Eq. 6.8 with Eq. 6.6, a relation between f and the Reynolds number $Re_P = \frac{\rho_a u_{sl} \lambda}{\mu_a}$ characterising the air layer is obtained:

$$f = \frac{2\lambda^2}{\kappa} \frac{1}{Re_P}. \tag{6.9}$$

Under the hypothesis of an isotropic porous medium, which seems reasonable by looking at the roughness elements distribution of the experimentally produced SH coatings (see Fig. 3.7), the permeability can be expressed as (see e.g. Bear 1988, Chapter 5):

$$\kappa = \frac{\phi \lambda^2}{96 \Theta^2}, \tag{6.10}$$

where ϕ and Θ are the porosity and the tortuosity of the porous medium, respectively. The porosity can be evaluated as the ratio between the void volume and the total volume of the medium, while the tortuosity can be defined as the ratio between the actual length covered by the air flow and the total porous medium length (see the schematic in Fig. 6.8). By multiplying the pressure loss in Eq. 6.6 by the elementary cross-section S, the drag over V can be estimated:

$$D = \Delta p L \lambda = f L^2 \frac{1}{2} \rho_a u_{sl}^2, \tag{6.11}$$

which can be further divided by the elementary surface L^2 to provide a measure of a drag per unit surface area. Finally, the latter can be scaled over the whole sphere surface providing, with the aid of Eqs. 6.9 and 6.10:

$$\delta F_{por} = f \frac{1}{2} \rho_a u_{sl}^2 4\pi r^2 = \frac{384\Theta^2}{\phi} \pi \mu_a u_{sl} \frac{r^2}{\lambda}. \tag{6.12}$$

In order to evaluate the relative order of magnitude between the detrimental roughness contribution and the beneficial slip effect, Eq. 6.12 can be compared to Eq. 6.5:

$$\frac{\delta F_{por}}{\delta F_{sl}} = \frac{384\Theta^2 \pi \mu_a u_{sl} r^2}{6\pi \mu_l \ell_{sl} V_\infty \phi \lambda} = \frac{64\Theta^2}{\phi} \left(\frac{\mu_a}{\mu_l} \right) \frac{r^2}{\ell_{sl} \lambda} \frac{u_{sl}}{u_\infty}, \tag{6.13}$$

which, exploiting the relation in Eq. 6.7, becomes:

$$\frac{\delta F_{por}}{\delta F_{sl}} \approx \frac{96\Theta^2}{\phi} \left(\frac{\mu_a}{\mu_l} \right) \left(\frac{r}{\lambda} \right). \tag{6.14}$$

The model in Eq. 6.14 thus predicts that the relative importance of the detrimental mechanism modelled via the porous medium approach with respect to the beneficial slip contribution increases with the tortuosity Θ. Moreover, the expression in Eq. 6.4 can be developed in order to reach an explicit relation between the drag variation ΔC_D and Θ. Normalising Eq. 6.4 by the reference drag force F_{St} and injecting the expression in Eq. 6.14, the following relation is obtained:

$$\Delta C_D = -\frac{\ell_{sl}}{\lambda} \frac{\lambda}{r} + \frac{96\Theta^2}{\phi} \left(\frac{\mu_a}{\mu_l} \right) \left(\frac{\ell_{sl}}{\lambda} \right), \tag{6.15}$$

where the two contributions due to the slip and the tortuosity are still discernible.

In the case of the randomly distributed SH coatings, the negligible drag modification shown in §6.1.1 implies that a balance between δF_{por} and δF_{sl} is achieved. This is retrieved via Eq. 6.14 by imposing $\delta F_{por} \approx \delta F_{sl}$, which gives:

$$\Theta \approx \sqrt{\frac{\phi}{96} \left(\frac{\mu_l}{\mu_a} \right) \left(\frac{\lambda}{r} \right)} \approx \mathcal{O}\left(10^0 - 10^1\right), \tag{6.16}$$

where the order of magnitude range was estimated via the properties of the tested spheres and liquid. In order for the model to be meaningful, the estimated Θ range must correspond to values experimentally achievable. First, a quick literature review (see e.g. Bear 1988, Chapter 5) shows that the range identified in Eq. 6.16 agrees fairly well with values usually reported. Second, a preliminary estimation of the actual Θ value of the produced coatings was performed exploiting the 3D microscopy images introduced in §3.3.1. The available images were binarised setting a threshold equal to the roughness size λ. Then, an A^* path detection algorithm from a starting node SN to a target node TN was implemented (see e.g. Ueland *et al.* 2017). The basic

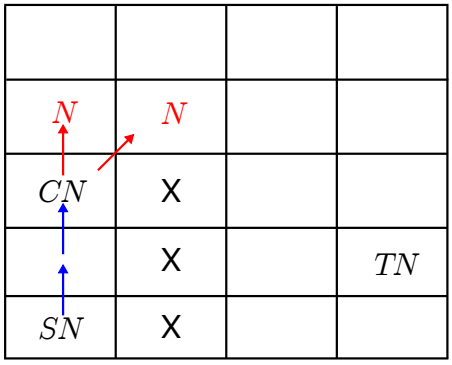

Figure 6.9 – Schematic of the A^* algorithm principles. The optimal path from the starting node SN to the target node TN is sought, taking into account the presence of the obstacles X. The next node N is selected from the current node CN by minimising a cost function that takes into account the distance $N - TN$ and the distance $CN - N$.

principles of the code are resumed by the schematic in Fig. 6.9. For each current node CN, the algorithm minimises the cost function $f(N)$ to select the following node N:

$$f(N) = g(N) + h(N), \tag{6.17}$$

where $g(N)$ is the cost based on the distance from N to TN and $h(N)$ is the cost based on the distance from CN to N. The optimal path is therefore progressively evaluated from SN to TN. The output of this algorithm applied to the actual SH coatings microscope images is reported in Fig. 6.10, where the case of the SH-220 coating is taken as an example. The value $\Theta = 1.6$ is estimated in the optimal path case in Fig. 6.10(a). However, by artificially forcing the code to follow non-optimal paths, the tortuosity value can quickly be increased. For example, the value $\Theta = 3.2$ is retrieved in Fig. 6.10(b). This shows that a precise and statistically relevant Θ estimation from the available information on the produced SH coatings is not straightforward. However, the order of magnitude of the evaluated Θ falls within the range estimated in Eq. 6.16 for the model to be meaningful. In fact, the A^* algorithm applied to the other SH coatings provided the same Θ order of magnitude.

One final assessment of the developed model can be made via another set of experimental results available in literature (Modak & Bhaumik 2017), which tested SH falling spheres in liquids with higher viscosities than glycerine, thus influencing the term $\frac{\mu_a}{\mu_l}$ in Eq. 6.14. Drag reduction of SH spheres characterised by micron-sized surface roughness elements was reported, when compared to reference smooth spheres. However, some assumptions are performed to make the comparison possible, since in the cited study several information about the SH coatings is missing. The kind of SH coatings tested in Modak & Bhaumik (2017) is qualitatively similar to the randomly distributed surface roughness coatings shown in Fig. 3.7. Since Ybert *et al.* (2007) showed that the apparent slip length scaled with the horizontal spacing of the roughness elements, λ is taken equal to 10 µm, which is the spacing measured by Modak & Bhaumik (2017). The ΔC_D derived from the terminal drag analysis of Modak & Bhaumik (2017) is reported in Fig. 6.11 as a function of $\frac{\lambda}{r}$, for the two investigated liquids, honey (superscript h, $\mu_l^h \approx 5.07\,\mathrm{Pa\,s}$) and golden-syrup (superscript gs, $\mu_l^{gs} \approx 25.50\,\mathrm{Pa\,s}$). It is evident from Fig. 6.11 that the reported experimental data are well approximated by the shown linear fit. In detail, the following linear

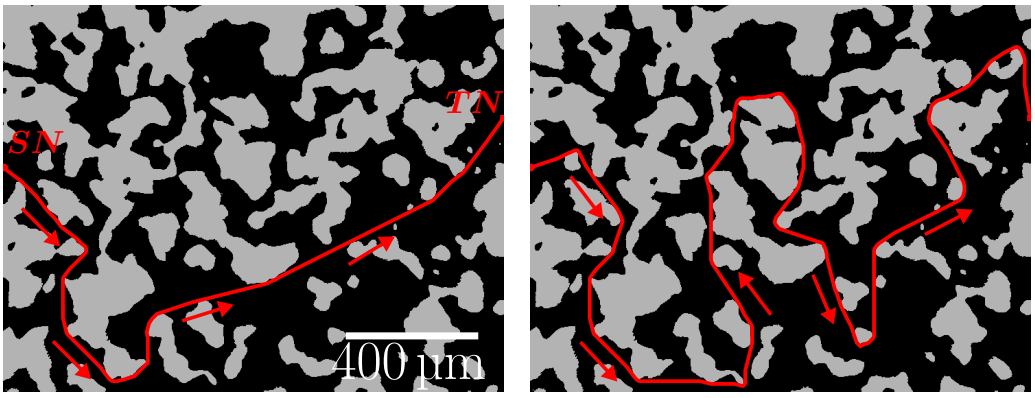

(a) (b)

Figure 6.10 – Result of the A^* algorithm for the path detection applied on a SH-220 3D digital microscope image. The grey and black regions indicate the area above and below the binarisation threshold, which was set equal to λ. (a), optimal path resulting in $\Theta = 1.6$. (b), non-optimal path resulting in $\Theta = 3.2$. The starting and target nodes are indicated by the symbols *SN* and *TN*, respectively. The path direction is indicated by the red arrows.

laws are inferred:

$$\Delta C_D^h = -c^h \frac{\lambda}{r} + q^h, \tag{6.18a}$$

$$\Delta C_D^{gs} = -c^{gs} \frac{\lambda}{r} - q^{gs}, \tag{6.18b}$$

where $c^h \approx 7.9$, $q^h \approx 8.8 \times 10^{-3}$, $c^{gs} \approx 13.3$ and $q^{gs} \approx 2.3 \times 10^{-3}$. The magnitude of the evaluated coefficients can then be compared to the model prediction in Eq. 6.15. In fact, by focusing attention on the slip contribution (the first term on the right hand side in Eq. 6.15), the following relations are retrieved:

$$\frac{\ell_{sl}^h}{\lambda} = c^h \approx 7.9, \tag{6.19a}$$

$$\frac{\ell_{sl}^{gs}}{\lambda} = c^{gs} \approx 13.3, \tag{6.19b}$$

where the order of magnitude of the slip length ℓ_{sl} with respect to the roughness elements size λ agrees with the predictions available in literature (Vinogradova 1999). The same approach can be followed for the tortuosity contribution (the second term on the right hand side in Eq. 6.15), providing:

$$\left(\frac{\Theta^2}{\phi}\right)^h = \frac{q^h}{96\left(\frac{\mu_a}{\mu_l}\right)c^h}, \tag{6.20a}$$

$$\left(\frac{\Theta^2}{\phi}\right)^{gs} = \frac{q^{gs}}{96\left(\frac{\mu_a}{\mu_l}\right)c^{gs}}. \tag{6.20b}$$

No information is available on the porosity ϕ of the SH coatings produced by Modak & Bhaumik (2017). However, in the honey case in Eq. 6.20(a), the highest possible value $\phi = 1$ results into

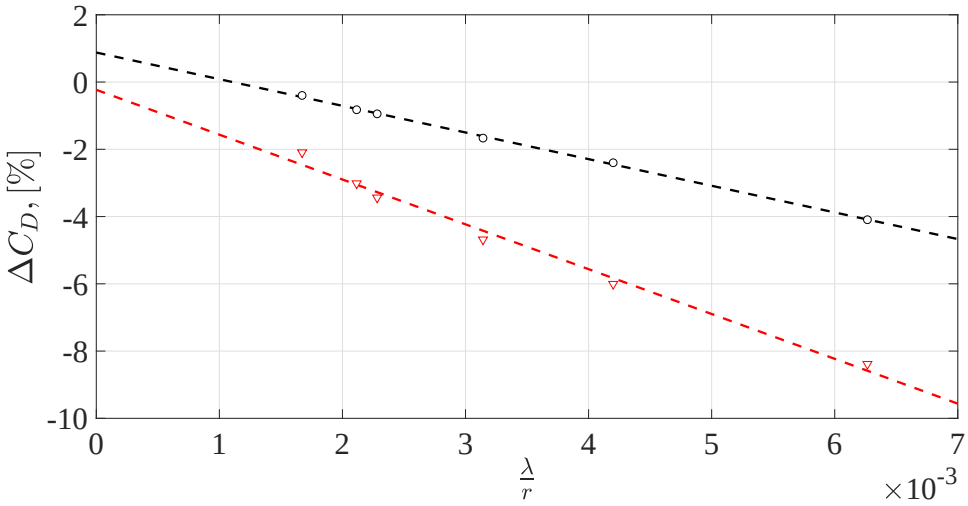

Figure 6.11 – Variation of the terminal drag coefficient as a function of the non-dimensional surface roughness derived from the results by Modak & Bhaumik (2017). ∘, experimental data in honey. ▽, experimental data in golden-syrup. (- - -), linear fit of the data in honey. (- - -), linear fit of the data in golden-syrup.

$\Theta = 1.8$, while the lower limiting case $\Theta = 1$ is reached for $\phi = 0.3$. Similarly, in the golden-syrup case in Eq. 6.20(b), the highest possible value $\phi = 1$ results into $\Theta = 1.6$, while the lower limiting case $\Theta = 1$ is reached for $\phi = 0.4$. Reasonable ranges of the SH coatings properties are therefore inferred by analysing the reported experimental results in the perspective of the model proposed in this section.

All together, these estimations show that the model proposed in Eqs. 6.14 and 6.15 is a plausible explication of the experimental results evaluated with the performed experimental campaign and available in literature. The negligible drag variation evidenced in Byon *et al.* (2010), Ahmmed *et al.* (2016) could also be viewed in the framework of the proposed model, since the investigated nano-sized surface roughness could result into a decrease of the magnitude of the beneficial slip contribution in Eq. 6.15. A further assessment of the proposed mechanism in the low Reynolds number regime should be performed by manufacturing SH coatings where the parameters λ, Θ and ϕ could be prescribed to the desired values. A first attempt in this direction was performed by manufacturing via a 3D printing technique SH spheres with aligned cylindrical pillars, which likely resulted into $\Theta \approx 1$. The first results show a promising slight drag reduction improvement with respect to randomly distributed SH coatings. Due to the preliminary nature of the described technique, the manufacturing procedure and the terminal drag results are presented in Appendix E.

6.2 Intermediate Reynolds Number

This section discusses the results of the falling sphere tests in water-glycerine mixtures, which were executed to analyse the intermediate terminal Reynolds number regime, $2.5 \times 10^1 < Re_\infty < 1.1 \times 10^3$. For the sake of clarity, the tests overview presented in Fig. 6.1 at the beginning of this chapter is here reported in Fig. 6.12 highlighting the investigated region. The low Re_∞ tests

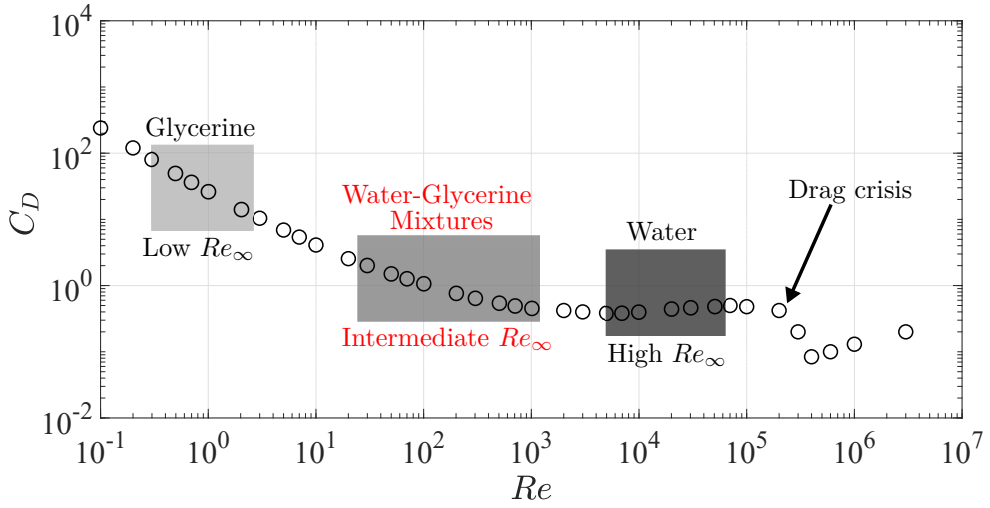

Figure 6.12 – Drag coefficient C_D as a function of the Reynolds number Re for reference spheres. ○, experimental data from Lapple & Sheperd (1940). The grey-shaded rectangles indicate the whole Re_∞ ranges analysed with the falling sphere experimental campaigns. The red color highlights the region investigated in this section.

in glycerine analysed the SH coatings behaviour in a regime where no wake symmetry breaking could occur, identifying a negligible effect on terminal drag. The intermediate Re_∞ regime was therefore chosen to analyse the region where transitions of the wake of a fixed sphere occur, which were shown in Chapter 2 to be connected to the onset of path instabilities of a moving body and to the hydrodynamic loads acting on it. The objective of these tests was thus to evidence a possible interconnectivity between the air layer behaviour and the wake-path instability development. In the next paragraph, the hydrodynamic performance of falling spheres is thus discussed, with a special focus on the onset of transversal motion.

These results were presented in a preliminary form at the 11^{th} *International Symposium on Turbulence and Shear Flow Phenomena* (Castagna *et al.* 2019*b*).

6.2.1 Hydrodynamic Performance

The intermediate Re_∞ region analysed in this section shows, in the case of reference spheres reported in Fig. 6.12, a significant drag coefficient reduction for increasing Re_∞. Based on the experimental data by Lapple & Sheperd (1940), the drag coefficient varies of $\approx 80\,\%$ between the two extreme Re_∞ characterising the analysed region. The evaluated results were thus expected to vary depending on the actual Re_∞ value attained by the falling sphere. An approximate value of the Re_∞ reached at terminal conditions by the spheres is therefore reported in Tab. 6.1 for all the three tested water-glycerine mixtures (see nomenclature in §4.3). One remark concerning the investigated d range should be provided: by following the indications in §B.2 concerning the blockage effects, which were shown to become progressively more important for decreasing Re_∞, a maximum $d = 10\,\text{mm}$ resulting into a blockage factor $\delta = 0.09$ was chosen, as in the case of the glycerine tests in §6.1. It is evident from data in Tab. 6.1 that the Re_∞ ranges covered by the mixtures tend to overlap. These ranges were *a priori* estimated via Eq. 4.3 describing the vertical free motion of a sphere in order to assure the tests to cover the whole

d, [mm]	$W020\_G080$	$W030\_G070$	$W040\_G060$
5	25	100	290
8	65	250	680
10	110	390	1030

Table 6.1 – Terminal Reynolds number Re_∞ achieved by the falling spheres in the water-glycerine mixtures (see nomenclature in §4.3, based on the volumetric fractions of the two components). An average value among all the investigated coatings is reported per each diameter and mixture. The colors discriminate between the Re_∞ values below (blue) and above (red) the first transition region of the fixed sphere case ($Re_{cr,1} \approx 212$, see §2.1).

fixed sphere wake transitions region (see §2.1). In fact, the mixture $W020\_G080$ characterised by the highest volumetric fraction of glycerine resulted into spheres falling at Re_∞ below the loss of wake axisymmetry of a fixed sphere ($Re_{cr,1} \approx 212$). The intermediate mixture $W030\_G070$ then covered a region across all the transition processes. Finally, the mixture $W040\_G060$ with the lowest glycerine fraction raised up to $Re_\infty \sim 10^3$, which by inspecting Fig. 6.12 is approximately five times smaller than the lowest Re_∞ studied in the pure water tests. For these reasons, special attention is given in the following to the results of spheres in the different mixtures that reached approximately the same Re_∞. In fact, since from a pure hydrodynamic point of view the nature of their wake should be similar, eventual significant differences could be connected to some other driving parameters than the simple Re_∞. Due to the high amount of available data, in the following only the results for the spheres that allow the development of the discussion are reported. All the other velocity profiles are shown in Appendix F. Similarly to the low Re_∞ scenario, no significant effects on terminal drag due to SH coatings are evaluated. The variations of the estimated $C_{D\infty}$ of SH spheres with respect to the corresponding reference are limited to a largest value of $\approx 6\,\%$, for all the analysed mixtures. For this reasons, the drag data are also reported in Appendix F, since the conclusions on terminal drag straightforwardly derive from the vertical velocity profiles shown in the following of this section.

Region Below The Transitions

The blue color introduced in Tab. 6.1 underlines that all the spheres in the $W020\_G080$ mixture and the $d = 5\,\text{mm}$ spheres in the $W030\_G070$ mixture lie in the Re_∞ region where a steady-state axisymmetric wake develops behind a fixed sphere. As discussed in §2.1, $Re_\infty \approx 20$ can be taken as the best estimate of the appearance of the recirculation region behind the body. Then, by progressively increasing Re_∞, a steady axisymmetric vortex ring appears and grows in intensity. However, even at the highest $Re_\infty \approx 110$ here taken into consideration, no wake symmetry breaking should occur, at least in the case of an ideal perfect smooth sphere.

The results of $d = 5\,\text{mm}$ spheres in the $W020\_G080$ mixture in Fig. 6.13 therefore show that the expected $u_z^\star$ behaviour is retrieved. After the initial transient accelerating phase, all the spheres reach the terminal velocity. Interestingly, no evident effect of the surface coating is noticed. Both in the transient phase and at terminal conditions the $u_z^\star$ of all the spheres result superposed, in a scenario qualitatively similar to the glycerine tests in §6.1. In fact, a negligible $u_{tr}^\star$ profile along the whole drop was evaluated, with values within the experimental noise, and is therefore not reported. These findings support the discussion in §6.1 on the absence of noteworthy effects on terminal drag at low Re_∞ and, even if no proof can be given, the question of a possible validity of the tortuosity influence at Re_∞ beyond the Stokes' regime arises.

Attention is then turned to the two cases that allow a cross-comparison between mixtures,

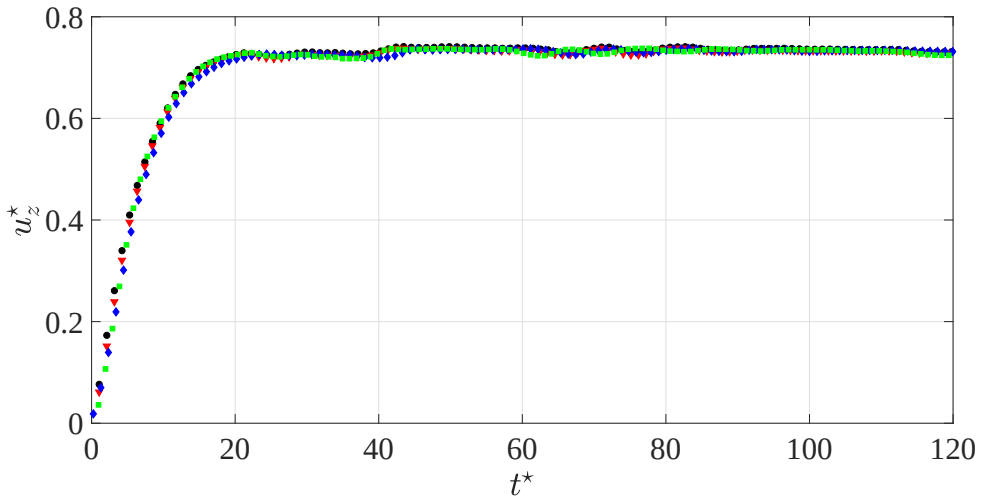

Figure 6.13 – Instantaneous vertical velocity $u_z^\star$ for all the analysed coatings in the mixture $W020\_G080$ for the $d = 5\,\text{mm}$ spheres. ●, reference. ▼, SH-NAR. ♦, SH-220. ■, SH-80. The visible oscillations are due to small residual air bubbles attached to the tank lateral walls, which did not interact with the sphere falling at the centre of the tank cross-section but negatively affected the images post-processing.

i.e. $d = 10\,\text{mm}$ spheres in the $W020\_G080$ mixture and $d = 5\,\text{mm}$ spheres in the $W030\_G070$ mixture (see Tab. 6.1, where they are shown to attain $Re_\infty \approx 100$). The $u_z^\star$ profiles reported in Fig. 6.14 show a similar behaviour in the two cases, with an attained $u_\infty^\star \approx 1.1$. A slight $u_\infty^\star$ decrease is noted in Fig. 6.14(a) for the SH-80 sphere, thus involving a resulting drag augmentation (see Eq. 6.2). However, a more marked difference among the coatings can be detected only during the transient phase ($t^\star < 20$), where spheres with larger $\frac{\lambda}{d}$ lie above the reference curve, especially in Fig. 6.14(b). This mild influence of SH coatings can be further clarified via the analysis of the corresponding $u_{tr}^\star$ profiles reported in Fig. 6.15. For the sake of clarity, each image compares the reference spheres results with a single SH coating. Therefore, the left side of Fig. 6.15 analyses the $d = 10\,\text{mm}$ spheres in the $W020\_G080$ mixture for increasing $\frac{\lambda}{d}$ from Fig. 6.15(a) to Fig. 6.15(e). Analogously, the right side of Fig. 6.15 analyses the $d = 5\,\text{mm}$ spheres in the $W030\_G070$ mixture for increasing $\frac{\lambda}{d}$ from Fig. 6.15(b) to Fig. 6.15(f). No effect on $u_{tr}^\star$ of the SH-NAR coating is detected in both mixtures (see Figs. 6.15(a) and 6.15(b)). Interestingly, a $\frac{\lambda}{d}$ increase results into a progressively strengthening of a $u_{tr}^\star$ peak, which is particularly evident in the SH-80 case in Figs. 6.15(e) and 6.15(f). This $\frac{\lambda}{d}$ influence on $u_{tr}^\star$ agrees with the trend identified in Fig. 6.14 on the $u_z^\star$ magnitude in the transient phase. Moreover, the relative $u_{tr}^\star$ behaviour of the spheres in the two mixtures is similar. By comparing the ascending portion of the $u_{tr}^\star$ peak in Fig. 6.15, a $\frac{\lambda}{d}$ increase progressively determines an earlier onset of transversal motion, which will be further discussed in the following. However, it is important to note that the magnitude of the evidenced peak reaches only approximately four times the baseline values, which represents a limited transversal motion, as will be further discussed. In fact, in the terminal part of the drop in Fig. 6.15 the $u_{tr}^\star$ of all the SH coatings goes back to the reference profile, further confirming the limited relevance of transversal motion on such low Re_∞ values. This testifies that in the analysed regime where ideally both the body geometry and wake are axisymmetric the influence of the SH coatings on the onset of transversal motion

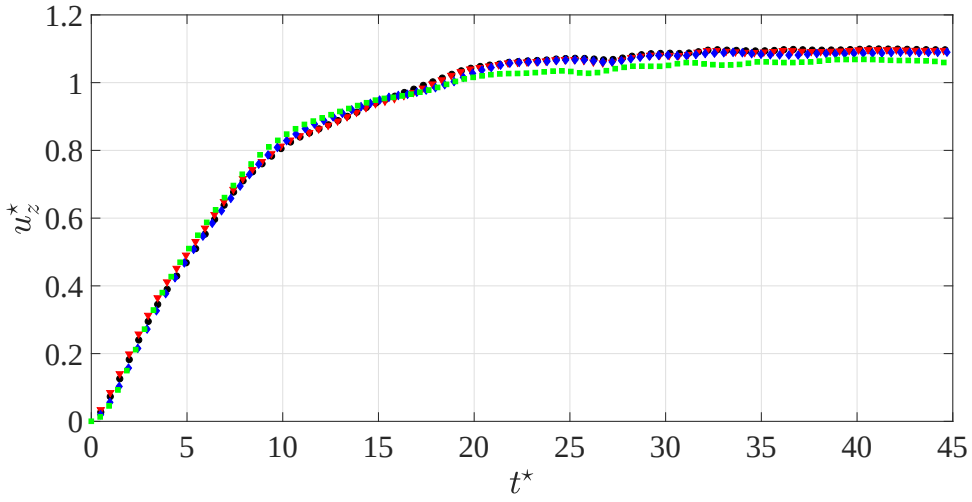

(a)

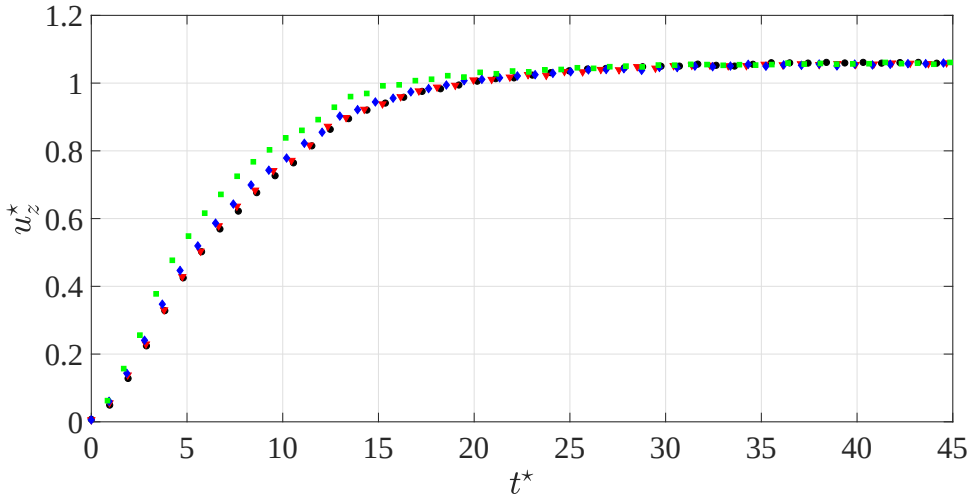

(b)

Figure 6.14 – Instantaneous vertical velocity $u_z^\star$ for all the analysed coatings, for the tests with Re_∞ in the range $100-110$. (a), $d = 10\,\text{mm}$ spheres in the $W020\_G080$ mixture. (b), $d = 5\,\text{mm}$ spheres in the $W030\_G070$ mixture. ●, reference. ▼, SH-NAR. ♦, SH-220. ■, SH-80.

and its magnitude in the subsequent stages of the drop is limited. One possible reason for the establishment of the limited transversal motion could be identified in the non perfect sphericity of the manufactured SH spheres (see Tabs. C.5 and C.6), since the process of onset of wake and path instability is sensible to geometric imperfections (Jenny *et al.* 2004).

In the following paragraph, this concept is further developed by showing how a non-perfect sphericity can derive from the interaction of the air layer initially trapped among the surface roughness elements of SH coatings with the flow. To clarify this issue, a regime where wake transitions and path oscillations occur has to be analysed.

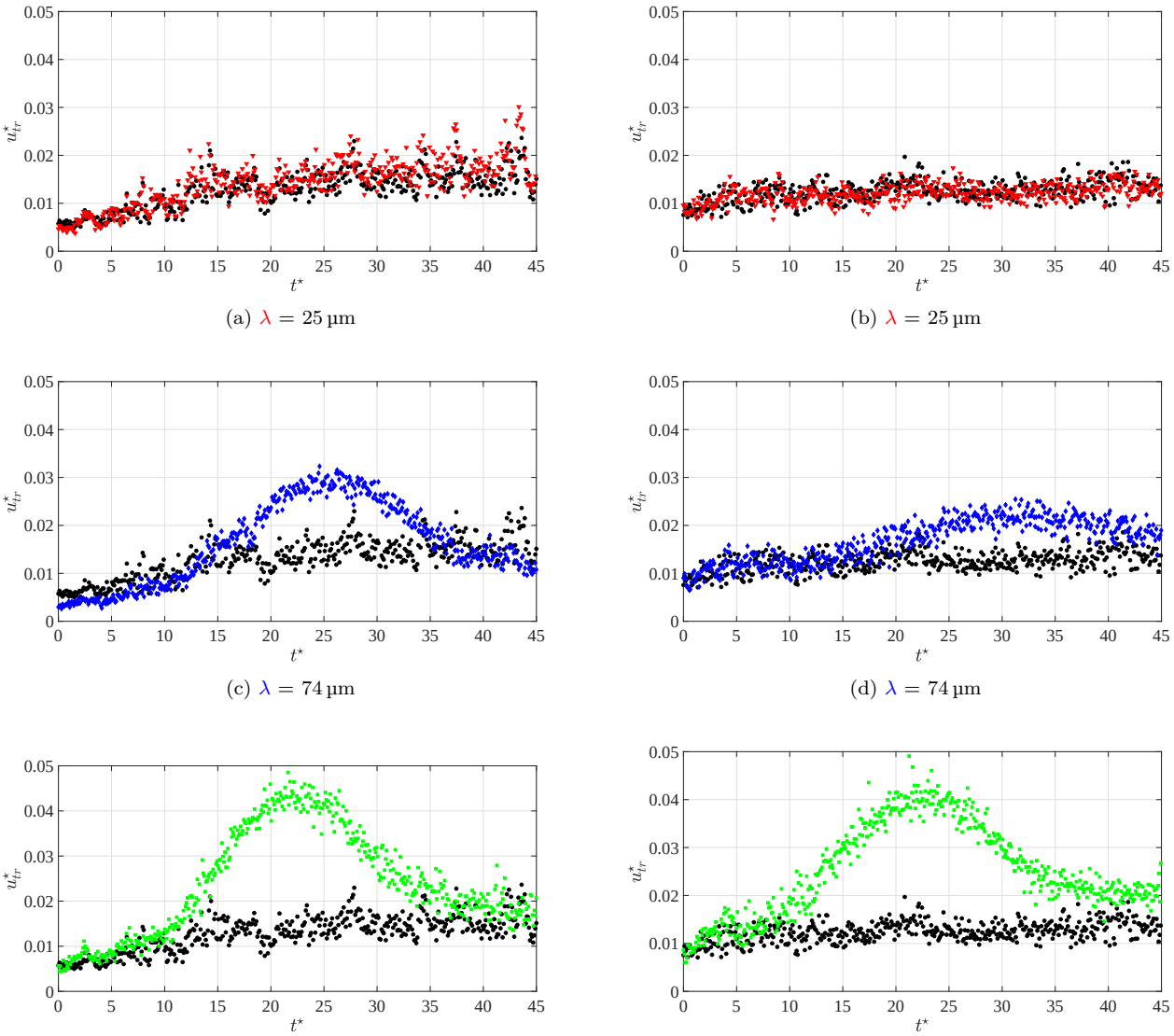

(a) $\lambda = 25\,\mu m$ (b) $\lambda = 25\,\mu m$

(c) $\lambda = 74\,\mu m$ (d) $\lambda = 74\,\mu m$

(e) $\lambda = 142\,\mu m$ (f) $\lambda = 142\,\mu m$

Figure 6.15 – Instantaneous transversal velocity $u^\star_{tr}$ for all the analysed coatings, for the tests with Re_∞ in the range $100 - 110$. (left), $d = 10\,mm$ spheres in the $W020\_G080$ mixture. (right), $d = 5\,mm$ spheres in the $W030\_G070$ mixture. •, reference. ▼, SH-NAR. ♦, SH-220. ■, SH-80. The non-dimensional surface roughness $\frac{\lambda}{d}$ increases from top to bottom.

Transitions Region

The red color in Tab. 6.1 indicates the spheres in the $W030\_G070$ and $W040\_G060$ mixtures that attained a Re_∞ equal or larger to the values where transitions in the wake of a fixed sphere occur. Since in the performed falling sphere tests a refined control of Re_∞ was not straightforward, no distinction between first and second wake transitions is performed in the following. This is also due to the fact that no information on the effect of SH coatings on the corresponding critical Reynolds numbers was *a priori* available. It is evident from Tab. 6.1 that the $d = 8\,\text{mm}$ spheres in the $W030\_G070$ mixture and the $d = 5\,\text{mm}$ spheres in the $W040\_G060$ mixture are the two cases that reached the most comparable Re_∞ values (the two differ of $\approx 15\,\%$, being in the range $250 - 290$. For this reason, a similar analysis to the previous paragraph is conducted. The $u_z^\star$ profiles of the two considered cases are reported in Fig. 6.16. As in the previous paragraph, the behaviour of sphere reaching approximately the same Re_∞ is comparable, with $u_\infty^\star \approx 1.3$ in both cases. No significant differences are detected at terminal conditions, thus still implying a negligible effect of SH coatings on terminal drag, at least under the investigated conditions. However, the $\frac{\lambda}{d}$ trend in the transient phase evidenced at lower Reynolds number is here more marked. The $u_z^\star$ profiles of the SH coatings with larger $\frac{\lambda}{d}$ lie above the corresponding reference curve during the accelerating phase. This may be related to the strong differences appearing in the $u_{tr}^\star$ profiles, which are reported in Fig. 6.17. Coherently to the previous discussion, each image compares the reference spheres results with a single SH coating. Therefore, the left side of Fig. 6.17 analyses the $d = 8\,\text{mm}$ spheres in the $W030\_G070$ mixture for increasing $\frac{\lambda}{d}$ from Fig. 6.17(a) to Fig. 6.17(e). Analogously, the right side of Fig. 6.17 analyses the $d = 5\,\text{mm}$ spheres in the $W040\_G060$ mixture for increasing $\frac{\lambda}{d}$ from Fig. 6.17(b) to Fig. 6.17(f). Conversely to the previous case at lower Reynolds number, a significant transversal motion occurs for reference spheres. The $u_{tr}^\star$ in the $W030\_G070$ mixture progressively increases along the drop reaching magnitudes approximately ten times larger than the beginning of the drop. The trend is enhanced in the $W040\_G060$ case, where $u_{tr}^\star$ reaches approximately fifteen times the initial value, while reducing at $t^\star \approx 30$ its rate of augmentation. In both cases, no significant effects of the SH-NAR coating are evaluated in Figs. 6.17(a) and 6.17(b), except for a slight early onset of the transversal motion. The latter is made more evident by progressively increasing $\frac{\lambda}{d}$ in both mixtures. However, while the SH-220 and SH-80 coatings in Figs. 6.17(c) and 6.17(e) in the mixture $W030\_G070$ show larger values than the reference once terminated the ascending part of the $u_{tr}^\star$ peak, in Figs. 6.17(d) and 6.17(f) in the mixture $W040\_G060$ the same values of the reference are retrieved. Interestingly, the SH-80 coating in Fig. 6.17(f) shows a $u_{tr}^\star$ oscillating behaviour after the peak achievement at $t^\star \approx 27$. This will be shown in §6.3 to occur also at higher Reynolds number in the pure water tests, thus probably being connected to the stronger shed of vortices in the wake.

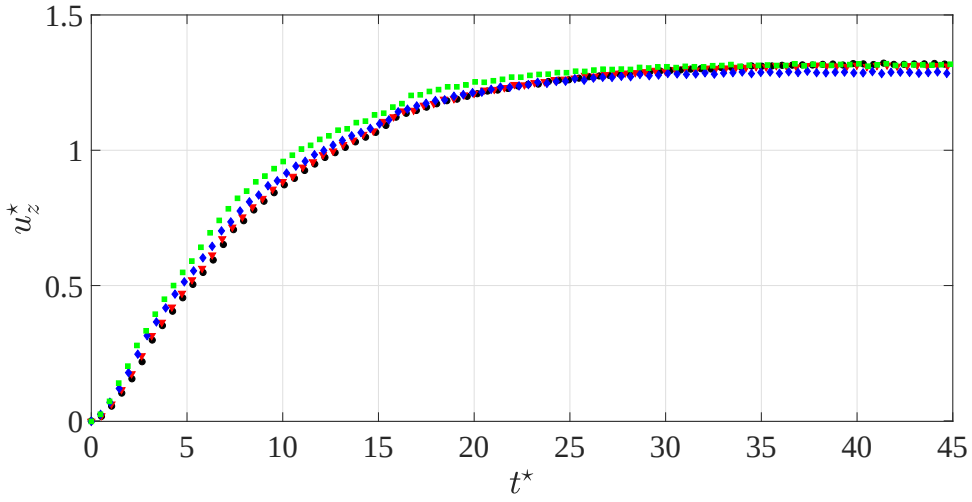

(a)

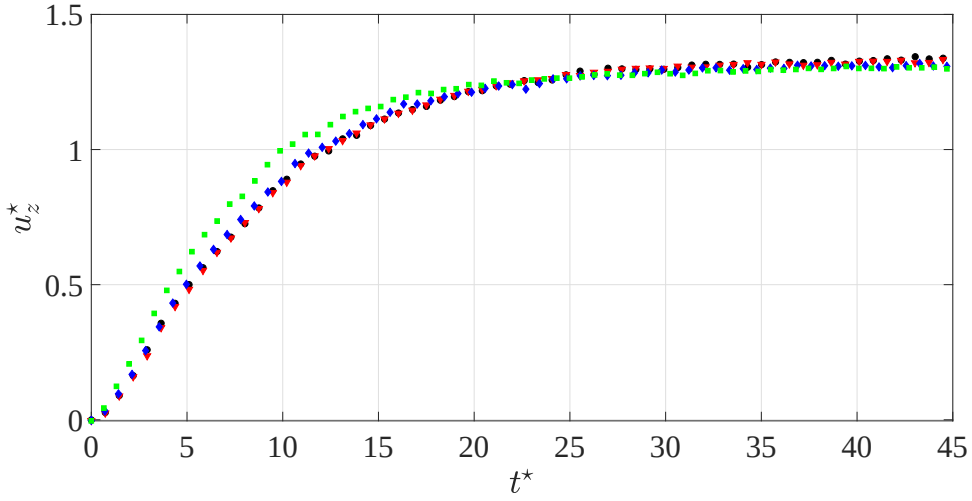

(b)

Figure 6.16 – Instantaneous vertical velocity $u_z^\star$ for all the analysed coatings, for the tests with Re_∞ where wake transitions of a fixed sphere occur. (a), $d = 8\,\text{mm}$ spheres in the $W030\_G070$ mixture. (b), $d = 5\,\text{mm}$ spheres in the $W040\_G060$ mixture. ●, reference. ▼, SH-NAR. ♦, SH-220. ■, SH-80.

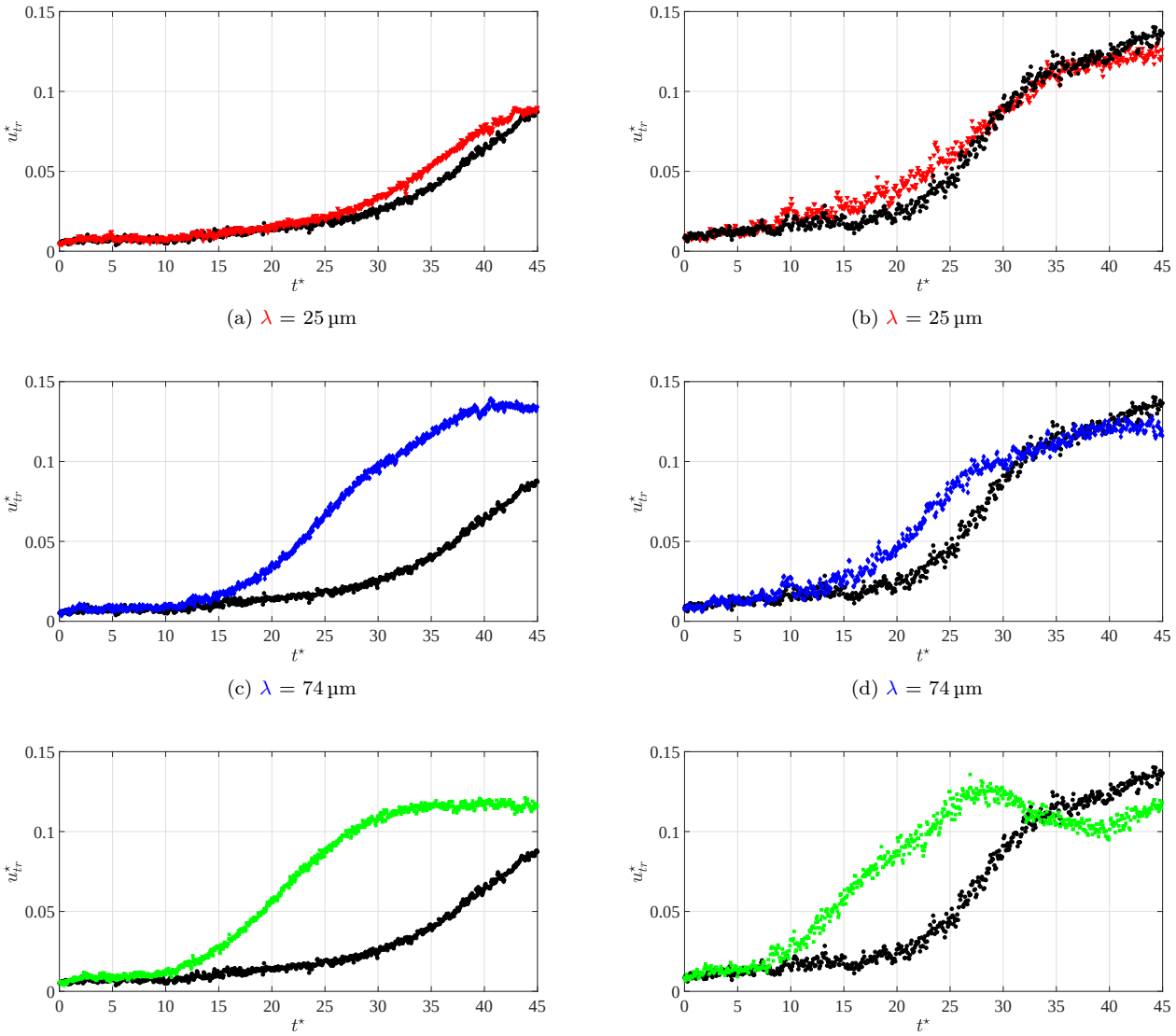

(a) $\lambda = 25\,\mu m$ (b) $\lambda = 25\,\mu m$

(c) $\lambda = 74\,\mu m$ (d) $\lambda = 74\,\mu m$

(e) $\lambda = 142\,\mu m$ (f) $\lambda = 142\,\mu m$

Figure 6.17 – Instantaneous transversal velocity $u^\star_{tr}$ for all the analysed coatings, for the tests with Re_∞ where wake transitions of a fixed sphere occur. (left), $d = 8\,mm$ spheres in the $W030\_G070$ mixture. (right), $d = 5\,mm$ spheres in the $W040\_G060$ mixture. •, reference. ▼, SH-NAR. ♦, SH-220. ■, SH-80. The non-dimensional surface roughness $\frac{\lambda}{d}$ increases from top to bottom.

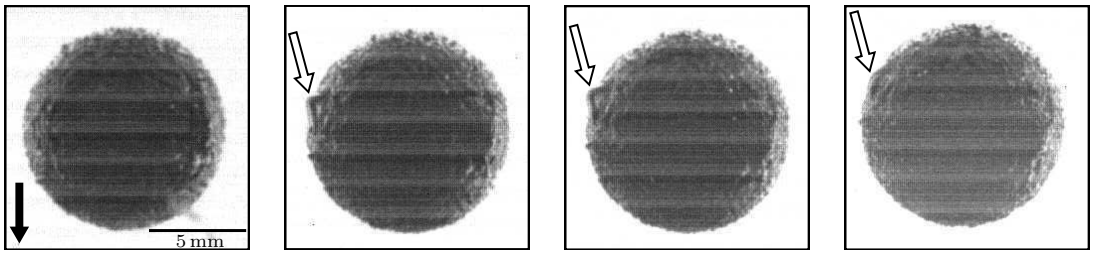

(a) $t^\star = \tilde{t}^\star$ (b) $t^\star = \tilde{t}^\star + 3$ (c) $t^\star = \tilde{t}^\star + 4$ (d) $t^\star = \tilde{t}^\star + 6$

Figure 6.18 – Typical snapshots recorded in high magnification configuration illustrating the slight movement and deformation of the air plastron (indicated by white arrows) around a $d = 10\,\text{mm}$, SH-80 coated sphere in the mixture $W030\_G070$. The black arrow represents the direction of gravity. The variable $\tilde{t}^\star$ designates a randomly chosen time origin.

The identified influence of SH coatings on the onset of transversal motion opens an interesting perspective towards the comprehension of the parameters controlling the phenomenon. First, a qualitative evidence of the influence of other parameters than the simple Re_∞ range is provided. In fact, an investigation of the near-wall phenomena via the high-magnification configuration (see §4.1.1) seems to preliminarily indicate an interaction between the air layer and the flow. The sequence in Fig. 6.18 shows a slight air layer deformation and motion for a $d = 10\,\text{mm}$, SH-80 sphere in the $W030\_G070$ mixture. The sequence was chosen being made of the highest quality available images in a Re_∞ range where wake transition surely occurred (see Tab. 6.1). The deformed air pocket identified in Fig. 6.18 lies in the rear-side of the falling sphere and close to the equator. A possible connection with the angle of the laminar boundary layer separation and subsequent transition to turbulence might exist. Moreover, the deformed pocket moves along the solid wall and continuously modifies its shape, which might be due to an instantaneous compliance to the surrounding flow. This first clue of the plastron compliance to the flow will be shown in §6.3 to be strongly promoted in the pure water tests, were the typical relative velocities between body and surrounding liquid are higher. In detail, the compliance phenomenon could be driven by the local competition between the separation-induced suction ($\sim \rho_l u_D^2$, u_D being the gravity/buoyancy scaling velocity introduced in §4.2.3) and the capillary pressure ($\sim \frac{\gamma}{d}$, with γ the air-liquid surface tension), which can be qualitatively represented by introducing the Weber number such as:

$$\mathcal{W}e_D = \frac{\rho_l u_D^2 d}{\gamma}. \tag{6.21}$$

The advantage of this non-dimensional number lies in the fact that can be *a priori* estimated once the properties of the working fluid and of the sphere are known. Moreover, the $\mathcal{W}e_D$ definition in Eq. 6.21 can be developed by injecting the u_D definition provided in Eq. 4.7(b), which gives:

$$\mathcal{W}e_D = \frac{\rho_l g}{\gamma}\left(\zeta - 1\right) d^2. \tag{6.22}$$

This expression shows that for a chosen mixture the sphere diameter may be the main control parameter of the flow-interface interaction, since ζ slightly varies among the different coatings. Similarly, the expression in Eq. 6.22 highlights that two spheres with the same properties falling into two different liquids will show a different relative behaviour between the destabilising inertial term ($\sim \rho_l u_D^2$) and the stabilising capillary contribution ($\sim \frac{\gamma}{d}$), with a possible influence on the

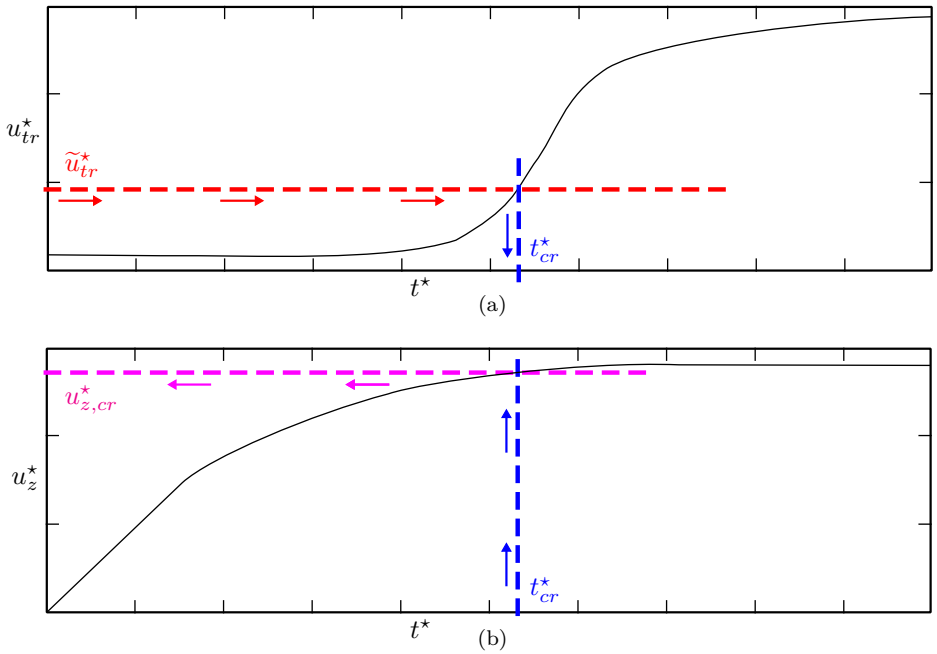

Figure 6.19 – Schematic of the approach implemented to identify the vertical velocity value at critical conditions $u^\star_{z,cr}$. A threshold $\widetilde{u}^\star_{tr}$ is imposed on the transversal velocity profile $u^\star_{tr}$ in (a), thus identifying the corresponding critical time $t^\star_{cr}$. The latter is then used to enter the $u^\star_z$ chart in (b). The coloured arrows indicate the path direction.

instantaneous air layer behaviour with respect to the flow. This perspective is thus adopted to further compare the spheres analysed above in terms of onset of transversal motion.

The approach is resumed by the schematic in Fig. 6.19. Starting from the $u^\star_{tr}$ profiles shown in Figs. 6.15 and 6.17, a threshold transversal velocity value $\widetilde{u}^\star_{tr}$ is imposed, which allows to identify a critical time $t^\star_{cr}$ of the onset of transversal motion. The choice of the threshold transversal velocity value $\widetilde{u}^\star_{tr} = 0.05$ was based on the maximum value of the $u^\star_{tr}$ peak identified in Fig. 6.15, which corresponds to the case where negligible transversal motion was detected. Moreover, by looking at the $u^\star_{tr}$ profiles in Fig. 6.17 where transversal motion is significant, the chosen threshold results sufficiently high to be above the $u^\star_{tr}$ values at the beginning of the drop ($t^\star < 10$). This assures a meaningful detection of the critical time values, which otherwise could be excessively biased by too large uncertainties in the point detection. The $t^\star_{cr}$ value can then be injected into the corresponding $u^\star_z$ profiles shown in Figs. 6.14 and 6.16, thus allowing the identification of the vertical velocity value at critical conditions $u^\star_{z,cr}$. Accordingly, the corresponding critical Reynolds number based on the dimensional critical vertical velocity $u_{z,cr}$ can be defined as:

$$Re_{cr} = \frac{u_{z,cr} d}{\nu_l}. \tag{6.23}$$

By introducing the Reynolds number $Re_D = \frac{u_D d}{\nu_l}$, and since by definition $u^\star_{z,cr} = \frac{u_{z,cr}}{u_D}$, it can be shown that:

$$Re_{cr} = u^\star_{z,cr} Re_D, \tag{6.24}$$

with the advantage that Re_D can be estimated before the tests execution and $u^\star_{z,cr}$ is readily retrieved from the evaluated velocity profiles. Analogously, a Weber number can be estimated

at critical conditions as:

$$\mathcal{W}e_{u_{z,cr}} = \frac{\rho_l u_{z,cr}^2 d}{\gamma}, \tag{6.25}$$

which can be connected to the Weber number defined in Eq. 6.21 as:

$$\mathcal{W}e_{u_{z,cr}} = \left(u^\star_{z,cr}\right)^2 \mathcal{W}e_D. \tag{6.26}$$

The results of the proposed approach applied to the two extreme coatings, i.e. reference NC and SH-80, are resumed in Tab. 6.2. For the sake of clarity, the results for the SH-NAR and SH-220 coatings are not reported in Tab. 6.2, lying in between the shown data. Following the discussion in §D.1, the Capillary number $Ca_D = \frac{\mu_l u_D}{\gamma}$ is shown. However, values at least one order of magnitude lower than the glycerine tests are evaluated ($Ca_D \sim 10^1$ in glycerine tests), due to the lower μ_l of the mixtures. This implies an increased influence of surface tension on the air-liquid interface at the expense of viscous effects, thus reinforcing the role of the considered Weber number. The latter could be evaluated at critical conditions via the detected critical vertical velocity. In fact, the transversal motion resulted too weak in the reference spheres case for the mixture $W20\_G80$ and for the $d = 5\,\text{mm}$ spheres in $W30\_G70$ to detect the corresponding $u^\star_{z,cr}$. The latter assumes the same value for the $d = 10\,\text{mm}$ spheres in $W20\_G80$ and the $d = 5\,\text{mm}$ spheres in $W30\_G70$, at comparable $Re_\infty \approx 100$. Comparing the $d = 8\,\text{mm}$ NC spheres in $W30\_G70$ with the $d = 5\,\text{mm}$ NC spheres in $W40\_G60$, an $\approx 3\,\%$ difference on $u^\star_{z,cr}$ is noticed, which again confirms the meaningfulness of comparing spheres in the same Re_∞ region. Interestingly, in both cases the SH-80 coating results into an $\approx 10\,\%$ $u^\star_{z,cr}$ decrease, thus implying an onset of transversal motion at lower vertical velocity. These considerations are also retrieved in the corresponding Re_{cr} values. The SH-80 coating therefore determines an onset of transversal motion al lower critical Reynolds number with respect to the corresponding reference sphere.

To summarise, spheres falling in the same Re_∞ range show similar behaviour in terms of Re_{cr}, with differences being highlighted by varying the surface coating, from reference to SH-80 case. However, in Fig. 6.17 differences in the $u^\star_{tr}$ behaviour where highlighted, which cannot therefore be explained by simply considering the Reynolds number alone. The origin of the identified differences may be clarified by looking in Tab. 6.2 at the $\mathcal{W}e_{u_{z,cr}}$ values. As discussed above, the Weber number describes the relative effect on the air-liquid interface of the destabilising inertial effects with respect to the stabilising surface tension. Simultaneously, the Reynolds number in the wake transitions region can be interpreted as an hydrodynamic perturbation to the state of the air-liquid interface: the progressively strengthening of the vortex shedding in the wake might influence the behaviour of the air layer initially trapped among the surface roughness elements. Starting from the values in Tab. 6.2 a scenario can be proposed. For the spheres at $Re_\infty \approx 100$ (blue color), the transitions region is too far to possibly result into significant perturbations on the air layer. Interpreting the $\mathcal{W}e_{u_{z,cr}}$ as the receptivity of the air layer to the hydrodynamic perturbations, a larger value would imply an eventually enhanced compliance to the perturbation. However, since the latter is weak, the $d = 10\,\text{mm}$ SH-80 spheres in $W20\_G80$ and the $d = 5\,\text{mm}$ SH-80 spheres in $W30\_G70$ do not show significant differences in terms of the transversal motion (see Figs. 6.15(e) and 6.15(f)). Conversely, the spheres at $Re_\infty \approx 250 - 290$ (red color) lie in the wake transitions region, where therefore the wake hydrodynamic perturbation might be important. The receptivity to this perturbation can then effectively be different in magnitude depending on the actual $\mathcal{W}e_{u_{z,cr}}$ value. The $d = 8\,\text{mm}$ SH-80 spheres in $W30\_G70$ show a $\mathcal{W}e_{u_{z,cr}} \approx 88$ which could result into an enhanced receptivity of the air layer to the flow compared to the $d = 5\,\text{mm}$ SH-80 spheres in $W40\_G60$ with $\mathcal{W}e_{u_{z,cr}} \approx 28$. This could explain the different $u^\star_{tr}$ behaviour evidenced in Figs. 6.17(e) and 6.17(f).

However, a further insight in the analysed phenomenon is given by looking at the $\frac{\lambda}{d}$ effect in the case of the first sphere where significant transversal motion was detected, i.e. $d = 8\,\text{mm}$

	$W20\_G80$		$W30\_G70$				$W40\_G60$	
	NC	SH-80	NC	SH-80	NC	SH-80	NC	SH-80
d, [mm]	9.99	10.87	5.00	5.59	8.00	8.56	5.00	5.59
Re_∞	110		100		250		290	
ρ_l, [kg m^{-3}]	1220		1197				1172	
μ_l, [kg m^{-1} s^{-1}]	9.2×10^{-2}		3.5×10^{-2}				1.6×10^{-2}	
ν_l, [m^2 s^{-1}]	7.5×10^{-5}		3.0×10^{-5}				1.4×10^{-5}	
γ, [mN m^{-1}]	65.8		66.6				67.5	
u_D, [m s^{-1}]	0.72	0.67	0.52	0.47	0.66	0.61	0.52	0.47
Re_D	96	97	88	88	178	178	190	192
$\mathcal{W}e_D$	-	84	-	22	-	58	-	22
Ca_D	-	0.94	-	0.25	-	0.33	-	0.11
$u^\star_{z,cr}$	-	1.03	-	1.03	1.32	1.23	1.28	1.14
Re_{cr}	-	100	-	91	235	219	243	219
$\mathcal{W}e_{u_{z,cr}}$	-	89	-	23	-	88	-	28
$Ca_{u_{z,cr}}$	-	0.97	-	0.26	-	0.41	-	0.13

Table 6.2 – Driving parameters describing the effect of the air layer compliance on the onset of path instabilities. The colors follow the code introduced in Tab. 6.1: $Re_\infty = \frac{u_\infty d}{\nu_l}$ below (blue) and above (red) the first transition region of the wake of a fixed sphere. ρ_l, μ_l, ν_l, indicate the liquid density, dynamic and kinematic viscosity. γ, surface tension of the air-liquid interface. u_D, scaling velocity introduced in §4.2.3 to describe the gravity-buoyancy effects. $Re_D = \frac{u_D d}{\nu_l}$, $\mathcal{W}e_D = \frac{\rho_l u_D^2 d}{\gamma}$, $Ca_D = \frac{\mu_l u_D}{\gamma}$ indicate the Reynolds, Weber and Capillary numbers based on u_D. $u^\star_{z,cr}$, critical non-dimensional vertical velocity identified via the threshold imposed on the transversal velocity $u^\star_{tr}$. $Re_{cr} = u^\star_{z,cr} Re_D$, critical Reynolds number. $\mathcal{W}e_{u_{z,cr}} = \left(u^\star_{z,cr}\right)^2 \mathcal{W}e_D$, $Ca_{u_{z,cr}} = u^\star_{z,cr} Ca_D$ indicate the Weber and Capillary numbers evaluated at critical conditions.

	NC	SH-NAR	SH-220	SH-80
$u^\star_{z,cr}$	1.32	1.31	1.24	1.23
Re_{cr}	235	232	221	219
$\mathcal{W}e_D$	-	61	60	58
$\mathcal{W}e_{u_{z,cr}}$	-	105	93	88
$\mathcal{W}e_\lambda$	-	0.3	0.8	1.4

Table 6.3 – Focus on the $\frac{\lambda}{d}$ influence in the case of the $d = 8$ mm spheres in the mixture $W30\_G70$, at $Re_\infty \approx 250$. Same parameters as Tab. 6.2, with $\mathcal{W}e_\lambda = \frac{\rho_l u^2_{z,cr} \lambda}{\gamma}$ emphasising the role of the surface roughness on the onset of transversal motion and air layer receptivity.

in the mixture $W30\_G70$, whose data are reported in Tab. 6.3 for all the analysed coatings. The $\mathcal{W}e_{u_{z,cr}}$ parameter was shown to be suitable to compare the behaviour of different spheres in different mixtures falling at approximately the same Re_∞, whereas Tab. 6.3 suggests that it is not able to correctly catch the influence of $\frac{\lambda}{d}$ for the different coatings spheres in the same mixture. In fact, a decreasing $\mathcal{W}e_{u_{z,cr}}$ trend for increasing $\frac{\lambda}{d}$ is estimated, which would imply a decreasing air layer receptivity, in contrast with the $u^\star_{tr}$ behaviour shown in Fig. 6.17. A detailed analysis of each component on the Weber number definition (see e.g. Eq. 6.25) indicates that ρ_l and γ cannot strongly influence its relative variation for different coatings and mixtures, due to their limited modification for varying liquids. Similarly, the choice of the velocity scale cannot be the driving parameter of the Weber number variation, since u_D, u_∞ or $u_{z,cr}$ are someway related one another. More interestingly, the choice of a length scale varying over several orders of magnitudes can render the Weber number suitable to describe macroscopic (e.g. using d) or microscopic behaviour. In fact, the qualitative visualisations in Fig. 6.18 suggest that the typical size of the deformed air pocket is more close, at least as order of magnitude, to the surface roughness size than to the macroscopic sphere dimension d. This suggests the introduction of a modified Weber number:

$$\mathcal{W}e_\lambda = \frac{\rho_l u^2_{z,cr} \lambda}{\gamma}, \tag{6.27}$$

where the length scale is set equal to λ. The values reported in Tab. 6.3 show its ability in correctly describing the receptivity of the air layer to the hydrodynamic perturbation. In fact, increasing $\mathcal{W}e_\lambda$ values are estimated for increasing $\frac{\lambda}{d}$, in agreement with the evidenced effects on $u^\star_{tr}$. Moreover, the value $\mathcal{W}e_\lambda = 1$ can be physically interpreted as the threshold describing the relative dominance of inertial and capillary effects. Interestingly, $\mathcal{W}e_\lambda \ll 1$ as in the SH-NAR case resulted in negligible $u^\star_{tr}$ variations with respect to the reference NC in Fig. 6.17. Conversely, $\mathcal{W}e_\lambda$ approaching the unitary value, i.e. the SH-220 case, determined a more significant effect on the transversal motion, which was finally exalted by the SH-80 coating at $\mathcal{W}e_\lambda > 1$.

Finally, the coatings effects on Re_{cr} visible in Tab. 6.3 are explicitly depicted in Fig. 6.20, via the introduction of the critical Reynolds number variation:

$$\Delta Re_{cr} = \frac{Re^{SH}_{cr} - Re^{NC}_{cr}}{Re^{NC}_{cr}}. \tag{6.28}$$

The same test case $d = 8\,\text{mm}$, SH-80 spheres in the mixture $W30\_G70$ was chosen. The $u^\star_{tr}$ curves on the left side of Fig. 6.17 progressively showed the onset of transversal motion at lower $t^\star$ for increasing $\frac{\lambda}{d}$. This fact is evidenced in Fig. 6.20, where SH coatings are shown to result into a reduction of the Reynolds number where onset of transversal motion is detected. The Re_{cr} reduction is stronger for larger $\frac{\lambda}{d}$, up to $\approx 7\,\%$ in the SH-80 case. These results are qualitatively contradictory with the 2D DNS findings over a partial slip smooth wall cylinder by Legendre *et al.* (2009), where slip was found to delay the onset of recirculation and vortex shedding. The reasons might be identified in the influence of 3D phenomena, which are absent in the 2D wake of a cylinder, and on the partial slip boundary condition over the ideal smooth wall that cannot take into account the possible motion and deformation of the air-liquid interface. This hypothesis is qualitatively supported by some interesting results concerning the transition to turbulence process in wall bounded flows. In fact, Picella (2019) (see e.g. Fig. 6.6 at p. 90 in the cited study, here reported in Fig. 6.21 for clarity) numerically showed that SH surfaces modelled via a homogeneous partial slip flat wall (HSL) and a heterogeneous sequence of no-slip/free-shear flat patches (SNS) have the same retarding effect (with respect to the flat no-slip reference PPF) in the analysed K-type transition process. However, SH surfaces where the air-liquid interface could comply to the flow (MVB) showed a significant advancement of the transition to turbulence

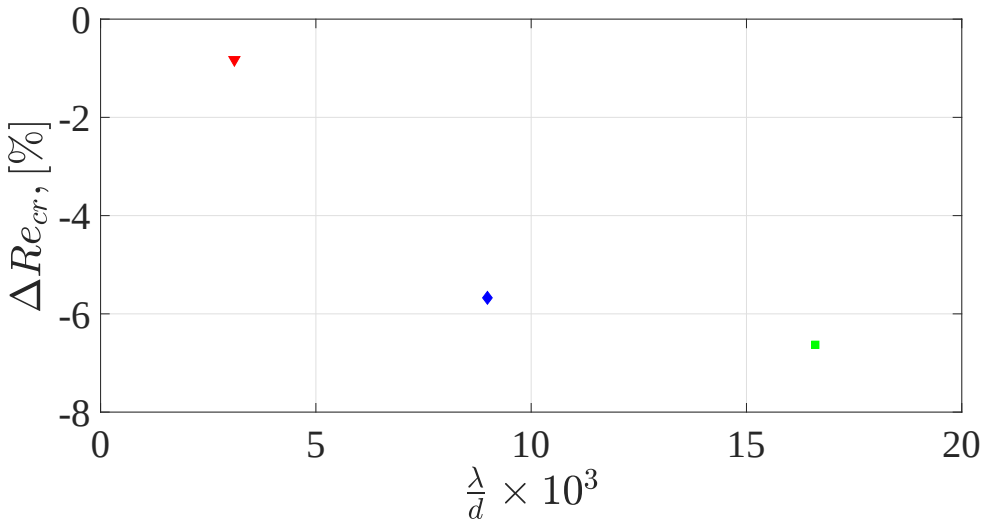

Figure 6.20 – Variation of the critical Reynolds number ΔRe_{cr} (see Eq. 6.28) of SH coatings with respect to the reference, for the $d = 8$ mm, SH-80 spheres in the mixture $W30\_G70$, as a function of the non-dimensional surface roughness $\frac{\lambda}{d}$. ▼, SH-NAR. ♦, SH-220. ■, SH-80.

with respect to the ideal flat SH surfaces, the reason being identified in the strong connection between interface deformation and pressure fluctuations in the near-wall region. These results thus corroborate the findings presented in this section, even if in Picella (2019) the interface deformation was described via a linearised form of the Young-Laplace equation and is thus not comparable with the experimental results here presented (the interface being also pinned to the roughness elements edges). Further indications of the effects of wall deformation on transition to turbulence were provided by Cherubini *et al.* (2013) via a global optimization analysis in a boundary layer flow over a wall with a 3D no-slip bump. The analysis of the energy gain $E(T)$ growth in time (Fig. 4 in the cited study, here reported in Fig. 6.22 in the $Re = 300$ case) showed that a significant increment (with respect to the reference Blasius flow) was obtained for large enough non-dimensional bump height $k = \frac{\ell}{\delta^*}$ (ℓ being the dimensional height and δ^* the Blasius displacement thickness), with a threshold value located somewhere around the unitary value. In the present water-glycerine tests, the $d = 10$ mm, SH-80 sphere in the mixture $W030\_G070$ ($Re_\infty \sim 4 \times 10^2$) can be taken as test case. A gross bump height estimation can be obtained as $k \approx \frac{\ell}{\delta^*}$, where $\ell \sim 10^{-4} - 10^{-3}$ m was estimated from images sequences of the type shown in Fig. 6.18. The displacement thickness can then be scaled as $\frac{\delta^*}{\delta} \sim 10^{-1}$ (expression valid for flow over flat plates, here taken as first approximation), where the laminar boundary layer thickness scales as $\delta \sim dRe_\infty^{-1/2}$. All together, $k \approx \mathcal{O}\left(10^0\right)$ is obtained, which shows, at least qualitatively, that the conditions analysed in this section are comparable to the case where significant transition promotion was found in Cherubini *et al.* (2013).

In the next section, the Re_∞ increase in the pure water tests will be shown to further promote the identified phenomena.

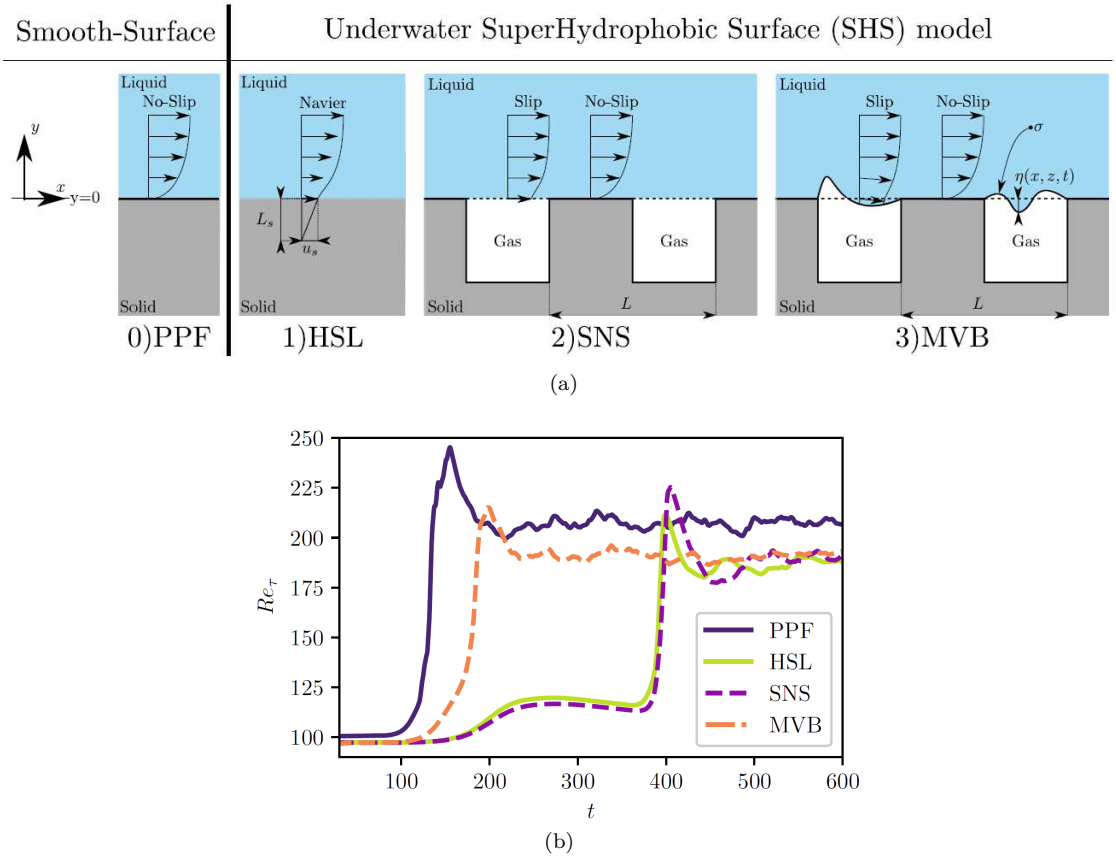

Figure 6.21 – SH wall effects on the transition to turbulence process (adapted from Picella 2019). (a), nomenclature and schematic of the considered models. PPF, Plane Poiseuille Flow. HSL, Homogeneous Slip Length. SNS, Slip/No-Slip. MVB, MoVing Boundary. (b), effect of the different wall typologies on the temporal evolution of the friction Reynolds number Re_τ.

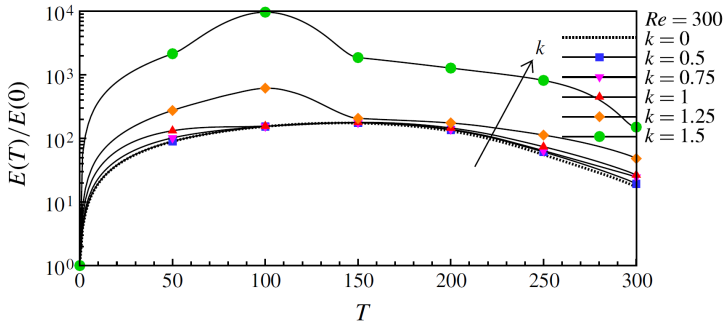

Figure 6.22 – Evolution of the optimal energy gain as a function of target time (adapted from Cherubini *et al.* 2013). The arrow indicates increasing non-dimensional bump height.

6.3 High Reynolds Number

This section discusses the results of the falling sphere tests in double-distilled water, which were executed to analyse the high terminal Reynolds number regime, $4.4 \times 10^3 < Re_\infty < 6.3 \times 10^4$. For the sake of clarity, the tests overview presented in Fig. 6.1 at the beginning of this chapter is here reported in Fig. 6.23 highlighting the investigated region. As discussed in §2.1, this regime is referenced in literature as *sub-critical*. The laminar boundary layer developing on the solid surface of the falling sphere undergoes separation and then the resulting separated shear layers transition to turbulence in the rear-side of the body. The drag coefficient is almost independent of the Reynolds number, showing a value ≈ 0.5. In the next section, following the indications provided by the results at intermediate Re_∞ in §6.2, the behaviour of the air layer initially trapped among the roughness elements of the SH surface is analysed. Then, the detected phenomena are connected to the instantaneous hydrodynamic loads acting on the falling sphere. Finally, the effects on terminal drag are discussed and interpreted.

A part of these results was presented (in a preliminary form) at the $23^{ème}$ *Congrès Français de Mécanique* (Castagna *et al.* 2017) and then published in *Journal of Fluid Mechanics* (Castagna *et al.* 2018*b*). Moreover, a joint contribution deriving from a collaboration between our team and LTRAC Laboratory, Monash University, Melbourne, Australia was presented at *21st Australasian Fluid Mechanics Conference* (Castagna *et al.* 2018*a*).

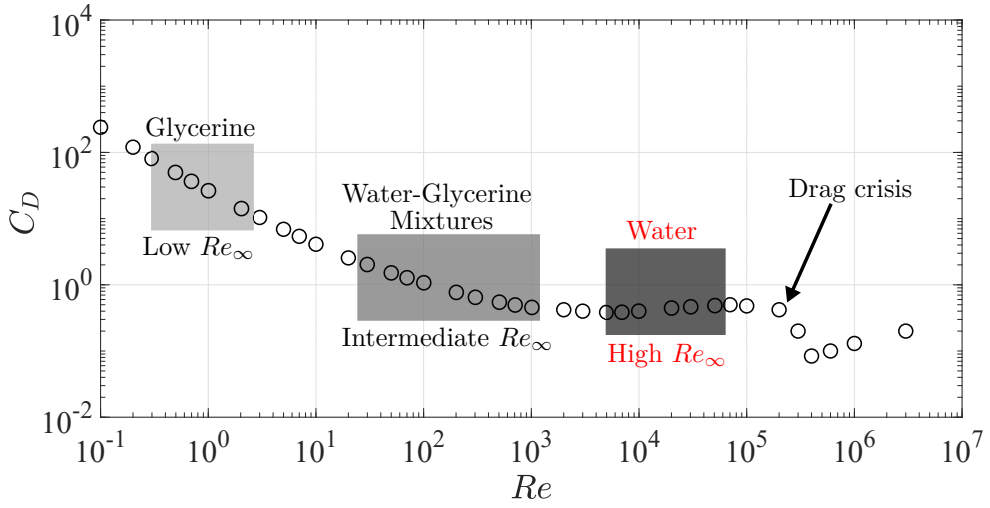

Figure 6.23 – Drag coefficient C_D as a function of the Reynolds number Re for reference spheres. ∘, experimental data from Lapple & Sheperd (1940). The grey-shaded rectangles indicate the whole Re_∞ ranges analysed with the falling sphere experimental campaigns. The red color highlights the region investigated in this section.

6.3.1 Plastron Deformation

In §2.1, the role of the vorticity generated at the body surface and then shed in the wake was highlighted. To resume, the development of the wake instabilities can be viewed from the perspective of the achievement of a critical vorticity amount ω_{cr} (Leal 1989). In fact, a balance between the vorticity produced at the wall of the body and the amount of vorticity that the wake

is able to evacuate exists. When the former dominates the latter, an accumulation of vorticity downstream of the body occurs, until the critical ω_{cr} value is reached and the wake is obliged to find a new configuration to be able to evacuate the larger amount of vorticity. This change of the nature of the wake is referenced in literature as transition process.

In the framework of freely falling spheres in the sub-critical regime, the production of vorticity at the sphere surface is expected to be concentrated within the laminar boundary layer developing along the sphere wall, which is characterised by its thickness $\delta \sim dRe_\infty^{-1/2}$. The vorticity generated in the boundary layer can thus be scaled as $\omega \sim \frac{\Delta u}{\delta}$, with Δu the typical velocity jump across the boundary layer (see e.g. Batchelor 1967, Chapter 5). In the case of SH spheres, the velocity jump across the boundary layer can be scaled as $\Delta u \sim u_\infty - u_{sl}$, where u_{sl} is the slip velocity. Under the assumption that in the sub-critical regime $C_{D\infty} \approx 0.5$, Eq. 4.3 describing the vertical motion of a free falling sphere provides $u_\infty \approx k_D u_D$ when evaluated at terminal conditions ($k_D \sim 10^0$), which yields $\Delta u \sim u_D - u_{sl}$. Under the hypothesis of a non-deformable air layer encapsulating the sphere, the slip length model can be introduced to connect u_{sl} to the wall shear stress τ_w via the slip length ℓ_{sl}, and considering as a first approximation $\ell_{sl} \sim \lambda$ (Ybert *et al.* 2007):

$$u_{sl} \sim \lambda \left.\frac{\partial u}{\partial n}\right|_w, \tag{6.29}$$

n being the normal direction to the wall (subscript w). Coupling Eq. 6.29 with the expression of the wall shear stress:

$$\tau_w = \mu_l \left.\frac{\partial u}{\partial n}\right|_w = \rho_l u_\tau^2, \tag{6.30}$$

u_τ being the friction velocity, yields:

$$u_{sl} \sim \lambda \frac{u_\tau^2}{\nu_l}. \tag{6.31}$$

Moreover, under the assumption that in the sub-critical regime the magnitude of the viscous drag is $\sim 10\,\%$ of the total drag, the following expression can be achieved:

$$\tau_w S_\tau \approx \frac{1}{10}\frac{1}{2}\rho_l u_\infty^2 S C_{D\infty}, \tag{6.32}$$

$S_\tau = 4\pi\left(\frac{d}{2}\right)^2$ being the sphere wetted surface and $S = \pi\left(\frac{d}{2}\right)^2$ the sphere cross-section. The expression in Eq. 6.32 implies that:

$$\tau_w \approx \frac{1}{160}\rho_l u_\infty^2. \tag{6.33}$$

The relation $u_\infty \sim u_D$ can then be injected into Eq. 6.33 yielding, with the help of Eq. 6.30:

$$u_\tau = k u_D, \tag{6.34}$$

where the scaling parameter $k = \mathcal{O}(10^{-1})$. A final expression for the velocity jump across the boundary layer can then be obtained via Eqs. 6.31 and 6.34:

$$\Delta u \sim u_D - \lambda\frac{u_\tau^2}{\nu_l} \sim u_D - \lambda k u_D \frac{u_\tau}{\nu_l} \sim u_D\left(1 - k\frac{\lambda}{\delta_\nu}\right), \tag{6.35}$$

$\delta_\nu = \frac{\nu_l}{u_\tau}$ being the viscous length scale. The non-dimensional vorticity production can thus be scaled, via Eq. 6.35, as:

$$\omega^\star = \frac{\omega d}{u_D} = A\left(1 - k\frac{\lambda}{\delta_\nu}\right)\frac{d}{\delta}, \tag{6.36}$$

where $A = \mathcal{O}(10^0)$ is a scaling parameter inserted to justify the equal symbol. The relation in Eq. 6.36 predicts that in the no-slip limit $\omega^\star \sim Re_\infty^{1/2}$, while for a given sphere diameter the production of vorticity decreases linearly with the slip length, which is assimilated to the surface roughness typical size. The evolution of the dimensionless vorticity computed according to Eq. 6.36 is shown in Fig. 6.24(a) as a function of $Re_D = \frac{u_D d}{\nu_l} = \frac{Re_\infty}{k_D}$, for the range of slip lengths $\ell_{sl} \sim \lambda$ experimentally evaluated (see Tab. 3.1). The dashed line represents the limit between an axisymmetric and a non-axisymmetric wake behind the sphere that was proposed by Magnaudet & Mougin (2007) in their numerical study of wake instabilities of fixed 3D spheroidal bubbles. Their empirical law (see Eq. (4.1) in Magnaudet & Mougin 2007) is here reported for completeness:

$$\frac{\omega_{cr} d}{2u_\infty} \approx 12.5 + 4.3 \times 10^{-3} Re_\infty. \tag{6.37}$$

The main result of their criterion is the crucial importance of the amount of vorticity produced at the body surface and injected in the flow. The law proposed by Magnaudet & Mougin (2007) is properly normalized in order to be comparable with this study. The Reynolds number Re_D field analysed in Fig. 6.24(a) approximately corresponds to the Re_∞ range investigated by Magnaudet & Mougin (2007). By forcing the no-slip curve to intersect the instability criterion curve at the Reynolds number where the first bifurcation of the sphere wake occurs ($Re_\infty \approx 212$ or equivalently $Re_D \approx 129$), the value $A = 3.86$ in Eq. 6.36 was evaluated. Interestingly, for large enough slip values the model predicts the amount of surface vorticity to go back below the line describing the first regular bifurcation. In this case, at large enough Reynolds number the vorticity flux advected downstream prevails over the vorticity generation at the surface: not enough vorticity is accumulated for the transition to occur (Leal 1989; Legendre *et al.* 2009). The detailed view in Fig. 6.24(b) shows the behaviour in the critical region: larger slip induces an increase of the critical Reynolds number $Re_{D,cr}$ at which the transition occurs. The linear relationship between $Re_{D,cr}$ and the non-dimensional slip length $\frac{\lambda}{d}$ is reported in Fig. 6.24(c), where the slope of the fitting line is approximately equal to 0.9. The model thus predicts, under the hypothesis of an ideal non-deformable slip wall, a delay effect on the transition occurrence due to the slip. The following of this section dedicated to the high Re_∞ results will show how the assumptions that have led to the development of this simplified vorticity model may not be fulfilled in experimental tests.

In fact, a typical snapshot of a SH-80 sphere ($d = 5\,\mathrm{mm}$) during its falling motion recorded with the high magnification configuration is shown in Fig. 6.25. This image clearly illustrates the deformation of the air plastron as testified by the presence of a huge protrusion located at the backside of the sphere. The plastron macroscopic deformation can be quantified by introducing the aspect ratio χ such that:

$$\chi = \frac{d_{eq}}{d}, \tag{6.38}$$

where d_{eq} denotes an equivalent diameter defined as follows:

$$d_{eq} = 2\sqrt{\frac{\mathcal{S}}{\pi}}, \tag{6.39}$$

with $\mathcal{S}$ the surface area delineated by the deformed interface. Based on the MATLAB® image processing toolbox, a contour finding algorithm has been developed to estimate $\mathcal{S}$. The output of this algorithm applied to the image shown in Fig. 6.25(a) is illustrated in Fig. 6.25(b). In practice, $\mathcal{S}$ is estimated via the computation of the white area. The proposed approach was applied over the available sphere diameter range in order to detect possible qualitative and quantitative modifications of the air layer behaviour. In fact, as shown in Figs. 6.26 and 6.27,

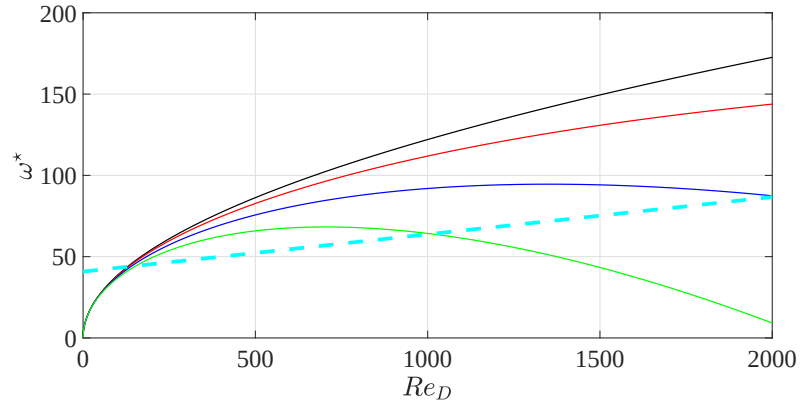

(a)

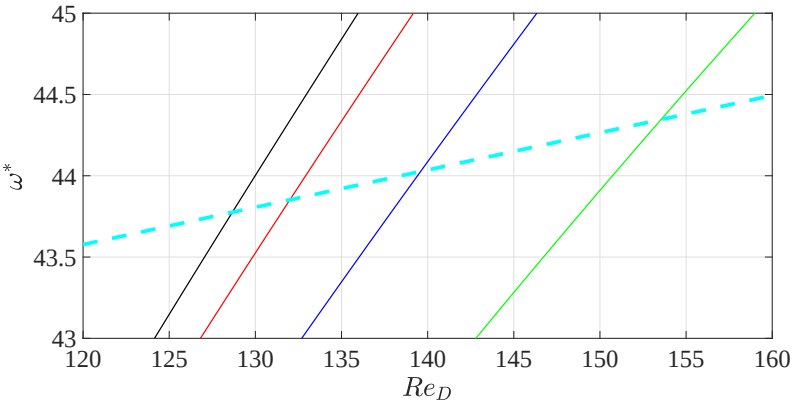

(b)

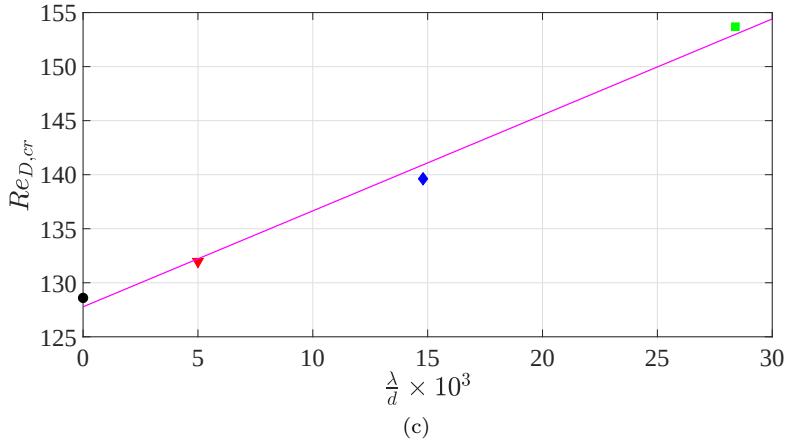

(c)

Figure 6.24 – Model for the production of vorticity at the surface of a sphere. (——), no-slip $\lambda = 0\,\mu m$. (——), $\lambda = 25\,\mu m$. (——), $\lambda = 74\,\mu m$. (——), $\lambda = 142\,\mu m$. (a) non-dimensional vorticity $\omega^\star$ as a function of the Reynolds number Re_D (see Eq. 6.36). (- - -), empirical law by Magnaudet & Mougin (2007), reported in Eq. 6.37. (b), detail of the critical region in (a). (c), critical Reynolds number $Re_{D,cr}$ as a function of the non-dimensional slip length $\frac{\lambda}{d}$. (——), fit of the data in the least-mean squares sense.

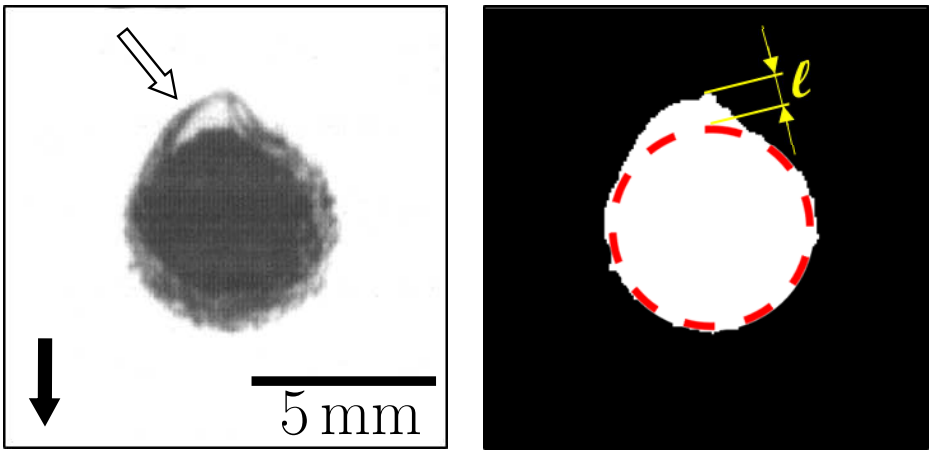

(a) (b)

Figure 6.25 – (a), typical image recorded during the fall of a SH-80 sphere ($d = 5$ mm) in pure water using the high magnification configuration. The black arrow denotes the direction of gravity. The white arrow indicates the region where the plastron deformation is visible. (b), binarised image resulting from the contour finding algorithm used to compute the aspect ratio χ. The red dashed line (- - -) symbolises the sphere contour. The yellow variable ℓ denotes the typical length scale of the observed protrusion.

the plastron shape is extremely sensitive to the sphere diameter or equivalently the Reynolds number. Indeed, while the sequence in Fig. 6.26 ($d = 5$ mm) is characterized by the presence of a single protrusion, the sequence in Fig. 6.27 ($d = 20$ mm) reveals the presence of multiple air pockets. Note however that the typical length scale ℓ of the protrusions observed in the tests in pure water (see Fig. 6.25(b)) remains roughly constant ($\approx 1.5 \pm 0.5$ mm) independently of d and λ. From the image post-processing of the high magnification configuration, it is found that χ decreases from around 1.2 for the smallest SH spheres (i.e., $d = 5$ mm) to about 1 for the largest SH spheres (i.e., $d = 25$ mm). In other words, although the local normalized curvature $\frac{d}{\ell}$ increases with the sphere diameter, at the same time the global shape of the plastron tends to be spherical. This means that the idealized shape assumed to derive the expression in Eq. 6.36 is more likely to be achieved for the largest sphere diameter analysed in the pure water tests.

As emphasised in Figs. 6.26 and 6.27, the interface distortion occurs at the rear-side of the spheres, which undergoes the massive separation of the laminar boundary layer typical of the sub-critical regime. As discussed in §6.2, the competition between separation-induced suction and capillary pressure can be described by introducing the Weber number. The developments in §6.2.1 highlighted the main role played by the length scale choice in the Weber number definition. From the qualitative visualisations in Figs. 6.26 and 6.27, the sphere size d seems to be the most suitable sphere property to describe the macroscopic deformation of the air layer in the pure water tests. This choice is supported by the fact that the same qualitative plastron behaviour was detected for all the SH coatings, with differences arising for large d variations.

The high Re_∞ analysed in this section allows the discussion of an additional phenomenon, usually referred to as *wetting* or transition from the Cassie-Baxter to the Wenzel state. To briefly describe it, an analogy with channel flows is performed. The We_D definition in Eq. 6.21 differs from that usually used in internal flows (see e.g. Seo *et al.* 2015), where the interaction between

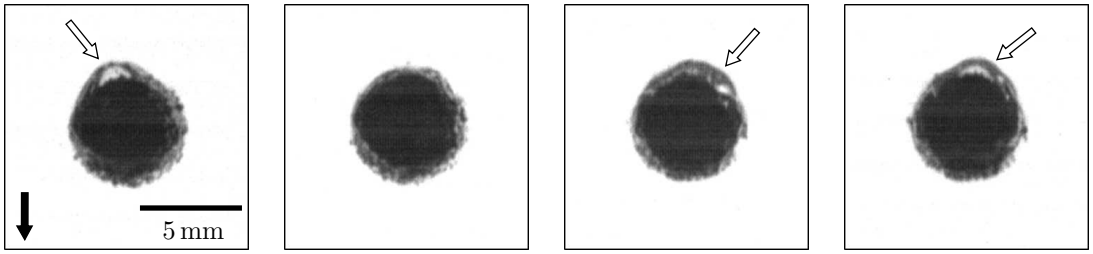

(a) $t^\star = \widehat{t^\star}$ (b) $t^\star = \widehat{t^\star} + 3$ (c) $t^\star = \widehat{t^\star} + 10$ (d) $t^\star = \widehat{t^\star} + 13$

Figure 6.26 – Typical snapshots recorded in high magnification configuration illustrating the movement and deformation of the air plastron (indicated by white arrows) around a $d = 5\,\text{mm}$, SH-80 coated sphere, falling in pure water. The black arrow represents the direction of gravity. The variable $\widehat{t^\star}$ designates a randomly chosen time origin.

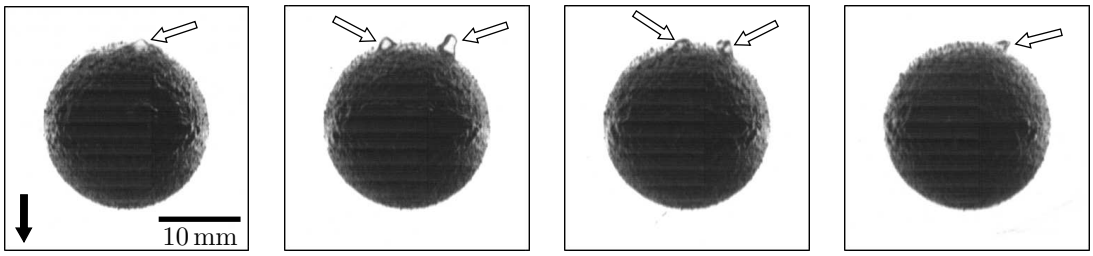

(a) $t^\star = \tilde{t}^\star$ (b) $t^\star = \tilde{t}^\star + 1$ (c) $t^\star = \tilde{t}^\star + 2$ (d) $t^\star = \tilde{t}^\star + 3$

Figure 6.27 – Same as Fig. 6.26, for a $d = 20\,\text{mm}$, SH-80 coated sphere, falling in pure water. The variable $\tilde{t}^\star$ designates a randomly chosen time origin.

the flow and the air-liquid interface is quantified via viscosity-based variables:

$$\mathcal{W}e^{+} = \frac{\rho_l u_\tau \nu_l}{\gamma}, \tag{6.40}$$

the reason being that the wake of the sphere studied in this section is predominated by the form drag. By further re-working the expression in Eq. 6.40, and exploiting Eq. 6.34, a relation between the two definitions of the Weber number is obtained:

$$\mathcal{W}e^{+} = \frac{\rho_l u_\tau \nu_l}{\gamma}\frac{u_\tau}{u_\tau}\frac{d}{d} = k^2\frac{\rho_l u_D^2 d}{\gamma}\frac{\nu_l}{u_\tau}\frac{1}{d} = k^2\mathcal{W}e_D\frac{\delta_\nu}{d}. \tag{6.41}$$

By considering that $\mathcal{W}e_D = \mathcal{O}(10^1 - 10^2)$ and $\delta_\nu = \mathcal{O}(10^{-6} - 10^{-5})$ m, the $\mathcal{W}e^{+}$ in the pure water tests is found to vary in the range $10^{-4} - 10^{-3}$. Furthermore, in channel flows a criterion based on the maximum tolerable non-dimensional surface texture size that may lead to transition from the Cassie-Baxter to the Wenzel state can be formulated (see e.g. Seo *et al.* 2015). The texture size expressed in viscous units:

$$\lambda^{+} = \frac{\lambda u_\tau}{\nu_l}, \tag{6.42}$$

shows an $\mathcal{O}(10^1)$, which is an order of magnitude sufficiently low to expect that the plastron failure does not occur (Seo *et al.* 2015). This is consistent with the fact that the release of air bubbles in the wake during the drop was never observed, except when the sphere hit the bottom of the tank.

To resume, two parameters able to describe the air layer compliance to the flow were introduced, i.e. χ and $\mathcal{W}e_D$. However, an important remark has to be made about their relationship. Although both of them characterise the interaction between the plastron and the local stresses induced by the wake, χ is perfectly suited to provide an *a posteriori* quantitative description of the interface deformation. However, a reliable estimation of χ suffers from a severe limitation. Indeed, the computation of χ is based on a 2D projection of a phenomenon which is likely 3D. Unfortunately, the out-of-plane deformations, although perceptible, are hidden due to the sphere opacity. This is the reason why $\mathcal{W}e_D$ is more convenient to be used rather than χ. In fact, since $\mathcal{W}e_D$ is set *a priori*, it should be regarded as a qualitative indicator of plastron deformation.

Even if the limitations in the χ evaluation from the available 2D images were evident, the detection of the position where the bulge up of the air pocket starts and ends seemed appealing. For this reason, the preliminary results of an algorithm developed in MATLAB® for the detection of the instantaneous position of the air pocket in the rear-side of the falling sphere are briefly discussed. Sequences of images in the high magnification configuration as the one already presented in Figs. 6.26 and 6.27 were analysed. A schematic of the objective of the code, which was based on the detection of the sphere and air pocket with respect to the background via a binarisation procedure, is represented in Fig. 6.28. Once estimated the direction of the instantaneous velocity vector $\mathbf{u}$ via the algorithm described in Chapter 5, the angles ϑ_b and ϑ_e that indicate the beginning and the end of the air protrusion could be evaluated. The position of the air pocket was estimated by comparing the image with deformed interface with the contour of the solid sphere. The time evolution of the two angles could provide information about the motion of the air pocket in the 2D plane available in the image. However, it is important to highlight that in no way the results of this algorithm could describe the complex 3D motion of the air pockets which is evident in the recorded videos. The high spatial resolution necessary to investigate at least qualitatively the plastron deformation forced the use of a smaller recording window ($\approx 12 \times 7$ cm^2) than the one used in the 3D trajectory tests. This meant that to get a statistically relevant

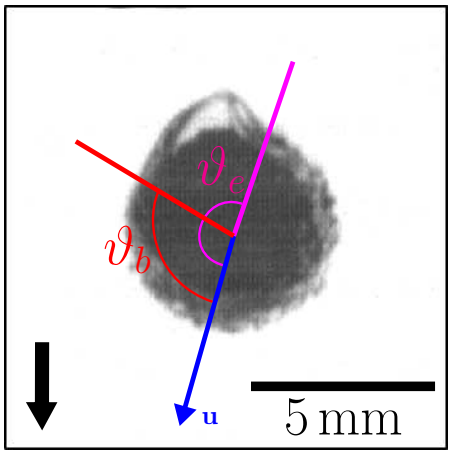

Figure 6.28 – Schematic of the approach implemented to estimate the instantaneous position of the air pocket. The symbols ϑ_b and ϑ_e indicate the beginning and end angle of the air protrusion, respectively. The black arrow indicates the direction of gravity. The snapshot is taken from a sequence of a drop in pure water of a $d = 5\,\mathrm{mm}$, SH-220 sphere, at a tank height where the terminal velocity was attained. The instantaneous velocity vector **u** is not aligned with the direction of gravity due to a non-negligible transversal motion.

amount of data multiple videos should be taken at each tank height of interest, for each of the analysed coatings and diameters. Such kind of analysis, necessary to eventually link the plastron motion and deformation to the flow separation in the sub-critical regime, was considered too time demanding and well beyond the purpose of the performed qualitative visualizations. In any case, the preliminary results of the analysis are shown in Fig. 6.29 for the same sphere introduced in Fig. 6.28, at a tank height where the sphere had already attained the terminal velocity u_∞. The high temporal resolution (1300 fps) coupled with the size of the recording window resulted into a total available time $t^\star \approx 15$, or equivalently $t \approx 0.14\,\mathrm{s}$, which approximately corresponds to one fourth of the total drop time. As evident from Fig. 6.29, all detected phenomena occur in the rear-side of the sphere, that is behind the equator defined at 90° and 270° with respect to the instantaneous **u** direction. This is at least qualitatively consistent with the position of the boundary layer separation, which in the analysed sub-critical regime can be considered at $\approx 85°$ (Achenbach 1972). In Fig. 6.29, the angle ϑ_b varies in the range 93° to 141°, whereas the angle ϑ_e in the range 183° to 251°. The large instantaneous angles variations that are occasionally noticed (e.g. at $t^\star \approx 5$) are an indication of the limitations of the current analysis, which cannot take into account the out-of-plane motion and deformation of the air protrusion. All in all, bearing in mind the limitations of the proposed analysis, the implemented approach could open some interesting perspectives in view of an estimation of instantaneous information on the air pocket behaviour.

To resume, while χ can be considered as an *a posteriori* quantitative evaluation of the deformation of the air pocket with connected limitations on its value estimation, $\mathcal{W}e_D$ can easily provide an *a priori* qualitative estimation. Interestingly, an explicit scaling between $\mathcal{W}e$ and χ can be retrieved via a development of the definition of the latter. Assuming that $d_{eq} \approx d + \ell$, the expression in Eq. 6.38 can be reformulated as follows:

$$\chi = 1 + \frac{\ell}{d}. \tag{6.43}$$

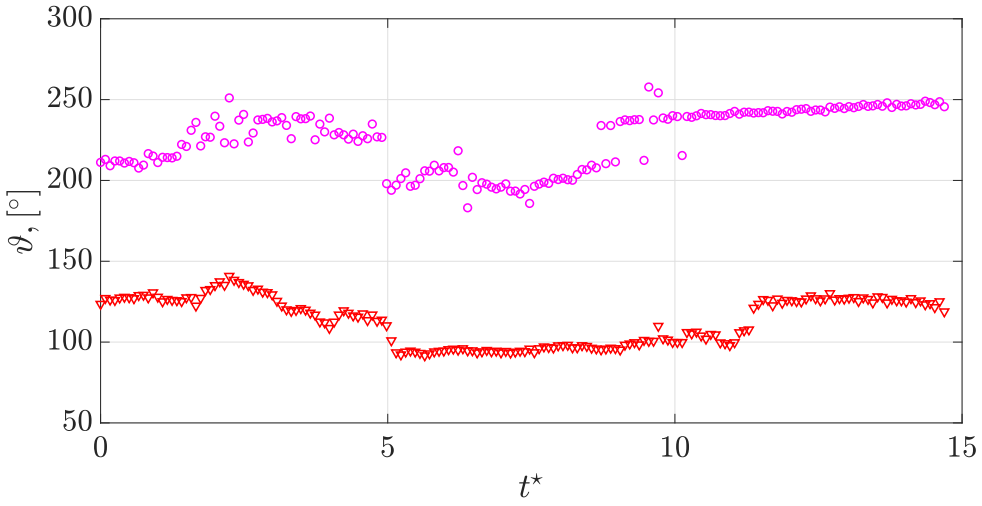

Figure 6.29 – Temporal evolution of the angles (defined in Fig. 6.28) describing the beginning and end of the air protrusion. ▽, ϑ_b angle. ○, ϑ_e angle.

The approximated relation $d_{eq} \approx d + \ell$ provides χ variations from around 1.2 for the small diameter spheres toward the unitary value for the largest diameter spheres, in good agreement with the definition given in Eq. 6.39. Since ℓ is found almost uniform, Eq. 6.43 implies that $d \sim (\chi - 1)^{-1}$, which injected in the re-worked $\mathcal{W}e_D$ expression in Eq. 6.22 provides:

$$\mathcal{W}e_D \sim (\chi - 1)^{-2}. \tag{6.44}$$

In other words, in the tests performed in pure water, low values of $\mathcal{W}e$ are associated to large χ and *vice versa*. This relation will be shown to have strong implications on the hydrodynamic loads, that is lift and drag, which are discussed in the next paragraph.

6.3.2 Hydrodynamic Performance

In the case of a freely falling body, the wake nature influences the hydrodynamic loads experienced by the body and thus the path followed during the drop (see §2.2). The analysis of the 3D trajectory, and therefore of the vertical and transversal motion, can thus be exploited to quantitatively evaluate the instantaneous hydrodynamic loads acting on the falling sphere (see §2.2.1), possibly providing information on the connection between the air plastron behaviour and the wake.

The discussion in §6.3.1 highlighted that three parameters must be considered in the attempt to describe the behaviour of SH coatings:

- the terminal Reynolds number Re_∞, which describes the nature of the wake;
- the non-dimensional ratio $\frac{\lambda}{d}$, which characterises (under the assumption $\ell_{sl} \sim \lambda$) the amount of slip;
- the Weber number $\mathcal{W}e_D$, which is indicative of the air layer receptivity to the hydrodynamic perturbation.

However, in the sub-critical regime analysed in this section, the Re_∞ has a negligible effect on the drag experienced by reference no-slip spheres, the drag coefficient being approximately uniform for varying Re_∞ (see the highlighted region in Fig. 6.23). This implies that any influence of SH coatings on the results shown in the next paragraphs is expected to be mainly due to the amount of slip and the state of the air-liquid interface. The analysis is started with the discussion of the vertical motion and then continued with the description of transversal phenomena in the following paragraph.

Vertical Motion

The analysis of the vertical motion can be started by looking at the vertical velocity profile of the reference sphere in the case of the smallest analysed diameter $d = 5\,\text{mm}$, which is reported in Fig. 6.30(a). The experimental data show an acceleration from an initial zero vertical velocity $u_z^\star$ towards the terminal velocity $u_\infty^\star$, which is reached once transient effects vanish. A good agreement is noted between experimental data and the profile predicted via Eq. 4.3 at the early stage of the drop and at terminal conditions. In detail, the deviation between the experimentally evaluated $u_\infty^\star$ and the value predicted via Eq. 4.3 represents only 0.2 % of the predicted value. These considerations give further proof of the accuracy of the performed measurements. In fact, due to the high ratio between sphere and liquid density ($\zeta \approx 7$), Eq. 4.3 was expected to well describe the vertical motion of the analysed spheres. Moreover, the execution of ten tests for each sphere allowed for the evaluation of the uncertainties of the presented measurements, which are shown in the insert in Fig. 6.30(a). The magnitude of the uncertainty represents approximately $\pm$ 2.5 % of $u_\infty^\star$. A significant departure of experimental data from the predicted profile arises for $t^\star$ within the range $10 - 40$. The experimental velocity drop is induced by a vertical acceleration $a_z^\star$ decrease occurring between $t^\star \approx 10$ and $t^\star \approx 20$, as evident in Fig. 6.30(b). Such phenomenon has been reported by other authors (see e.g. Mordant & Pinton 2000) and is induced by the onset of instabilities in the wake of the sphere, which promotes a sudden drag increase (Jenny *et al.* 2004). More surprisingly, from $t^\star \approx 20$ to $t^\star \approx 40$ the measured sphere acceleration exceeds its predicted value, which balances the previous acceleration reduction and enables the reference sphere to reach its predicted terminal velocity, provided that $u_\infty^\star = \int_0^\infty a_z^\star dt^\star$.

In the case of SH spheres, the same qualitative phenomena of the reference case are retrieved in Fig. 6.31. However, the inspection of the $u_z^\star$ profiles in Fig. 6.31(a) shows that the departure of experimental data from the predicted profile is anticipated to $t^\star \approx 7$, which means that the SH coating promotes an earlier onset of instabilities than the reference sphere. As in the case of the reference sphere, the effect detected on $u_z^\star$ is accompanied by a sudden decrease of the acceleration $a_z^\star$, reported in Fig. 6.31(b). However, unlike the reference sphere, the measured $a_z^\star$ then collapses at $t^\star \approx 16$ on the predicted trend. Accordingly, the terminal velocity achieved by the SH sphere is much lower than its predicted value, as emphasised in Fig. 6.31(a). In the specific case displayed in Figs. 6.30 and 6.31, i.e. $d = 5\,\text{mm}$, the detected $u_\infty^\star$ performance is a first indication of an increase of terminal drag coefficient due to the SH coating, as is well described by Eq. 6.2 connecting $C_{D\infty}$ to the non-dimensional terminal velocity.

In both Figs. 6.30(a) and 6.31(a) the exponential model introduced in Eq. 4.6 fitted on the experimental data shows a satisfactory accuracy in describing the initial part of the drop and the terminal conditions. In detail, the deviation on the $u_\infty^\star$ estimation reaches a maximum value $\approx$ 1.2 % in the reference sphere case when evaluated with respect to the experimental value. The magnitude of this deviation seems consistent with the results reported in Fig. B.2 in Appendix B, where the fitting procedure was executed with respect to the curve predicted via Eq. 4.3 and a large amount of data at terminal conditions was available. By performing the same type of analysis that led to the results in Fig. B.2, experimental data can be progressively suppressed

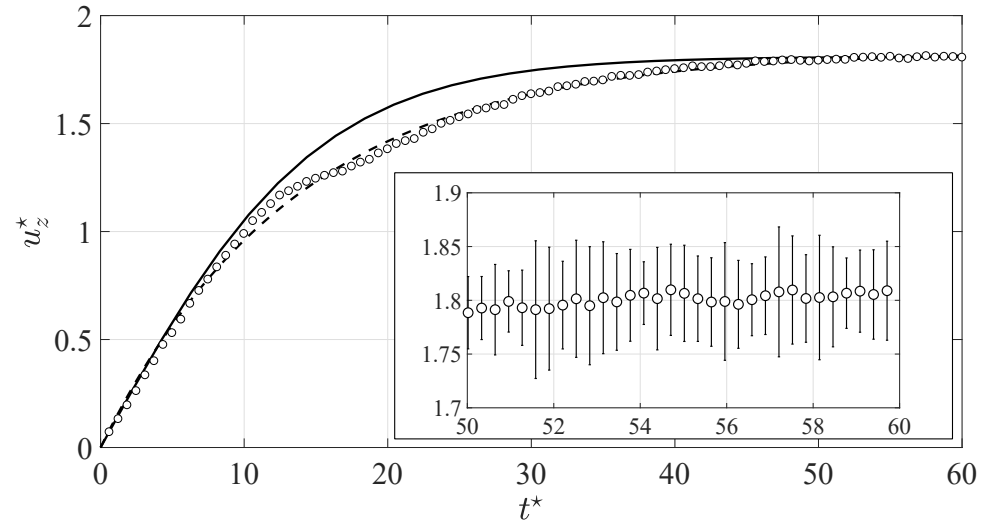

(a)

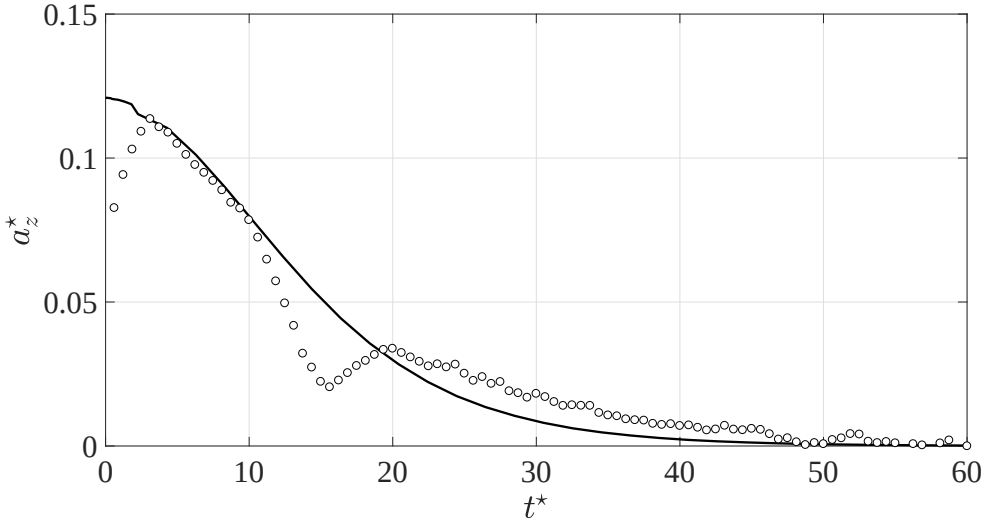

(b)

Figure 6.30 – Instantaneous vertical motion of the $d = 5$ mm, reference stainless steel spheres in pure water. (a), vertical velocity $u_z^\star$. (b), vertical acceleration $a_z^\star(t)$. ∘, experimental data (for the sake of clarity, one point out of two is reported). (——), prediction according to Eq. 4.3. (- - -), exponential model according to Eq. 4.6 fitted on experimental data ((a) only). The insert in (a) shows the error bars (95% confidence level) in the terminal region, the magnitude being representative of the uncertainties along the whole drop.

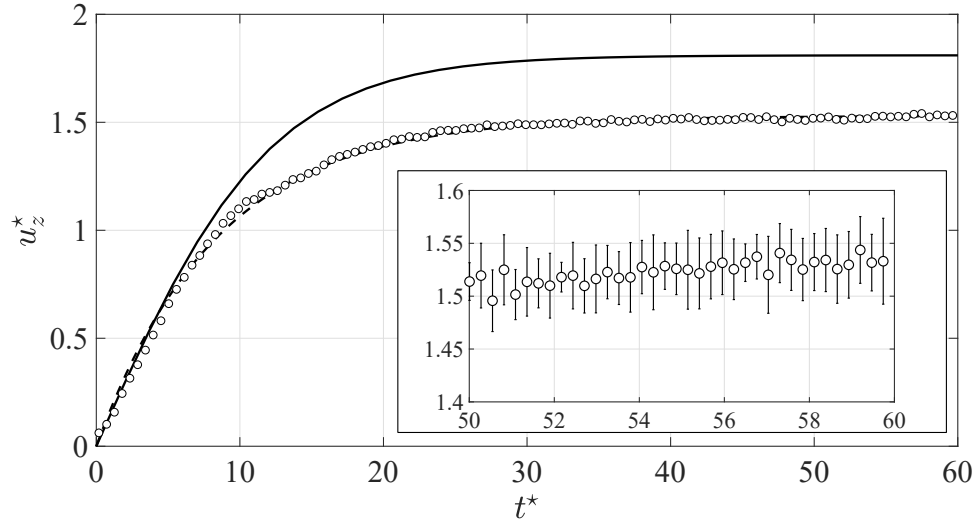

(a)

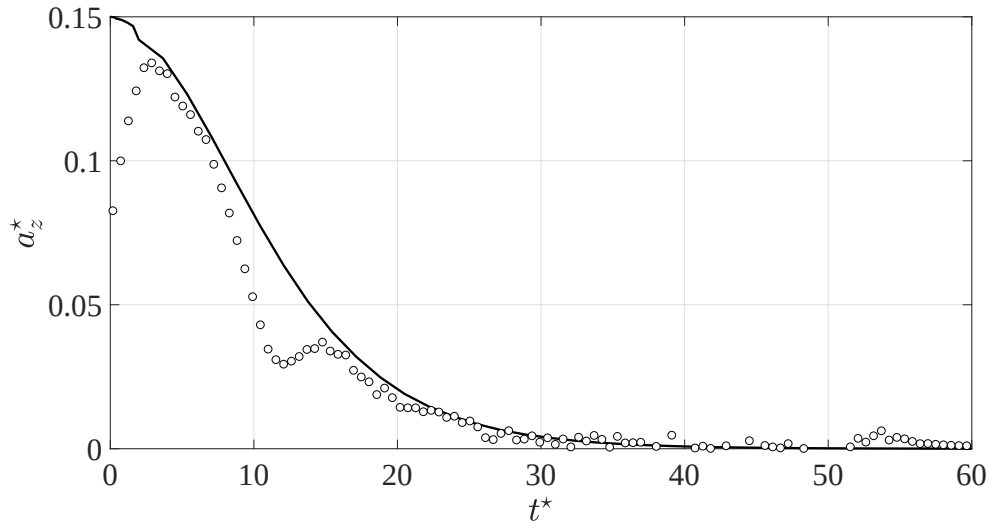

(b)

Figure 6.31 – Same as Fig. 6.30, for the $d = 5$ mm, SH-80 spheres.

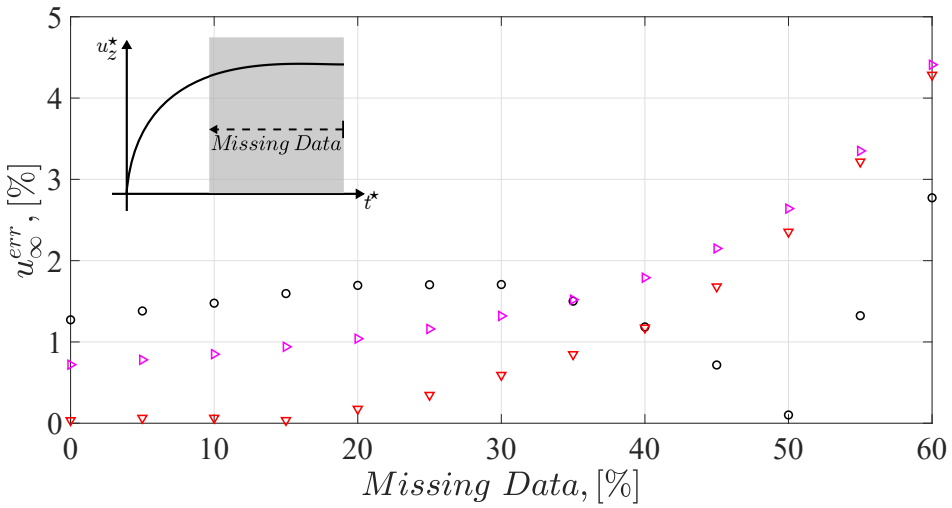

Figure 6.32 – Evolution of the error on the estimation of the terminal velocity $u_\infty^\star$ via the exponential model described by Eq. 4.6 with respect to the experimental data, for $d = 5\,\text{mm}$ spheres in pure water. ○, reference sphere. ▽, SH-80 sphere. ▷, data from Fig. B.2 estimated via the semi-empirical law in Eq. 4.3. The horizontal axis indicates the percentage of data removed from the terminal part of the experimental velocity profile, as schematically depicted in the insert.

in the fitting procedure to test the robustness of the algorithm. The results for $d = 5\,\text{mm}$ reference and SH-80 spheres are shown in Fig. 6.32. The profile of the SH-80 spheres follows an increasing estimation error for decreasing available experimental data, which is consistent with the results shown in Fig. B.2. However, the error magnitude for low percentages of missing data is lower than the case predicted via Eq. 4.3. This is due to the fact that the exponential model is able to follow to a satisfactory level the experimental profile even in the transient region (see Fig. 6.31(a)), which was not the case with the predicted profile (see Fig. 4.11). Conversely, the reference sphere results in Fig. 6.32 show a non-monotonic trend, which is due to the fact that the experimental velocity data fall back on the predicted profile after the initial departure (see Fig. 6.30(a)). In fact, depending on the amount of data of the transient region considered in the fitting procedure, the corresponding terminal velocity estimation could oscillate around the experimental value, with a resulting over or under estimation. The accuracy of the fitting method is confirmed by the limited ($< 5\,\%$) error on the $u_\infty^\star$ estimation even for large percentages of suppressed data ($60\,\%$), which correspond to an instantaneous vertical velocity $u_z^\star \approx 80\,\%$ of the corresponding terminal value.

The robustness of the fitting via the exponential model in Eq. 4.6 is of fundamental importance for the analysis of the performance of large diameter spheres. In fact, the limited tank height resulted into a progressively lower availability of data at terminal conditions for increasing d (see details in Appendix B). The issue is well represented in Fig. 6.33, where the $u_z^\star$ profile of the most severe case, that is $d = 25\,\text{mm}$, for the reference spheres in pure water is reported. The available data are interrupted at $t^\star \approx 20$, right after the departure of experimental data from the predicted curve. The reached instantaneous $u_z^\star$ is $\approx 81\,\%$ of the terminal velocity predicted via Eq. 4.3. The expected error on the $u_\infty^\star$ estimation performed via the exponential fitting is therefore $\approx 5\,\%$, based on the results in Fig. 6.32. This prediction is confirmed by

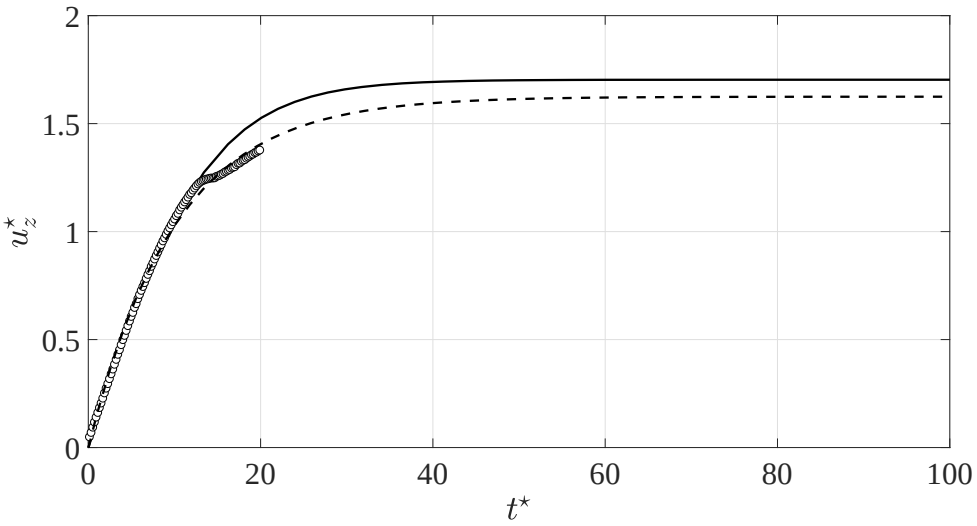

Figure 6.33 – Instantaneous vertical velocity $u_z^\star$ of the $d = 25$ mm, reference stainless steel spheres in pure water. ∘, experimental data (for the sake of clarity, one point out of two is reported). (——), prediction according to Eq. 4.3. (- - -), exponential model according to Eq. 4.6 fitted on experimental data.

d, [mm]	$u_{z,max}^\star$, [%]	u_∞^{err}, [%]
5	100	1.5
8	98.3	1.6
10	93.2	1.8
15	91.0	2.6
20	85.0	4.0
25	81.0	4.5

Table 6.4 – Robustness of the exponential fitting model with respect to available experimental data for reference spheres in pure water. The symbol $u_{z,max}^\star$ indicates the maximum experimentally attained velocity, whereas the symbol u_∞^{err} indicates the error on the estimation of the terminal velocity performed via the exponential model in Eq. 4.6. Both the quantities are normalised via the terminal velocity predicted via Eq. 4.3.

the exponential profile in Fig. 6.33, which reaches a terminal velocity $\approx 4.5\,\%$ lower than the predicted value. The underestimation of $u^\star_\infty$ is predominantly due to the lack of experimental data at terminal conditions. The same analysis was performed for all the investigated diameters and the corresponding values are reported in Tab. 6.4 for the reference spheres. The same order of magnitude of the estimation error can thus be considered valid for SH spheres, where a suitable $C_D(Re)$ law is no more available, thus preventing a prediction via Eq. 4.3. All in all, these evaluations of the $u^\star_\infty$ estimation error highlight that the results at terminal conditions shown in this section are quantitatively reliable for the low range of analysed diameters, while they should be viewed from a qualitative perspective for the larger diameters.

An overview of the vertical motion results for all the analysed coatings is provided in Fig. 6.34. In Fig. 6.34(a) the $d = 5\,\text{mm}$ spheres are compared, showing an interesting trend at terminal conditions as a function of the ratio $\frac{\lambda}{d}$. Larger surface roughness determines a decrease of the non-dimensional attained terminal velocity. In the transient region, only the SH-80 curve is clearly detached from the others. The d increase determines a modification of the identified trends. As highlighted by Fig. 6.34(b) for the $d = 15\,\text{mm}$ spheres, the curves tend to overlap each other. Finally, in the $d = 25\,\text{mm}$ spheres case in Fig. 6.34(c), the identified trend is reversed: the SH-220 and SH-80 curves lie above the reference, at least in the available experimental data range, with possible effects on the non-available terminal conditions. All together, the trends identified with the analysis of the vertical motion highlighted the influence of phenomena occurring in the transient accelerating phase on the reached terminal conditions. This is the core of the discussion of the next paragraph, where the transversal motion is investigated.

Transversal Motion

In this paragraph, focus is put on the instantaneous transversal loads induced by the flow that act on the falling spheres. Resulting from the asymmetric distribution of vorticity released in the wake, the lift force $\mathbf{L}$ is a very well suited indicator of instability onset, whose effects on the vertical motion were shown in the previous paragraph to be non-negligible. The time history of the lift coefficient:

$$C_L = \frac{L}{\frac{1}{2}\rho_l u_z^2 \pi \left(\frac{d}{2}\right)^2}, \tag{6.45}$$

where $L = |\mathbf{L}|$, was estimated by following the procedure introduced in §2.2.1. In fact, Shew *et al.* (2006), Fernandes *et al.* (2008) showed that the vorticity-dependent loads $\boldsymbol{F}$ and $\boldsymbol{\Gamma}$ in the generalised Kirchhoff equations reported in Eqs. 2.6 can be estimated from the temporal evolutions of the trajectory, velocity and acceleration of the falling sphere. In detail, the frame of reference rotating with the sphere shown in Fig. 6.35 is considered: the 1-direction is parallel to the instantaneous sphere velocity vector, the 2-direction is perpendicular to the 1-direction so that the plane 1-2 is always vertical. The third direction is orthogonal to the 1-2 plane, hence being always horizontal. The forces acting along the 1-direction are therefore the drag magnitude D and the component of the gravity-buoyancy force F_{b1}. Along the 2-direction act the components L_2 and F_{b2} of the lift and gravity-buoyancy forces, respectively. Finally, only the component L_3 of the lift force acts along the 3-direction. In the considered reference system, $\boldsymbol{u} = (u, 0, 0)$ and $\boldsymbol{\Lambda}$ is time independent with a $\frac{1}{2}$ coefficient on the diagonal due to the considered spherical geometry (see e.g. Magnaudet & Eames 2000). The point symmetry of the analysed geometry also simplifies the handling of the rotational degrees of freedom, which reduce to (Shew

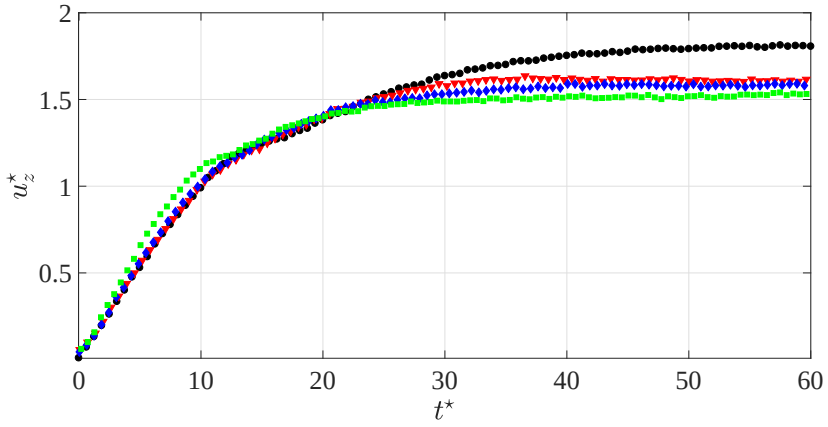

(a)

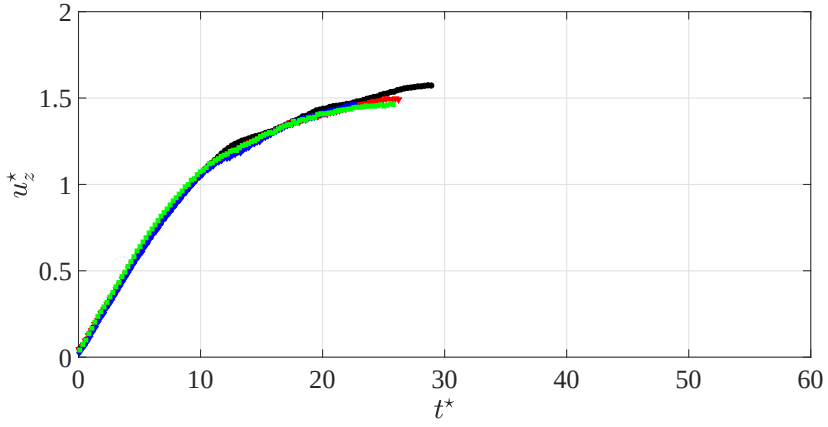

(b)

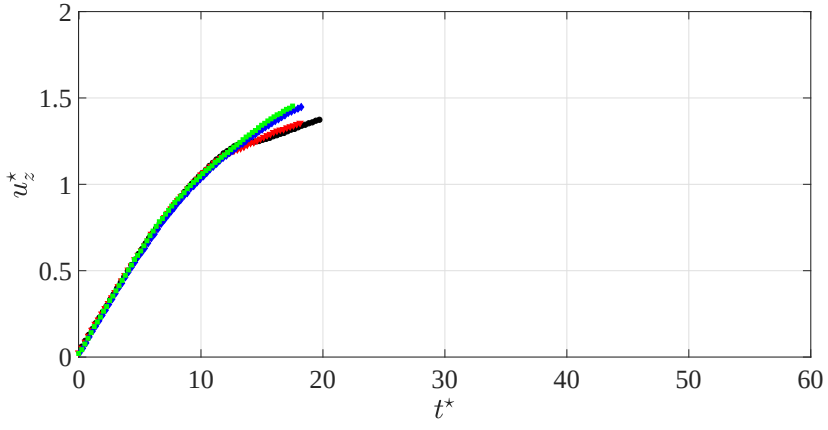

(c)

Figure 6.34 – Instantaneous vertical velocity $u_z^\star$ for all the analysed coatings in pure water. ●, reference. ▼, SH-NAR. ♦, SH-220. ■, SH-80. (a), $d = 5\,\text{mm}$. (b), $d = 15\,\text{mm}$. (c), $d = 25\,\text{mm}$.

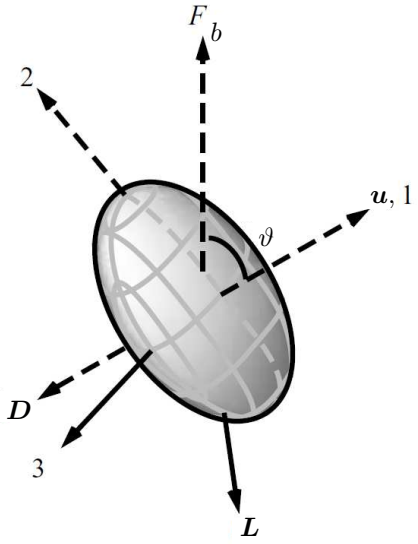

Figure 6.35 – Schematic of the coordinate system $(1, 2, 3)$ considered for the estimation of the hydrodynamic loads acting on the free falling sphere (adapted from Shew *et al.* 2006). $\boldsymbol{u}$, body velocity. ϑ, pitch angle. $\boldsymbol{D}$, drag force. $\boldsymbol{L}$, lift force. $\boldsymbol{F}_b$, gravity-buoyancy force. The vector directions are valid for the rising bubble case studied in Shew *et al.* (2006). The dashed lines lie in the $1-2$ plane.

et al. 2006):

$$\Omega_1 = \frac{d\phi}{dt}\cos\vartheta, \tag{6.46a}$$

$$\Omega_2 = \frac{d\phi}{dt}\sin\vartheta, \tag{6.46b}$$

$$\Omega_3 = -\frac{d\vartheta}{dt}, \tag{6.46c}$$

where ϑ is the pitch angle between $\boldsymbol{u}$ and the vertical direction, and ϕ is the azimuthal angle between the horizontal projection of the 1-direction and a fixed horizontal line. All the above assumptions reduce the problem to the following set of equations:

$$(m + \Lambda_{11})\frac{du}{dt} = D + F_{b1}, \tag{6.47a}$$

$$\Omega_3 (m + \Lambda_{11}) V = L_2 + F_{b2}, \tag{6.47b}$$

$$-\Omega_2 (m + \Lambda_{11}) V = L_3, \tag{6.47c}$$

where $F_{b1} = (\rho_s - \rho_l)\mathcal{V} g \cos\vartheta$ and $F_{b2} = (\rho_s - \rho_l)\mathcal{V} g \sin\vartheta$. The only unknowns in Eqs. 6.47 are the instantaneous drag and lift magnitudes, since from the available 3D sphere motion it is possible to evaluate:

$$\vartheta = \arccos\left(\frac{u_z}{u}\right), \tag{6.48a}$$

$$\frac{d\phi}{dt} = \frac{u_x \frac{du_y}{dt} - u_y \frac{du_x}{dt}}{u_{tr}^2}, \tag{6.48b}$$

where the Cartesian coordinate system (x, y, z) was introduced in Fig. 4.1 and u_{tr} is the transversal velocity. The knowledge of the instantaneous evolution of the velocity vector therefore enables the calculation of the time evolution of the forces acting on the falling sphere. Notice that Eqs. 6.47 predict a purely vertical falling when a zero lift force acts on the sphere, in agreement with the findings that link the transversal motion with the wake instabilities (see e.g. Mougin & Magnaudet 2002*a*). In that case, Eqs. 6.47 reduce to Eq. 4.3.

The C_L evolution calculated from the experimental data for $d = 5\,\text{mm}$ ($\mathcal{W}e_D \approx 20$) and $d = 20\,\text{mm}$ ($\mathcal{W}e_D \approx 360$) spheres is shown in Fig. 6.36. The shaded rectangles indicate the region at the early stage of motion where the signal-to-noise ratio is too low for the lift force estimation to be reliable. In practice, the difficulty is well explained by an examination of Eqs. 6.46 and 6.48, since at the very beginning of the drop $\boldsymbol{u}$ is approximately aligned with the vertical direction, resulting into a poor estimation of derivatives and angles. For the same reason, the discussion of the transversal motion in the intermediate Re_∞ regime was based on $u^\star_{tr}$, without showing the corresponding hydrodynamic loads. In fact, a too weak transversal motion resulted into a less significant C_L analysis. At the beginning of the motion C_L is almost zero, meaning that the wake is axisymmetric and accordingly the trajectory is approximately vertical. Then, C_L suddenly increases as a result of the loss of axisymmetry of the wake, which originates from instabilities arising in the wake (Magnaudet & Eames 2000; Horowitz & Williamson 2010*b*). These instabilities promote path unsteadiness, together with the departure of the vertical velocity data from the predicted curve discussed in the previous paragraph. However, in Fig. 6.36(a) the amplitude of path excursions is moderate (see e.g. the axes scales in Fig. 4.7) due to lift fluctuation damping caused by the high ζ values considered in this section. Once lift fluctuations vanish, C_L remains almost constant, which implies the sphere to follow an oblique trajectory. Note that for the $d = 20\,\text{mm}$ spheres in Fig. 6.36(b) the discussed limitation on the tank height comes into play, hindering the attainment of lift steady state. Nevertheless, the wake transition as well as the damping of the lift fluctuation after the peak are clearly visible.

The analysis of the transient region in Fig. 6.36 allows for the definition of a characteristic time τ at which the wake instability occurs, in conformity with the critical conditions estimation performed in the intermediate Re_∞ case in §6.2.1. In practice, τ is estimated as the time where the condition $C_L = 0.05$ is first met. This threshold value was chosen in order to assure the detection of the instability to be above the experimental uncertainties of the lift coefficient (an indication of the magnitude of the uncertainties is reported in the inserts in Fig. 6.36). The relative behaviour of SH coatings with respect to the reference can be quantified via:

$$\Delta\tau = 1 - \frac{\tau_{SH}}{\tau_{NC}}, \tag{6.49}$$

whose evolution is displayed in Fig. 6.37 with respect to the dimensionless roughness $\frac{\lambda}{d}$ for different sphere diameters. It appears that the data are well fitted by the linear relationship:

$$\Delta\tau \approx \alpha_\tau \frac{\lambda}{d}, \tag{6.50}$$

where α_τ represents the slope of the law. The positive $\Delta\tau$ values indicate that the SH coatings trigger the wake instability earlier than the reference spheres. These findings agree with the results of Jenny *et al.* (2004), Fernandes *et al.* (2007) who reported earlier transition of asymmetric bodies, since the χ variation due to the deformed air layer determines a modification of the falling sphere sphericity.

A best fit in the least-mean squares sense of experimental data in Fig. 6.37 allowed for the evaluation of the slope α_τ in Eq. 6.50 for each analysed d. The corresponding evolution as a function of $\mathcal{W}e_D$ reported in Fig. 6.38 shows that, in the range analysed in this section:

$$\alpha_\tau \sim \mathcal{W}e_D^m, \tag{6.51}$$

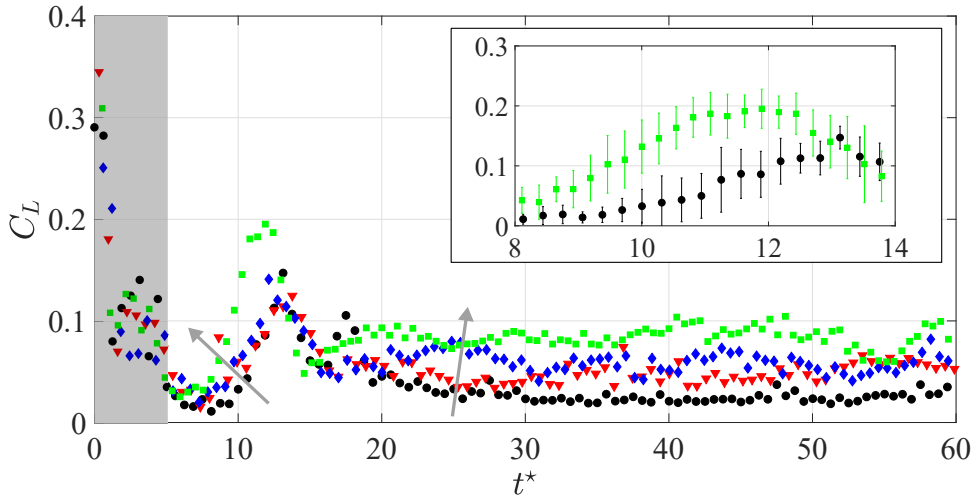

(a)

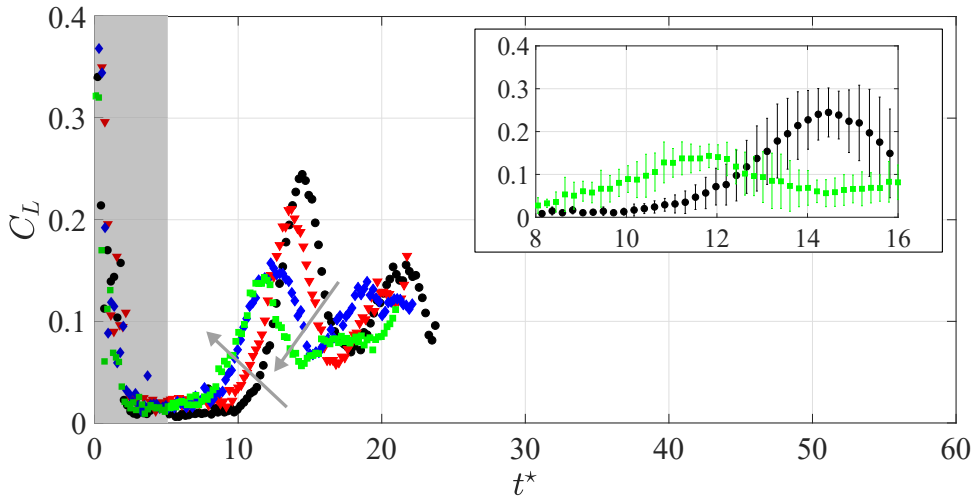

(b)

Figure 6.36 – Time evolution of the lift coefficient C_L for all the analysed coatings in pure water. (a), $d = 5\,\text{mm}$. (b), $d = 20\,\text{mm}$. ●, reference. ▼, SH-NAR. ♦, SH-220. ■, SH-80. For the sake of clarity, one point out of two is reported. The grey arrows indicate increasing $\frac{\lambda}{d}$. The shaded regions identify the portion of drop where lift estimation is corrupted by low signal-to-noise ratio. The two inserts show the errorbars (95% confidence level) in the wake instability occurrence region.

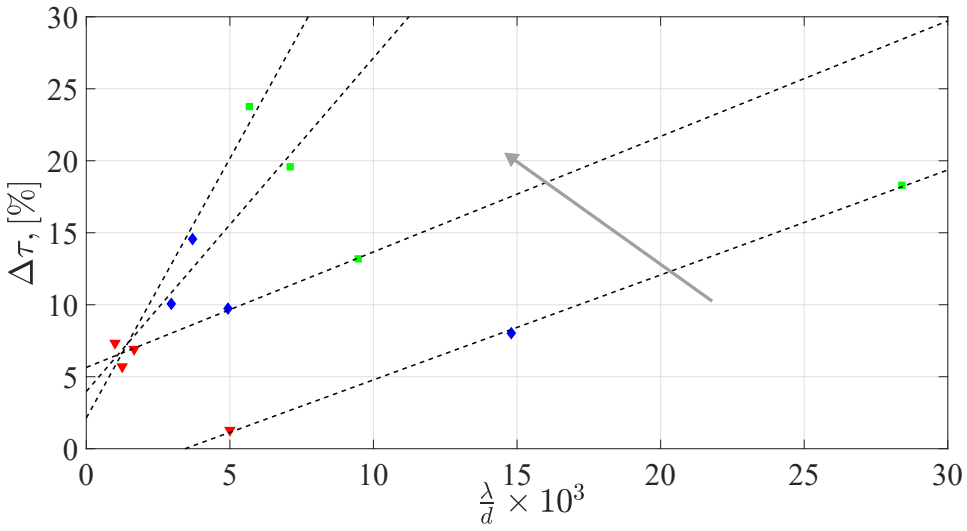

Figure 6.37 – Influence of the surface properties on the characteristic time τ at which wake instabilities occur (see Eq. 6.49 for the $\Delta\tau$ definition). ▼, SH-NAR. ♦, SH-220. ■, SH-80. (- - -), best fit of Eq. 6.50 in the least-mean squares sense. The grey arrow indicates increasing $\mathcal{W}e_D$. For the sake of readability, only results for $d = 5$, 15, 20 and 25 mm are reported.

where the exponent m of the power law abruptly changes around a critical Weber number $\mathcal{W}e_{cr}$. In detail, the following quantitative relations well describe the experimental data:

$$\begin{cases} \alpha_\tau = \widetilde{\alpha}_\tau & \text{if} \quad \mathcal{W}e_D < \mathcal{W}e_{cr} \\ \alpha_\tau = \widetilde{\alpha}_\tau \left(B \frac{\mathcal{W}e_D}{\mathcal{W}e_{cr}} - 1 \right) & \text{if} \quad \mathcal{W}e_D \geq \mathcal{W}e_{cr} \end{cases} \tag{6.52}$$

where $\mathcal{W}e_{cr} \approx 190$ and the constants $\widetilde{\alpha}_\tau \approx 7.7$ and $B \approx 2$.

The detected scaling law as a function of $\mathcal{W}e_D$ can thus explain the SH coatings influence on the onset of instabilities previously highlighted via Fig. 6.36. In fact, the change in α_τ observed at $\mathcal{W}e_{cr}$ coincides with a significant modification of the magnitude of both the lift fluctuations during the transient phase and the lift force in the steady regime. For $\mathcal{W}e_D < \mathcal{W}e_{cr}$ (see Fig. 6.36(a)), SH coatings tend to increase lift, especially in the steady state regime. Conversely, for $\mathcal{W}e_D \geq \mathcal{W}e_{cr}$ (see Fig. 6.36(b)), the lift amplitude is reduced. Since the lift force is intimately related to the intensity of vorticity around the body, these findings suggest that the high interface distortion which is achieved on average when $\mathcal{W}e_D < \mathcal{W}e_{cr}$ leads to an increase of the amount of vorticity released in the wake. On the contrary, the production of vorticity seems to be mitigated when the condition $\mathcal{W}e_D \geq \mathcal{W}e_{cr}$ is met, which would imply that the ideal expression in Eq. 6.36 is assessed (in agreement with $\chi \to 1$).

All together, the presented results on the vertical and transversal motion evidenced an influence of SH coatings on both transient and terminal phases of the drop. Therefore, the next paragraph is dedicated to the analysis of the classical parameter studied in available literature to evaluate the SH coatings effectiveness, that is terminal drag.

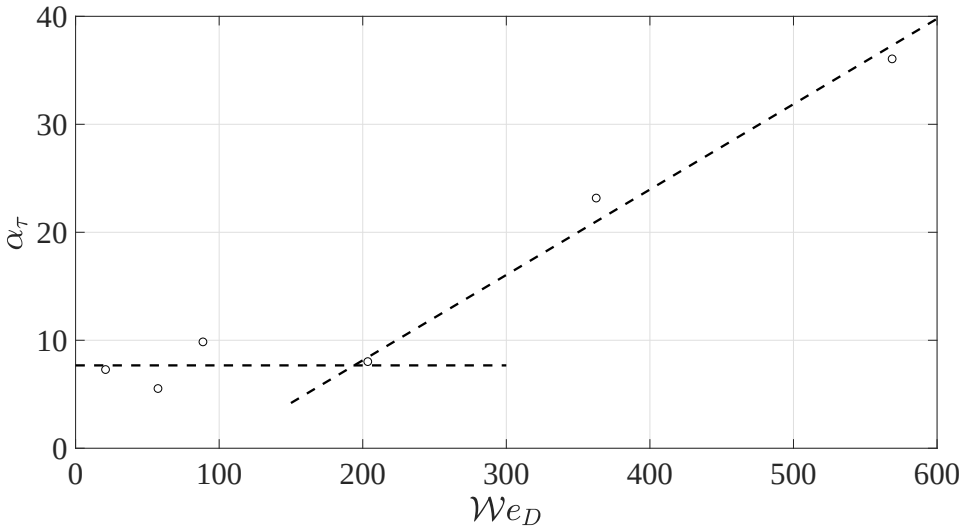

Figure 6.38 – Evolution of the slope α_τ in Eq. 6.50 with respect to We_D. ∘, experimental data. (- - -), best fit of Eqs. 6.52 in the least-mean squares sense.

Terminal Conditions

The evolution of the terminal drag coefficient $C_{D\infty}$ as a function of the terminal Reynolds number Re_∞ is shown in Fig. 6.39. As discussed in the paragraph dealing with the vertical motion, a d increase determined a decrease of available experimental data in the terminal region of the drop. The issue was overcome by estimating the $u^\star_\infty$ values via the exponential fitting technique described by Eq. 4.6. The values presented in Fig. 6.39 must therefore be viewed with caution, keeping in mind the magnitude of the $u^\star_\infty$ estimation error presented in Tab. 6.4. For assessment purposes, data obtained by Lapple & Sheperd (1940), Horowitz & Williamson (2010*a*) (for spheres falling rectilinearly) as well as those estimated from the results provided by Ahmmed *et al.* (2016), McHale *et al.* (2009) for smooth and SH spheres have also been reported in Fig. 6.39.

As far as reference NC spheres are concerned, a fairly good agreement between the measurements and the data reported in previous studies is observed over the overlapping Re_∞ range, with the exception of the work of McHale *et al.* (2009), which will be interpreted later. Beyond $Re_\infty \approx 3 \times 10^4$, the experimental data deviate slightly from those of Lapple & Sheperd (1940), which may be due to the increasing incertitude of the exponential fitting procedure.

For what concerns SH coatings, a sizeable influence on $C_{D\infty}$ of both interface deformation (i.e. We_D) and slip (i.e. $\frac{\lambda}{d}$) is noted. The ΔC_D evolution for the smallest sphere (i.e. $d = 5\,\text{mm}$) is shown in Fig. 6.40 as a function of the surface roughness. For comparison, the drag change reported by Ahmmed *et al.* (2016) at a comparable Re_∞ is also displayed. An excellent agreement is found between data of this study and those of Ahmmed *et al.* (2016), whose SH spheres are characterised by a nano-sized surface roughness. The experimental data trend in Fig. 6.40 suggests that the drag change can be well approximated by the following law:

$$\Delta C_D = \alpha_D \frac{\lambda}{d} + \Delta C_{D,0}, \tag{6.53}$$

where $\Delta C_{D,0}$ represents the drag change extrapolated at virtually zero surface roughness and

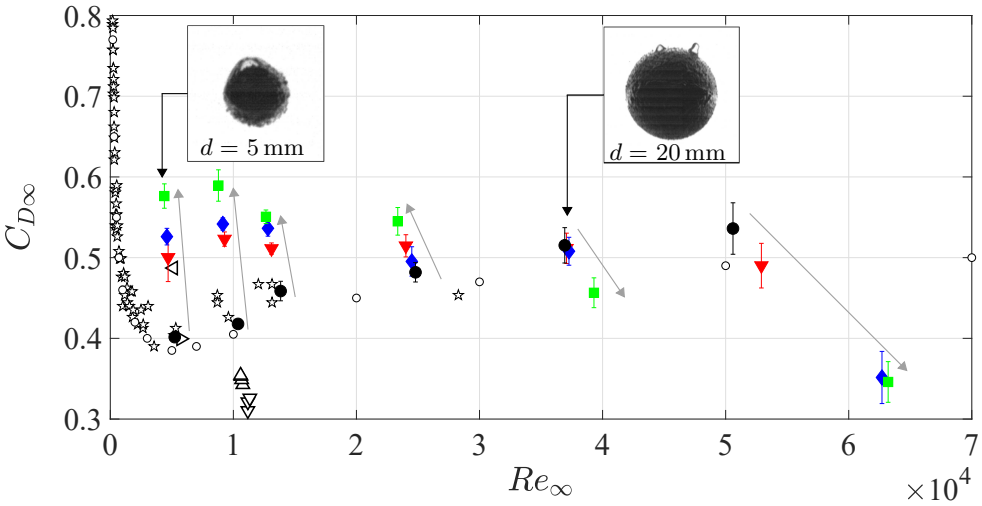

Figure 6.39 – Terminal drag coefficient $C_{D\infty}$ as a function of terminal Reynolds number Re_∞ for all the investigated spheres in pure water. ●, reference. ▼, SH-NAR. ♦, SH-220. ■, SH-80. ☆, spheres falling rectilinearly (Horowitz & Williamson 2010*a*). ▷, reference sphere (Ahmmed *et al.* 2016). ◁, SH sphere (Ahmmed *et al.* 2016). △, $d = 25\,\mathrm{mm}$ reference spheres (McHale *et al.* 2009). ▽, $d = 25\,\mathrm{mm}$ SH spheres with air plastron (McHale *et al.* 2009). ○, experimental data from Lapple & Sheperd (1940). The error bars represent the 95 % confidence level. The grey arrows indicate increasing surface roughness thickness. The inserts sampled from the sequences in Figs. 6.26 and 6.27 show the qualitative modification of the air layer deformation.

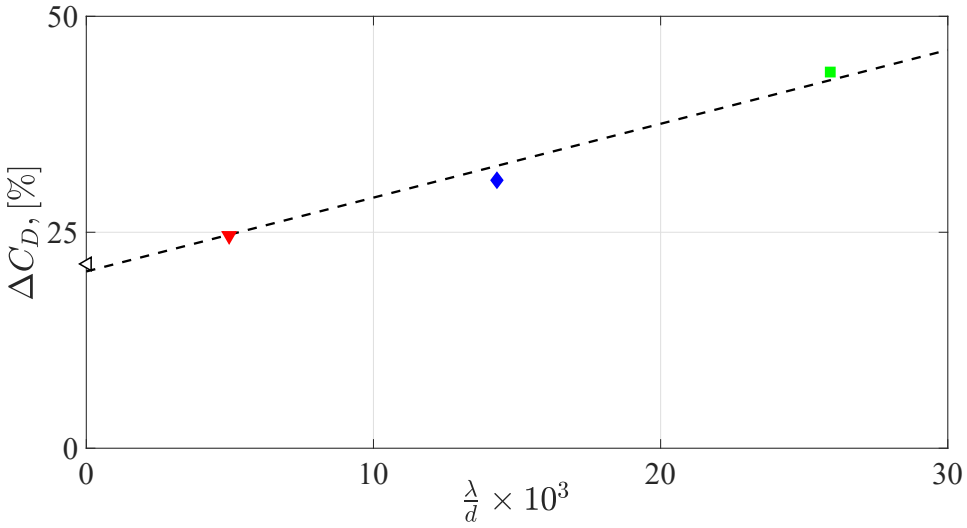

Figure 6.40 – Terminal drag coefficient variation with respect to the reference sphere as a function of the non-dimensional roughness, for $d = 5\,\mathrm{mm}$ spheres in pure water. ▼, SH-NAR. ♦, SH-220. ■, SH-80. ◁, SH sphere (Ahmmed *et al.* 2016). (- - -), best fit according to Eq. 6.53 in the least-mean squares sense.

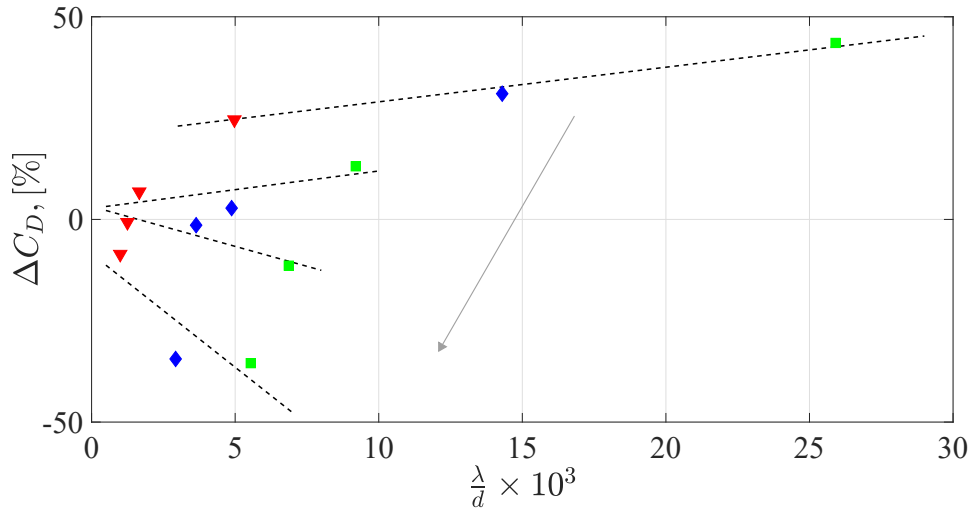

Figure 6.41 – Terminal drag coefficient variation with respect to the reference sphere as a function of the non-dimensional roughness. ▼, SH-NAR. ♦, SH-220. ■, SH-80. (- - -), best fit of Eq. 6.53 in the least-mean squares sense. The grey arrow indicates increasing $\mathcal{W}e_D$. For the sake of readability, only results for $d = 5$, 15, 20 and 25 mm are reported.

α_D indicates the drag rate of change.

As evidenced in Fig. 6.41, this linear trend applies also to the other tested sphere diameters. Drag increase with respect to the reference by up to + 45 % is found for the smallest spheres (low $\mathcal{W}e_D$), whereas a significant drag reduction down to − 35 % is noticed for the largest spheres (high $\mathcal{W}e_D$). The indicated values are therefore much larger than the estimated uncertainties on the $u^\star_\infty$ estimation reported in Tab. 6.4.

This trend reversal is exalted by Fig. 6.42, where the α_D evolution as a function of $\mathcal{W}e_D$ normalised by the critical value $\mathcal{W}e_{cr}$ is shown. Following the approach developed for α_τ, a scaling law of the type:

$$\alpha_D \sim \mathcal{W}e_D^n, \tag{6.54}$$

is found. Similarly to α_τ, an abrupt change of trend is clearly visible at $\mathcal{W}e_{cr}$ such that the experimental data can be well described by:

$$\begin{cases} \alpha_D = \widetilde{\alpha}_D & \text{if} \quad \mathcal{W}e_D < \mathcal{W}e_{cr} \\ \alpha_D = C - E\frac{\mathcal{W}e_D}{\mathcal{W}e_{cr}} & \text{if} \quad \mathcal{W}e_D \geq \mathcal{W}e_{cr} \end{cases} \tag{6.55}$$

with the constants $\widetilde{\alpha}_D \approx 0.9$, $C \approx 4.5$ and $E \approx 3.4$. For $\mathcal{W}e_D < \mathcal{W}e_{cr}$, α_D is roughly constant and positive meaning that drag increases with increasing plastron thickness. Conversely, for $\mathcal{W}e_D > \mathcal{W}e_{cr}$, α_D becomes negative which yields the drag reduction observed in Fig. 6.39.

The drag changes experimentally observed encompass the different trends reported in previous works (McHale *et al.* 2009; Ahmmed *et al.* 2016). In fact, the evidenced plastron deformation might provide an attractive way to explain the available results within an unified framework. Indeed, according to the $\mathcal{W}e_D$ expression in Eq. 6.22, the Weber number characterising the studies of McHale *et al.* (2009), Ahmmed *et al.* (2016) is about 20, which is comparable to the smallest value reached with the $d = 5$ mm spheres in pure water. Based on the results presented in this section, a drag increase would be expected, which is not reported by McHale

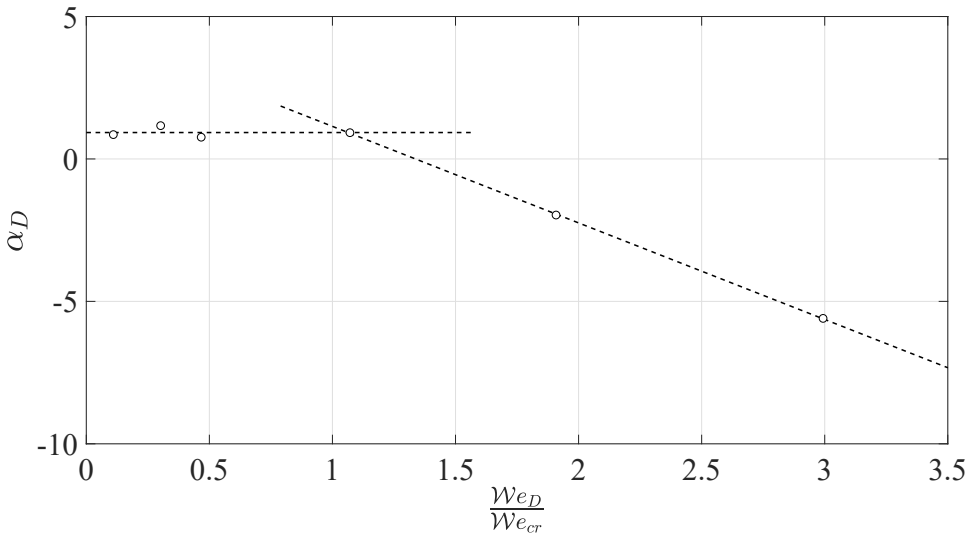

Figure 6.42 – Evolution of the slope α_D in Eq. 6.53 with respect to the normalised Weber number $\frac{\mathcal{W}e_D}{\mathcal{W}e_{cr}}$. ∘, experimental data. (- - -), best fit of Eqs. 6.55 in the least-mean squares sense.

et al. (2009) (see the corresponding points in Fig. 6.39). This illustrates that a comprehensive relationship between $\mathcal{W}e_D$ and χ needs to be properly established. In fact, a possible explanation of these apparently discordant results arises by further developing Eq. 6.44. To this end, Eq. 6.22 injected into Eq. 6.43 yields:

$$\chi = 1 + \sqrt{\frac{\rho_l(\zeta - 1)g\ell^2}{\gamma}}\mathcal{W}e_D^{-1/2}. \tag{6.56}$$

The strength of this expression lies in the ability to take into account the influence of ζ, whose values are approximately 2.2 in the work of Ahmmed *et al.* (2016) (PTFE spheres) and 1.2 in the study of McHale *et al.* (2009) (acrylic spheres). Based on the assumption that the magnitude ℓ of the air layer protrusions is comparable to that observed in this work for pure water tests (no information is provided in the cited works), the χ evolution according to Eq. 6.56 is shown in Fig. 6.43. A critical aspect ratio $\chi_{cr} \approx 1.1$ can be introduced, corresponding to the critical Weber number $\mathcal{W}e_{cr} \approx 190$ identified in Fig. 6.38. The overall discussion performed in this section shows that highly deformed plastron, i.e. $\chi > \chi_{cr}$, yields drag increase, whereas a plastron almost spherical in average, i.e. $\chi < \chi_{cr}$, results into drag mitigation. Focusing the attention on the $\mathcal{W}e_D \approx 20$ region, it appears clearly that the aspect ratio featuring the study of McHale *et al.* (2009) lies below χ_{cr}. This perfectly agrees with the drag reduction these authors reported. Conversely, drag increase observed in this study and in the work of Ahmmed *et al.* (2016) falls within the region of highly deformed plastron, i.e. $\chi > \chi_{cr}$. All together, these results clearly emphasise that, under the investigated operating conditions, the plastron compliance plays a key role in the performance of SH surfaces.

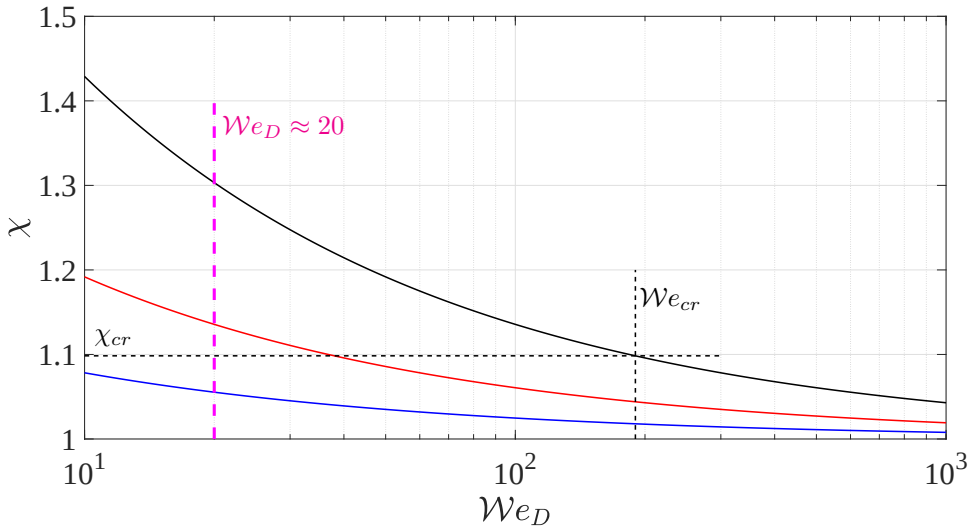

Figure 6.43 – Variation of the aspect ratio χ as a function of We_D according to Eq. 6.56. (——), $\zeta \approx 7$ experimental value of the spheres produced in this work in pure water. (——), $\zeta \approx 2.2$ by Ahmmed *et al.* (2016). (——), $\zeta \approx 1.2$ by McHale *et al.* (2009). (- - -), indication of the critical Weber number $We_{cr} \approx 190$ and of the corresponding critical aspect ratio $\chi_{cr} \approx 1.1$. (- - -), indication of the Weber number $We_D \approx 20$ where the three studies can be compared.

6.4 Discussion

To resume, the experimental results at low, intermediate and high Re_∞ presented in this chapter evidenced the strong influence of SH coatings on the dynamics of free falling spheres once regimes characterised by a non-symmetric wake behind the body are considered. It can thus be speculated, exploiting the qualitative plastron visualisations shown in Figs. 6.18, 6.26 and 6.27, that a strong connection between the wake and the air layer dynamics exists. This raises the issue of a possible feedback of the plastron motion and deformation on the flow. The evidenced plastron deformation shares some properties, at least qualitatively, with freely rising bubbles (Ellingsen & Risso 2001). Basically, the main difference is that bubbles adapt their entire shape to the flow whereas in this work only a thin layer is compliant. This is the reason why the maximum χ values observed in §6.3.1 (≈ 1.2) are much lower compared to those of fully deformable bodies (Mougin & Magnaudet 2002*b*). Nevertheless, it is reasonable to assume that the physical mechanisms driving the body-flow interaction are comparable, at least qualitatively.

Therefore, a schematic representation of this interaction is proposed in Fig. 6.44. The starting point of the feedback loop is the magnitude of the hydrodynamic perturbation represented by the wake developing behind the falling sphere, which is described by the attained Reynolds number range. The latter can be evaluated as Re_∞ when an estimation of u_∞ is available, or as Re_{cr} if a technique to estimate critical conditions in implemented as in §6.2.1. When the perturbation magnitude is too weak, negligible SH effects were detected, as in §6.1 in glycerine tests or in §6.2 in water-glycerine tests before the occurrence of wake transitions. When the perturbation magnitude is large enough, the receptivity of the air layer must be investigated. In this chapter, the Weber number was shown to be the most convenient non-dimensional number to describe this property, indicating the relative magnitude between destabilising dynamic pressure

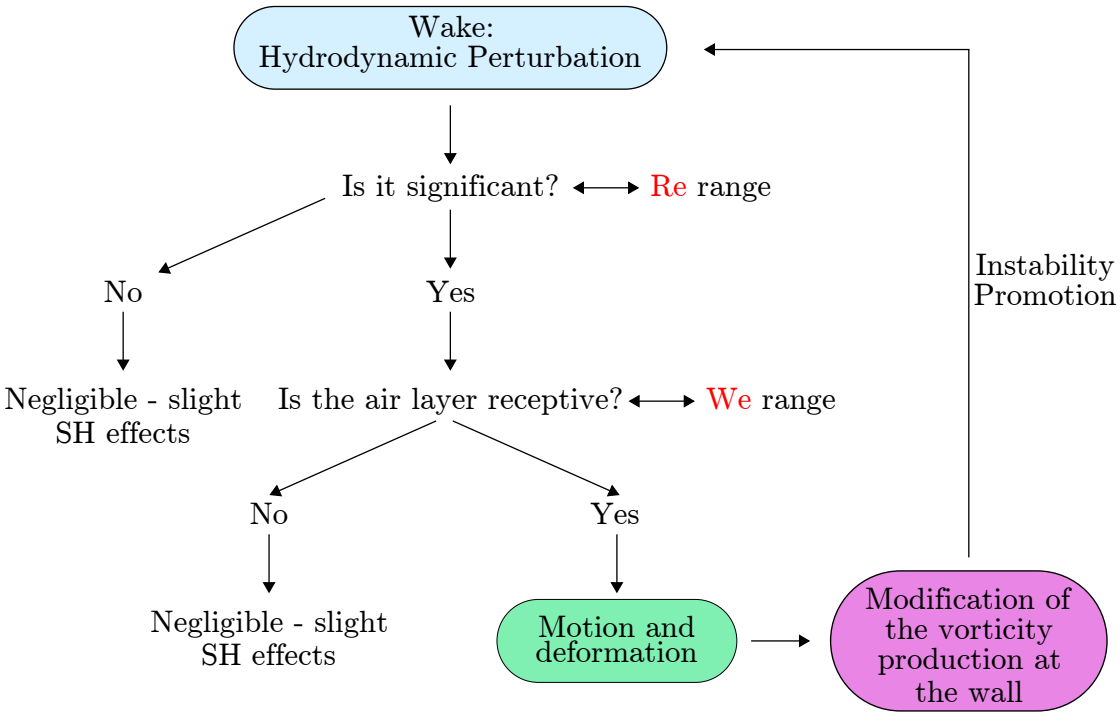

Figure 6.44 – Possible driving mechanism of the air layer compliance to the flow on SH spheres. The red color identifies the two parameters controlling the feedback loop, the Reynolds number Re and the Weber number We, whose defining quantities have been discussed along the chapter.

and stabilising capillary pressure. The choice of a microscopic (i.e. λ) or macroscopic (i.e. d) length scale was based on the detected size of the deformed air pockets. In the water-glycerine tests, the perturbed air layer resulted in deformed pockets whose size $\sim \lambda$. The corresponding $\mathcal{W}e_\lambda$ was shown to be able to discriminate between low and high air layer receptivity, explaining the different $u^\star_{tr}$ trends. For much larger hydrodynamic perturbation in pure water tests, $\mathcal{W}e_D$ was shown to be able to explain the identified trends for increasing sphere macroscopic dimension d. Overall, the large air layer receptivity resulted into the motion and deformation of the plastron in the rear-side of the falling sphere, which could imply a modification of the boundary condition at the sphere wall, possibly leading to a significant variation of the vorticity production at the body surface and accordingly of the intensity of vorticity evacuated in the wake (see e.g. Mougin & Magnaudet 2002*b*; Legendre *et al.* 2009). Therefore, a feedback effect on the wake characteristics is guessed, which in this study led to an instability promotion. Since the hydrodynamic loads experienced by the falling sphere are intimately connected to both pressure and vorticity distributions, the proposed air layer compliance mechanism perfectly integrates with the identified loads modifications due to SH coatings discussed in §6.3.2. Significant effects on the mechanism of noise generation by the interaction between body and flow may thus exist, as was briefly introduced in Chapter 1.

Chapter 7

Numerical Approach

7.1 Introduction

One of the main outputs of the experimental results discussed in Chapter 6 is the influence of the behaviour of the air layer initially trapped among the roughness elements of the SH coatings on the hydrodynamic performance of free falling spheres. In detail, the interconnection between the flow around the falling sphere and the deformation of the air plastron was proposed in the schematic in Fig. 6.44. To resume, the wake developing behind the falling sphere could be interpreted as a hydrodynamic perturbation directly influencing the state of the air layer. In fact, the unsteady pressure gradient induced by the massive separation around the falling sphere could promote the deformation of the air-liquid interface and the motion of air pockets on the wall. The subsequent modification of the vorticity production at the wall could thus influence the magnitude of the vorticity evacuated by the wake, with a possible impact on the wake nature itself and therefore on the pressure distribution around the sphere. Obviously, such a kind of feedback loop seems to be governed by near-wall phenomena. Preliminary attempts to investigate the latter were performed via the execution of high-magnification visualisations. However, experimental limitations such as the compromise between spatial resolution and sufficient number of available images prevent a complete description of the detected phenomena. The numerical approach could thus alleviate the identified limitations, possibly adding information on the studied problematic. This is the perspective that led to the development of the numerical method discussed in this chapter.

Two approaches could be followed to numerically reproduce the SH coatings behaviour. First, a full description of the SH coating texture and air layer could be performed. This approach implies the simulation of a multiphase flow, with an instantaneous tracking of the air-liquid interface which should be coupled with the surrounding flow pressure field. Such a scenario is well suited for numerical works focused on the microscopic problem describing the behaviour of the air-liquid interface in a single surface roughness element (see e.g. Alinovi 2018, Chapter 3), whereas becomes more demanding when the interest is put on the description of a macroscopic SH wall, as in the present work. This is due to the fact that the simultaneous resolution of all the involved scales should be performed, from the microscopic roughness element length scales up to the macroscopic geometry dimensions. Some Direct Numerical Simulations (DNS) on a turbulent channel flow with a resolution of the SH coating texture and a coupling of the air-liquid interface deformation with the instantaneous pressure field recently appeared (see e.g. Cartagena *et al.* 2018), but were generally limited to Re and We ranges achievable in real-life experiments only with micron-sized devices.

However, the overall observation of the described SH coating modelling techniques suggests a possible path to be followed in order to take into account the significant effect of the air layer deformation without the need to perform a fully-resolved DNS over a SH macroscopic wall. The main steps can be resumed as follows:

1. a simulation over a reference no-slip flat wall could be run under the desired operating conditions, thus providing information on the local instantaneous pressure field;

2. the latter could be injected into a Young-Laplace type equation, which connects the local pressure variation across the air-liquid interface Δp_{LA} to its deformation. A linearised form of the cited equation, valid under the assumption of limited interface deformation with respect to the geometry scales (Seo *et al.* 2018; Picella 2019) can be written as:

$$\nabla^2 \eta \approx \frac{\Delta p_{LA}}{\gamma}, \tag{7.1}$$

where γ represents the surface tension, in agreement with the nomenclature introduced in the previous chapters. When large enough interface deformation is achieved, non-linear terms on the left-hand side of Eq. 7.1 should be taken into account (Seo *et al.* 2018). However, the physical importance of Eq. 7.1 lies in the estimation of the interface deformation when the latter is subjected to the calculated pressure field;

3. the effect of the interface deformation should then be coupled with the beneficial slippage effect due to the interaction of the air layer with the flow. To do that, a macroscopic approach based on the concept of the slip length ℓ_{sl} over a homogeneous wall can be implemented. This implies modelling the lubricating effect of SH coatings due to presence of the air layer via the boundary condition originally introduced by Navier (1823) and later developed by Maxwell (1879), which connects the tangential component of the velocity at the wall (the so-called slip velocity u_{sl}) to the local shear rate, via ℓ_{sl}. The real SH textured surface is thus modelled via a fictitious equivalent smooth surface where the non-penetration and partial slip boundary conditions are imposed (Legendre *et al.* 2009):

$$\mathbf{n} \cdot \mathbf{u} = 0, \tag{7.2a}$$

$$\mathbf{n} \times \mathbf{u} = 2\ell_{sl} \mathbf{n} \times (\mathbf{S} \cdot \mathbf{n}), \tag{7.2b}$$

where $\mathbf{n}$ is the local normal to the surface and $\mathbf{S} = \frac{1}{2}\left(\nabla \mathbf{u} + (\nabla \mathbf{u})^T\right)$ indicates the rate of strain tensor ($(\cdot)^T$ being the transpose operation). A zero slip length thus allows to retrieve the reference non-penetration, no-slip boundary condition. Referring to the scheme in Fig. 7.1, the expression in Eq. 7.2(b) can be simply re-written as:

$$\mathbf{u}_{sl} = \ell_{sl} \left.\frac{\partial \mathbf{u}}{\partial \mathbf{n}}\right|_w, \tag{7.3}$$

which shows that ℓ_{sl} corresponds to the length between the smooth wall edge and the point where the extrapolated velocity profile reaches the zero value. Therefore, ℓ_{sl} can be interpreted as the virtual distance below the surface where the no-slip condition would be satisfied (Lauga *et al.* 2007). In the general case of a curved surface where all the terms composing the $\mathbf{S}$ tensor should be considered, Einzel *et al.* (1990) demonstrated that the general expression in Eq. 7.2(b) could still be reduced to the form in Eq. 7.3 considering the contribution of the surface curvature on ℓ_{sl};

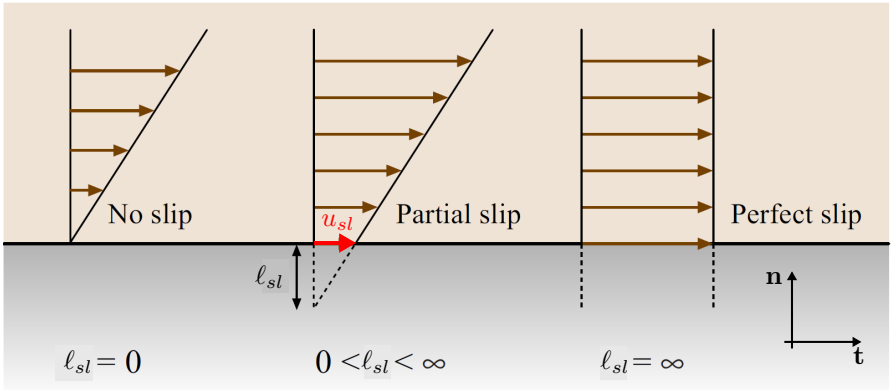

Figure 7.1 – Schematic of the boundary condition at the wall (adapted from Lauga *et al.* 2007), where **n** and **t** indicate the normal and tangential directions, respectively. From left to right: no slip model with a zero tangential velocity component at the wall, partial slip model where a slip velocity u_{sl} at the wall along **t** is connected to the wall shear stress via the slip length ℓ_{sl}, perfect slip as the limit case of infinite slip length.

4. considering a flow in a macroscopic geometry with characteristic size L and at Reynolds number Re, the coupled analysis of deformation and slip effects should ideally lead to a model of an effective slip length ℓ_{sl}^{eff}, which can be written as:

$$\ell_{sl}^{eff} = f\left(\frac{\ell_{sl}}{L}, \frac{\eta}{L}, Re, 3D - 2D, ...\right). \tag{7.4}$$

Ideally, the model in Eq. 7.4 could automatically take into account all the phenomena that influence the actual slip at the wall with respect to the imposed value ℓ_{sl}, e.g. Reynolds number range, deformation magnitude, three-dimensional or two-dimensional configurations, surfactants concentration Γ if taken into account (see e.g. §D.2). As a result, the flow over a SH surface could be analysed via a simulation over a macroscopically homogeneous wall where a partial slip condition is imposed via the use of the identified ℓ_{sl}^{eff} value.

The effective slip length model thus represents the main objective of the implementation of such a logical path. The following of the chapter describes the implemented numerical approach, which can be viewed as a first simplified step in the proposed analysis direction. For this reason, the next section is dedicated to the description of the analysed problem.

A part of these results was presented in a preliminary form at the *European Drag Reduction and Flow Control Meeting 2019* (Castagna *et al.* 2019*a*).

7.2 Problem Statement

The starting point of the numerical approach is an analogy with the results of the falling sphere experiments discussed in Chapter 6. The schematic in Fig. 7.2 compares the characteristic dimensions which can be identified in the case of a deformed air plastron in the rear-side of the falling SH sphere with an imposed fixed wall deformation described by:

$$y_w = \delta \cos\left(\frac{2\pi x}{\Lambda}\right), \tag{7.5}$$

	d, [mm]					
	5	8	10	15	20	25
$\frac{w}{d}$	1.00	0.86	0.77	0.54	0.1	0.08
$\frac{\ell}{d}$	0.30	0.20	0.15	0.10	0.08	0.06

Table 7.1 – Ranges of the non-dimensional ratios between the characteristic sizes of the deformed air layer in the falling sphere experimental tests (see definition in Fig. 7.2).

	FW	LD	ID	HD
$\frac{\delta}{h}$	0	0.050	0.075	0.100
$\frac{\Lambda}{h}$	1			
Re_m	$1-750$			
ℓ_{sl}, [µm]	$0-100$			
$\frac{\ell_{sl}}{h}$	$0-0.01$			

Table 7.2 – Ranges of the parameters investigated in the numerical simulations. The wavelength Λ and wave amplitude δ of the lower wall of a channel of mean height h were introduced in Eq. 7.5. Re_m represents the Reynolds number based on the maximum velocity in the channel. The slip length ℓ_{sl} range is reported both in dimensional and non-dimensional form.

where δ is the wave amplitude and Λ the wavelength. The air pocket height ℓ and width w can thus be compared to the deformed wall amplitude δ and wavelength Λ, respectively. Moreover, in order to dispose of a macroscopic reference length, the sinusoidal surface described by Eq. 7.5 is considered as the lower wall of a channel with height h (see Fig. 7.3, where the Cartesian coordinate system $(\mathbf{e}_x, \mathbf{e}_y, \mathbf{e}_z)$ is introduced). The latter is measured between the lower wall mean height and the channel upper wall, which is flat. The channel height h can thus be compared to the sphere macroscopic dimension d, i.e. its diameter. As shown in Fig. 7.3, the wave is considered uniform in the spanwise direction $\mathbf{e}_z$ and fixed in time.

Interestingly, an estimation of the air layer deformation characteristic sizes from the images presented in Chapter 6 allows to define the variation range of each non-dimensional length, as reported in Tab. 7.1. The ratio $\frac{w}{d}$ is shown to vary in the range $0.08 - 1.00$ for decreasing d, whereas $\frac{\ell}{d}$ lies in the range $0.06 - 0.30$. Since the analysis of all the possible combinations was not feasible, a choice on the analysed geometry properties, i.e. the corresponding $\frac{\delta}{h}$ and $\frac{\Lambda}{h}$ ratios, had to be performed. The numerically investigated values are resumed in Tab. 7.2. In order to fix some of the parameters possibly influencing the effective slip length in Eq. 7.4, the ratio $\frac{\Lambda}{h}$ was set equal to the unitary value, implying a wavelength of the lower wavy wall equal to the channel height. Moreover, the range $0 - 0.10$ was selected for the non-dimensional ratio $\frac{\delta}{h}$. The value $\frac{\delta}{h} = 0$ was representative of the reference flat wall (indicated hereinafter as FW). A low deformation (LD) case is considered with $\frac{\delta}{h} = 0.05$, which is the typical value taken into account in experimental and numerical studies over wavy walls (Hudson *et al.* 1996; Cherukat *et al.* 1998) and in works analysing heat exchangers (see e.g. Errico & Stalio 2015). A high deformation (HD) with $\frac{\delta}{h} = 0.10$, twice the LD value, was considered as the upper limit. Finally, an intermediate deformation (ID) with $\frac{\delta}{h} = 0.075$ was investigated.

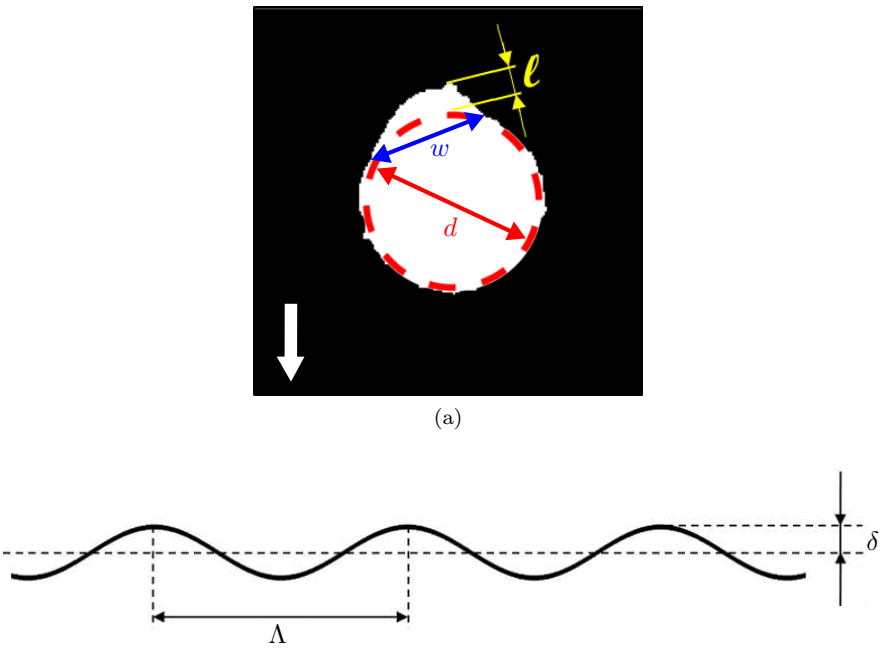

(a)

(b)

Figure 7.2 – Analogy between the characteristic dimensions of: (a), the deformed air layer in the rear-side of a falling SH sphere (the white arrow indicates the direction of gravity) and (b), a fixed wall deformation (see Eq. 7.5). The air pocket height ℓ (in yellow color in the image) and width w correspond to the sinusoidal wall deformation amplitude δ and wavelength Λ, respectively. The macroscopic sphere size d corresponds to the channel height h.

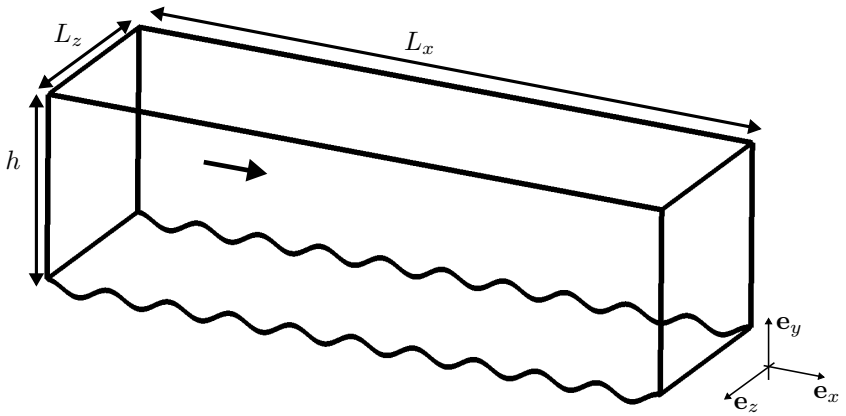

Figure 7.3 – Schematic of the channel flow computational domain. A Cartesian coordinate system is considered, where $(\mathbf{e}_x, \mathbf{e}_y, \mathbf{e}_z)$ indicate the streamwise, wall-normal and spanwise directions, respectively. The channel has a streamwise length L_x and a spanwise width L_z. A distance h from the mean height of the wavy lower wall to the flat upper wall is imposed. The wavy lower wall is described by the expression in Eq. 7.5.

7.2.1 Analytical Solution

Since water is considered as the working liquid interacting with the SH surface, the incompressible flow through the channel depicted in Fig. 7.3 is considered. The flow is driven by an imposed flow rate at the inlet. The governing equations for the unsteady incompressible flow of a Newtonian fluid in a channel can be written as follows:

$$\nabla \cdot \mathbf{u} = 0, \tag{7.6a}$$

$$\frac{\partial \mathbf{u}}{\partial t} + (\mathbf{u} \cdot \nabla)\,\mathbf{u} = -\frac{\nabla p}{\rho_l} + \nu_l \nabla^2 \mathbf{u}, \tag{7.6b}$$

where p is the pressure field, ρ_l is the fluid density and ν_l is the fluid kinematic viscosity. In laminar conditions, which are the operating conditions investigated in this chapter, the Poiseuille analytical solution and its modification due to slip at the lower wall can be readily retrieved. The problem is schematically depicted in Fig. 7.4, where the 2D laminar flow between two fixed flat walls separated by an height h is represented. Under the hypothesis of steady-state and fully developed horizontal flow along the streamwise direction ($\mathbf{u} = u\mathbf{e}_x$), the expression in Eq. 7.6(a) involves that $u = u(y)$. Moreover, the projection of Eq. 7.6(b) along the wall normal direction $\mathbf{e}_y$ implies that $p = p(x)$, while the corresponding projection along the streamwise direction $\mathbf{e}_x$ reduces to:

$$0 = -\frac{\partial p}{\partial x} + \mu_l \frac{\partial^2 u}{\partial y^2}, \tag{7.7}$$

where μ_l is the fluid dynamic viscosity. The integration of Eq. 7.7 in the wall normal direction $\mathbf{e}_y$ enables to retrieve the following velocity profile expression:

$$u(y) = \frac{\frac{\partial p}{\partial x}}{2\mu_l} y^2 + c_1 y + c_2, \tag{7.8}$$

where the value of the constants c_1 and c_2 depends on the boundary conditions imposed at the walls. Since in the performed simulations only the lower channel wall was modelled as SH, the two cases of no-slip over both walls and partial slip on the lower wall are considered. In the first case, since $u(0) = u(h) = 0$, the following expressions for the velocity profile $u(y)$, the maximum velocity u_{max}, and the shear stress at the lower wall τ_w are retrieved:

$$u(y) = -\frac{\frac{\partial p}{\partial x} h^2}{2\mu_l} \left[\frac{y}{h}\left(1 - \frac{y}{h}\right)\right], \tag{7.9a}$$

$$u_{max} = -\frac{\frac{\partial p}{\partial x} h^2}{8\mu_l}, \tag{7.9b}$$

$$\tau_w = -\frac{\partial p}{\partial x}\frac{h}{2}, \tag{7.9c}$$

which predict a parabolic profile with a maximum velocity at the centre of the channel. In the case of a partial slip on the lower wall, the two boundary conditions modify to $u(0) = \ell_{sl} \left.\frac{\partial u}{\partial y}\right|_{y=0}$

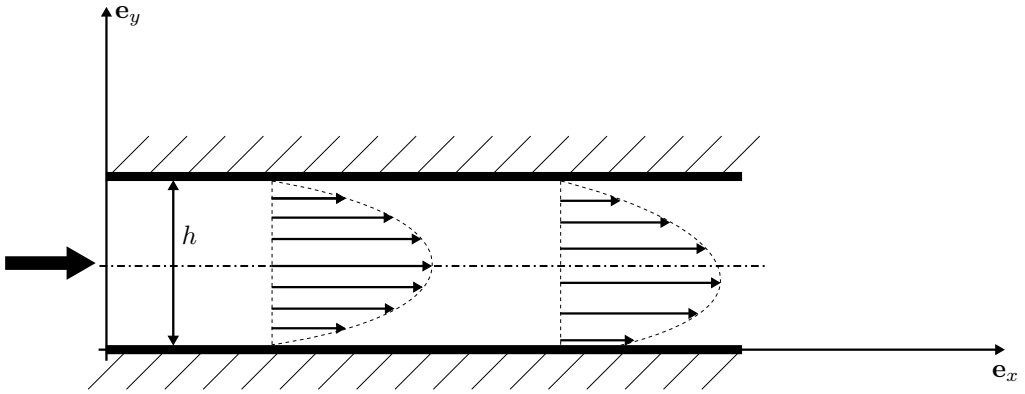

Figure 7.4 – Poiseuille laminar parabolic profile between two walls at distance h. In the case of the no-slip condition imposed on both walls (on the left), the profile is symmetric with respect to the channel central axis (indicated by the dash-dotted line) with a maximum velocity at the centre of the channel. In the case of the partial slip condition imposed on the lower wall (on the right), the maximum velocity shifts toward the lower wall.

and $u(h) = 0$, which determine the following expressions:

$$u(y) = -\frac{\frac{\partial p}{\partial x} h^2}{2\mu_l} \left(\frac{\ell_{sl}}{h + \ell_{sl}} + \frac{y}{h + \ell_{sl}} - \frac{y^2}{h^2} \right), \tag{7.10a}$$

$$u_{max} = -\frac{\frac{\partial p}{\partial x} h^2}{8\mu_l} \left[\frac{h^2}{(h + \ell_{sl})^2} + \frac{4\ell_{sl}}{h + \ell_{sl}} \right], \tag{7.10b}$$

$$\tau_w = -\frac{\partial p}{\partial x} \frac{h^2}{2\,(h + \ell_{sl})}, \tag{7.10c}$$

which predict a non-symmetric velocity profile with a maximum velocity u_{max} value approaching the lower wall for increasing ℓ_{sl}.

7.2.2 Simulations Overview

The numerical implementation of the channel flow configuration introduced in the previous paragraphs was performed in this study via the open source software OpenFOAM®, release V5.0 (OpenFOAM Foundation 2019) (indicated as OF hereinafter). However, the mesh generation was performed via the software Pointwise®, release V18.0 (Pointwise 2019) (indicated as PW hereinafter). The generated files were then imported into OF. For an exhaustive review of the Finite Volume Method (FVM) as the approach to solve the incompressible flow here considered and its practical implementation in OF, the interested reader is referred to e.g. Moukalled *et al.* (2016). Some details of the method implemented in this study are provided in Appendix G, including a description of the PISO algorithm (Pressure-Implicit with Splitting of Operators) selected as solver to estimate the pressure and velocity fields. The Appendix G could be useful for the reader who might want to reproduce the results presented in the following of the chapter. However, no loss of clarity should be encountered by proceeding with the reading of the present chapter.

The results commented in this chapter are restricted to simulations run in laminar conditions, where a direct comparison with the analytical solution developed in §7.2.1 is possible.

Drawing again a parallel with experimental results, the numerically investigated conditions reveal interesting with respect to the boundary layer evolution along the sphere wall. In fact, as discussed in Chapter 2, a laminar boundary layer develops along the front-side of the sphere. Then, depending on the actual Reynolds number regime, the boundary layer undergoes different separation and transition scenarios. The latter were properly described defining the angle ϑ with respect to the direction of the flow, underlying the relevance of the region around the sphere equator, i.e. $\vartheta = 90°$. Moreover, high magnification visualisations (see e.g. Fig. 6.18) demonstrated the first signs of the air layer deformation to occur in the rear-side of the falling sphere, not far from the equator. The results presented in this chapter can thus provide useful preliminary information in a region close to boundary layer transition and/or separation, where a significant air layer deformation already occurs.

In available literature the transition phenomenon is typically studied as a function of the flow Reynolds number, which can be defined via the maximum streamwise velocity u_m, $Re_m = \frac{u_m h/2}{\nu_l}$, or via the bulk velocity u_b that assures the desired flow rate, $Re_b = \frac{u_b h/2}{\nu_l}$. Both numerical and experimental studies agree in the estimation of $Re_m \approx 1000$ as the minimum threshold below which turbulence cannot be sustained in channel flows with smooth walls (see e.g. Orszag & Kells 1980; Carlson *et al.* 1982, for details). Moreover, since smooth and wavy walls are compared in the following, the results presented will be limited to the range $1 \leq Re_m \leq 750$ (see Tab. 7.2). A 3D test case was run at $Re_m = 750$ prescribing the largest analysed wave amplitude $\frac{\delta}{h}$ at the lower wall (HD case). The initial turbulent field evaluated by running the turbulent smooth channel DNS proposed by Kim *et al.* (1987) slowly decayed back to the corresponding laminar solution, thus showing that the considered Re_m threshold is not large enough to sustain turbulence. In all the simulations, the desired flow rate was imposed by prescribing the u_b value at the inlet when setting the boundary conditions for the velocity field, the relation between Re_m and Re_b being straightforward since in laminar Poiseuille flow $u_b = \frac{2}{3}u_m$.

Referring to the notation introduced in Fig. 7.3, a channel length $L_x = 30\Lambda$ was prescribed in the streamwise direction. Since the results presented in the following are evaluated in the central part of the channel, the chosen L_x value assured the absence of any possible influence of the inlet and outlet boundaries. Even if 2D laminar simulations are run, OF requires the generation of a 3D mesh: the spanwise channel width L_z was thus set equal to the channel height h. Finally, the analysed dimensional slip length ℓ_{sl} was in the range 0 µm to 100 µm, with the zero value corresponding to the reference no-slip case and the largest value representing 1 % of h (see Tab. 7.2). This range was chosen to simulate the same order of magnitude of the roughness elements of the experimentally produced coatings, since, depending on the surface characteristics, the slip length can reach an order of magnitude as large as $\mathcal{O}(10^1)$ with respect to the roughness elements size (Vinogradova 1999). Taking into account all the parameters resumed in Tab. 7.2, the resulting total number of performed simulations is $\mathcal{O}(10^2)$.

The identified macroscopic dimensions of the channel (L_x, h, L_z) coupled with a mesh refinement analysis to establish the number of grid points per each wave (details in Appendix G) resulted into a structured hexahedra mesh with a number of grid points $1143 \times 39 \times 2$ in the $\mathbf{e}_x, \mathbf{e}_y, \mathbf{e}_z$ directions, respectively. The total number of grid points was therefore $\approx 8.9 \times 10^4$. A collocated arrangement was used to store the calculated variables. Moreover, in order to assure a proper amount of points in the near-wall region, a symmetric (with respect to the channel centreline) hyperbolic tangent distribution of the grid points was imposed in the $\mathbf{e}_y$ direction (Vinokur 1983), while a uniform distribution was considered in the streamwise direction. A representation of the obtained mesh typology in the region close to the wall undulation ($\frac{\Lambda}{h} = 1$ and $\frac{\delta}{h} = 0.05$) is reported in Fig. 7.5. The grid points result aligned in the $\mathbf{e}_y$ direction, while they mimic the wall wave in the streamwise direction.

One important quality parameter influencing the accuracy of the results presented in the

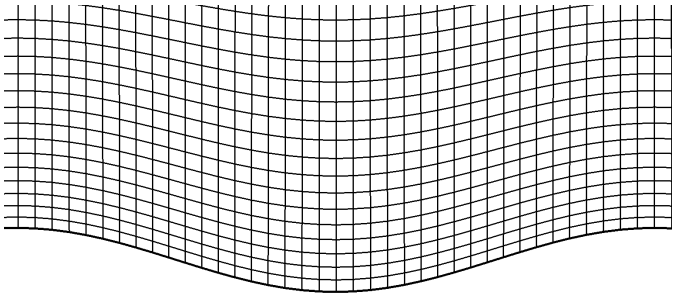

Figure 7.5 – Detail of the region in proximity of the lower wavy wall of a mesh generated in Pointwise® in the case $\frac{\Lambda}{h} = 1$ and $\frac{\delta}{h} = 0.05$. The number of grid points per each wave in the streamwise direction is equal to 39.

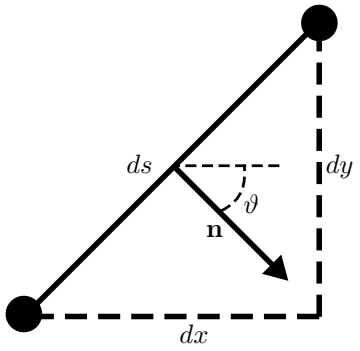

Figure 7.6 – Schematic of the estimation of the local slope of the wall. The two consecutive grid points (black dots) are separated by a distance ds, which projected on the Cartesian axes provides the lengths dx and dy. The latter are connected to ds via the local slope angle ϑ, positive in the counter-clockwise direction, which defines the direction of the outward normal $\mathbf{n}$ with respect to the horizontal direction.

following is the estimation of the ability of the generated mesh to accurately reproduce the wavy wall geometry, whose analytical law was introduced in Eq. 7.5. In fact, the local slope $\frac{dy}{dx}$ of the wall could be estimated via the known coordinates of the two next available grid points. This allowed for the identification of the local outward normal direction $\mathbf{n} = (\cos\vartheta, \sin\vartheta)$, where $\vartheta = -\left(90° - \text{atan}\left(\frac{dy}{dx}\right)\right)$, as shown in Fig. 7.6. The local evaluated ϑ angle is compared in Fig. 7.7 to the value retrieved via the analytical law in Eq. 7.5 in the case of the HD mesh. The maximum error in the estimation of the wall local angle $\Delta\vartheta = \frac{\vartheta_{mesh} - \vartheta}{\vartheta}$ reached 0.5 % in the HD case, while decreased down to 0.3 % in the LD case. These values will be recalled in the next section to justify the accuracy of the approach implemented to analyse the results.

One example of the sampled streamwise velocity profile is compared in Fig. 7.8 to the analytical Poiseuille solution at the highest investigated Re_m. The percentage error in the estimation of the maximum velocity u_m is $\mathcal{O}(10^{-1})$ in both cases of no-slip (Fig. 7.8(a)) and partial slip (Fig. 7.8(b)) lower wall. The profile reported in Fig. 7.8(c) is a detail of the near-wall region of Fig. 7.8(b), showing that the computed solution is able to correctly represent the imposed slip at the wall.

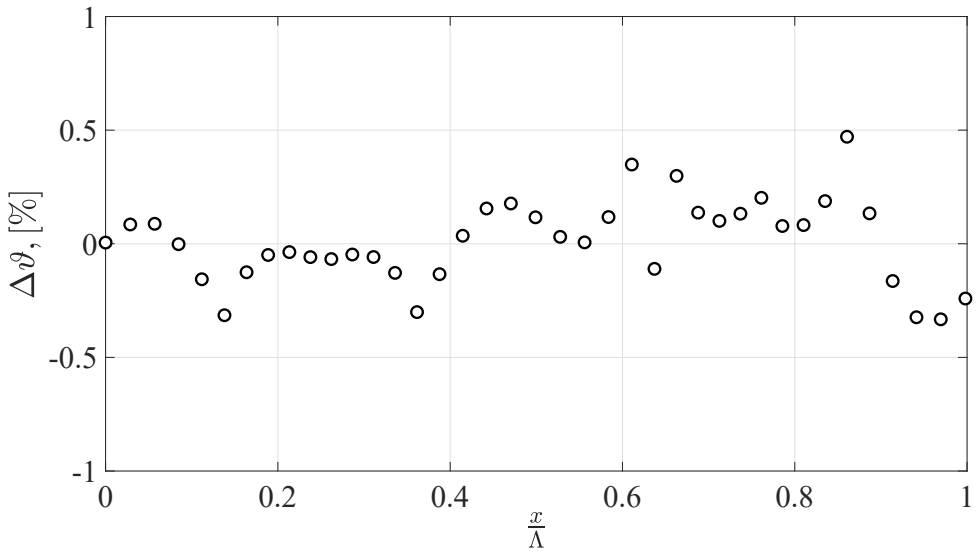

Figure 7.7 – Accuracy on the estimation of the local wall slope angle for the HD mesh along one non-dimensional wavelength. The value estimated from the generated mesh is compared to the angle retrieved via the imposed analytical law in Eq. 7.5. In the case of the LD mesh, the maximum error $\Delta\vartheta$ decreases to 0.3 %.

7.3 Analysis Methodology

As discussed in §7.1, the main interest in the macroscopic description of a SH coating would be the achievement of an effective slip length model able to consider all the possible phenomena that influence the SH behaviour. Due to the large amount of parameters that should be taken into account, the general formulation expressed in Eq. 7.4 is reduced in this study to:

$$\ell_{sl}^{eff} = f\left(\frac{\ell_{sl}}{h}, \frac{\delta}{h}, Re\right). \tag{7.11}$$

Moreover, the sought ℓ_{sl}^{eff} behaviour would be valid in laminar 2D conditions in a channel flow. In fact, exploiting the slip velocity and wall shear stress expressions introduced in Eqs. 6.29 and 6.30, the following relationship can be retrieved:

$$\ell_{sl}^{eff} \approx \mu_l \frac{u_{sl}^{eff}}{\tau_w^{eff}}. \tag{7.12}$$

The effective slip velocity u_{sl}^{eff} is evaluated by averaging over the whole wall wave the local slip velocity values on the lower partial slip wall of the channel, i.e. $u_{sl}^{eff} \approx \frac{1}{L}\int_{s_0}^{s_0+L} u_{sl}(s)ds$, where s indicates the curvilinear abscissa and L the inlet-outlet distance of the control volume (see §7.3.1). Then, from the analytical solution in §7.2.1, the wall shear stress can be estimated as:

$$\tau_w^{eff} = \frac{h\Delta p}{2L}, \tag{7.13}$$

A method to estimate the equivalent pressure loss Δp along the control volume is required. This is the topic of the next paragraph, where an integral approach is developed.

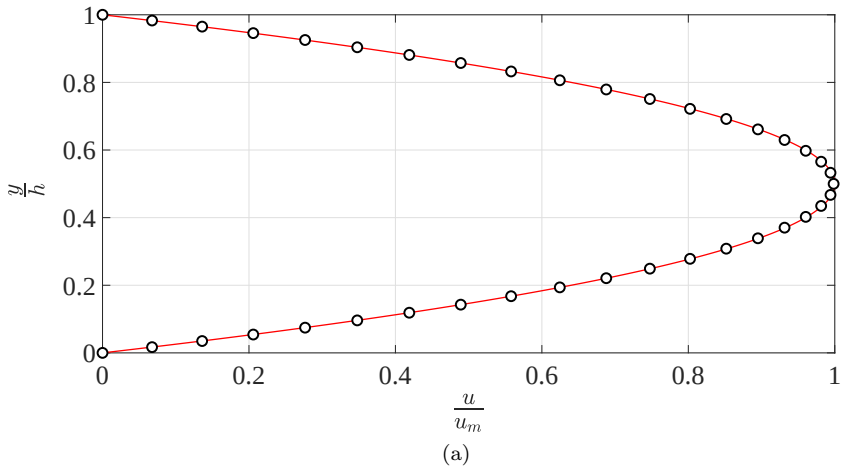

(a)

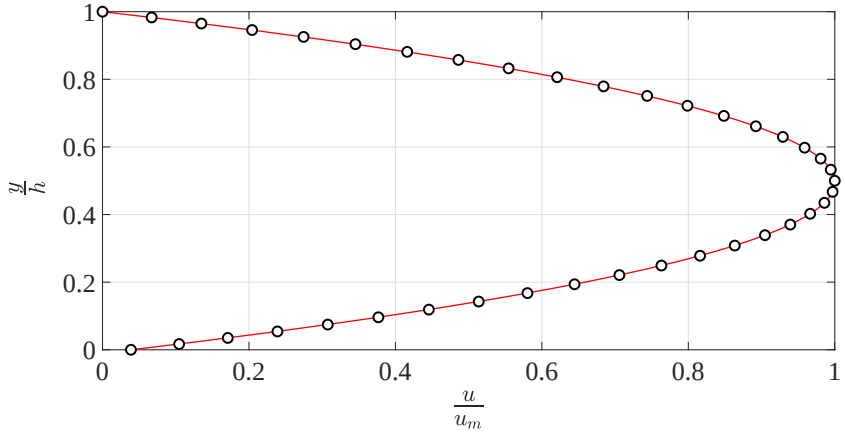

(b)

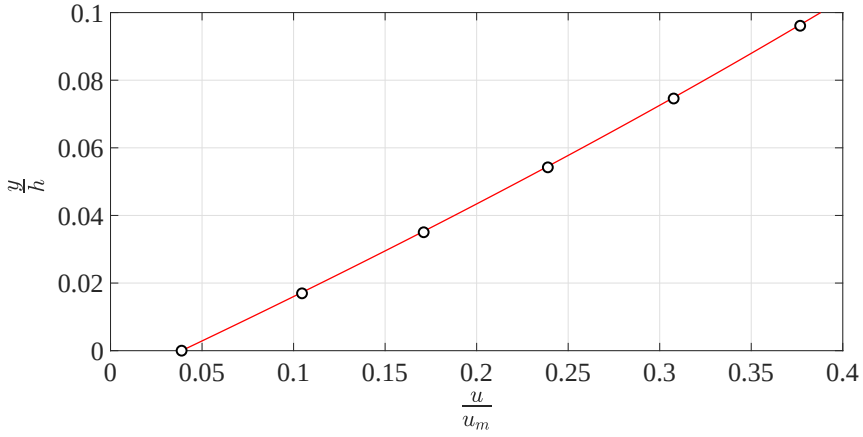

(c)

Figure 7.8 – Comparison of the computed streamwise velocity profiles (○) with respect to the corresponding analytical solution (—) developed in §7.2.1. (a), no-slip lower wall. (b), partial slip lower wall with $\ell_{sl} = 100\,\mu\text{m}$. (c), detail of the near-wall region of (b).

7.3.1 Integral Approach

The method selected to present the results of the performed simulations is based on an integral approach over an area in the central part of the analysed channel. The schematic in Fig. 7.9 shows that, once chosen the number of waves inside the control volume, four boundaries can be identified: the bottom (*bot*) and top (*top*) walls, together with the inlet (*inl*) and the outlet (*out*). To assure the control volume to be sufficiently far from the boundary *Inlet* and *Outlet* patches of the computational domain, four waves in the centre of the channel were considered. The governing equations introduced via Eqs. 7.6 can be re-written here in indicial notation (indices (i, j, k) in a 3D configuration), which will facilitate the following developments. By considering an incompressible, steady-state flow, the continuity equation can be written as:

$$\frac{\partial u_i}{\partial x_i} = 0, \tag{7.14}$$

where u_i indicates the *i-th* component of the velocity vector $\mathbf{u} = u\mathbf{e}_x + v\mathbf{e}_y$. After integration over the 3D control volume V_c, the expression in Eq. 7.14 becomes:

$$\int_{V_c} \frac{\partial u_i}{\partial x_i} dV = 0, \tag{7.15}$$

where a simplified notation with one single integration symbol is used, with the typology of integral suggested by the corresponding letter. The volume integral can then be transformed into the corresponding surface integral over the control volume surface S_c:

$$\int_{S_c} u_i n_i dS = 0, \tag{7.16}$$

with n_i representing the local outward normal to the surface. An explicit evaluation of the normal vector components on each of the boundaries of the control surface leads to:

$$-\int_{S_{inl}} u dS + \int_{S_{out}} u dS + \int_{S_{bot}} (u\cos\vartheta + v\sin\vartheta)\, dS = 0, \tag{7.17}$$

where ϑ describes the local slope of the lower wall, as was shown in Fig. 7.6. Finally, considering a unitary width along the third direction, the integral form of the continuity equation in the Cartesian coordinates system $(\mathbf{e}_x, \mathbf{e}_y, \mathbf{e}_z)$ can be written as:

$$-\int_0^h u_{inl} dy + \int_0^h u_{out} dy + \int_{-\delta}^{\delta} u_{bot} dy - \int_0^L v_{bot} dx = 0. \tag{7.18}$$

The same approach can be followed for the momentum equation introduced in Eq. 7.6(b), which can re-written at steady-state in indicial form as:

$$\rho_l u_j \frac{\partial u_i}{\partial x_j} = \frac{\partial}{\partial x_j}\left(-p\delta_{ij} + 2\mu_l S_{ij}\right), \tag{7.19}$$

where δ_{ij} is the Kronecker delta and S_{ij} represents the *i-j* component of the rate of strain tensor introduced in §7.2. The integration over the control volume and the transformation of volume integrals into surface integrals leads to:

$$\int_{S_c} \rho_l u_i u_j n_j dS = -\int_{S_c} p\delta_{ij} n_j dS + \int_{S_c} 2\mu_l S_{ij} n_j dS. \tag{7.20}$$

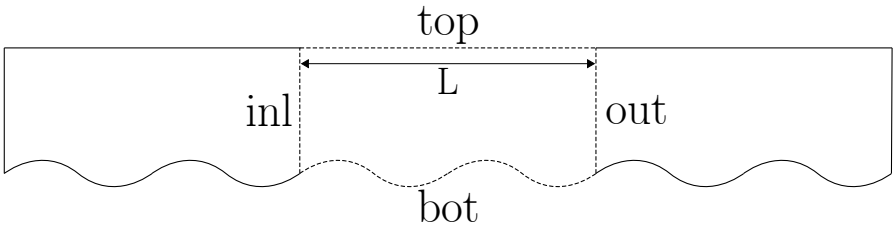

Figure 7.9 – Schematic of the control volume defined for the implementation of the integral approach in the post-processing of the 2D laminar simulations. Four boundaries can be identified: *bot*, bottom wavy wall. *top*, top flat wall. *inl*, inlet. *out*, outlet. The symbol L indicates the inlet-outlet distance.

Since interest is focused on an integral balance along the streamwise direction, the projection of Eq. 7.20 along $\mathbf{e}_x$ gives:

$$\int_{S_c} \rho_l u u_j n_j dS = -\int_{S_c} p n_i \cdot \mathbf{e}_x dS + \int_{S_c} 2\mu_l S_{xj} n_j dS. \tag{7.21}$$

The explicit evaluation of each term on the control volume borders finally gives:

$$-\int_0^h \rho_l u_{inl}^2 dy + \int_0^h \rho_l u_{out}^2 dy = \int_0^h p_{inl} dy - \int_0^h p_{out} dy - \int_{-\delta}^{\delta} p_{bot} dy$$
$$+2\mu_l \left(-\int_0^h S_{xx,inl} dy + \int_0^h S_{xx,out} dy + \int_0^L S_{xy,top} dx + \int_{-\delta}^{\delta} S_{xx,bot} dy - \int_0^L S_{xy,bot} dx \right). \tag{7.22}$$

Special care is put on the treatment of the spatial derivatives inside the terms S_{ij}, since the wavy wall results into grid points not aligned in the streamwise direction (see Fig. 7.5). In fact, as shown by Marquillie & Ehrenstein (2002), a relation between the physical and the Cartesian coordinates can be written, in the case of the gradient operator, on the form:

$$\widetilde{\nabla} = \nabla + \mathbf{G}_{y_w}, \tag{7.23}$$

where for a law of the wall y_w dependent on the streamwise coordinate (see Eq. 7.5) the operator $\mathbf{G}_{y_w}$ writes as:

$$\mathbf{G}_{y_w} = \left(-\frac{\partial y_w}{\partial x} \frac{\partial}{\partial y}, 0 \right). \tag{7.24}$$

One final effort is made to retrieve an analogous expression for the integral energy balance, which reveals interesting since the analysis of a performance parameter connected to the dissipation $\varepsilon = 2\frac{\mu_l}{\rho_l} S_{ij} S_{ij}$ will be used as comparison method of the different simulations. An expression for the energy equation in indicial notation is readily retrieved via a multiplication by u_i of Eq. 7.19, which gives:

$$\rho_l u_j \frac{\partial E}{\partial x_j} = -\frac{\partial p u_i}{\partial x_i} + 2\mu_l \frac{\partial u_i S_{ij}}{\partial x_j} - 2\mu_l S_{ij} \frac{\partial u_i}{\partial x_j}, \tag{7.25}$$

where Eq. 7.14 was exploited to eliminate the corresponding pressure term and the kinetic energy definition $E = \frac{1}{2} u_i u_i$ was used. The integration over the control volume V_c and the transformation of volume integrals into surface integrals result into:

$$\int_{S_c} \rho_l E u_j n_j dS = -\int_{S_c} p u_i n_i dS + 2\mu_l \int_{S_c} u_i S_{ij} n_j dS - \int_{V_c} \rho_l \varepsilon dV. \tag{7.26}$$

	Mass Eq. 7.18	Momentum Eq. 7.22	Energy Eq. 7.27
Residual, [%]	-	1	2

Table 7.3 – Upper limit of the estimated percentage error in the mass, momentum and energy balances discussed in §7.3.1. In the mass balance, the residual is non-significant with respect to the two other cases.

The evaluation of the expression in Eq. 7.26 over each boundary of the control volume finally gives:

$$\begin{aligned}\int_0^h \rho_l E_{out} u_{out} dy - \int_0^h \rho_l E_{inl} u_{inl} dy = \int_0^h p_{inl} u_{inl} dy - \int_0^h p_{out} u_{out} dy \\ +2\mu_l \left(- \int_0^h S_{xx,inl} u_{inl} dy - \int_0^h S_{xy,inl} v_{inl} dy + \int_0^h S_{xx,out} u_{out} dy + \int_0^h S_{xy,out} v_{out} dy \right. \\ \left. + \int_{-\delta}^{\delta} S_{xx,bot} u_{bot} dy + \int_{-\delta}^{\delta} S_{xy,bot} v_{bot} dy - \int_0^L S_{xy,bot} u_{bot} dx - \int_0^L S_{yy,bot} v_{bot} dx \right) \\ - \int_{V_c} \rho_l \varepsilon dV, \end{aligned} \tag{7.27}$$

where the dissipation term is evaluated via an integration over the whole control volume (with unitary width in the third direction).

Before presenting the results in the next section, a further validation of the executed simulations can be obtained via the integral mass, momentum and energy balances obtained in Eqs. 7.18, 7.22 and 7.27, respectively. In fact, an ideally zero value should be evaluated by summation and subtraction of all the terms appearing in the budgets. The residual can therefore be viewed as an indication of the error performed in the followed approach. The estimated errors are resumed in Tab. 7.3. The mass balance in Eq. 7.18 was found to be always satisfied with residuals much lower than the momentum case, which is not surprising since the incompressibility constraint is explicitly requested by the PISO algorithm (see details in Appendix G) during the run. For this reason, attention is focused on momentum and energy balances. In the case of Eq. 7.22, the residual was found to slightly increase from the FW to the HD case, while being independent on Reynolds number and imposed slip. The maximum value in the case $\frac{\delta}{h} = 0.1$ is $\approx 0.9\,\%$ when evaluated with respect to the terms describing the pressure difference between inlet and outlet of the control volume (the first two terms on the right-hand side in Eq. 7.22). The same analysis performed on the energy balance in Eq. 7.27 shows residuals about two times the values retrieved via the momentum balance (normalised with respect to the first two terms on the right-hand side in Eq. 7.27), which is not surprising since the energy terms scale as the cube of a velocity, that is one order larger than the corresponding momentum terms.

7.3.2 Equivalent Pressure Loss

The kinetic energy balance in Eq. 7.27 is exploited to estimate an equivalent pressure loss along the channel, which allows for the analysis of the effects of the undulation and slip set on the channel lower wall. In fact, as shown by Chassaing (2000, Chapter 5), the integral of the dissipation rate can be expressed as the product between an equivalent pressure loss Δp across

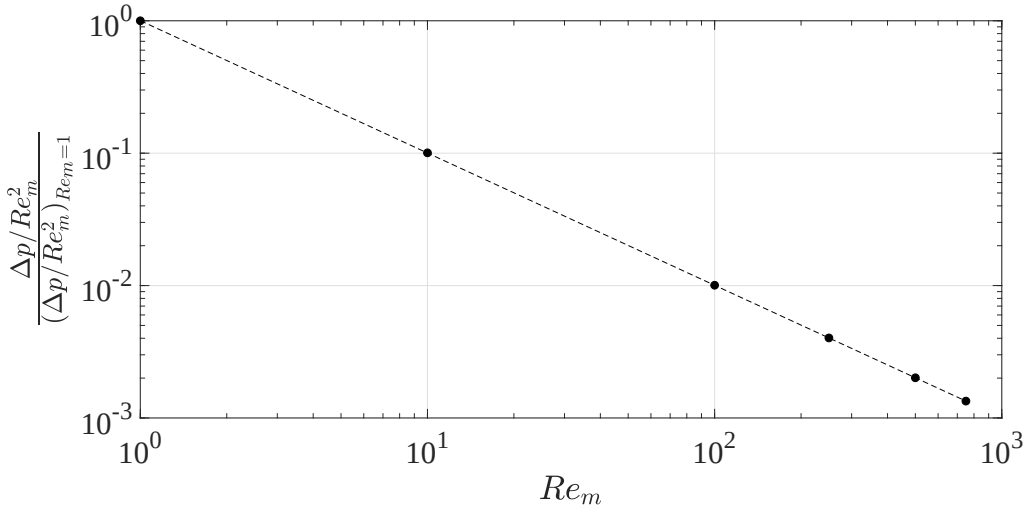

Figure 7.10 – Evolution of the ratio $\frac{\Delta p}{Re_m^2}$ over the whole analysed Re_m range for the case of a no-slip, flat lower wall (FW) of the channel. The ratio $\frac{\Delta p}{Re_m^2}$, which is representative of the scaling of the friction factor f, is normalised with respect to its value at $Re_m = 1$. (- - -), linear fit in the least-mean squares sense of the data, which highlights the unitary negative slope.

the control volume and the volumetric flow rate Q_V:

$$\int_{V_c} \rho_l \varepsilon dV = \Delta p Q_V. \tag{7.28}$$

The estimation of the dissipation term via the computed velocity field thus enables the Δp evaluation. The laminar solution developed in §7.2.1 shows that Δp scales as the maximum velocity in the channel, which implies $\Delta p \sim Re_m$. Moreover, the expression of Δp via a Darcy formalism (see e.g. Eq. 6.6 in §6.1.2) allows to write:

$$\Delta p \sim f Re_m^2, \tag{7.29}$$

which implies that the friction factor f is expected to scale as $f \sim \frac{1}{Re_m}$. This is verified in Fig. 7.10, where the evolution of the ratio $\frac{\Delta p}{Re_m^2}$ (normalised with respect to the value at $Re_m = 1$) with respect to Re_m is shown. A negative unitary slope in the logarithmic chart is verified in the case of no-slip, FW simulations over the whole analysed Re_m range, thus further validating the followed approach.

7.4 Results

7.4.1 Effective Slip Length

The approach developed in the previous section thus allows to estimate an equivalent pressure loss Δp along the control volume, which is injected in Eq. 7.13 to achieve an estimation of the effective wall shear stress τ_w^{eff}. The latter is then used in Eq. 7.12 to evaluate the effective slip length ℓ_{sl}^{eff}. The evaluated results are reported in Fig. 7.11 for $\frac{\delta}{h}$ varying from the LD up to

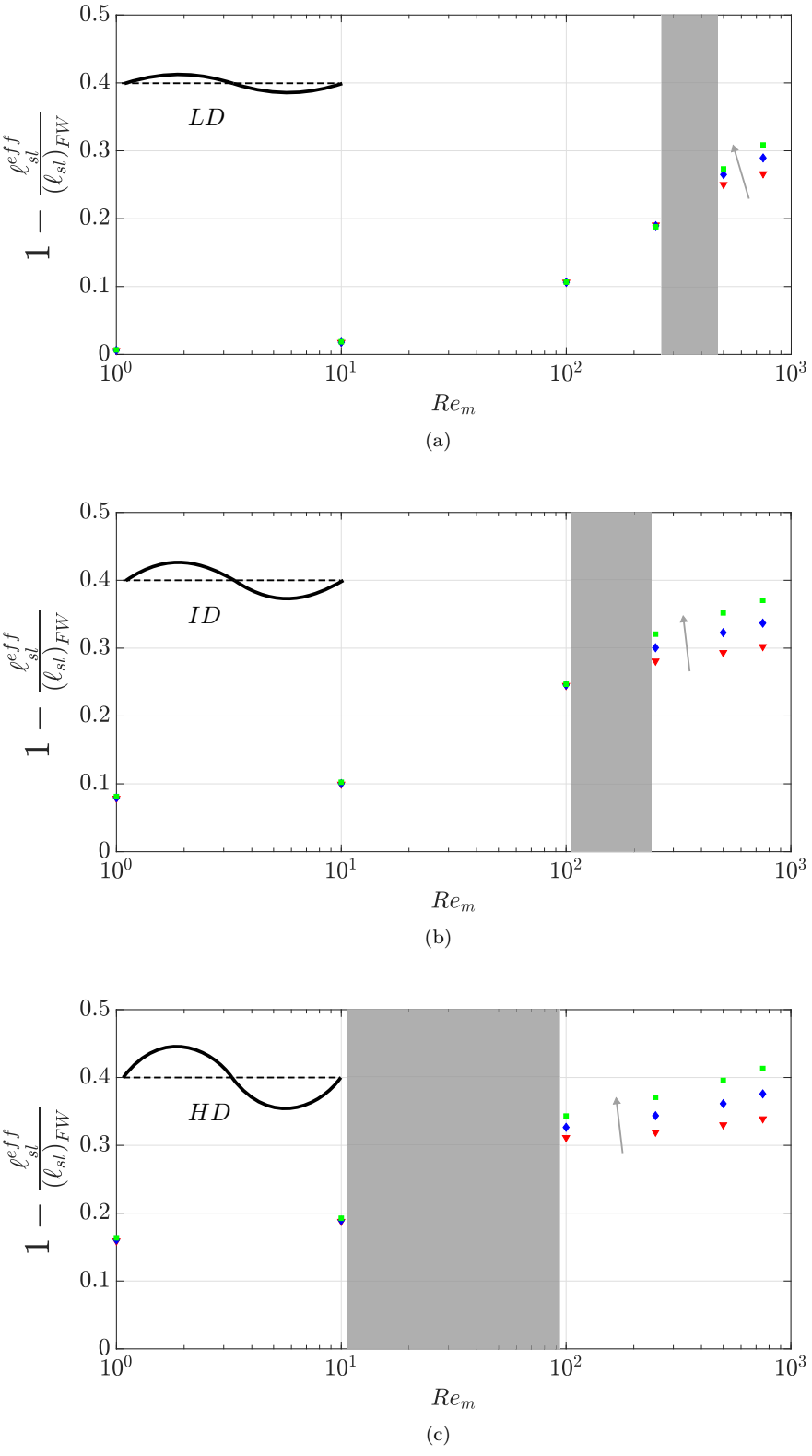

Figure 7.11 – Evolution of the normalised (with respect to the corresponding FW simulation with the same $\frac{\ell_{sl}}{h}$) effective slip length ℓ_{sl}^{eff} over the whole analysed Re_m range. (a), LD configuration with $\frac{\delta}{h} = 0.05$. (b), ID configuration with $\frac{\delta}{h} = 0.075$. (c), HD configuration with $\frac{\delta}{h} = 0.10$. ▼, $\ell_{sl} = 10\,\mu m$. ♦, $\ell_{sl} = 50\,\mu m$. ■, $\ell_{sl} = 100\,\mu m$. The gray arrows indicate increasing $\frac{\ell_{sl}}{h}$. The gray-shaded rectangles indicate the regions where the onset of recirculation inside the valleys of the lower wavy wall occurs.

the HD configuration, each value being normalised by the corresponding flat wall simulation featuring the same imposed $\frac{\ell_{sl}}{h}$. It is apparent that ℓ_{sl}^{eff} on a wavy, lower wall results always smaller than the corresponding imposed slip length ℓ_{sl} over the whole analysed Re_m range. Only the lowest analysed Re_m and $\frac{\delta}{h}$ in Fig. 7.11(a) show a negligible or slight ℓ_{sl}^{eff} variation with respect to ℓ_{sl}. In fact, for $Re_m \leq 10$, ℓ_{sl}^{eff} shows an increasing variation with respect to the FW case for increasing $\frac{\delta}{h}$, up to $\approx 20\,\%$ in the HD case in Fig. 7.11(c). Interestingly, in such a low Re_m the influence of the imposed ℓ_{sl} value is negligible, all the points being overlapped. However, for increasing Re_m, the possible detrimental slip length variation goes up to $\approx 40\,\%$ in the HD configuration in Fig. 7.11(c). Conversely to the low Re_m region, the points at different imposed ℓ_{sl} are no more overlapped. These results highlight that, under the investigated conditions, the wall deformation may result into significant detrimental effects on the imposed microscopic slip length at the wall, with possible effects on the drag estimation. Interestingly, a someway qualitative agreement with the experimental results on falling spheres is found. At fixed Re_m, an augmentation of the wall deformation $\frac{\delta}{h}$ determines an increase of the detrimental ℓ_{sl}^{eff} reduction with respect to ℓ_{sl}, which could be compared with the drag increase of SH spheres characterised by high aspect ratio χ (see the left region in Fig. 6.39). However, the proposed approach is based on integral quantities and is thus not able to analyse the local characteristics of the flow. In fact, the ℓ_{sl}^{eff} behaviour for increasing Re_m underlined in Fig. 7.11 is connected to the onset of recirculation inside the valleys of the wavy lower wall of the channel. The latter was identified in a progressively lower Re_m range for increasing $\frac{\delta}{h}$, as indicated by the gray-shaded regions in Fig. 7.11. The LD configuration resulted into a recirculation onset in the region $250 < Re_m < 500$. The latter shifted down to $10 < Re_m < 100$ in the HD case. The onset of separation and backflow thus appears to enhance the differences among the investigated ℓ_{sl} values. However, this clearly implies that a macroscopic approach based only on an integral balance over a control volume inside the channel might not be enough to describe the detected phenomena. For this reason, a path towards a progressively more detailed description of the problem is pursued in the following of the chapter. To begin with, an attempt to separately describe the effects of wall deformation and partial slip is performed in the next section.

7.4.2 Slip and Deformation Effects

When comparing a simulation in the FW, no-slip configuration with a simulation over a wavy wall with partial slip, the wall geometry and the slip boundary condition simultaneously influence the evaluated performance indicator, i.e. Δp. Ideally, the best picture to achieve a modelling of the effects of the two variables would be a decoupling of their influence. In this perspective, the following approach can be followed:

1. compare the results of a partial slip, wavy wall simulation with the corresponding no-slip, wavy wall case. This step allows the investigation of the effects of an increase of the slip length ℓ_{sl};

2. compare the results of a no-slip, wavy wall simulation with the corresponding no-slip, flat wall case. This second step allows the analysis of the effects of an increase of the interface deformation, which in the considered simplified model is represented by the amplitude δ.

In detail, in the performed numerical campaign the order of magnitude of the parameters governing the two effects was different, since a similarity with the experimental tests over macroscopic SH surfaces was sought. As was shown in Tab. 7.2, the maximum imposed δ value corresponds to $10\,\%$ of the mean channel height h. Conversely, the ℓ_{sl} largest value reaches only $1\,\%$ of h. Larger effect of partial slip at the wall could be analysed by progressively increasing the ratio

$\frac{\ell_{sl}}{h}$ (see e.g. Niavarani & Priezjev 2009). However, since the dimensional ℓ_{sl} order of magnitude is dictated by experimental limitations, the high $\frac{\ell_{sl}}{h}$ scenario would correspond in practice to micron- or nano-sized applications, which is not the interest of this manuscript.

Slip Length Effect

The effects of increasing ℓ_{sl} are analysed by comparing the Δp at fixed $\frac{\delta}{h}$ and varying the slip length value. In detail, the pressure loss evaluated via the dissipation term of the wavy, partial slip wall (subscript *sl*) is normalised by the correspondent wavy, no-slip wall (subscript *no-sl*). The results for the two extreme cases, FW and HD, are reported in Fig. 7.12. In the flat wall case in Fig. 7.12(a), a progressively larger Δp reduction is evaluated for increasing ℓ_{sl} at the lower wall. In detail, $\ell_{sl} = 10\,\mu\text{m}$ results into an $\approx 0.5\,\%$ Δp variation, whereas the largest analysed $\ell_{sl} = 100\,\mu\text{m}$ increases the gain up to $\approx 6\,\%$. Interestingly, the non-dimensional Δp magnitude is approximately uniform over the analysed Re_m range. A similar scenario is noticed in the HD case reported in Fig. 7.12(b), where the Δp variation magnitude for increasing ℓ_{sl} is the same than the FW case. A slight Δp increasing trend appears for the largest analysed ℓ_{sl} at $Re_m \geq 100$, which is probably related to the onset of recirculation inside the valleys of the wavy lower wall. However, in the $\ell_{sl} = 100\,\mu\text{m}$ case the maximum Δp variation with respect to the average value over the whole Re_m range is limited to $0.2\,\%$. Therefore, considering a uniform non-dimensional Δp along the whole analysed Re_m range seems a reasonable approximation even at the highest investigated $\frac{\delta}{h}$. The intermediate geometries LD and ID provided the same behaviour evidenced in the two extreme cases here discussed.

The performed assumption suggests that the relative performance between wavy, partial slip channel and the corresponding wavy, no-slip channel is independent on the actual $\frac{\delta}{h}$ and Re_m values, at least under the investigated ranges of the considered parameters. A performance indicator function only of the imposed slip length ℓ_{sl} can thus be considered. This approach is well described in Fig. 7.13, where the Δp evolution as a function of $\frac{\ell_{sl}}{h}$ is shown for the range of slip length investigated in the performed numerical campaign. The pressure loss is properly normalised by the corresponding wavy, no-slip case. Interestingly, a linear relationship is retrieved, which can be well described by the following law:

$$1 - \frac{(\Delta p)_{sl}}{(\Delta p)_{no-sl}} \approx \alpha \frac{\ell_{sl}}{h}, \tag{7.30}$$

where the slope value is estimated to be $\alpha \approx 5.7$. This linear relation thus implies that, independently of $\frac{\delta}{h}$ and Re_m, an increase of the slip length over a range that could correspond to realistic macroscopic applications could result into non-negligible effects on the evaluated equivalent pressure loss along the channel. However, in §7.4.1 the ℓ_{sl}^{eff} analysis suggested that, depending on the considered Re_m region, the slip length effect could be significant or non-relevant with respect to the wall deformation influence. For this reason, in the next paragraph the effect of the wall undulation is analysed at fixed slip at the wall.

Wall Deformation Effect

The second step of the investigation consists in analysing the effect of the wall deformation alone, without the coupling with the slip length effects. To do that, the results in terms of the pressure loss of the wavy, no-slip wall (indicated by the subscript D, which stand for deformation, in agreement with the nomenclature used along this chapter) are compared to the reference no-slip, FW configuration. The results shown in Fig. 7.14 for the whole range of analysed $\frac{\delta}{h}$ indicate an increasing non-dimensional Δp trend for increasing Re_m, with a different behaviour between

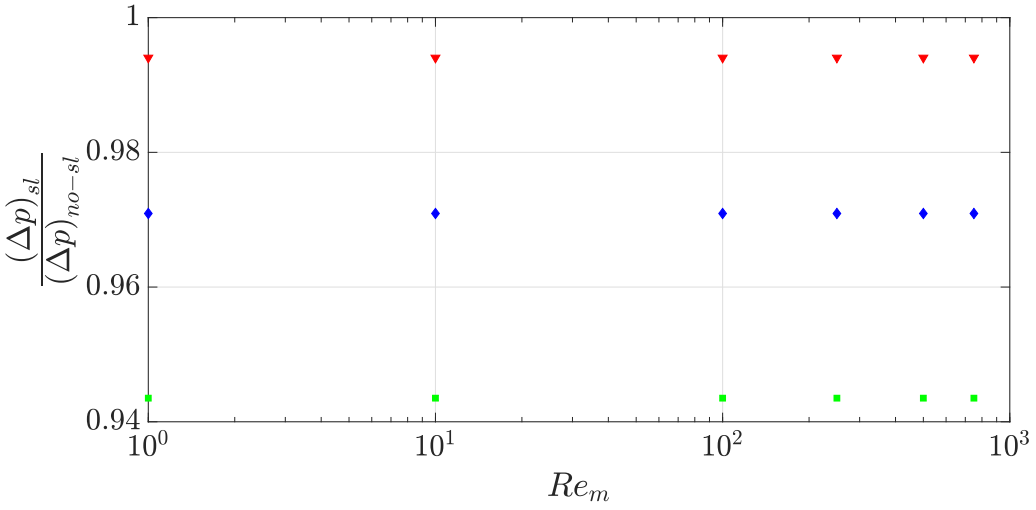

(a)

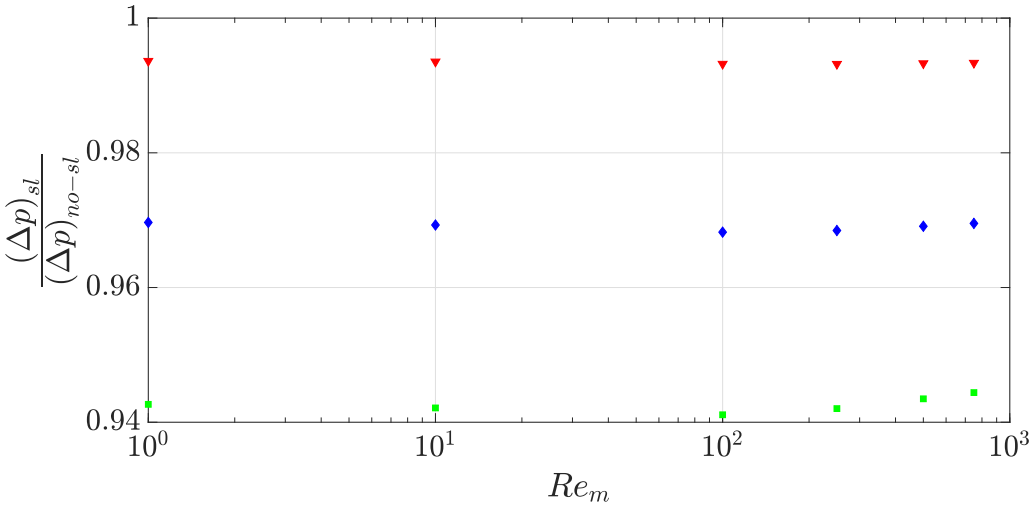

(b)

Figure 7.12 – Evolution of the normalised (with respect to the no-slip case featuring the same $\frac{\delta}{h}$) pressure loss Δp over the whole analysed Re_m range. (a), FW configuration with $\frac{\delta}{h} = 0$. (b), HD configuration with $\frac{\delta}{h} = 0.10$. ▼, $\ell_{sl} = 10\,\mu m$. ♦, $\ell_{sl} = 50\,\mu m$. ■, $\ell_{sl} = 100\,\mu m$. The same behaviour is retrieved for the intermediate cases: LD, ($\frac{\delta}{h} = 0.05$) and ID, ($\frac{\delta}{h} = 0.075$).

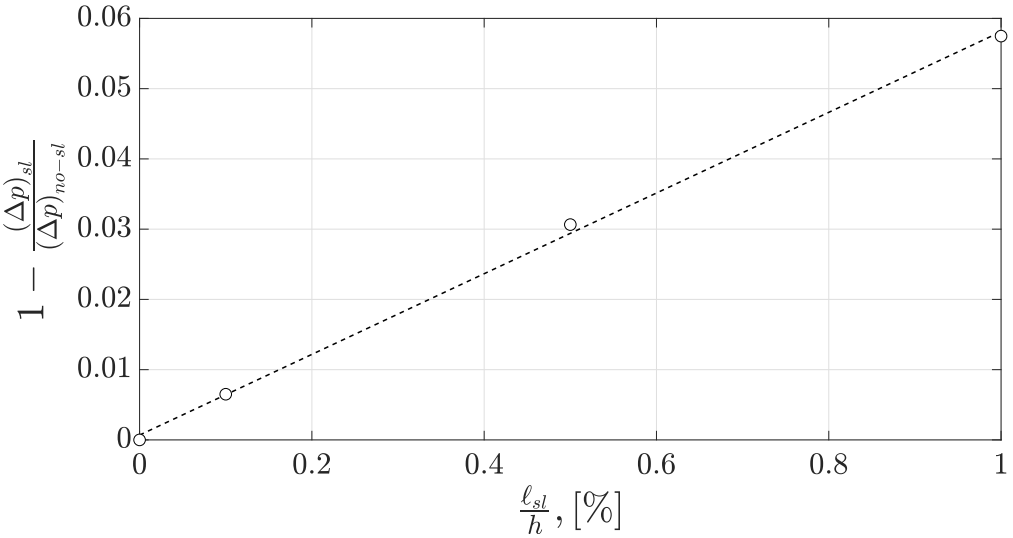

Figure 7.13 – Evolution of the normalised (with respect to the no-slip case featuring the same $\frac{\delta}{h}$) pressure loss Δp over the whole analysed $\frac{\ell_{sl}}{h}$ range. An average normalised pressure loss value is evaluated for each slip length over the whole analysed $\frac{\delta}{h}$ range. (- - -), best fit in the least-mean squares sense of the linear relation in Eq. 7.30.

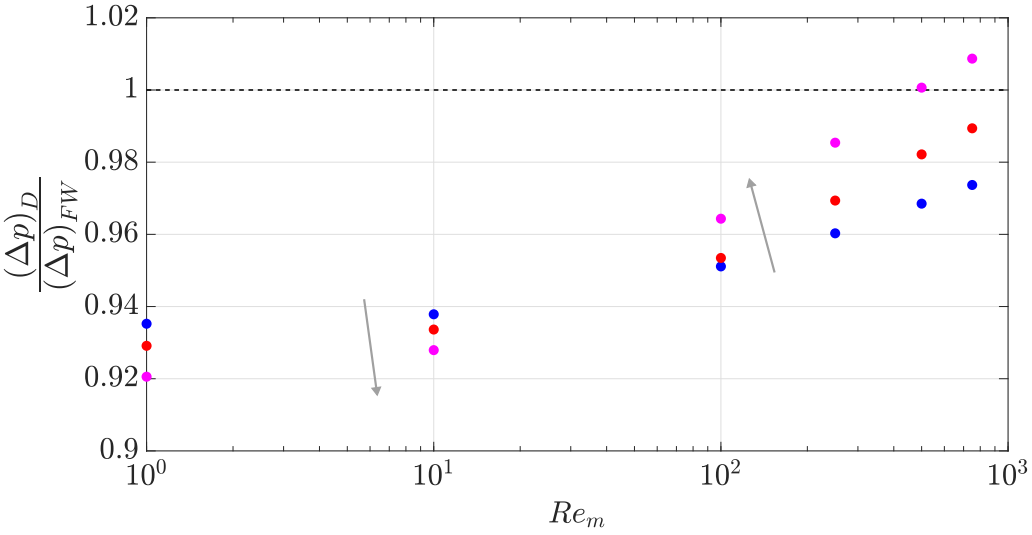

Figure 7.14 – Evolution of the normalised (with respect to the no-slip, flat wall case) pressure loss Δp over the whole analysed Re_m range for no-slip, wavy lower wall of the channel (the subscript D stands for deformation). ●, LD case ($\frac{\delta}{h} = 0.05$). ●, ID case ($\frac{\delta}{h} = 0.075$). ●, HD case ($\frac{\delta}{h} = 0.10$). (- - -), unitary reference value discriminating between pressure loss augmentation and decrease. The gray arrows indicate increasing $\frac{\delta}{h}$.

low ($Re_m < 10^2$) and high ($Re_m > 10^2$) Reynolds number regions. For low Re_m, the increasing $\frac{\delta}{h}$ enhances the pressure loss decrease with respect to the flat wall configuration, whereas for larger Re_m the trend is reversed. At $Re_m \geq 5 \times 10^2$ the HD wall deformation ($\frac{\delta}{h} = 0.10$) is large enough to determine an augmentation of the pressure loss with respect to the corresponding reference FW configuration. The trend reversal seems to occur in the proximity of the region where recirculation inside the valleys of the wavy wall was identified. To get more insight of the reasons of the described phenomena, some significant terms appearing in the integral momentum balance in Eq. 7.22 are analysed in more detail in the next section.

7.4.3 Integral Terms

Instead than looking only at Δp evaluated via the estimation of the dissipation term over the whole control volume, the relative weight of some major terms in the integral balances introduced in §7.3.1 can be investigated. However, due to the large amount of parameters, the evolution of the relative magnitude of the terms over the analysed ranges of Reynolds number and wall deformation is shown only for the no-slip wall case.

The presence of a wall undulation implies the appearance in the momentum balance in Eq. 7.22 of the pressure term $T_{p,bot} = -\int_{-\delta}^{\delta} p_{bot} dy$, which vanishes in the FW case. It is thus interesting to evaluate the magnitude of the identified pressure term at the bottom wall with respect to the corresponding stress contribution $T_{s,bot} = 2\mu_l \left(\int_{-\delta}^{\delta} S_{xx,bot} dy - \int_0^L S_{xy,bot} dx \right)$. The ratio between the two integral terms is reported in Fig. 7.15. The $T_{p,bot}$ term in the LD case at low Re_m resulted close to the zero value and negative, which explains its absence in the proposed logarithmic graph. This issue may be due to the low magnitude of the pressure term in the case of low wall deformation at low Reynolds number and the related approximations hidden in the discrete evaluation of the integrals. Intuitively, the magnitude of the pressure contribution at the lower wavy wall increases with the wave amplitude $\frac{\delta}{h}$. This trend is retrieved over the whole analysed Re_m range, implying that at sufficiently high $\frac{\delta}{h}$ and Re_m the pressure contribution may result larger than the corresponding stress term. Interestingly, for each $\frac{\delta}{h}$ the data at Re_m larger than the region of onset of recirculation suggest that:

$$\frac{T_{p,bot}}{T_{s,bot}} \sim Re_m^{\alpha_{ps}}, \tag{7.31}$$

which implies an exponential growth of the pressure contribution with respect to the stress term once backflow is present in the valleys of the wavy lower wall.

Since the stress term $T_{s,bot}$ considered in Fig. 7.15 was estimated with a wavy, lower wall, the question of the influence of the undulation on the stress contribution arises. To clarify this point, the $T_{s,bot}$ term is compared to the corresponding contribution at the top wall $T_{s,top} = 2\mu_l \int_0^L S_{xy,top} dx$. The same approach developed above is followed to retrieve the relative magnitude evolution shown in Fig. 7.16. At low Re_m, the relative magnitude of the components at the bottom and top walls is approximately the same. The difference between the $\frac{\delta}{h}$ values appearing at $Re_m = 1$ may be due to the fact that, for increasing wave amplitude, the stress on the bottom wall acts on a dimensional larger length. For increasing Re_m, the difference between the two integral terms increases. However, the variations are limited with respect to Fig. 7.15 (please note that only one decade is plotted on the vertical axis in Fig. 7.16). The $\frac{\delta}{h}$ augmentation appears to increase the difference between the stress components on the bottom and lower walls over the whole Re_m range. In the recirculation region, a power-law of the type introduced in Eq. 7.31 seems to well describe the relative behaviour of the two stress components, thus

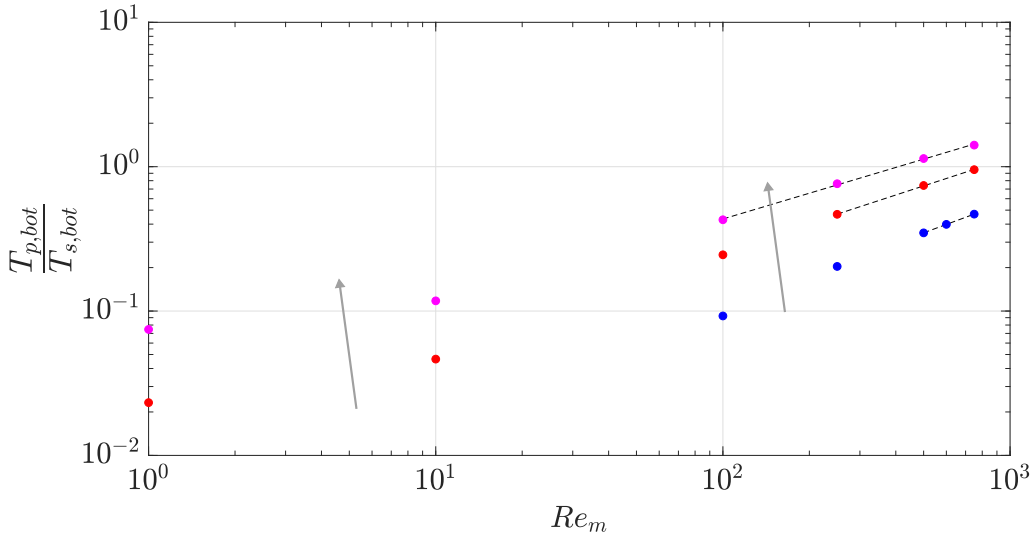

Figure 7.15 – Evolution of the relative magnitude of the pressure and stress terms at the lower wavy wall, in the no-slip case. •, LD case ($\frac{\delta}{h} = 0.05$, one additional point was added at $Re_m = 6 \times 10^2$). •, ID case ($\frac{\delta}{h} = 0.075$). •, HD case ($\frac{\delta}{h} = 0.10$). (- - -), best fit of Eq. 7.31 in the least-mean squares sense limited to the region where recirculation was detected. The gray arrows indicate increasing $\frac{\delta}{h}$.

implying a relative reduction (negative exponent) of the $T_{s,bot}$ magnitude with respect to $T_{s,top}$ for increasing Re_m.

Finally, the $T_{s,top}$ term considered in Fig. 7.16 was estimated at the top, flat wall of a channel with a bottom, wavy wall. Even if a macroscopic channel height h is considered, a possible influence of the lower wall undulation on the top wall may still exist. To clarify this point, the stress term $T_{s,top}$ at the top wall of a wavy channel is compared in Fig. 7.17 to the same term evaluated in the FW configuration. In fact, in Fig. 7.17 the relative magnitude of the stress term at the top wall in the wavy and flat configuration is shown to vary between $\approx -3\,\%$ at low Re_m and $\approx +5\,\%$ at the largest analysed Re_m. While in the low Re_m region a clear trend as a function of $\frac{\delta}{h}$ is not identifiable, once recirculation occurs data seems again to be well fitted by a power-law of the type discussed above. A limited but still non-negligible influence of the undulation of the lower, wavy wall is estimated on the behaviour of the stress term on the top, flat wall.

Overall, in this section a look was given to the integral terms appearing in the momentum balance in Eq. 7.22 describing the pressure and stress behaviours at the walls of the channel. At large Re_m and $\frac{\delta}{h}$, the stress contribution at the top wall was shown to increase with respect to the FW reference (see Fig. 7.17), and at the same time the pressure contribution at the lower, wavy wall was shown to become progressively more significant (see Fig. 7.15). These indications thus agree with the identified Δp trend in Fig. 7.14, which was shown to possibly increase with respect to the FW case for large enough Re_m and $\frac{\delta}{h}$.

The path towards a more detailed description of the detected phenomena can still be pursued by adopting a local approach to investigate the flow inside the valley of the lower, wavy wall. This is the subject of the next section.

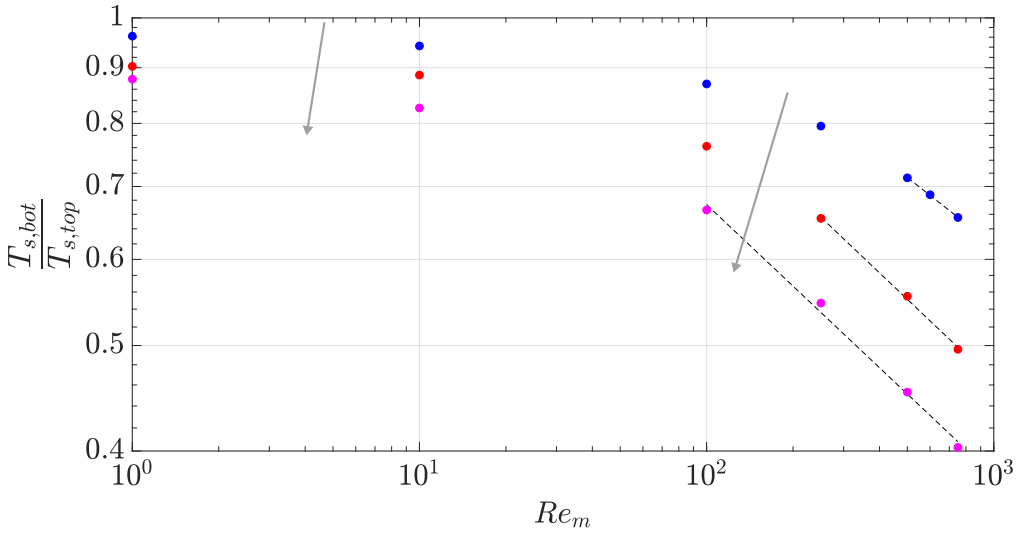

Figure 7.16 – Evolution of the relative magnitude of the stress terms at the bottom and top no-slip walls. •, LD case ($\frac{\delta}{h} = 0.05$, one additional point was added at $Re_m = 6 \times 10^2$). •, ID case ($\frac{\delta}{h} = 0.075$). •, HD case ($\frac{\delta}{h} = 0.10$). (- - -), line indicating the power-law connecting $T_{s,bot}$ to $T_{s,top}$ in the Re_m region where recirculation appeared. The gray arrows indicate increasing $\frac{\delta}{h}$.

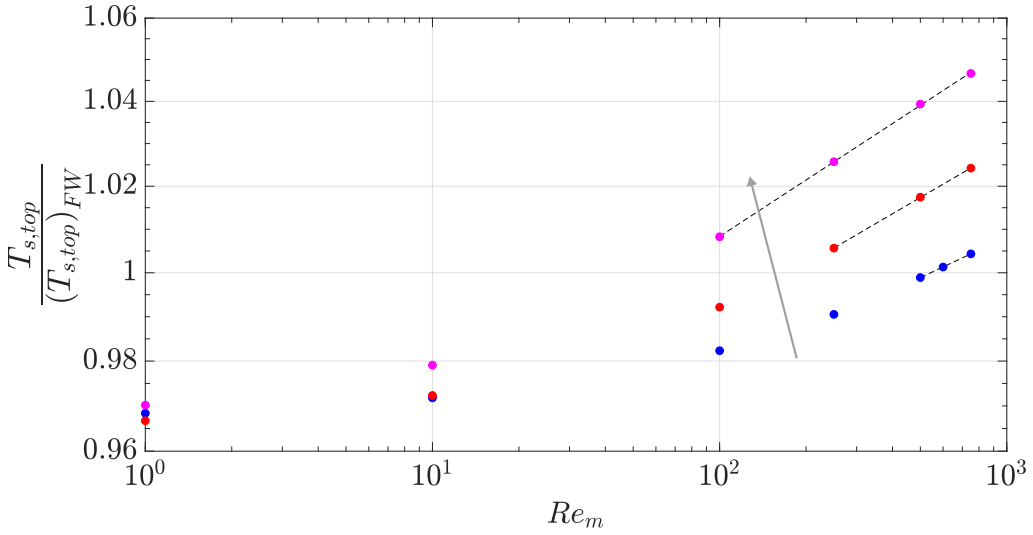

Figure 7.17 – Evolution of the relative magnitude of the stress terms at the top wall in the case of wavy and flat lower wall. •, LD case ($\frac{\delta}{h} = 0.05$, one additional point was added at $Re_m = 6 \times 10^2$). •, ID case ($\frac{\delta}{h} = 0.075$). •, HD case ($\frac{\delta}{h} = 0.10$). (- - -), line indicating the power-law connecting $T_{s,top}$ to $(T_{s,top})_{FW}$ in the Re_m region where recirculation appeared. The gray arrow indicates increasing $\frac{\delta}{h}$.

7.4.4 Local Approach

At low Re_m, the wall undulation was shown in Fig. 7.14 to result into a reduced Δp with respect to the FW case, and the trend was enhanced by a $\frac{\delta}{h}$ increase. The reasons may be understood via a direct investigation of the near wall region. An example of the quantities characterising the region near the lower wavy wall is reported in Fig. 7.18 in the case of a no-slip, HD configuration at $Re_m = 1$. The pressure field in the near-wall region is shown in Fig. 7.18(a), normalised with respect to its maximum value located at $\frac{x}{\Lambda} \approx 0.3$ and with the effect of the streamwise pressure gradient being subtracted. A slight asymmetry across the wave peak is noted, which is someway qualitatively similar to the results presented by Niavarani & Priezjev (2009), where the nature of the phenomenon was not discussed. The issue is detectable also in Fig. 7.18(b), where the same normalised pressure field evaluated at the lower wall is shown. In fact, the value at the wave peak $\frac{x}{\Lambda} \approx 0.5$ is evaluated via interpolation of the two next available points and results slightly lower than 97 %. Even if no clear demonstration can be given, the pressure field behaviour in the ascending and descending parts of the undulation is probably connected to the different nature of the flow in the two portions, which can be viewed as the flow in a convergent and a divergent section. Finally, the wall shear stress normalised by the corresponding flat wall case is reported in Fig. 7.18(c). The corrugated wall determines a peak of the stress at $\frac{x}{\Lambda} \approx 0.5$ which is approximately two times the value of the flat wall configuration. Conversely, a stress reduction is evaluated in the valley, where the positive values indicate the absence of recirculation. A quite good agreement is found with data from Niavarani & Priezjev (2009) at comparable wavenumber $\frac{2\pi\delta}{\Lambda}$, with the magnitude of the stress at the peak and in the valley dependent on the imposed geometry. Altogether, the sequence of regions with varying pressure and wall stress with respect to the reference flat configuration may determine an overall decrease of the pressure loss over the control volume, as was reported in Fig. 7.14, at least at very low Re_m where inertia effects do not dominate. A Re_m increase can then result into an augmentation of the adverse effect of the pressure acting on the ascending part of the wave and an onset of back-flow in the descending portion, possibly leading to detrimental effects on the pressure loss, as was shown in Fig. 7.14.

In fact, the progressive change of the Δp behaviour occurring in the analysed Re_m region is also influenced by the onset of recirculation inside the valleys of the lower wavy wall of the channel. As discussed in many available works (see e.g. Leneweit & Auerbach 1999), in an internal flow on a geometry with wavy walls the separation of the flow in the diverging portion of the wave is influenced by both ratios $\frac{\Lambda}{h}$ and $\frac{\delta}{h}$. Since $\frac{\Lambda}{h} = 1$ in this study, a $\frac{\delta}{h}$ increase is expected to promote the onset of recirculation at progressively lower Re_m. Based on the available data, an indication of the Re_m region where the onset of recirculation occurs is provided in Tab. 7.4, which resumes the ranges previously depicted in Fig. 7.11.

	LD	ID	HD
Re_m	250 - 500	100 - 250	10 - 100

Table 7.4 – Range of Re_m where the onset of flow separation inside the valley of the wavy, lower wall of the channel occurs (see also Fig. 7.11). The lower limit represents the last available simulation where recirculation is not detected. The higher limit represents the first available simulation where recirculation is detected.

A decreasing Re_m range for increasing $\frac{\delta}{h}$ is detected. As an example, $Re_m = 250$ is high enough for recirculation to occur in the HD and ID cases, while backflow is detected with the $\frac{\delta}{h} = 0.05$ of the LD configuration only for $Re_m \geq 500$. The corresponding detail of the flow in the valley at $Re_m = 250$ is reported in Fig. 7.19 in the LD and HD cases. The lower

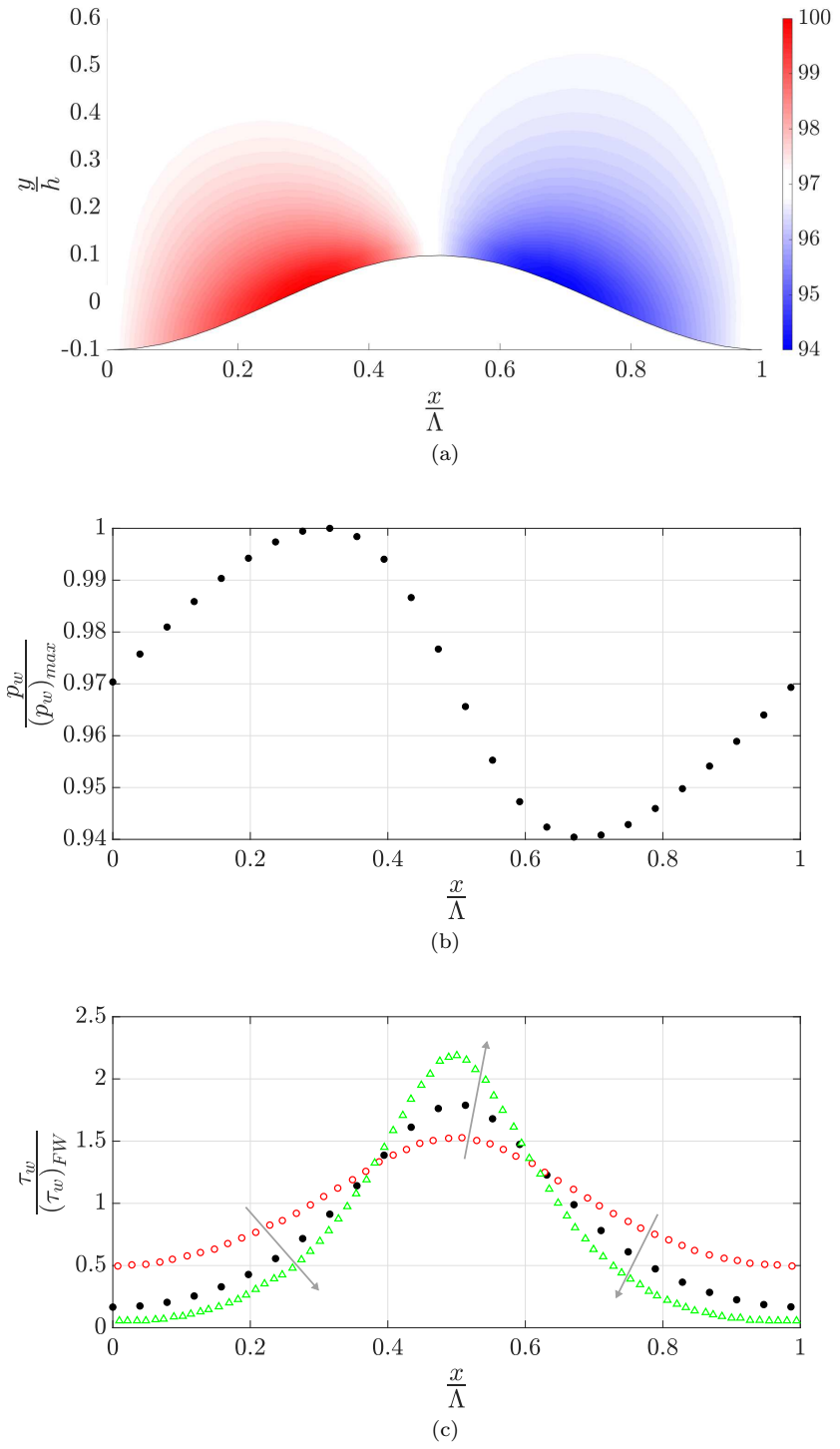

Figure 7.18 – Details of the near wall region quantities for the no-slip, HD case ($\frac{\delta}{h} = 0.10$) at $Re_m = 1$, along one non-dimensional wave $\frac{x}{\Lambda}$ of the channel lower wall. (a), pressure field normalised with respect to the maximum value located at $\frac{x}{\Lambda} \approx 0.3$ and where the streamwise pressure gradient effect has been subtracted. The color scale is expressed in percentage. (b), detail of the same quantity in (a) at the lower wall of the channel. (c), wall shear stress τ_w normalised with respect to the FW case. •, result of the performed DNS (wavenumber $\frac{2\pi\delta}{\Lambda} = 0.63$). For comparison purposes, the data extracted from Niavarani & Priezjev (2009) in the same operating conditions are reported: ○, $\frac{2\pi\delta}{\Lambda} = 0.28$. △, $\frac{2\pi\delta}{\Lambda} = 0.70$. The gray arrows indicate increasing wavenumber.

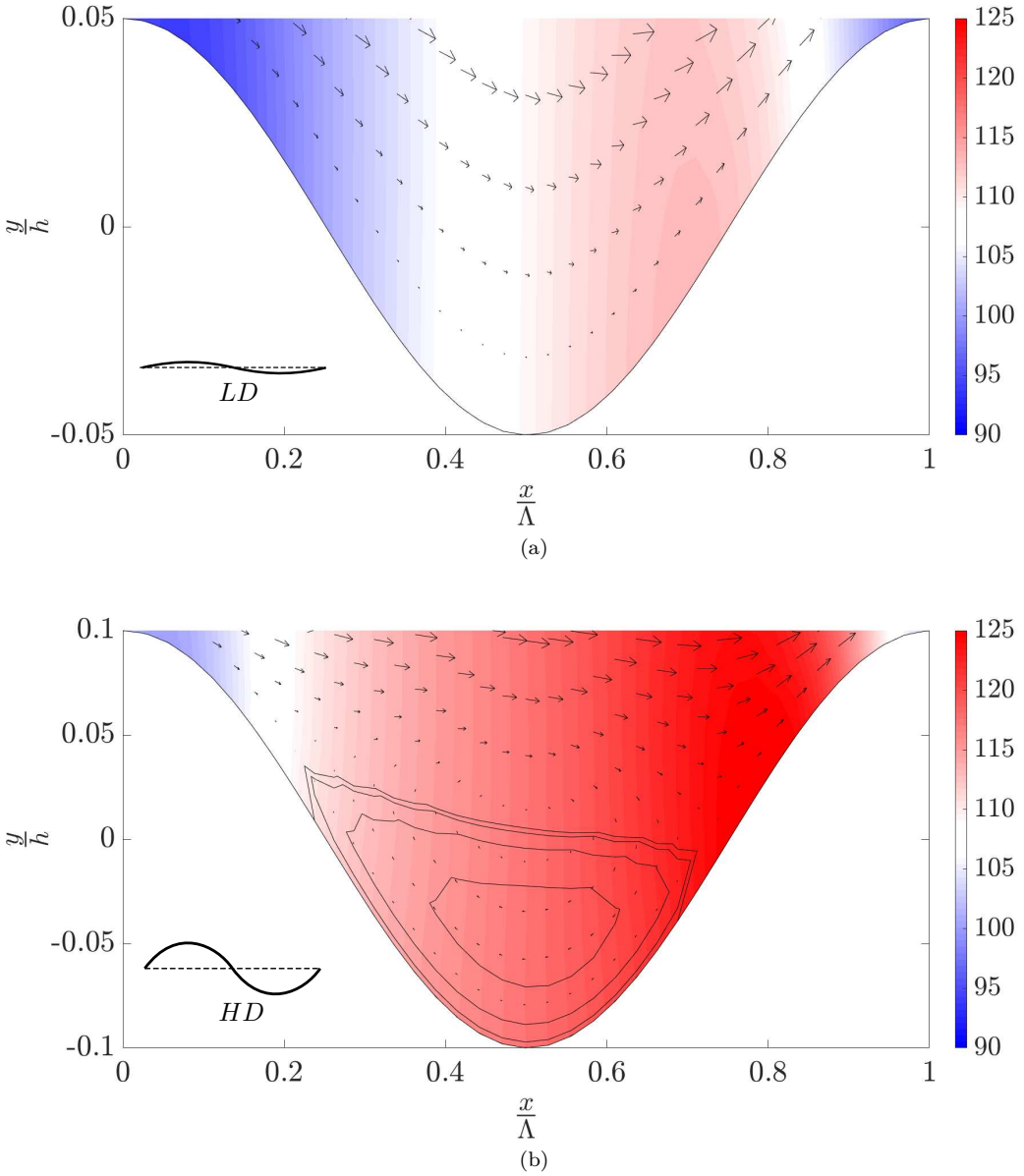

Figure 7.19 – Detail of the pressure and velocity fields in the valley of no-slip, wavy wall simulations at $Re_m = 250$. The color scale expressed in percentage describes the pressure normalised with the flat wall values and with the effect of the streamwise pressure gradient subtracted. The black arrows indicate the direction and magnitude of the velocity field. (a), LD configuration ($\frac{\delta}{h} = 0.05$). (b), HD configuration ($\frac{\delta}{h} = 0.10$). The streamlines indicate the region where backflow is detected.

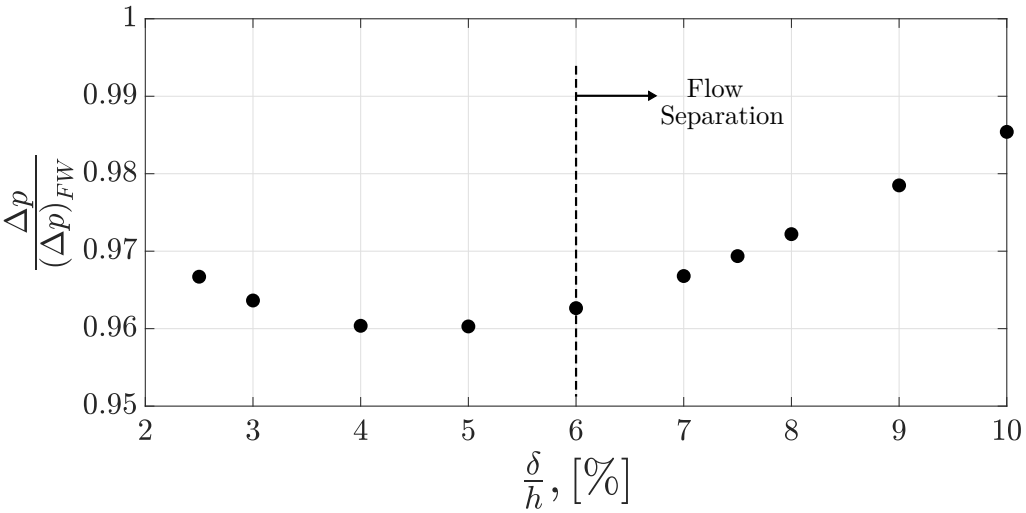

Figure 7.20 – Evolution of the normalised (with respect to the no-slip, flat wall case) pressure loss Δp at $Re_m = 250$ in the no-slip wall case, for a wall deformation $\frac{\delta}{h}$ in the range $0.025 - 0.10$. (- - -), first available simulation where backflow is detected inside the wavy wall valleys.

deformation $\frac{\delta}{h} = 0.05$ in Fig. 7.19(a) results into a smooth flow able to follow the wall undulation. The corresponding pressure field values increase of $\approx 10\,\%$ with respect to the FW case in the ascending part of the wave, while decrease approximately of the same amount in the region close to the peak. Conversely, the deformation augmentation in Fig. 7.19(b) determines the appearance of a region of backflow, highlighted by the evaluated streamlines. The corresponding pressure field reaches values $\approx 25\,\%$ larger than the FW configuration in the ascending part of the wave, whereas the minimum pressure is unvaried.

Obviously, more refined simulations along the Re_m axis should be executed to perform an accurate analysis on the effects of the wall deformation on the onset of flow separation. One preliminary indication of the $\frac{\delta}{h}$ effects was retrieved by focusing attention on $Re_m = 250$ and refining the available data in terms of wall deformation. The simulations were run only in the no-slip case, and the corresponding normalised pressure loss is reported in Fig. 7.20. The no-slip results vary in the range $\approx 96\,\%$ to $99\,\%$, coherently with what was shown in Fig. 7.14. In detail, starting from the lowest analysed $\frac{\delta}{h}$ values, the pressure loss decreases until the onset of backflow is reached. In fact, $\frac{\delta}{h} = 0.06$ is the first available simulation where negative streamwise velocity values were detected, and accordingly the normalised Δp increases with respect to the previous available value. This implies that the actual $\frac{\delta}{h}$ resulting into backflow appearance can be guessed to lie in the range $0.05 - 0.06$. In the framework of a refined analysis of the geometry effects on the onset of recirculation, the dissipation term on the integral energy balance could therefore be chosen as a parameter to quantitatively describe the phenomenon. This preliminary result could open an interesting perspective to analyse the slip length effects on the onset of recirculation in a wavy channel geometry. In fact, once detected the threshold $\frac{\delta}{h}$ (at fixed Re_m) where backflow appears in the no-slip case, refined simulations in terms of wall deformation could be run in the proximity of the threshold. The slip length at the wall could then be modified to investigate the effects of partial slip on the onset of flow separation inside the valleys.

7.5 Discussion

To resume, this chapter presented the results of a numerical approach that followed directly the results of the experimental campaigns on free falling SH spheres. In fact, the schematic reported in Fig. 6.44 underlying the interconnection between flow and air layer deformation can be considered as the starting point of the discussed numerical approach. In an attempt to achieve a simplified description of a macroscopic SH surface, a channel flow in laminar conditions was considered, where the air-liquid interface deformation was modelled via a fixed deformation of the channel lower wall and the slippage effect due to the air layer was modelled via a Navier condition. The ideal output would be an effective slip length model able to take into account all the possible effects influencing the actual slip at the wall. However, the attention was focused on the variation of the wave amplitude describing the deformed wall and on the magnitude of the imposed microscopic slip length, whose ranges were representative of macroscopic applications. The ℓ_{sl}^{eff} results in Fig. 7.11 showed that at low Re_m an increase of the wall deformation determines a decrease of the actual slip at the wall with respect to the imposed ℓ_{sl} value. The variation of the latter has negligible effects on ℓ_{sl}^{eff}. Conversely, for increasing Re_m the occurrence of flow separation in the valleys of the lower, wavy wall results into a progressively lower ℓ_{sl}^{eff}. In this case, the deformation augmentation is detrimental towards the achieved ℓ_{sl}^{eff}. This shows that depending on the flow typology in the diverging portion of the wave, the $\frac{\delta}{h}$ and $\frac{\ell_{sl}}{h}$ influence on ℓ_{sl}^{eff} may be different. To get more insight on the evidenced phenomena, a path from an integral approach towards a more detailed analysis was followed, which enable to highlight the role played by the pressure and stress terms in the momentum balance. The pressure contribution was shown in Fig. 7.15 to become progressively more important for increasing Re_m and $\frac{\delta}{h}$. The results are finally well supported by a local analysis of the phenomena occurring in the wall valleys, which allowed to provide additional details of the pressure and stress behaviour in the near-wall region.

Chapter 8

Conclusions and Perspectives

The main objective of this work was a contribution towards a deeper insight of the effects of the development of a boundary layer over a SH wall. This nature-inspired coating has attracted attention of scientists in the last twenty years since an air layer is trapped among the surface roughness elements when in contact with a liquid. In the framework of marine surface and underwater vessels considered in this work, this property may lead to significant friction reduction. The consequent possible hydrodynamic performance improvement, which implies an eventual fuel saving, perfectly takes place in today's environmental and economical context. To translate the complex real-life issue into a problem experimentally analysable at laboratory scale, the spherical geometry was chosen as bluff-body prototype. The large amount of literature available on reference spheres is accompanied by a lack of significant amount of data on the SH effects on this type of geometry. The merit of this work thus lies in the experimental analysis of SH coatings effects over a large range of operating conditions. To the knowledge of our team, this is probably one of the very first works covering such a large range. Furthermore, the experimental results were exploited as starting point of a numerical approach, whose objective was a first step towards a more robust modelling of the SH surface effects on the flow.

The SH coatings were produced by an in-house developed manufacturing procedure based on a low-cost spray technique suitable for large scale applications. Digital microscopy and goniometry were exploited to characterise the produced coatings, providing the necessary information to later connect the hydrodynamic performance results with the wall properties. The most relevant parameter describing the surface texture was found in the surface roughness size λ, which was varied during the manufacturing phase by embedding powders with different nominal particle size. All along the manuscript, λ was considered as an indication of the magnitude of the air layer thickness on the SH wall.

The experimental tests consisted in the free fall under gravity in a liquid at rest of reference and SH spheres. The analysed large range of Reynolds number was spanned by varying both the sphere (i.e. diameter) and liquid (i.e. water-glycerine mixtures with varying volumetric fractions) properties. The recorded drop videos were then post-processed via in-house implemented codes that allowed the reconstruction of the three-dimensional trajectory, together with the instantaneous velocity and acceleration profiles. The latter were of fundamental importance to analyse not only the terminal conditions but also the accelerating transient phase, where path instabilities were detected. The main findings could thus be resumed as a function of the considered falling regime:

- at low Reynolds number, the transversal motion of the falling sphere was negligible and

the SH coatings resulted into non-significant terminal drag variations with respect to the reference. A porous medium model was developed to assess the relative magnitude of the beneficial slip effect due to the presence of the air layer and the detrimental interaction between the air motion and the roughness elements;

- at intermediate Reynolds number, negligible SH coatings effects on terminal drag were still evaluated. However, early onset of transversal motion was detected in regimes where the break of the wake axisymmetry occurred. The latter was shown to possibly interact with the motion and deformation of the air layer initially trapped among the surface roughness elements. Two non-dimensional numbers were identified to describe the nature of this interaction: the Reynolds number, indicating the magnitude of the wake hydrodynamic perturbation and the Weber number, characterising the receptivity of the air layer to the wake hydrodynamic perturbation;
- at high Reynolds number, an enhancement of the air layer deformation initially detected at intermediate Reynolds number was found. The onset of significant transversal motion was promoted by SH coatings. This resulted into both drag augmentation and decrease, depending on the relative macroscopic air layer deformation with respect to the sphere size.

All together, these experimental results led to the development of a model describing the compliance mechanism of the air layer to the flow. If the hydrodynamic perturbation due to the wake is significant (i.e. Reynolds number range), the air layer receptivity (i.e. Weber number range) may result into its deformation and motion around the rear-side of the falling sphere. The subsequent variation of the wall boundary condition may lead to a modification of the vorticity production at the sphere surface, with effects on the vorticity evacuated by the wake, thus possibly modifying the characteristics of the latter.

Some limitations of the experimental tests towards the analysis of the near-wall phenomena were overcome by a numerical approach on an incompressible laminar channel flow. A macroscopic description of the SH coatings was adopted, by modelling the SH wall via a Navier partial slip condition and the air layer deformation via a fixed deformation of the channel wall. The main goal of such a kind of approach can be identified in the development of an effective slip length model. To do that, a performance indicator was identified via the implementation of an integral approach, which allowed for the definition of an equivalent pressure loss over the analysed control volume based on the estimation of the dissipation rate in the energy balance. The increase of the wall deformation generally resulted into reduced effective slip length with respect to the microscopic slip length imposed at the channel wall. To get more insight on the phenomenon, an attempt to separately describe the effects of wall deformation and of slip at the wall was performed. Depending on the relative deformation of the wall with respect to the channel height, beneficial or detrimental effects on the pressure loss were estimated. The analysis was further refined by investigating the relative weight of some integral terms appearing in the momentum balance. A progressively increasing contribution of the pressure term at the wavy wall was identified for increasing amplitude of the wall undulation. Finally, a local approach was presented to analyse in more detail the flow inside the valleys of the wavy wall, thus underlying the influence of the onset of flow separation on the presented results.

All in all, this study represents a contribution towards a more reliable and robust description of SH coatings effects, and many further research activities may take advantage of the presented results. Some of these developments were undertaken, in a preliminary way, in the last months of the thesis and are here briefly described.
First, a more exhaustive characterisation of the air layer as a function of the SH wall properties seems necessary. To achieve that, a possible innovative route to follow is the implementation

of a Schlieren-based technique, usually exploited to track the air-liquid interface in free-surface flows. No trace of the application of this type of technique on SH surfaces was found in available literature at the moment of redaction of this manuscript. The method exploits the shadow created by a back-light interacting with the surface of a non-opaque SH coating to estimate the average thickness of the air layer. In practice, the latter is estimated via the recording of high spatial resolution snapshots of the same non-opaque SH surface with and without air layer. The air layer disappearance is obtained via air dissolution into the liquid, by simply waiting a large enough amount of time. The principles of the technique together with some raw preliminary results are detailed in Appendix A.

Second, at low Reynolds number, the porous medium model developed in §6.1.2 proposed the tortuosity Θ to be the key quantity controlling the relative magnitude of beneficial slip and detrimental surface roughness effects on terminal drag of SH falling spheres. It appeared therefore straightforward to implement a method able to play on the Θ values. The availability of a 3D printer in the laboratory was thus exploited to design and manufacture a SH coating with controlled tortuosity. In detail, in order to assess the possibility to reduce drag by minimising tortuosity, the $\Theta \approx 1$ value was sought. The details of the manufacturing procedure are provided in Appendix E. In the same Appendix, the promising preliminary results in terms of terminal drag reduction are discussed.

Third, since the experimental falling sphere results evidenced the importance of both Reynolds and Weber numbers, a possible development could be represented by the execution of fixed sphere tests in a hydrodynamic tunnel, where the magnitude of the two parameters could be more easily separately controlled. In fact, the major limitation encountered in the analysis of the falling sphere experimental results was the inability to *a priori* control the exact values of the Reynolds and Weber numbers and to achieve a large number of combinations of the two parameters. Conversely, regions of the Reynolds-Weber space non-analysed via the falling sphere tests could easily be investigated in a hydrodynamic tunnel by modifying the dimensions of the studied body and the velocity of the flow. Moreover, the analysis of the wake behaviour via Laser Velocimetry (e.g. PIV) could provide some interesting information on the SH coatings effects, possibly confirming the experimental findings here presented. In fact, the air layer compliance mechanism depicted in Fig. 6.44 guessed an influence of the SH coatings on the amount of vorticity evacuated in the wake. A quantitative investigation of the mean and instantaneous velocity field in the wake could thus provide the necessary information to further validate the experimental results presented in this manuscript. A vertical hydrodynamic tunnel was designed and manufactured, where the flow is driven by gravity. Based on the typical size of the body to be studied and on the attainable flow velocity, a largest $Re \sim 10^3$ value can be investigated. The experimental set-up is thus suited to study the region of occurrence of wake transitions of a fixed sphere. The investigation of a higher Re regime could be pursued by further exploiting the collaboration with LTRAC Laboratory, Monash University, Melbourne, Australia. The results of the wake investigation of reference and SH spheres are not included in this manuscript due to their preliminary nature. Further efforts are needed in the future to obtain the desired information of the SH coatings effects on the body wake.

Finally, the modelling approach followed in the numerical part of this study could be further extended towards more challenging operating conditions, i.e. turbulent flows. In fact, the simplified approach implemented in this manuscript provided results someway in good agreement, at least qualitatively, with experimental results. The air-liquid interface deformation was found in both cases to strongly impact the flow over the SH surface. The eventually retrieved scaling laws could reveal useful towards the modelling of SH coatings behaviour, thus avoiding a full resolution of the problem. In fact, when interest is put on the description of a macroscopic SH surface, the complete resolution of the problem would imply the analysis of a multiphase flow, with scales

going from the microscopic texture up to the macroscopic geometry of the domain. This appears extremely challenging with the current computational resources. This kind of approach could be fruitfully followed further extending the collaboration with Pr. Alessandro Bottaro, Universitá degli Studi di Genova, Scuola Politecnica, Dipartimento di Ingegneria Civile, Chimica e Ambientale, or with other teams. The complementarity experiments - numerics will allow to achieve useful information that would not be accessible by exploiting only one of the two approaches, e.g. by numerically analysing fields or regimes that are not easily experimentally retrievable. Preliminary turbulent DNS in a channel configuration with a bump on the partial slip lower wall were run, which could provide interesting information on the influence of the deformed SH interface on the near-wall quantities of the flow. Since further effort is required in the simulation analysis, the preliminary results of the performed DNS are not included in this study.

Bibliography

Achenbach, E. 1972 Experiments on the flow past spheres at very high Reynolds numbers. *J. Fluid Mech.* **54**, 565–575.

Achenbach, E. 1974 The effects of surface roughness and tunnel blockage on the flow past spheres. *J. Fluid Mech.* **65**, 113–125.

Ahmmed, K. M. T., Patience, C. & Kietzig, A.-M. 2016 Internal and external flow over laser-textured superhydrophobic polytetrafluoroethylene (PTFE). *ACS Appl. Mater. Interfaces* **8**, 27411–27419.

Airbus 2019*a* Webpage. `https://www.airbus.com/newsroom/press-releases/en/2019/06/how-the-albatross-is-inspiring-next-generation-of-aircraft-wings.html`, Accessed: September 2019.

Airbus 2019*b* Webpage. `https://www.airbus.com/newsroom/news/en/2019/07/airbus-conceptual-airliner-to-inspire-new-generation-engineers.html`, Accessed: September 2019.

Alinovi, E. 2018 Modeling the flow over superhydrophobic and liquid-impregnated surfaces. PhD thesis, Università degli Studi di Genova.

Aljallis, E., Sarshar, M. A., Datla, R., Sikka, V., Jones, A. & Choi, C.-H. 2013 Experimental study of skin friction drag reduction on superhydrophobic flat plates in high Reynolds number boundary layer flow. *Phys. Fluids* **25**, 025103.

Amromin, E., Kopriva, J., Arndt, R. E. A. & Wosnik, M. 2006 Hydrofoil drag reduction by partial cavitation. *J. Fluid. Eng.* **128**, 931–936.

Atanov, Y. A. & Berdenikov, A. I. 1981 Viscous flow of liquid glycerin-polyethyleneglycol-water mixtures. *J. Eng. Phys.* **41** (4), 1104–1107.

Auton, T. R., Hunt, J. C. R. & Prud'homme, M. 1988 The force exerted on a body in inviscid unsteady non-uniform rotational flow. *J. Fluid Mech.* **197**, 241–257.

Barish, J. A. & Goddard, J. M. 2013 Anti-fouling surface modified stainless steel for food processing. *Food Bioprod. Process.* **91**, 352–361.

Barthlott, W. & Neinhuis, C. 1997 Purity of the sacred lotus, or escape from contamination in biological surfaces. *Planta* **202**, 1–8.

Basset, A. B. 1888 *A Treatise on Hydrodynamics*. Cambridge: Deighton, Bell and Co. London: George Bell and Sons.

Batchelor, G. K. 1967 *An Introduction to Fluid Dynamics*. Cambridge University Press.

Bear, J. 1988 *Dynamics of fluids in porous media*. Dover Publications Inc.

Bhushan, B. & Jung, Y. C. 2011 Natural and biomimetic artificial surfaces for superhydrophobicity, self-cleaning, low adhesion, and drag reduction. *Prog. Mater. Sci.* **56**, 1–108.

Bigas, M., Cabruja, E., Forest, J. & Salvi, J. 2006 Review of CMOS image sensors. *Microelectron. J.* **37**, 433–451.

Bogdevich, V. G., Kobets, G. F., Kozyuk, G. S., Migirenko, G. S., Mikuta, V. I.,

Mironov, B. P., Novikov, B. G., Tétyanko, V. A. & Shtatnov, Y. V. 1980 Some questions relating to the control of flows near a wall. *J. Appl. Mech. Tech. Phys.* **21** (5), 657–665.

Boussinesq, M. J. 1885 Sur la résistance qu'oppose un liquide indéfini en repos, sans pesanteur, au mouvement varié d'une sphère solide qu'il mouille sur toute sa surface, quand les vitesses restent bien continues et assez faibles pour que leurs carrés et produits soient négligeables. In *Comptes Rendus Hebdomadaires des Séances de l'Académie des Sciences*, , vol. 100, pp. 935–937. Paris, Gauthier-Villars, Imprimeur-Libraire.

Bradley, D. & Roth, G. 2007 Adaptive thresholding using integral image. *J. Graph. Tools* **12** (2), 13–21.

Brennen, C. E. 2014 *Cavitation and Bubble Dynamics*. Cambridge University Press.

Brizard, M., Megharfi, M., Mahé, E. & Verdier, C. 2005 Design of a high precision falling-ball viscometer. *Rev. Sci. Instrum.* **76**, 025109.

Buades, A., Coll, B. & Morel, J. M. 2005 A review on image denoising algorithms, with a new one. *Multiscale Model. Simul.* **4** (2), 490–530.

Burcher, R. & Rydill, L. 1994 *Concepts in Submarine Design*. Cambridge Ocean Technology Series, Cambridge University Press.

Byon, C., Nam, Y., Kim, S. J. & Ju, Y. S. 2010 Drag reduction in stokes flows over spheres with nanostructured superhydrophilic surfaces. *J. Appl. Phys.* **107**, 066102.

Carlson, D. R., Widnall, S. E. & Peeters, M. F. 1982 A flow-visualization study of transition in plane Poiseuille flow. *J. Fluid Mech.* **121**, 487–505.

Cartagena, E. J. G., Arenas, I., Bernardini, M. & Leonardi, S. 2018 Dependence of the drag over super hydrophobic and liquid infused surfaces on the textured surface and weber number. *Flow Turbul. Combust.* **100**, 945–960.

Cassie, A. B. D. & Baxter, S. 1944 Wettability of porous surfaces. *T. Faraday Soc.* **40**, 546–551.

Castagna, M., Eisfelder, M. P., Taylor, H., Mazellier, N., Kourta, A. & Soria, J. 2018*a* Effects of super-hydrophobic coatings on free falling spheres. In 21^{st} *Australasian Fluid Mechanics Conference, Adelaide, Australia. December 10-13*.

Castagna, M., Mazellier, N. & Kourta, A. 2017 Super-hydrophobic coating effects on the drag of a sphere. In $23^{ème}$ *Congrès Français de Mécanique, Lille, France. August 28 to September 1*.

Castagna, M., Mazellier, N. & Kourta, A. 2018*b* Wake of super-hydrophobic falling spheres: influence of the air layer deformation. *J. Fluid Mech.* **850**, 646–673.

Castagna, M., Mazellier, N. & Kourta, A. 2019*a* Effect of the interface curvature on the flow on super-hydrophobic surfaces. In *European Drag Reduction and Flow Control Meeting, Bad Herrenalb, Germany. March 26-29*.

Castagna, M., Mazellier, N. & Kourta, A. 2019*b* Transition to turbulence of the wake of super-hydrophobic spheres. In 11^{th} *International Symposium on Turbulence and Shear Flow Phenomena, Southampton, United Kingdom. July 30 to August 2*.

Castagna, M., Mazellier, N., Passaggia, P.-Y. & Kourta, A. 2019*c* Modelling the influence of roughness distribution on the effectiveness of super-hydrophobic coatings in laminar flows: a porous medium approach. *Phys. Rev. Fluids* **Submitted**.

Ceccio, S. L. 2010 Friction drag reduction of external flows with bubble and gas injection. *Annu. Rev. Fluid Mech.* **42**, 183–203.

Chang, E. J. & Maxey, M. R. 1995 Unsteady flow about a sphere at low to moderate Reynolds number. Part 2. Accelerated motion. *J. Fluid Mech.* **303**, 133–153.

Chassaing, P. 2000 *Mécanique des Fluides*. Collection POLYTECH, CÉPADUÈS-ÉDITION.

Cheng, N.-S. 2008 Formula for the viscosity of a glycerol-water mixture. *Ind. Eng. Chem. Res.* **47**, 3285–3288.

Cheng, N.-S. 2009 Comparison of formulas for drag coefficient and settling velocity of spherical particles. *Powder Technol.* **189**, 395–398.

Cherubini, S., De Tullio, M. D., De Palma, P. & Pascazio, G. 2013 Transient growth in the flow past a three-dimensional smooth roughness element. *J. Fluid Mech.* **724**, 642–670.

Cherukat, P., Na, Y. & Hanratty, T. J. 1998 Direct numerical simulation of a fully developed turbulent flow over a wavy wall. *Theoret. Comp. Fluid Dyn.* **11**, 109–134.

Choi, C.-H., Ulmanella, U., Kim, J., Ho, C.-M. & Kim, C.-J. 2006 Effective slip and friction reduction in nanograted superhydrophobic microchannels. *Phys. Fluids* **18**, 087105.

Clark III, H. & Deutsch, S. 1991 Microbubble skin friction reduction on an axisymmetric body under the influence of applied axial pressure gradients. *Phys. Fluids* **3** (12), 2948–2954.

Clift, R., Grace, J. R. & Weber, M. E. 1978 *Bubbles, Drops, and Particles*. Academic Press, Inc.

Cossu, C. & Morino, L. 2000 On the instability of a spring-mounted circular cylinder in a viscous flow at low Reynolds numbers. *J. Fluids Struct.* **14**, 183–196.

Coustols, E. & Schmitt, V. 1990 Synthesis of experimental riblet studies in transonic conditions. In *Turbulence Control by Passive Means*, pp. 123–140. Kluwer Academic Publishers.

Cuenot, B., Magnaudet, J. & Spennato, B. 1997 The effects of slightly soluble surfactants on the flow around a spherical bubble. *J. Fluid Mech.* **339**, 25–53.

Daniello, R. J., Waterhouse, N. E. & Rothstein, J. P. 2009 Drag reduction in turbulent flows over superhydrophobic surfaces. *Phys. Fluids* **21**, 085103.

Dean, B. & Brushan, B. 2010 Shark-skin surfaces for fluid-drag reduction in turbulent flow: a review. *Phil. Trans. R. Soc. A* **368**, 4775–4806.

Deutsch, S. & Castano, J. 1986 Microbubble skin friction reduction on an axisymmetric body. *Phys. Fluids* **29** (11), 3590–3597.

Di Felice, R. 1996 A relationship for the wall effect on the settling velocity of a sphere at any flow regime. *Int. J. Multiphase Flow* **22** (3), 527–533.

Di Felice, R., Gibilaro, L. G. & Foscolo, P. U. 1995 On the hindered settling velocity of spheres in the inertial flow regime. *Chem. Eng. Sci.* **50** (18), 3005–3006.

Drelich, J. 2013 Guidelines to measurements of reproducible contact angles using a sessile-drop technique. *Surf. Innov.* **1**, 248–254.

Drelich, J., Chibowski, E., Meng, D. D. & Terpilowsli, K. 2011 Hydrophilic and superhydrophilic surfaces and materials. *Soft Matter* **7**, 9804–9828.

Einzel, D., Panzer, P. & Liu, M. 1990 Boundary condition for fluid flow: curved or rough surfaces. *Phys. Rev. Lett.* **64** (19), 2269–2272.

Elbing, B. R., Winkel, E. S., Lay, K. A., Ceccio, S. L., Dowling, D. R. & Perlin, M. 2008 Bubble-induced skin-friction drag reduction and the abrupt transition to air-layer drag reduction. *J. Fluid Mech.* **612**, 201–236.

Ellingsen, K. & Risso, F. 2001 On the rise of an ellipsoidal bubble in water: oscillatory paths and liquid-induced velocity. *J. Fluid Mech.* **440**, 235–268.

Epps, B. & Truscott, T. T. 2010 Evaluating derivatives of experimental data using smoothing splines. *Mathematical Methods in Engineering International Symposium, IPC, Coimbra, Portugal* pp. 29–38.

Ern, P., Risso, F., Fabre, D. & Magnaudet, J. 2012 Wake-induced oscillatory paths of bodies freely rising or falling in fluids. *Annu. Rev. Fluid Mech.* **44**, 97–121.

Errico, O. & Stalio, E. 2015 Direct numerical simulation of low-Prandtl number turbulent convection above a wavy wall. *Nucl. Eng. Des.* **290**, 87–98.

Fabre, D., Auguste, F. & Magnaudet, J. 2008 Bifurcations and symmetry breaking in the wake of axisymmetric bodies. *Phys. Fluids* **20**, 051702.

Faxén, H. 1922 Der widerstand gegen die bewegung einer starren kugel in einer z̈hen flüssigkeit, die zwischen zwei parallelen ebenen wänden eingeschlossen ist. *Ann. Phys.* **373** (10), 89–119.

Fernandes, P. C., Ern, P., Risso, F. & Magnaudet, J. 2008 Dynamics of axisymmetric bodies rising along a zigzag path. *J. Fluid Mech.* **606**, 209–223.

Fernandes, P. C., Risso, F., Ern, P. & Magnaudet, J. 2007 Oscillatory motion and wake instability of freely rising axisymmetric bodies. *J. Fluid Mech.* **573**, 479–502.

Feuvrier, A. 2015 Contrôle bio-inspiré d'un sillage turbulent par stratégie passive ou auto-adaptative. PhD thesis, Université d'Orléans.

Fidleris, B. & Whitmore, R. L. 1961 Experimental determination of the wall effect for spheres falling axially in cylindrical vessels. *Br. J. Appl. Phys.* **12**, 490–494.

Flickr Gallery 2019 Webpage. `https://www.flickr.com/photos/rachelyin/3203932476/`, Accessed: September 2019.

Flude, M. J. C. & Daborn, J. E. 1982 Viscosity measurement by means of falling spheres compared with capillary viscometry. *J. Phys. E: Sci. Instrum.* **15**, 1313–1321.

OpenFOAM Foundation 2019 Webpage. `https://www.openfoam.org`, Accessed: September 2019.

Francis, A. W. 1933 Wall effect in falling ball method for viscosity. *Physics* **4**, 403–406.

Fukuda, K., Tokunaga, J., Nobunaga, T., Nakatani, T., Iwasaki, T. & Kunitake, Y. 2000 Frictional drag reduction with air lubricant over a super-waterrepellent surface. *J. Mar. Sci. Technol.* **5**, 123–130.

Gad-El-Hak, M. 2000 *Flow Control. Passive, Active, and Reactive Flow Management*. Cambridge University Press.

Galper, A. & Miloh, T. 1995 Dynamic equations of motion for a rigid or deformable body in an arbitrary non-uniform potential flow field. *J. Fluid Mech.* **295**, 91–120.

García-Mayoral, R. & Jiménez, J. 2011 Drag reduction by riblets. *Phil. Trans. R. Soc. A* **369**, 1412–1427.

Genzer, J. & Efimenko, K. 2006 Recent developments in superhydrophobic surfaces and their relevance to marine fouling: a review. *Biofouling* **22** (5), 339–360.

Ghidersa, B. & Dušek, J. 2000 Breaking of axisymmetry and onset of unsteadiness in the wake of a sphere. *J. Fluid Mech.* **423**, 33–69.

Goldburg, A. & Florsheim, B. H. 1966 Transition and strouhal number for the incompressible wake of various bodies. *Phys. Fluids* **9** (1), 45–50.

Granville, P. S. 1976 Elements on the drag of underwater bodies. *Tech. Rep.* SPD-672-01. Naval Sea Systems Command, Washington, DC.

Gruncell, B. R. K., Sandham, N. D. & McHale, G. 2013 Simulations of laminar flow past a superhydrophobic sphere with drag reduction and separation delay. *Phys. Fluids* **25**, 043601.

Gumowski, K., Miedzik, J., Goujon-Durand, S., Jenffer, P. & Wesfreid, J. E. 2008 Transition to a time-dependent state of fluid flow in the wake of a sphere. *Phys. Rev. E* **77**, 0555308(R).

Haberman, W. L. & Sayre, R. M. 1958 Motion of rigid and fluid spheres in stationary and moving liquids inside cylindrical tubes. *Tech. Rep.* Rep. No. 1143. Departement of the Navy, David Taylor Model Basin.

Henoch, C., Krupenkin, T. N., Kolodner, P., Taylor, J. A., Hodes, M. S., Lyons,

A. M., Peguero, C. & Breuer, K. 2006 Turbulent drag reduction using superhydrophobic surfaces. In 3^{rd} *AIAA Flow Control Conference, San Francisco, California, USA. June 5-8*.

Horowitz, M. & Williamson, C. H. K. 2010*a* The effect of Reynolds number on the dynamics and wakes of freely rising and falling spheres. *J. Fluid Mech.* **651**, 251–294.

Horowitz, M. & Williamson, C. H. K. 2010*b* Vortex-induced vibration of a rising and falling cylinder. *J. Fluid Mech.* **662**, 352–383.

Howe, M. 2002 *Theory of Vortex Sound*. Cambridge Texts in Applied Mathematics, Cambridge University Press.

Howe, M. S. 1995 On the force and moment on a body in an incompressible fluid, with application to rigid bodies and bubbles at high and low Reynolds numbers. *Q. J. Mech. Appl. Math.* **48**, 401–426.

Hudson, J. D., Dykhno, L. & Hanratty, T. J. 1996 Turbulence production in flow over a wavy wall. *Exp. Fluids* **20**, 257–265.

IEA 2019 Webpage. `https://www.iea.org/tcep/transport/`, Accessed: September 2019.

IMO 2019 MARPOL Convention. `http://www.imo.org/en/about/conventions/listofconventions/pages/international-convention-for-the-prevention-of-pollution-from-ships-(marpol).aspx`, Accessed: September 2019.

Issa, R. I. 1985 Solution of the implicitly discretised fluid flow equations by operator-splitting. *J. Comput. Phys.* **62**, 40–65.

Jasak, H. 1996 Error analysis and estimation for the finite volume method with applications to fluid flows. PhD thesis, Imperial College of Science, Technology and Medecine.

Jenny, M., Bouchet, G. & Dušek, J. 2003 Nonvertical ascension or fall of a free sphere in a Newtonian fluid. *Phys. Fluids* **15** (1), 9–12.

Jenny, M., Dušek, J. & Bouchet, G. 2004 Instabilities and transition of a sphere falling or ascending freely in a Newtonian fluid. *J. Fluid Mech.* **508**, 201–239.

Jiménez, J. 1994 On the structure and control of near wall turbulence. *Phys. Fluids* **6**, 944–953.

Johnson, T. A. & Patel, V. C. 1999 Flow past a sphere up to a Reynolds number of 300. *J. Fluid Mech.* **378**, 19–70.

Joubert, P. N. 2004 Some aspects of submarine design Part 1. Hydrodynamics. *Tech. Rep.* DSTO-TR-1622. Departement of Defence, Australian Government.

Khalighi, Y., Mani, A., Ham, F. & Moin, P. 2010 Prediction of sound generated by complex flows at low Mach numbers. *AIAA Journal* **48** (2), 306–316.

Kim, H. & Park, H. 2019 Diffusion characteristics of air pockets on hydrophobic surfaces in channel flow: Three-dimensional measurement of air-water interface. *Phys. Rev. Fluids* **4**, 074001.

Kim, I., Elghobashi, S. & Sirignano, W. A. 1998 On the equation for spherical-particle motion: effect of Reynolds and acceleration numbers. *J. Fluid Mech.* **367**, 221–253.

Kim, J., Moin, P. & Moser, R. 1987 Turbulence statistics in fully developed channel flow at low reynolds number. *J. Fluid Mech.* **177**, 133–166.

Kim, N., Kim, H. & Park, H. 2015 An experimental study on the effects of rough hydrophobic surfaces on the flow around a circular cylinder. *Phys. Fluids* **27**, 085113.

Koch, K., Bhushan, B., Jung, Y. C. & Barthlott, W. 2009 Fabrication of artificial lotus leaves and significance of hierarchical structure for superhydrophobicity and low adhesion. *Soft Matter* **5**, 1386–1393.

Lackenby, H. 1962 The thirty-fourth Thomas Lowe Gray Lecture: Resistance of ships, with special reference to skin friction and hull surface condition. *Proc. Instn. Mech. Eng.* **176**, 981–1014.

Lamb, Sir H. 1945 *Hydrodynamics*. Sixth Edition, First American Edition, Dover Publications, Inc., New York.

Landweber, L. & Miloh, T. 1980 Unsteady Lagally theorem for multipoles and deformable bodies. *J. Fluid Mech.* **96**, 33–46.

Lapple, C. E. & Sheperd, C. B. 1940 Calculation of particle trajectories. *Ind. Eng. Chem.* **32**, 605–617.

Lauga, E., Brenner, M. & Stone, H. 2007 Microfluidics: The no-slip boundary condition. In *Springer Handbook of Experimental Fluid Mechanics* (ed. C. Tropea, A. L. Yarin & J. F. Foss), chap. 19, pp. 1219–1240. Springer.

Lauga, E. & Stone, H. A. 2003 Effective slip in pressure-driven Stokes flow. *J. Fluid Mech.* **489**, 55–77.

Lawrence, C. J. & Mei, R. 1995 Long-time behaviour of the drag on a body in impulsive motion. *J. Fluid Mech.* **283**, 307–327.

Leal, L. G. 1989 Vorticity transport and wake structure for bluff bodies at finite Reynolds number. *Phys. Fluids* **1**, 124–131.

Lee, C. & Kim, C.-J. 2011 Underwater restoration and retention of gases on superhydrophobic surfaces for drag reduction. *Phys. Rev. Lett.* **106**, 014502.

Lee, C. & Kim, C.-J. 2012 Wetting and active dewetting processes of hierarchically constructed superhydrophobic surfaces fully immersed in water. *J. Microelectromech. S.* **21** (3), 712–720.

Legendre, D., Lauga, E. & Magnaudet, J. 2009 Influence of slip on the dynamics of two-dimensional wakes. *J. Fluid Mech.* **633**, 437–447.

Leidenfrost, J. G. 1756 De aquae communis nonnullis qualitatibus tractatus. `https://books.google.fr/books?id=r3JgAAAAcAAJ`.

Leneweit, G. & Auerbach, D. 1999 Detachment phenomena in low Reynolds number flows through sinusoidally constricted tubes. *J. Fluid Mech.* **387**, 129–150.

Lighthill, M. J. 1952 On sound generated aerodynamically. I. General theory. *Proc. R. Soc. Lond. Series A. Math. Phys.* **211** (1107), 564–587.

Liu, X., Tanaka, M. & Okutomi, M. 2013 Single-image noise level estimation for blind denoising. *IEEE Trans. Image Process.* **22** (12), 5226–5237.

Lommatzsch, T., Megharfi, M., Mahe, E. & Devin, E. 2001 Conceptual study of an absolute falling-ball viscometer. *Metrologia* **38**, 531–534.

Lovalenti, P. M. & Brady, J. F. 1993 The hydrodynamic force on a rigid particle undergoing arbitrary time-dependent motion at small Reynolds number. *J. Fluid Mech.* **256**, 561–605.

Luchini, P., Manzo, F. & Pozzi, A. 1991 Resistance of a grooved surface to parallel flow and cross-flow. *J. Fluid Mech.* **228**, 87–109.

Lyotard, N., Shew, W. L., Bocquet, L. & Pinton, J.-F. 2007 Polymer and surface roughness effects on the drag crisis for falling spheres. *Eur. Phys. J. B* **60**, 469–476.

Maass, C. & Schumann, U. 1996 Direct numerical simulation of separated turbulent flow over a wavy boundary. In *Flow Simulation with High-Performance Computers II* (ed. E. H. Hirschel), pp. 227–241. Springer.

Madavan, N. K., Deutsch, S. & Merkle, C. L. 1985 Measurements of local skin friction in a microbubble-modified turbulent boundary layer. *J. Fluid Mech.* **156**, 237–256.

Magarvey, R. H. & Bishop, R. L. 1961*a* Transition ranges for three-dimensional wakes. *Can. J. Phys.* **39**, 1418–1422.

Magarvey, R. H. & Bishop, R. L. 1961*b* Wakes in liquid-liquid systems. *Phys. Fluids* **4** (7), 800–805.

Magarvey, R. H. & MacLatchy, C. S. 1965 Vortices in sphere wakes. *Can. J. Phys.* **43**,

1649–1656.

Magnaudet, J. & Eames, I. 2000 The motion of high-Reynolds-number bubbles in inhomogeneous flows. *Annu. Rev. Fluid Mech.* **32**, 659–708.

Magnaudet, J & Mougin, G 2007 Wake instability of a fixed spheroidal bubble. *J. Fluid Mech.* **572**, 311–337.

Manen, J. D. Van & Oossanen, P. Van 1988 Resistance. In *Principles of Naval Architecture, Second Revision. Volume II. Resistance, Propulsion and Vibration* (ed. E. V. Lewis), chap. 5, pp. 1–109. The Society of Naval Architects and Marine Engineers.

Marquillie, M. & Ehrenstein, U. 2002 Numerical simulation of separating boundary-layer flow. *Comput. Fluids* **31**, 683–693.

Martell, M. B., Blair Perot, J. & Rothstein, J. P. 2009 Direct numerical simulations of turbulent flows over superhydrophobic surfaces. *J. Fluid Mech.* **620**, 31—-41.

Mauri, R. 2015 *Transport Phenomena in Multiphase Flows*. Springer.

Maxey, M. R. & Riley, J. J. 1983 Equation of motion for a small rigid sphere in a nonuniform flow. *Phys. Fluids* **26**, 883–889.

Maxwell, J. C. 1879 On stresses in rarefied gases arising from inequalities of temperature. *Phil. Trans. R. Soc. Lond.* **170**, 231–256.

McHale, G., Flynn, M. R. & Newton, M. I. 2011 Plastron induced drag reduction and increased slip on a superhydrophobic sphere. *Soft Matter* **7**, 10100.

McHale, G., Shirtcliffe, N. J., Evans, C. R. & Newton, M. I. 2009 Terminal velocity and drag reduction measurements on superhydrophobic spheres. *Appl. Phys. Lett.* **94**, 064104.

Meng, D.-S., Ju, Y. S. & Kim, C.-J. 2005 A comparative study of electrolysis and boiling for bubble-driven microactuations. In 13^{th} *International Conference on Solid-State Sensors, Actuators and Microsystems, Seoul, South Korea. June 5-9*.

Min, T. & Kim, J. 2004 Effects of hydrophobic surface on skin-friction drag. *Phys. Fluids* **16**, 55–58.

Ministère des Armées 2019 Actualité et Dossier de Presse. `https://www.defense.gouv.fr/fre/dga/actualite/inauguration-du-suffren-1er-sous-marin-du-programme-barracuda`, Accessed: September 2019.

Mittal, R. 1999*a* A Fourier–Chebyshev spectral collocation method for simulating flow past spheres and spheroids. *Int. J. Numer. Meth. Fluids* **30**, 921–937.

Mittal, R. 1999*b* Planar symmetry in the unsteady wake of a sphere. *AIAA Journal* **37** (3), 388–390.

Modak, C. D. & Bhaumik, S. K. 2017 Creeping flow dynamics over superhydrophobic ball: Slip effects and drag reduction. *Colloids Surf. A: Phys. Eng. Asp.* **529**, 998–1008.

Moisy, F., Rabaud, M. & Salsac, K. 2009 A synthetic Schlieren method for the measurement of the topography of a liquid interface. *Exp. Fluids* **46** (6), 1021–1036.

Mordant, N. & Pinton, J.-F. 2000 Velocity measurement of a settling sphere. *Eur. Phys. J. B* **18**, 343–352.

Mougin, G. & Magnaudet, J. 2002*a* The generalized Kirchhoff equations and their application to the interaction between a rigid body and an arbitrary time-dependent viscous flow. *Int. J. Multiph. Flow* **28**, 1837–1851.

Mougin, G. & Magnaudet, J. 2002*b* Path instability of a rising bubble. *Phys. Rev. Lett.* **88** (1), 014502.

Moukalled, F., Mangani, L. & Darwish, M. 2016 *The Finite Volume Method in Computational Fluid Dynamics*. Springer.

Mouterde, T., Lehoucq, G., Xavier, S., Checco, A., Black, C. T., Rahman, A.,

Midavaine, T., Clanet, C. & Quéré, D. 2017 Antifogging abilities of model nanotextures. *Nature Mater.* **16**, 658–663.

Natarajan, R. & Acrivos, A. 1993 The instability of the steady flow past spheres and disks. *J. Fluid Mech.* **254**, 323–344.

Navier, C. L. M. H. 1823 Mémoire sur les lois du mouvement des fluides. In *Mémoires de L'Académie Royale des Sciences de l'Institut de France*, , vol. 6, pp. 389–440. Paris, Gauthier-Villars, Imprimeur-Libraire.

Newton, I. 1687 Principia. Book II, Proposition XXXIX, Theorem XXXI. In *The mathematical principles of natural philosophy*. Daniel Adee (English Version, 1846, New York).

Niavarani, A. & Priezjev, N. V. 2009 The effective slip length and vortex formation in laminar flow over a rough surface. *Phys. Fluids* **21**, 052105.

Nilsson, M. A., Daniello, R. J. & Rothstein, J. P. 2010 A novel and inexpensive technique for creating superhydrophobic surfaces using Teflon and sandpaper. *J. Phys. D: Appl. Phys.* **43**, 1–5.

Nobach, H. & Honkanen, M. 2005 Two-dimensional Gaussian regression for sub-pixel displacement estimation in particle image velocimetry or particle position estimation in particle tracking velocimetry. *Exp. Fluids* **38**, 511–515.

Nosonovsky, M. & Bhushan, B. 2008 Biologically-inspired surfaces: broadening the scope of roughness. *Adv. Func. Mater.* **18**, 843–855.

Ohmi, K. & Li, H.-Y. 2000 Particle-tracking velocimetry with new algorithms. *Meas. Sci. Technol.* **11**, 603–616.

Orfanidis, S. J. 2010 *Introduction to SignalProcessing*. Rutgers University.

Ormières, D. & Provansal, M. 1999 Transition to turbulence in the wake of a sphere. *Phys. Rev. Lett.* **83** (1), 80–83.

Orszag, S. A. & Kells, L. C. 1980 Transition to turbulence in plane Poiseuille and plane Couette flow. *J. Fluid Mech.* **96**, 159–205.

Otsu, N. 1979 A threshold selection method from gray-level histograms. *IEEE Trans. Syst. Man. Cyber.* **9** (1), 62–66.

Palaparthi, R., Papageorgiou, D. T. & Maldarelli, C. 2006 Theory and experiments on the stagnant cap regime in the motion of spherical surfactant-laden bubbles. *J. Fluid Mech.* **559**, 1–44.

Paris Agreement 2015 United Nations, Report of the Conference of the Parties. In 21^{st} *Session, Paris, France. November 30 to December 13*.

Pavlov, V. V. 2006 Dolphin skin as a natural anisotropic compliant wall. *Bioinsp. Biomim.* **1**, 31–40.

Peaudecerf, F. J., Landel, J. R., Goldstein, R. E. & Luzzatto-Fegiz, P. 2017 Traces of surfactants can severely limit the drag reduction of superhydrophobic surfaces. *Proc. Natl. Acad. Sci. USA* **114** (28), 7254–7259.

Philip, J. R. 1972 Flows satisfying mixed no-slip and no-shear conditions. *J. Appl. Math. Phys.* **23**, 353–372.

Piao, L. & Park, H. 2015 Two-dimensional analysis of air-water interface on superhydrophobic grooves under fluctuating water pressure. *Langmuir* **31**, 8022–8032.

Picella, F. 2019 Retarder la transition vers la turbulence en imitant les feuilles de lotus. PhD thesis, École nationale supérieure d'arts et métiers - ENSAM.

Pointwise, Inc. 2019 Webpage. `https://www.pointwise.com`, Accessed: September 2019.

Pope, S. B. 2000 *Turbulent flows*. Cambridge University Press.

Pratt, V. 1987 Direct least-squares fitting of algebraic surfaces. *Comput. Graph.* **21**, 145–152.

Przadka, W., Miedzik, J., Gumowski, K., Goujon-Durand, S. & Wesfreid, J. E. 2008 The wake behind the sphere: analysis of vortices during transition from steadiness to unsteadiness. *Arch. Mech.* **60** (6), 467–474.

Raffel, M., Willert, C., Wereley, S. & Kompenhans, J. 2007 *Particle Image Velocimetry*. Springer.

Rapp, B. A. 2017 *Microfluidics: Modeling, Mechanics, and Mathematics*. Elsevier.

Ras, R. H. A. & Marmur, A., ed. 2017 *Non-Wettable Surfaces. Theory, Preparation and Applications*. The Royal Society of Chemistry.

Reinsch, C. H. 1967 Smoothing by spline functions. *Numerische Mathematik* **10**, 177–183.

Reneaux, J. 2004 Overview on drag reduction technologies for civil transport aircraft. In *European Congress on Computational Methods in Applied Sciences and Engineering, Jyväskylä, Finland. July 24-28*.

Reynolds, O. 1883 XXIX. An experimental investigation of the circumstances which determine whether the motion of water shall be direct or sinuous, and of the law of resistance in parallel channels. *Phil. Trans. R. Soc.* **174**, 935–982.

Rienstra, S. W. & Hirschberg, A. 2019 *An Introduction to Acoustics*. Eindhoven University of Technology.

Rothstein, J. P. 2010 Slip on superhydrophobic surfaces. *Annu. Rev. Fluid Mech.* **42**, 89–109.

Samaha, M. A., Tafreshi, H. V. & Gad-el-Hak, M. 2012 Superhydrophobic surfaces: from the lotus leaf to the submarine. *C. R. Mecanique* **340**, 18–34.

Schouveiler, L. & Provansal, M. 2002 Self-sustained oscillations in the wake of a sphere. *Phys. Fluids* **14** (11), 3846–3854.

Schultz, M. P. & Swain, G. W. 2000 The influence of biofilms on skin friction drag. *Biofouling* **15** (1–3), 129–139.

Seo, J., García-Mayoral, R. & Mani, A. 2015 Pressure fluctuations and interfacial robustness in turbulent flows over superhydrophobic surfaces. *J. Fluid Mech.* **783**, 448–473.

Seo, J., García-Mayoral, R. & Mani, A. 2018 Turbulent flows over superhydrophobic surfaces: flow-induced capillary waves, and robustness of air–water interfaces. *J. Fluid Mech.* **835**, 45–85.

Shew, W. L., Poncet, S. & Pinton, J.-F. 2006 Force measurements on rising bubbles. *J. Fluid Mech.* **569**, 51–60.

Song, D., Song, B., Hu, H., Du, X., Du, P., Choi, C.-H. & Rothstein, J. P. 2018 Effect of a surface tension gradient on the slip flow along a superhydrophobic air-water interface. *Phys. Rev. Fluids* **3**, 033303.

Stephani, K. A. & Goldstein, D. B. 2010 An examination of trapped bubbles for viscous drag reduction on submerged surfaces. *J. Fluid Eng.* **132**, 041303.

Stokes, G. G. 1851 On the effect of the internal friction of fluids on the motion of pendulums. *Trans. Cambridge Philos. Soc.* **IX**.

Sutterby, J. L. 1973*a* Falling sphere viscometer. *J. Phys. E: Sci. Instrum.* **6**, 1001–1005.

Sutterby, J. L. 1973*b* Falling sphere viscometry. I. wall and inertial corrections to stokes' law in long tubes. *Trans. Soc. Rheol.* **17** (4), 559–573.

Sutterby, J. L. 1973*c* Falling sphere viscometry. II. end effects in short tubes. *Trans. Soc. Rheol.* **17** (4), 575–585.

Szodruch, J. 1991 Viscous drag reduction on transport aircraft. In *29th Aerospace Sciences Meeting, Reno, Nevada, USA. January 7-10*.

Taneda, S. 1956 Experimental investigation of the wake behind a sphere at low reynolds numbers. *J. Phy. Soc. Jpn* **11**, 1104–1108.

Tanner, R. I. 1963 End effects in falling-ball viscometry. *J. Fluid Mech.* **17**, 161–170.

Taylor, G. I. 1928 The forces on a body placed in a curved or converging stream of fluid. *Proc. R. Soc. Lond. A* **120**, 260–283.

Tennekes, H. & Lumley, J. L. 1972 *A first couse in turbulence*. The MIT Press.

The Naked Scientists 2019 Webpage. `https://www.thenakedscientists.com/articles/science-features/biomimetics-borrowing-biology`, Accessed: September 2019.

Thompson, M. C., Leweke, T. & Provansal, M. 2001 Kinematics and dynamics of sphere wake transition. *J. Fluid Struct.* **15**, 575–585.

Tomboulides, A. G. & Orszag, S. A. 2000 Numerical investigation of transitional and weak turbulent flow past a sphere. *J. Fluid Mech.* **416**, 45–73.

Tourkine, P., Le Merrer, M. & Quéré, D. 2009 Delayed freezing on water repellent materials. *Langmuir* **25** (13), 7214–7216.

Townsin, R. L. 2003 The ship hull fouling penalty. *Biofouling* **19**, 9–15.

Truscott, T. T., Epps, B. P. & Munns, R. H. 2016 Water exit dynamics of buoyant spheres. *Phys. Rev. Fluids* **1**, 074501.

Truscott, T. T., Epps, B. P. & Techet, A. H. 2012 Unsteady forces on spheres during free-surface water entry. *J. Fluid Mech.* **704**, 173–210.

Ueland, E. S., Skjetne, R. & Dahl, A. R. 2017 Marine autonomous exploration using a lidar and slam. In *Proceedings of the ASME 2017* 36^{th} *International Conference on Ocean, Offshore and Arctic Engineering,*, , vol. 61880.

UltraTech International, Inc. 2019 Webpage. `https://www.spillcontainment.com/products/ever-dry`, Accessed: September 2019.

Vakarelski, I. U., Chan, D. Y. C., Marston, J. O. & Thoroddsen, S. T. 2013 Dynamic air layer on textured superhydrophobic surfaces. *Langmuir* **29**, 11074–11081.

Vakarelski, I. U., Chan, D. Y. C. & Thoroddsen, S. T. 2014 Leidenfrost vapour layer moderation of the drag crisis and trajectories of superhydrophobic and hydrophilic spheres falling in water. *Soft Matter* **10**, 5662–5668.

Vakarelski, I. U., Marston, J. O., Chan, D. Y. C. & Thoroddsen, S. T. 2011 Drag reduction by Leidenfrost vapor layers. *Phys. Rev. Lett.* **106**, 214501.

Vakarelski, I. U., Patankar, N. A., Marston, J. O., Chan, D. Y. C. & Thoroddsen, S. T. 2012 Stabilization of Leidenfrost vapour layer by textured superhydrophobic surfaces. *Nature* **489**, 274–277.

Veldhuis, C. H. J. & Biesheuvel, A. 2007 An experimental study of the regimes of motion of spheres falling or ascending freely in a Newtonian fluid. *Int. J. Multiphase Flow* **33**, 1074–1087.

Venkataraman, D. & Bottaro, A. 2012 Numerical modeling of flow control on a symmetric aerofoil via a porous, compliant coating. *Phys. Fluids* **24**, 093601.

Vincent, J. F. V., Bogatyreva, O. A., Bogatyrev, N. R., Bowyer, A. & Pahl, A.-K. 2006 Biomimetics: its practice and theory. *J. R. Soc. Interface* **3**, 471–482.

Vinogradova, O. I. 1999 Slippage of water over hydrophobic surfaces. *Int. J. Miner. Process.* **56**, 31–60.

Vinokur, M. 1983 On one-dimensional stretching functions for finite-difference calculations. *J. Comput. Phys.* **50**, 215–234.

Walsh, M. J., Sellers III, W. L. & McGinley, C. B. 1989 Riblet drag at flight conditions. *J. Aircraft* **26** (6), 570–575.

Walsh, M. J. & Weinstein, L. M. 1978 Drag and heat tkansfer on surfaces with small longitudinal fins. In *AIAA* 11^{th} *Fluid and Plasma Dynamics Conference, Seattle, Washington, USA. July 10-12*.

Wenzel, R. N. 1936 Resistance of solid surfaces to wetting by water. *Ind. Eng. Chem.* **28** (8), 988–994.

Werlé, H. 1980 Transition et décollement: Visualisations au tunnel hydrodynamique de l'ONERA. *Rech. Aérosp.* pp. 331–345.

Willmott, G. R. 2009 Slip-induced dynamics of patterned and Janus-like spheres in laminar flows. *Phys. Rev. E* **79**, 066309.

Ybert, C., Barentin, C., Cottin-Bizonne, C., Joseph, P. & Bocquet, L. 2007 Achieving large slip with superhydrophobic surfaces: Scaling laws for generic geometries. *Phys. Fluids* **19**, 123601.

Zhang, X., Shi, F., Niu, J., Jiang, Y. & Wang, Z. 2008 Superhydrophobic surfaces: from structural control to functional application. *J. Mater. Chem.* **18**, 621–633.

Zouaghi, S., Bellayer, S., Thomy, V., Dargent, T., Coffinier, Y., Andre, C., Delaplace, G. & Jimenez, M. 2019 Biomimetic surface modifications of stainless steel targeting dairy fouling mitigation and bacterial adhesion. *Food Bioprod. Process.* **113**, 32–38.

Zouaghi, S., Six, T., Bellayer, S., Moradi, S., Hatzikiriakos, S. G., Dargent, T., Thomy, V., Coffinier, Y., Andre, C., Delaplace, G. & Jimenez, M. 2017 Biomimetic nanostructured surfaces for antifouling in dairy processing. In *23ème Congrès Français de Mécanique, Lille, France. August 28 to September 1*.

Appendix A

Air Layer Thickness Estimation

A preliminary quantitative estimation of the air plastron thickness was implemented on non-opaque SH flat plates by exploiting a synthetic Schlieren method, as usually performed for air-liquid interface detection on free-surface flows (Moisy *et al.* 2009). A schematic of the experimental set-up is presented in Fig. A.1. A light source is placed at ideally infinite distance from the test section to supply parallel rays. Both white light and green laser (wavelength 532 nm) were tested. The SH flat plate is fixed on the internal wall of an optical glass cell. The system is hit by the incoming parallel rays, thus allowing the camera placed in front of the cell (at distance L from the surface of the SH plate) to take a snapshot of the shadow of the texture.

To understand the details of the working principle, the schematic in Fig. A.2 focuses on the behaviour of the light rays when crossing the different interfaces into play. Since the incoming rays are parallel, the refraction at the optical cell wall facing the light source is ideally negligible. The rays can thus still be considered parallel when crossing the cell wall thickness. The same scenario can be considered valid when the rays cross the interface with the transparent glass constituting the SH flat plate. Then, it is convenient to follow the route travelled by the rays following a reverse path, i.e. starting from the camera sensor. The ray coming to the camera sensor through the air (subscript a) between camera and cell has an angle of incidence ϑ_i, which is modified to the angle ϑ_g at the air-glass (subscript g) interface. The relation between the two is described by the Snell's law:

$$\frac{\sin\vartheta_g}{\sin\vartheta_i} = \frac{n_a}{n_g}, \tag{A.1}$$

where n is the refractive index of the material. Since $n_g \approx 1.5$ and $n_a \approx 1.0$, it results that

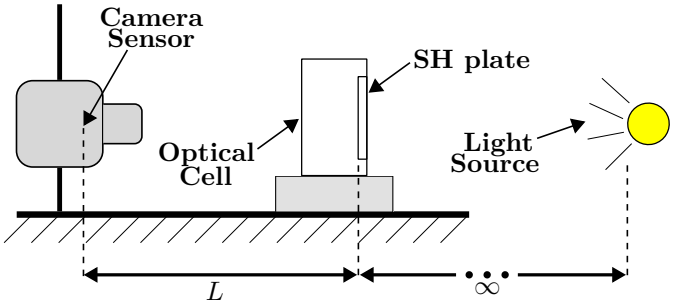

Figure A.1 – Schematic of the experimental set-up to estimate the air layer thickness.

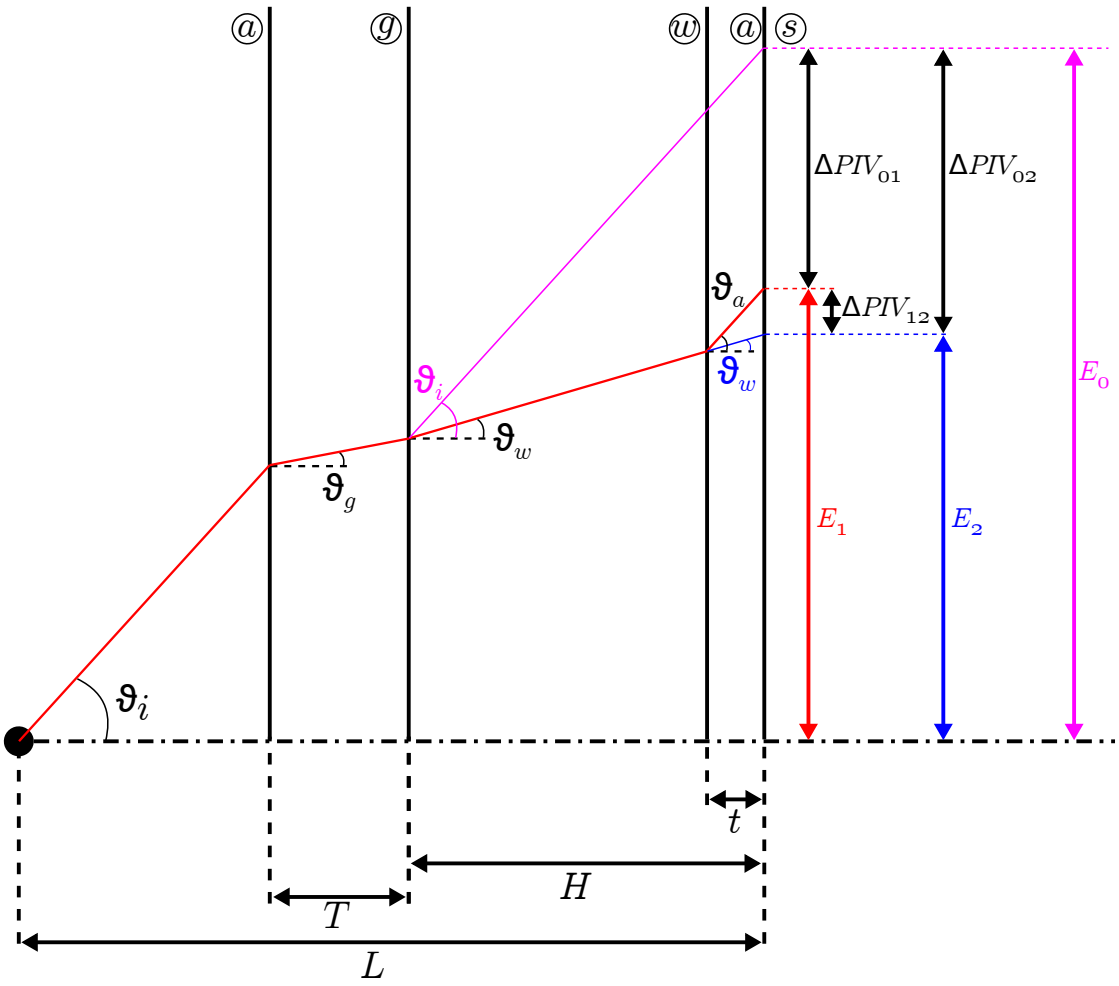

Figure A.2 – Schematic of the working principle of the Schlieren method to estimate the air layer thickness t. (—), path of the refracted ray, from the camera sensor (indicated by the • symbol) with incident angle ϑ_i, crossing the optical glass (letter g) cell wall with thickness T at angle ϑ_g, the water (letter w) layer with height H at angle ϑ_w and the air (letter a) layer at angle ϑ_a. The camera sensor is at distance L from the solid (letter s) surface of the SH plate. The numbers indicate the three considered configurations: 0, only air in the cell without water. 1, water filling the cell and air layer over the SH plate. 2, water filling the cell without air layer over the SH plate. (—), path of the ray in the configuration 0. (—), path of the ray in the configuration 2. ΔPIV, displacement between each couple of configurations estimated via direct correlation of the images.

$\vartheta_g < \vartheta_i$. Then, following the same approach for the glass-water (subscript w) interface:

$$\frac{\sin\vartheta_w}{\sin\vartheta_g} = \frac{n_g}{n_w}, \tag{A.2}$$

where $n_w \approx 1.4$, which implies $\vartheta_w > \vartheta_g$. Finally, the presence of the air layer over the SH plate implies at the water-air interface:

$$\frac{\sin\vartheta_a}{\sin\vartheta_w} = \frac{n_w}{n_a}. \tag{A.3}$$

This formulation is therefore valid for a homogeneous air layer thickness t, which can be considered a first approximation when $L \gg t$. The idea of the technique is then based on the successive recording of three snapshots in different configurations. First, the cell is filled only with air, without liquid. Second, the cell is filled with water (which was used as first attempt), thus implying the establishment of the air layer over the SH plate. Finally, a sufficient amount of time (the order of magnitude is some days) is waited for air dissolution into water. The last snapshot is therefore taken when water completely fills the cell, without air layer on the SH plate. The texture of the non-opaque SH-NAR coating then provided sufficient contrast to perform a direct correlation between each couple of the three discussed configurations. The magnification-shrinkage due to the presence or absence of the respective layers then produced a measurable displacement ΔPIV between each couple of images. The connection among the three displacements is easily retrievable via the schematic in Fig. A.2. In fact:

$$E_0 = (L - T - H)\tan\vartheta_i + T\tan\vartheta_g + H\tan\vartheta_i, \tag{A.4a}$$
$$E_1 = (L - T - H)\tan\vartheta_i + T\tan\vartheta_g + (H - t)\tan\vartheta_w + t\tan\vartheta_a, \tag{A.4b}$$
$$E_2 = (L - T - H)\tan\vartheta_i + T\tan\vartheta_g + H\tan\vartheta_w. \tag{A.4c}$$

The subtraction of each couple of the expressions in Eqs. A.4 gives:

$$\Delta PIV_{01} = H\left(\tan\vartheta_i - \tan\vartheta_w\right) + t\left(\tan\vartheta_w - \tan\vartheta_a\right), \tag{A.5a}$$
$$\Delta PIV_{02} = H\left(\tan\vartheta_i - \tan\vartheta_w\right), \tag{A.5b}$$
$$\Delta PIV_{12} = t\left(\tan\vartheta_a - \tan\vartheta_w\right). \tag{A.5c}$$

In the above system of equations, the length H can be measured on the experimental set-up. Since the measurement precision is $\mathcal{O}(10^{-6})$ m, while the H magnitude is $\mathcal{O}(10^{-3})$ m, the relative error is expected to be $\mathcal{O}(10^{-1})$ when expressed in relative percentage. One more unknown can be eliminated by coupling Eqs. A.1, A.2 and A.3, which results in $\vartheta_i = \vartheta_a$. The latter is an intuitive result since the system *glass wall - water layer* can be viewed as an equivalent material characterised by an intermediate refractive index. Therefore, the Snell's law indicates that the angles entering and exiting from this equivalent material (ϑ_i and ϑ_a) must be the same. Following these considerations, the system of Eqs. A.5 presents an equal number of unknowns and available equations. It can thus be solved and the corresponding thickness t can be estimated at each point where the equations are evaluated, i.e. at each available location deriving from the correlation procedure.

The preliminary raw results of one set of measurements on a SH-NAR plate in water, using white light as source, is shown in Fig. A.3. The evaluated t is approximately uniform over the whole available analysed region, except for a very limited area where non-realistic large values are estimated. This is probably due to local non uniformity of the air layer, which could negatively affect the correlation procedure. However, a raw estimation of the average air layer thickness results into $t_{ave} \approx 290\,\mu$m, which descends down to $t_{ave} \approx 260\,\mu$m removing the non-reliable

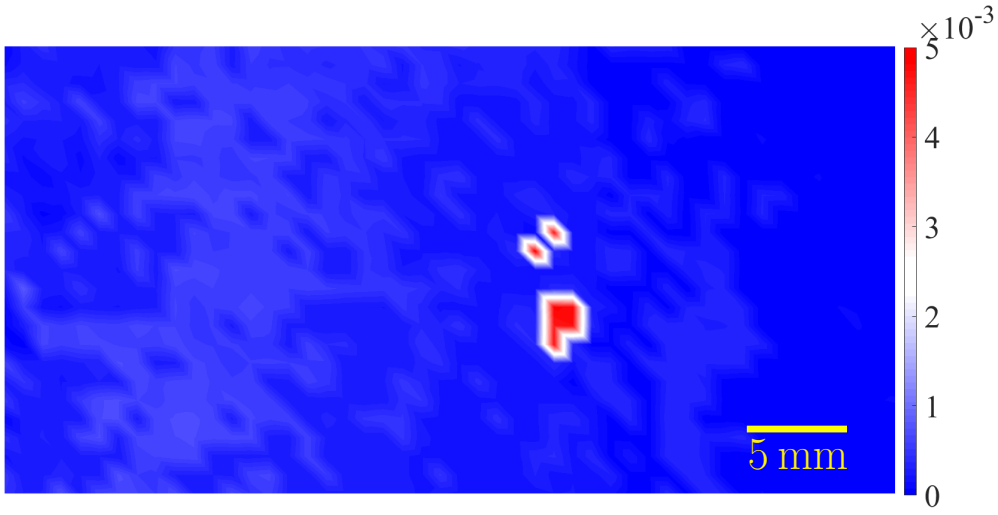

Figure A.3 – Preliminary estimation of the local air layer thickness t over a SH-NAR plate, obtained by solving the system of Eqs. A.5. The colorscale is expressed in m units.

region. To achieve a better reliability of the actual t estimated value, a deeper investigation and set-up ameliorations (e.g. increase of the spatial resolution, analysis of different liquids) are required. However, the preliminary results are encouraging in terms of order of magnitude of the estimated thickness, which seems to be compatible with the surface roughness size of the produced SH coatings.

Appendix B

Experimental Set-up Limitations

This Appendix discusses two practical limitations of the designed experimental set-up for falling sphere tests (see §4.1) that could influence the estimated hydrodynamic performance. Ideally, the latter should be compared in an infinite medium in order to exclude possible effects of the tank finite size. In practice, the designed rig is characterised by finite height and cross-section, as qualitatively shown in Fig. B.1. The two limitations are thus separately discussed in the next sections.

B.1 Finite Height

The finite height of the tank may impact the dynamics of the falling body by modifying its velocity or by limiting the time spent by the sphere at terminal conditions. This section is therefore initially dedicated to the discussion of the end effects on terminal velocity. Then, an approach to mitigate the absence of enough data at terminal conditions is proposed.

End effects take into account the slow down of the falling sphere when approaching a solid plane, like in the case of the lower part of a finite-height tank (see Fig. B.1(a)). Considering a sphere having reached its u_∞ and approaching the bottom side of a circular tank of diameter D and height H, the presence of significant end effects would imply a non-negligible reduction of the evaluated instantaneous vertical velocity (Flude & Daborn 1982). The question of which are the parameters that govern the relevance of the end effects arises. In fact, theoretical calculations and empirical evidence (Tanner 1963; Sutterby 1973*c*; Flude & Daborn 1982) showed that end effects become important for tanks with $\frac{H}{D} \sim 10^0$ and for a distance Δz between the falling sphere centre and the solid wall that becomes smaller than D. Moreover, end effects are enhanced by an increase of the ratio $\frac{d}{D}$. As an example, Sutterby (1973*c*) reported no end effects at $Re_\infty = 2$ for $\frac{H}{D} = 2$, $\frac{d}{D} = 0.125$ and $\Delta z \sim D$. As a general rule, assuming that in a practical experimental campaign $H \gg D$, $d \ll D$ and that the measurements are interrupted before reaching the tank lower wall, corrections due to the end effects are not necessary (Brizard *et al.* 2005).

Moreover, depending on the combination of tank and falling body properties, the height H could reveal inadequate to assure an exhaustive analysis of terminal conditions. In that case, the velocity profile of the falling sphere would be truncated right after terminal conditions are reached or even in the accelerating phase before u_∞ is achieved. If the interest is on the onset of transversal motion in the accelerating phase (see Chapter 6) the described issue does not cause any problem. However, no reliable information on the achieved u_∞ would be retrieved from a truncated velocity profile. The exponential model introduced in Eq. 4.6 in §4.2.3 to model the behaviour of the vertical velocity profile of a falling sphere can be further exploited in order to

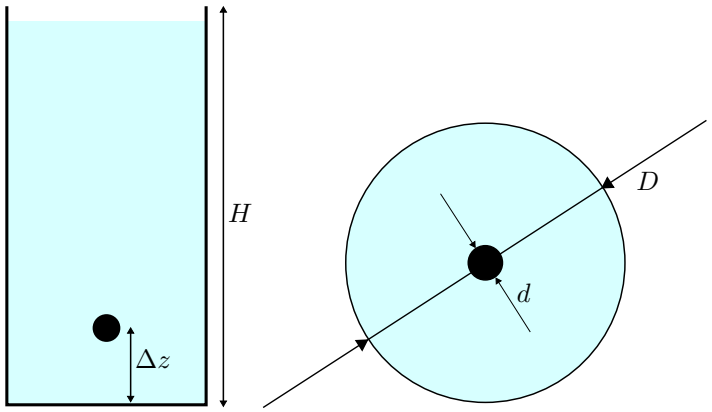

Figure B.1 – Schematic of the relevant parameters that govern the effects due to the finite size of the tank (diameter D and height H) on a falling sphere of diameter d. (a), end effects at a distance Δz from the tank lower wall. (b), edge effects.

obtain information on the attained terminal velocity u_∞. In detail, in §4.2.3 it was shown that the u_∞ estimation differs only of 0.3 % from the value predicted by the semi-empirical law in Eq. 4.3 in the case of a $d = 5$ mm reference sphere in water. However, such a good estimation was obtained by considering less than one second of data available after terminal conditions are reached. Larger available data would further ameliorate the exponential model estimation, but would not be compatible with a practical tank height. A reduction of the available data would likely result into a deterioration of the estimated u_∞ value. To test the robustness of the method, the procedure was repeated for the same sphere progressively reducing the amount of available data on the profile predicted via Eq. 4.3, starting from the last point available at terminal conditions. The corresponding error on the u_∞ estimation, evaluated as follows:

$$u_\infty^{err} = \frac{\left| u_\infty^{Eq.\ 4.6} - u_\infty^{Eq.\ 4.3} \right|}{u_\infty^{Eq.\ 4.3}}, \tag{B.1}$$

is reported in Fig. B.2 and indicates that even for 50 % of missing data on the terminal part of the velocity profile, the error u_∞^{err} on the estimation of the terminal velocity stays below 3 % of the predicted value. In detail, the exponential model in Eq. 4.6 tends to overestimate the u_∞ value with respect to the semi-empirical law in Eq. 4.3. However, since in the manuscript the interest is put on the relative performance variation of SH spheres with respect to the corresponding reference, the error performed in both cases would be of the same order of magnitude (considering the same amount of available points) and would likely balance one another.

Finally, the same approach was shown in §6.3.2 (see Tab. 6.4) to preserve its validity considering experimentally evaluated vertical velocity profiles.

B.2 Blockage Correction

Conversely to the end effects, edge effects corrections due to the finite size of the tank cross-section (see Fig. B.1(b)) may reveal important depending on the combination of the sphere and tank dimensions and on the falling regime. For this reason, this section is dedicated to the discussion of the blockage effects and of the correction method adopted in this work.

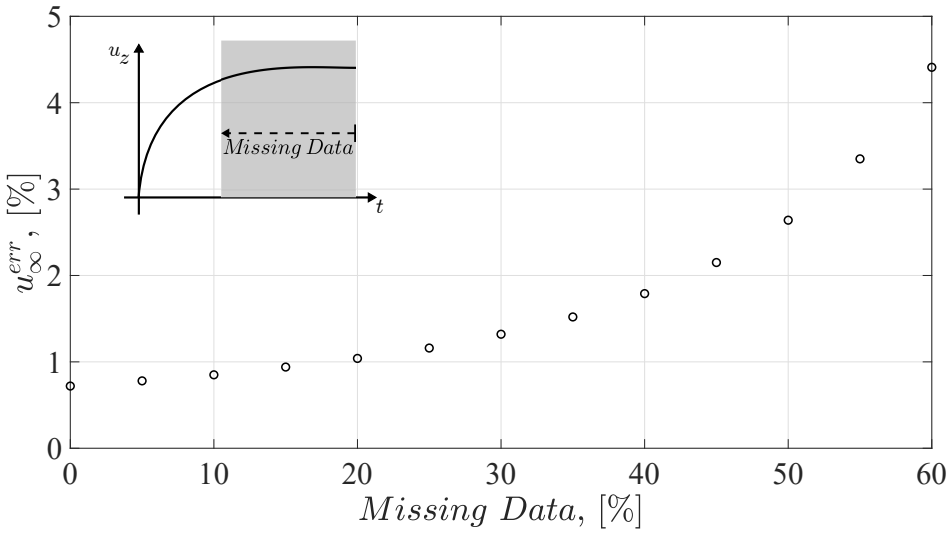

Figure B.2 – Evolution of the error on the estimation of the terminal velocity u_∞ via the exponential model described by Eq. 4.6 with respect to the semi-empirical prediction of Eq. 4.3 (see Eq. B.1). The horizontal axis indicates the percentage of data removed from the terminal part of the velocity profile evaluated via Eq. 4.3, as schematically depicted in the insert.

As discussed in §4.2.3, when a free falling/rising body moves into a finite-size cross-section tank filled with a liquid, a counter motion of the latter occurs, which balances the motion of the solid body and of the liquid dragged by it. An increasing ratio between the solid body and tank characteristic dimensions results into a larger retarding effect of the tank walls on the body motion. This effect, that has been attracting attention from centuries (Newton 1687), can be explained in terms of the solution of the flow around a solid sphere as a modification of the boundary conditions to be considered in order to solve the equations of motion (see e.g. Clift *et al.* 1978, and references therein). The studies dedicated to this phenomenon on falling spheres pointed out the relevance of the considered flow regime (i.e. Re_∞) and of the blockage factor δ expressed as the ratio $\frac{d}{L}$ between the sphere diameter and the tank cross-section characteristic size. Since the relationships between the parameters in the unbounded (subscript *unb*) and bounded (subscript *bou*) configurations were usually developed for circular cross-section tanks, the characteristic size L was taken equal to the tank diameter D. In the case of a non-circular cross-section, the equivalent diameter D_{eq} can simply be retrieved by evaluating the diameter of the equivalent circular tank that has the same cross-section surface of the real tank, which gives $D_{eq} = \frac{2L}{\sqrt{\pi}}$. As an example, in the case of a square cross-section tank, the length L can be considered equal to the tank width. Correction factors for the terminal drag ($\frac{F_{D\infty,bou}}{F_{D\infty,unb}}$) or velocity ($\frac{u_{\infty,bou}}{u_{\infty,unb}}$) ratios were proposed in the creeping flow regime (low Re_∞) based on analytical developments (Faxén 1922) and/or empirical investigation (Francis 1933; Haberman & Sayre 1958; Sutterby 1973*b*). However, since the extension of these laws at higher Re_∞ was generally not successful, the approach used outside the creeping flow regime was usually based on the fit of experimental data (Clift *et al.* 1978). Following this path, and since in this work a law with the following properties was sought:

- expressed in terms of the velocity ratio $\frac{u_{\infty,bou}}{u_{\infty,unb}}$,

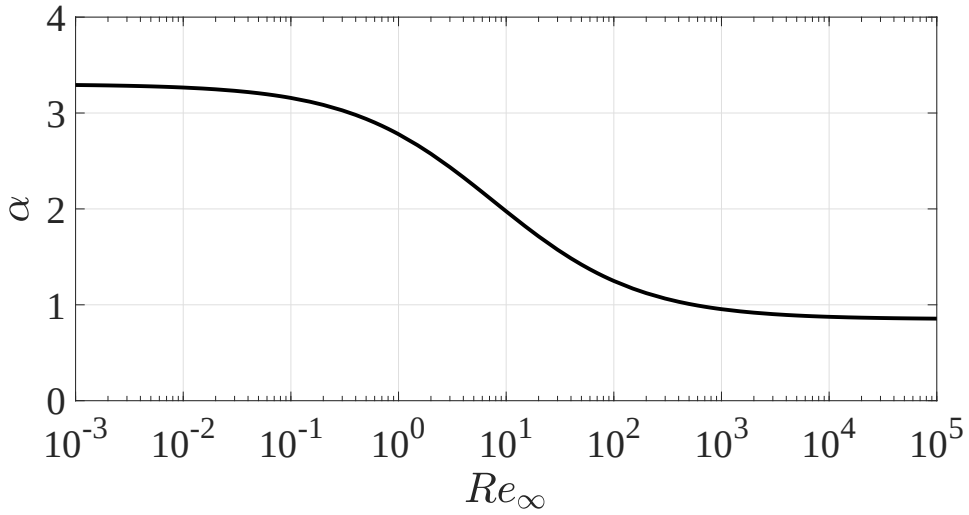

Figure B.3 – Exponent α of Eq. B.2 evaluated via Eq. B.3 as a function of the terminal Reynolds number Re_∞.

- valid over a large Re_∞ range,
- valid over a large δ range,

the study proposed by Di Felice (1996) was considered. In his work, the author exploited an analogy previously developed (Di Felice *et al.* 1995), where he compared the drag increase of a single sphere in a cylindrical tank due to the presence of the walls with the drag increase of a particle in a suspension due to the presence of neighbouring particles. The final form of the proposed relationship can be written as follows:

$$\frac{u_{\infty,bou}}{u_{\infty,unb}} = \left(\frac{1-\delta}{1-A\delta}\right)^{\alpha}, \tag{B.2}$$

where $A = 0.33$ does not depend on Re_∞ and δ. By fitting the experimental data of Fidleris & Whitmore (1961), Di Felice (1996) retrieved the following expression for the exponent α:

$$\frac{3.3-\alpha}{\alpha-0.85} = 0.27 Re_\infty^{0.64}, \tag{B.3}$$

which is represented in Fig. B.3 for the sake of completeness. For large enough Re_∞, the asymptotic value $\alpha = 0.85$ is obtained, which corresponds to the *inertial* regime discussed in Di Felice (1996). Moreover, Di Felice (1996) proposed the value $\alpha = 2.7$ to be valid entering the creeping flow regime.

The evolution of the ratio $\frac{u_{\infty,bou}}{u_{\infty,unb}}$ of bounded to unbounded terminal velocities as a function of Re_∞ is shown in Fig. B.4 for δ values in the range $0.025 - 0.25$. The latter was chosen to include all the blockage factors characterising the spheres and tank used in this study (see §4.3). From the analysis of Fig. B.4 it appears that the ratio $\frac{u_{\infty,bou}}{u_{\infty,unb}}$ decreases for increasing δ at fixed Re_∞. Conversely, at a fixed δ the Re_∞ increase mitigates the blockage effects.

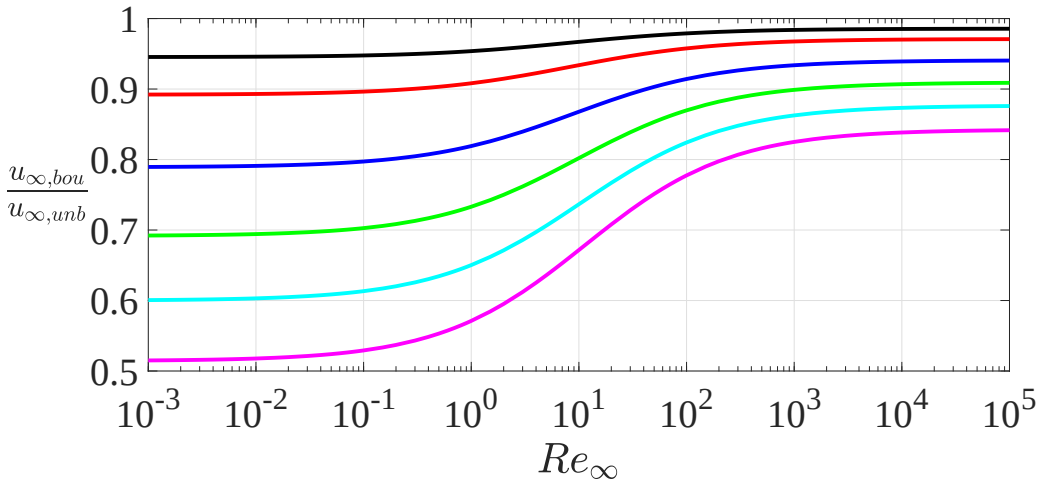

Figure B.4 – Ratio $\frac{u_{\infty,bou}}{u_{\infty,unb}}$ of bounded to unbounded terminal velocity as a function of the terminal Reynolds number Re_∞, from Eq. B.2. (—), $\delta = 0.025$. (—), $\delta = 0.05$. (—), $\delta = 0.10$. (—), $\delta = 0.15$. (—), $\delta = 0.20$. (—), $\delta = 0.25$. The reported δ range includes all the experimental blockage factors of this study.

Appendix C

Falling Sphere Test Details

This Appendix shows tables reporting some major properties of the performed falling sphere tests as well as of the tested spheres.

d, [mm]	$W100\_G000$	$W040\_G060$	$W030\_G070$	$W020\_G080$	$W000\_G100$
5	20.0	14.0	11.0	10.0	7.0
8	16.3	12.5	10.6	7.5	5.0
10	14.5	12.0	10.0	8.0	2.9
15	11.3	-	-	-	-
20	10.0	-	-	-	-
25	8.8	-	-	-	-

Table C.1 – Inter-frame vertical displacement Δz (expressed in percentage with respect to the corresponding sphere diameter d) of the falling sphere tests.

d, [mm]	$W100\_G000$	$W040\_G060$	$W030\_G070$	$W020\_G080$	$W000\_G100$
5	1000	1000	1000	700	200
8	1000	1000	1000	1000	400
10	1000	1000	1000	1000	800
15	1000	-	-	-	-
20	1000	-	-	-	-
25	1000	-	-	-	-

Table C.2 – Frame rate (expressed in fps) of the falling sphere tests.

d_{nom}, [mm]		NC	SH-NAR	SH-220	SH-80
5	d, [mm]	4.991 ± 0.008	5.026 ± 0.064	5.175 ± 0.018	5.481 ± 0.028
	m, [g]	0.5057	0.5086	0.5184	0.5317
	ρ_s, [kg m^{-3}]	7768 ± 40	7651 ± 288	7144 ± 78	6167 ± 94
8	d, [mm]	7.992 ± 0.006	8.043 ± 0.016	8.160 ± 0.014	8.413 ± 0.048
	m, [g]	2.0703	2.0782	2.0993	2.1329
	ρ_s, [kg m^{-3}]	7746 ± 16	7628 ± 44	7379 ± 38	6841 ± 120
10	d, [mm]	9.992 ± 0.006	10.032 ± 0.006	10.219 ± 0.022	10.488 ± 0.006
	m, [g]	4.0403	4.0410	4.0829	4.1312
	ρ_s, [kg m^{-3}]	7735 ± 12	7645 ± 12	7307 ± 46	6839 ± 10
15	d, [mm]	14.990 ± 0.004	15.049 ± 0.008	15.173 ± 0.016	15.435 ± 0.048
	m, [g]	13.6310	13.6721	13.7321	13.8314
	ρ_s, [kg m^{-3}]	7729 ± 6	7662 ± 12	7508 ± 22	7184 ± 66
20	d, [mm]	19.994 ± 0.004	20.056 ± 0.016	20.238 ± 0.038	20.677 ± 0.068
	m, [g]	32.3190	32.3576	32.5811	32.8612
	ρ_s, [kg m^{-3}]	7723 ± 6	7660 ± 18	7507 ± 42	7099 ± 70
25	d, [mm]	24.992 ± 0.006	25.055 ± 0.008	25.279 ± 0.382	25.617 ± 0.260
	m, [g]	63.1277	63.1620	63.8017	63.1445
	ρ_s, [kg m^{-3}]	7724 ± 6	7670 ± 6	7543 ± 342	7288 ± 222

Table C.3 – Measured properties of the analysed spheres in the mixture $W100\_G000$. d_{nom}, nominal diameter. d, actual diameter. m, mass (measurement accuracy 0.1 mg). ρ_s, density. Reported uncertainties represent the 95% confidence level.

d_{nom}, [mm]		NC	SH-NAR	SH-220	SH-80
5	d, [mm]	4.995 ± 0.004	5.039 ± 0.004	5.177 ± 0.049	5.592 ± 0.049
	m, [g]	0.5056	0.5078	0.5179	0.5439
	ρ_s, [kg m^{-3}]	7748 ± 2	7580 ± 19	7129 ± 201	5940 ± 155
8	d, [mm]	7.995 ± 0.004	8.045 ± 0.005	8.237 ± 0.066	8.555 ± 0.056
	m, [g]	2.0727	2.0763	2.1173	2.1521
	ρ_s, [kg m^{-3}]	7746 ± 1	7616 ± 14	7236 ± 175	6565 ± 129
10	d, [mm]	9.993 ± 0.003	10.032 ± 0.005	10.242 ± 0.096	10.530 ± 0.018
	m, [g]	4.0405	4.0414	4.1009	4.1652
	ρ_s, [kg m^{-3}]	7733 ± 6	7645 ± 13	7290 ± 205	6813 ± 35

Table C.4 – Same as Tab. C.3, for the mixture $W040\_G060$.

d_{nom}, [mm]		NC	SH-NAR	SH-220	SH-80
5	d, [mm]	4.995 ± 0.004	5.039 ± 0.004	5.177 ± 0.049	5.592 ± 0.049
	m, [g]	0.5056	0.5078	0.5179	0.5439
	ρ_s, [kg m^{-3}]	7748 ± 2	7580 ± 19	7129 ± 201	5940 ± 155
8	d, [mm]	7.995 ± 0.004	8.045 ± 0.005	8.237 ± 0.066	8.555 ± 0.056
	m, [g]	2.0727	2.0763	2.1173	2.1521
	ρ_s, [kg m^{-3}]	7746 ± 1	7616 ± 14	7236 ± 175	6565 ± 129
10	d, [mm]	9.993 ± 0.003	10.032 ± 0.005	10.242 ± 0.096	10.530 ± 0.018
	m, [g]	4.0405	4.0414	4.1009	4.1652
	ρ_s, [kg m^{-3}]	7733 ± 6	7645 ± 13	7290 ± 205	6813 ± 35

Table C.5 – Same as Tab. C.3, for the mixture $W030\_G070$.

d_{nom}, [mm]		NC	SH-NAR	SH-220	SH-80
5	d, [mm]	4.995 ± 0.004	5.039 ± 0.004	5.177 ± 0.049	5.592 ± 0.049
	m, [g]	0.5056	0.5078	0.5179	0.5439
	ρ_s, [kg m^{-3}]	7748 ± 2	7580 ± 19	7129 ± 201	5940 ± 155
8	d, [mm]	7.995 ± 0.004	8.045 ± 0.005	8.237 ± 0.066	8.555 ± 0.056
	m, [g]	2.0727	2.0763	2.1173	2.1521
	ρ_s, [kg m^{-3}]	7746 ± 1	7616 ± 14	7236 ± 175	6565 ± 129
10	d, [mm]	9.993 ± 0.003	10.032 ± 0.005	10.453 ± 0.095	10.869 ± 0.019
	m, [g]	4.0405	4.0414	4.1586	4.2912
	ρ_s, [kg m^{-3}]	7733 ± 6	7645 ± 13	6954 ± 191	6383 ± 32

Table C.6 – Same as Tab. C.3, for the mixture $W020\_G080$.

d_{nom}, [mm]		NC	SH-NAR	SH-220	SH-80
5	d, [mm]	4.995 ± 0.004	5.039 ± 0.004	5.264 ± 0.049	5.514 ± 0.050
	m, [g]	0.5056	0.5078	0.5223	0.5374
	ρ_s, [kg m^{-3}]	7748 ± 2	7580 ± 19	6839 ± 190	6122 ± 162
8	d, [mm]	7.995 ± 0.004	8.045 ± 0.005	8.405 ± 0.066	8.603 ± 0.055
	m, [g]	2.0727	2.0763	2.1386	2.1546
	ρ_s, [kg m^{-3}]	7746 ± 1	7616 ± 14	6879 ± 163	6463 ± 126
10	d, [mm]	9.993 ± 0.003	10.049 ± 0.005	10.391 ± 0.096	10.618 ± 0.018
	m, [g]	4.0405	4.0499	4.1155	4.1777
	ρ_s, [kg m^{-3}]	7733 ± 6	7622 ± 12	7006 ± 194	6665 ± 34

Table C.7 – Same as Tab. C.3, for the mixture $W000\_G100$.

Appendix D

Low Reynolds Number: Scaling Analysis

In §6.1.1, the absence of a noteworthy ability of randomly distributed SH coatings to reduce drag under the investigated conditions at low Re_∞ was shown. Several research groups tried in recent years to explain this limitation of SH drag reduction ability by taking into account different effects, which are summarised in Fig. D.1. In the following, an attempt to define a characteristic time for each of the identified mechanisms is performed. Then, the evaluated magnitude is compared to the drop time t_D defined in Eq. 4.7(a) to determine if the analysed mechanism could result significant or irrelevant during the sphere drop.

D.1 Interface Deformation

The negligible drag reducing ability of randomly distributed SH coatings on spheres may be linked to the deformation of the air-liquid interface, which was extensively investigated in Castagna *et al.* (2018*b*), Song *et al.* (2018). The latter investigated the influence of the shape of the air-liquid interface, observing that convex air-liquid interfaces maximised the slip velocity with respect to the concave counterpart. A characteristic time t_C of the interface deformation induced by capillary effects can be defined as the ratio between the sphere macroscopic dimension, i.e. d, and a characteristic velocity $u_C \sim \sqrt{\frac{\gamma}{\rho_l d}}$, with γ the liquid-air surface tension, which describes the ability of the interface to resist to the flow-induced deformation. The non-dimensional capillary time can thus be evaluated as:

$$t_C^\star = \frac{t_C}{t_D} \sim \frac{d}{u_C t_D} \approx \sqrt{\frac{\rho_l d u_D^2}{\gamma}} \approx \sqrt{Re_D Ca_D} \approx \mathcal{O}\left(10^1\right), \tag{D.1}$$

where the drop characteristic velocity u_D was defined in Eq. 4.7(b), the drop Reynolds number $Re_D = \frac{\rho_l d u_D}{\mu_l}$ and the drop capillary number $Ca_D = \frac{\mu_l u_D}{\gamma}$. It is found that the capillary time t_C is approximately one order of magnitude larger than the characteristic drop time t_D, meaning that an interface deformation is unlikely to occur. This fact was further verified by visualisations in the high-magnification configuration (see §4.1.1), whose objective was to detect a possible deformation of the air layer during the drop. However, conversely to the pure water tests (see e.g. Figs. 6.26 and 6.27), no macroscopic deformation of the air layer was noticed during the drop of all the investigated spheres: the motion and distortion, if present, were so limited that

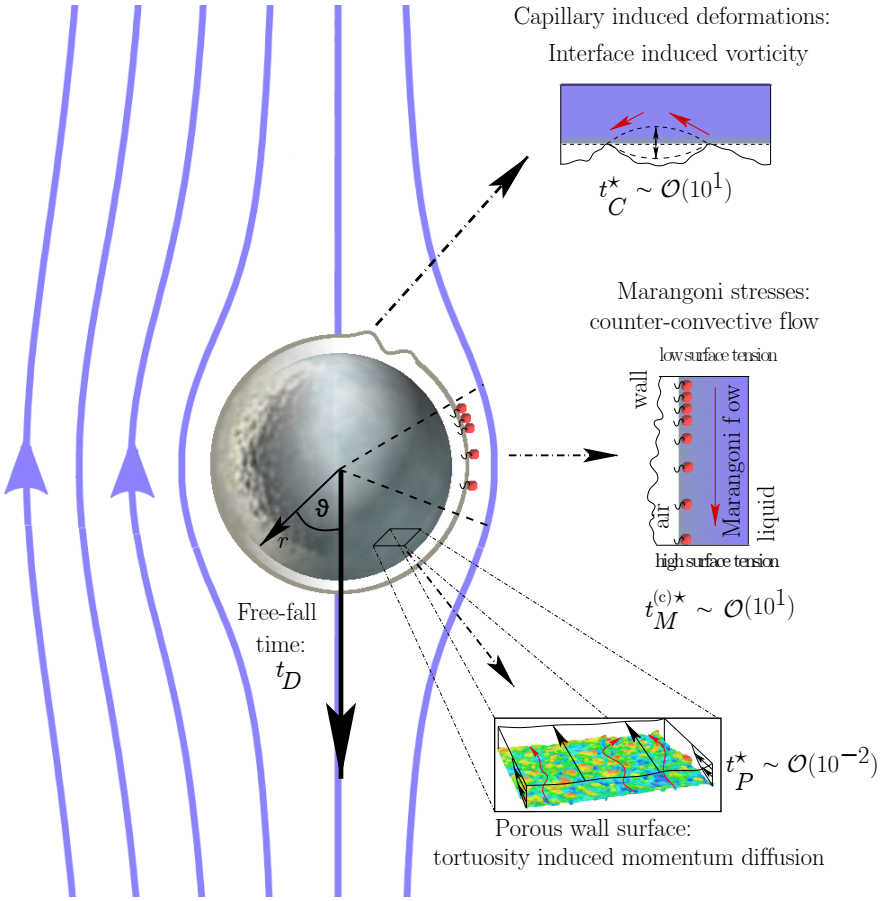

Figure D.1 – Schematic of the possible mechanisms influencing the drag reduction capabilities of SH coatings. Each mechanism is described by its non-dimensional characteristic time $t^\star$, normalised by the free-fall time t_D defined in Eq. 4.7(a).

were not detectable with the employed experimental set-up (please recall the spatial resolution $\approx 0.05\,\mathrm{mm\ px^{-1}}$).

D.2 Marangoni Stress

Peaudecerf *et al.* (2017) investigated the Marangoni flow (subscript M) generated as a result of the surface tension gradient due to the build-up of contaminants on the air-liquid interface. They showed that surfactant-induced stresses can become significant, even at very low contaminants concentrations, potentially yielding a no-slip boundary condition over the flat air-liquid interface. These results were extended by Song *et al.* (2018) who demonstrated that the Marangoni effect strength is dependent on the roughness arrangement. Comparing closed cavities and continuous grooves, they showed that the prevention of the surfactant build-up in the latter case induces a negligible surface tension gradient, restricting thereby the adverse effect of the Marangoni flow.

Two limit cases are here considered, depending on whether the contaminant dynamics is driven by interfacial convection or by adsorption-desorption kinetics (Cuenot *et al.* 1997;

Palaparthi *et al.* 2006; Peaudecerf *et al.* 2017).

D.2.1 Convection Dominated Dynamics

This limit case corresponds to the so-called *stagnant cap regime* (Palaparthi *et al.* 2006) in which the surfactants adsorbed at the interface accumulate at the rear part of the falling sphere (see Fig. 2.19(b)). For sufficiently long time, the surfactant concentration Γ may saturate and counter-balance the beneficial slip effect, thus resulting into a no-slip like surface. This mechanism is described by a transport equation on the form:

$$\frac{\partial \Gamma}{\partial t} \sim \frac{u_{sl}}{d} \frac{\partial \Gamma}{\partial \vartheta}, \tag{D.2}$$

where ϑ is the polar angle (see Fig. D.1) and the slip velocity u_{sl} is chosen as the characteristic velocity of the air-glycerine interface. From Eq. D.2, the Marangoni timescale becomes $t_M^{(c)} \sim \frac{\pi d}{u_{sl}}$, where the superscript c indicates the convection dominated case, therefore implying that an expression for u_{sl} is required. The latter is retrieved by the following simplified first order approach. As discussed in §4.2.2 equating drag and gravity-buoyancy forces at steady state, the terminal velocity u_∞ can be written as:

$$u_\infty = \frac{g\left(\zeta - 1\right)\rho_l d^2}{18\mu_l} = \frac{u_D}{18}\frac{\rho_l u_D d}{\mu_l} = \frac{u_D Re_D}{18}. \tag{D.3}$$

The stress τ at the wall can then be connected to u_{sl} via the slip length ℓ_{sl} as follows:

$$u_{sl} \sim \frac{\ell_{sl}\tau}{\mu_l}. \tag{D.4}$$

A simplified expression of the total SH sphere surface can then be written as:

$$S_{SH} = 4\pi\left(r + \lambda\right)^2 \approx 4\pi r^2 \left(1 + \frac{2\lambda}{r}\right), \tag{D.5}$$

where the last step was made possible since $d \gg \lambda$ (r being the sphere radius). The wall stress τ can thus be approximated as:

$$\tau \sim \frac{F_{SH}}{S_{SH}} \approx \frac{6\pi\mu_l\left(r - \ell_{sl}\right)u_\infty}{4\pi r^2\left(1 + \frac{2\lambda}{r}\right)} \approx \frac{3\mu_l u_\infty}{2r^2}\left(r - \ell_{sl}\right)\left(1 - \frac{2\lambda}{r}\right) \approx \frac{3}{2}\mu_l u_\infty \frac{r - \left(2\lambda + \ell_{sl}\right)}{r^2}, \tag{D.6}$$

where F_{SH} is the total Stokes' force acting on the SH sphere. The substitution of Eq. D.6 into Eq. D.4 leads to:

$$u_{sl} \approx \frac{3}{2}u_\infty\left(\frac{\ell_{sl}}{r} - \left(\frac{\ell_{sl}}{r}\right)^2 - \frac{2\lambda\ell_{sl}}{r^2}\right) \approx \frac{3}{2}\frac{\ell_{sl}}{r}u_\infty. \tag{D.7}$$

Using Eq. D.3, Eq. D.7 can be finally recast as:

$$u_{sl} \approx u_D \frac{Re_D}{6}\frac{\ell_{sl}}{d}. \tag{D.8}$$

Exploiting Eq. D.7, the non-dimensional Marangoni time in the convection dominated case can thus be estimated as:

$$t_M^{(c)\star} = \frac{t_M^{(c)}}{t_D} \sim \frac{\pi d\sqrt{\left(\zeta - 1\right)g}}{u_{sl}\sqrt{d}} \approx \frac{6\pi}{Re_D}\frac{d}{\ell_{sl}} \approx \mathcal{O}\left(10^1\right). \tag{D.9}$$

It is therefore found that under the investigated conditions the Marangoni time $t_M^{(c)}$ is thus at least one order of magnitude larger than the characteristic drop time t_D. In other words, the timescale of the sphere fall is so short in comparison to the surfactant convective timescale that the build up of eventual Maragoni forces cannot be an inhibiting mechanism for SH drag mitigation, at least when the dynamics of the contaminant is dictated by its convective flux.

D.2.2 Adsorption Dominated Dynamics

The second investigated limit case is related to the chemical affinity between the interface and the bulk. The characteristic timescale of this mechanism is $t_M^{(a)} = (\kappa_a C_b)^{-1}$, where κ_a is the adsorption coefficient and C_b is the bulk concentration. The value of κ_a varies strongly from surfactant to surfactant. For instance, Peaudecerf *et al.* (2017) varied the values of κ_a by seven orders of magnitude to tune the chemical affinity between surfactant and interface. In this experimental work, the type of impurities and their respective characteristic coefficients are unknown. Assuming a contamination by sodium dodecyl sulfate, a bulk concentration as low as 10^{-3} mol m^{-3} (well below the critical value reported in Peaudecerf *et al.* (2017) for this type of surfactant) would be enough for $t_M^{(a)\star} \sim \mathcal{O}(10^0)$. Obviously, such a low level of contamination is unavoidable, which implies that, in the experiments performed in this study, the dynamics of the Marangoni effects is dominated by adsorption kinetics rather than interfacial convection. However, in the next paragraph it is shown that in the performed tests the magnitude of the Marangoni effects is likely to be negligible.

D.2.3 Marangoni Stress Magnitude

It is important to keep in mind that, independently of the dynamics, the relative magnitude of the Marangoni force with respect to the viscous force is characterized by the Marangoni number (Cuenot *et al.* 1997):

$$Ma = \frac{R_G T \Gamma_m}{\mu_l u_\infty}, \tag{D.10}$$

with R_G the perfect gas constant, T the room temperature and Γ_m the interfacial concentration at equilibrium. In this study, using $T = 293$ K, $\Gamma_m = 10^{-5}$ mol m^{-2} (retrieved from the cited references), it is found that $Ma \leq 0.25$, which is way smaller in comparison to values set by Palaparthi *et al.* (2006) ($\mathcal{O}(10^1)$), Cuenot *et al.* (1997) ($\mathcal{O}(10^2 - 10^3)$) and Peaudecerf *et al.* (2017) ($\mathcal{O}(10^3 - 10^6)$).

Altogether, this scaling analysis shows that even if the contaminant dynamics cannot be neglected, the estimated Marangoni number is sufficiently small that the force induced by surface tension gradients are expected to have a very limited impact on the hydrodynamic performance.

D.3 Viscous Based Mechanism

An additional mechanism can be related to the ability of the external flow to transfer momentum across the air-liquid interface. In fact, McHale *et al.* (2011) analytically estimated an optimal thickness of an ideal non-deformable air layer over a smooth solid sphere, inside which the external flow was able to generate an internal circulation. This resulted into estimated drag reduction up to 30 %. However, Gruncell *et al.* (2013) further developed the concept via numerical simulations on a less idealised air layer representation. When baffles where inserted into the model, resulting into closed cavities on the rough sphere surface, the drag reducing ability was strongly decreased due to a limitation of the circulation inside the air layer. In the framework of the existence of an

air motion inside the air layer, the additional drag resulting from the interaction of the air with the roughness elements on the SH surface should be estimated. This diffusion-based mechanism acts inside the air layer and can be described by the characteristic time $t_P \sim \frac{\lambda^2}{\nu_a}$, which connects the height of the air layer λ with the air kinematic viscosity ν_a. The comparison with the drop time thus yields:

$$t_P^\star = \frac{t_P}{t_D} \sim \frac{\lambda^2 u_D}{\nu_a d} \approx \left(\frac{\lambda}{d}\right)^2 \frac{\nu_l}{\nu_a} Re_D \approx \mathcal{O}\left(10^{-2}\right), \tag{D.11}$$

where $\nu_l = \frac{\mu_l}{\rho_l}$ is the glycerine kinematic viscosity. The proposed mechanism thus shows a characteristic time sufficiently small with respect to the executed tests timescale to possibly result into significant effects on the drag. This laminar diffusion mechanism occurring inside the air layer may erode momentum because of the interaction of the moving air with the rough surface elements of the sphere. Therefore, in §6.1.2 the analogy with a flow across a porous medium is proposed.

Appendix E

Regularly Distributed Roughness Elements

One possible perspective to further develop the present work was addressed in the framework of falling spheres in the low Reynolds number regime (see §6.1). In fact, in §6.1.2 a porous medium model able to take into account the effect of the interaction between the moving air inside the air layer and the roughness elements on the SH surface was proposed. In detail, the key role of the roughness elements alignment was highlighted via the introduction of the tortuosity Θ.

The role of the roughness alignment with respect to the incoming flow is not a new concept, at least for channel and plates flows. The preliminary numerical works on the effects on the flow of longitudinal and transverse grooves without air layer (Luchini *et al.* 1991; Jiménez 1994) were followed by numerical and experimental studies focusing on the role of slip parallel and perpendicular to the incoming velocity (Lauga & Stone 2003; Min & Kim 2004; Choi *et al.* 2006). Generally, roughness elements (or slip length) aligned with the flow were found to maximise the slip with respect to the perpendicular counterpart. The physical reason was identified in the promotion of the growth of the strength of near-wall streamwise vortices by spanwise slip, which resulted into increased drag.

Following all these indications, this paragraph describes the manufacturing technique developed to produce SH coatings where the relative position of the roughness elements was controlled. Then, the preliminary results in terms on terminal drag are presented.

E.1 Manufacturing Procedure

A 3D-printing technique was implemented to produce a SH coating with regularly distributed cylindrical pillars. The approach consisted in printing two hemispherical shells to be fitted around a reference stainless steel sphere of the corresponding diameter. The fundamental steps of the design of the Computer-Aided Design (CAD) model are resumed in Fig. E.1 and are here listed for the sake of completeness:

1. once established the diameter of the reference sphere to be fitted in, an arc of the same radius (augmented of approximetely 3% to allow the introduction of the sphere) was sketched. A second arc to produce a coating thickness of 1 mm was then drawn. This thickness was chosen to avoid coating cracks during manufacturing and testing. The two arcs were connected by two straight lines and a revolution around the vertical axis was performed to produce a smooth hemispherical shell (see Fig. E.1(a));

2. a rectangle of the suited width and height was sketched on the vertical plane passing through the hemisphere vertical axis. A revolution around the former was then performed to create a cylindrical pillar of the desired diameter and height (see Fig. E.1(b));

3. a repetition of the pillar along the hemisphere curve was executed, by imposing the desired angular spacing whose value was *a priori* calculated by setting the total number of wanted elements (see Fig. E.1(c));

4. a circular repetition of each pillar around the hemisphere vertical axis was performed by calculating *a priori* the number of elements at each level (see Fig. E.1(d));

5. the operation was executed per each pillars row until when the hemisphere was completely covered (see Fig. E.1(e)).

Once the CAD model was completed, a *.stl* file was saved and imported into the 3D printer software *PreForm*. A Form 2 3D-printer (see Tab. E.1 for some technical specifications) by *formlabs* was used. This printer is based on the SLA (stereolithography) technique and requires, after the printing process, a washing step to eliminate the exceeding liquid resin residuals and a final curing under ultraviolet light. A transparent resin with the best possible spatial resolution of 25 µm was employed. The SH coating manufacturing procedure described in §3.2.1 was then followed to give the SH properties to the printed rough surface. The steps concerning the embedding of an intermediate powder layer were skipped, thus mimicking the procedure of the SH-NAR coating. The produced prototype consisted in an empty shell with an internal diameter equal to 10.25 mm, to be fitted around a $d = 10\,\mathrm{mm}$ reference NC stainless steel sphere. The NC sphere was glued to the shells internal wall and the two hemispheres were joined together. The resulting external diameter of the assembled SH sphere was therefore $d \approx 12.4\,\mathrm{mm}$. This is due to the 1 mm thickness of the shell wall and to the height of the cylindrical pillars, which was designed in order for the resulting coated surface to show $\lambda \approx 75\,\mu\mathrm{m}$. The sphere mass measurement allowed for the estimation of the assembled SH sphere density, which showed a value $\rho_s \approx 4600\,\mathrm{kg\,m^{-3}}$, intermediate between $\rho \approx 7700\,\mathrm{kg\,m^{-3}}$ of stainless steel and $\rho \approx 1100\,\mathrm{kg\,m^{-3}}$ of the cured resin. The CAD model was therefore designed to have a final SH coating whose elements spacing and size was comparable with the randomly distributed SH coatings characterised in §3.3. The regular imposed geometry also allowed an estimation at the SH sphere surface of the void fraction with respect to the total volume, providing a porosity $\phi \approx 0.65$. A comparison between the CAD model and the SH coated hemisphere is shown in Fig. E.1(f), which testifies the satisfactory alignment of the printed roughness elements with respect to the designed model.

Technology	Stereolithography (SLA)
Laser type	Class 1, 250 mW, 405 nm
Laser spot size (FWHM), [µm]	140
Build volume, [$\mathrm{mm^3}$]	145×145×175
Layer resolution, [µm]	25 - 100

Table E.1 – Some fundamental technical specifications of the Form 2 3D-printer.

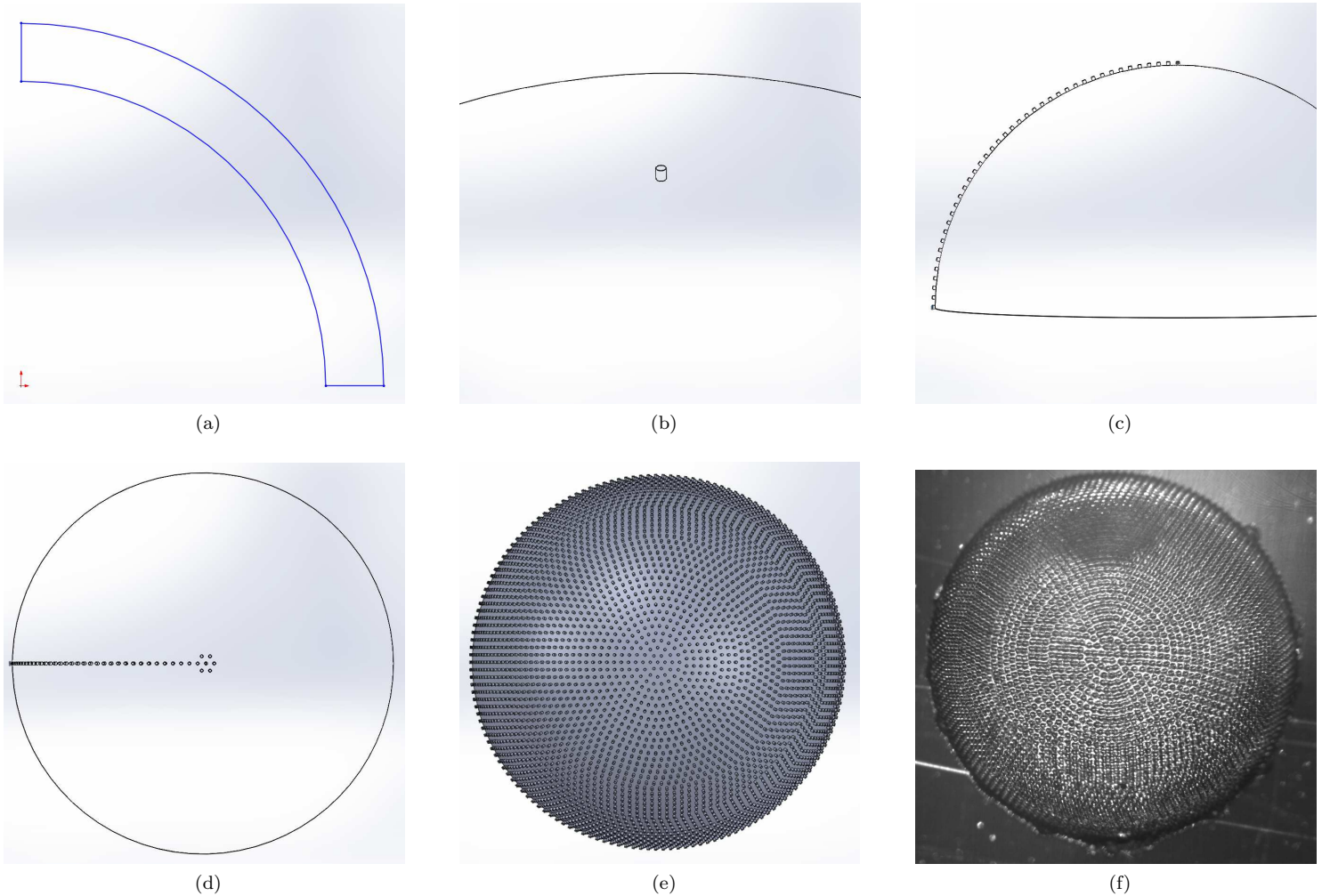

Figure E.1 – Regularly distributed roughness elements SH coating. (a), sketch of the section used to create the hemisphere with a revolution around the vertical axis. (b), cylindrical pillar on the top of the hemisphere. (c), repetition of the pillar along the hemisphere curve. (d), circular repetition of each pillar around the vertical axis. (e), complete CAD model of the hemisphere. (f), 3D-printed prototype after the application of the SH coating (shell with an internal diameter $d = 10.25\,\text{mm}$, to be fitted around a $d = 10\,\text{mm}$ reference stainless steel sphere).

E.2 Terminal Drag

The ΔC_D values shown in Fig. 6.7 in §6.1.1 are here reported in Fig. E.2, including the single available result for the regularly distributed SH coating sphere. The larger d and smaller ρ_s of the regularly distributed SH coating sphere resulted into a $Re_\infty \approx 2.4 \times 10^{-1}$ comparable to the $d = 10\,\text{mm}$ spheres. Interestingly, a slight drag reduction improvement with respect to the randomly distributed SH coatings is noted, with an average $\Delta C_D \approx -12\,\%$. Even if the errorbars are large enough to cover the gap between the experimental average values, this preliminary result confirms the potential role of the roughness distribution in influencing the drag variations in the analysed low Reynolds number regime. This result at least qualitatively supports the findings of the porous medium model developed in §6.1.2. In fact, aligned roughness elements likely result into $\Theta \approx 1$, thus minimising the detrimental roughness contribution to ΔC_D in Eq. 6.15. Finally, injecting in the ΔC_D expression in Eq. 6.15 the properties of glycerine and of the 3D printed sphere, together with the measured drag variation, the estimation $\frac{\ell_{sl}}{\lambda} \sim 10^1$ is obtained, which lies within the slip length order of magnitude prediction provided by Vinogradova (1999), thus further validating the meaningfulness of the proposed model.

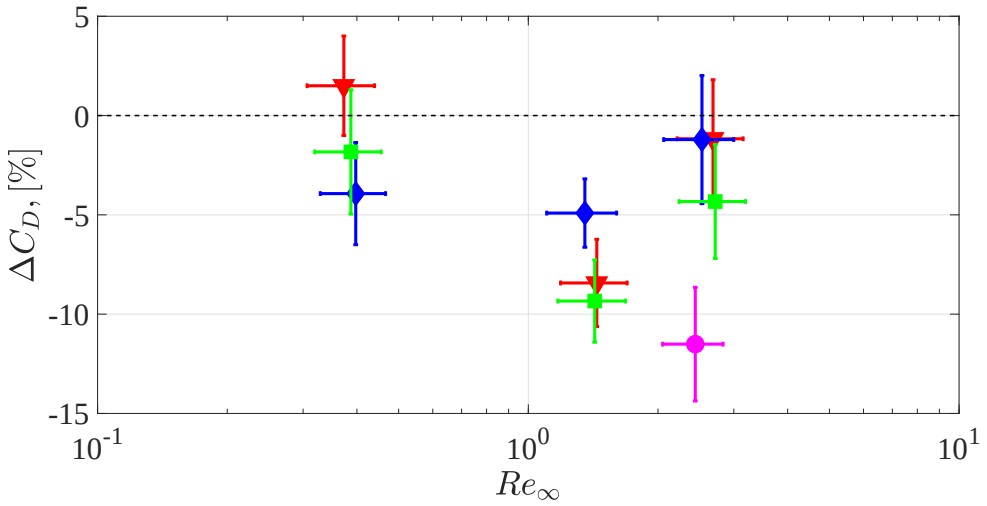

Figure E.2 – Variation of the terminal drag coefficient as a function of the terminal Reynolds number Re_∞ for the glycerine tests. ▼, SH-NAR. ♦, SH-220. ■, SH-80. ●, regularly distributed SH coating. The error bars represent the 95% confidence level. (- - -), reference value $\Delta C_D = 0$ indicating the limit between drag increase ($\Delta C_D > 0$) and decrease ($\Delta C_D < 0$) (see the ΔC_D definition in Eq. 6.3).

Appendix F

Intermediate Reynolds Number: Velocity Profiles and Terminal Drag

In this Appendix, the vertical and transversal velocity profiles of all the analysed spheres and mixtures are reported, together with an estimation of the terminal drag variation of SH coatings with respect to the reference. The following symbols and colors are used: ●, reference NC. ▼, SH-NAR. ⧫, SH-220. ■, SH-80.

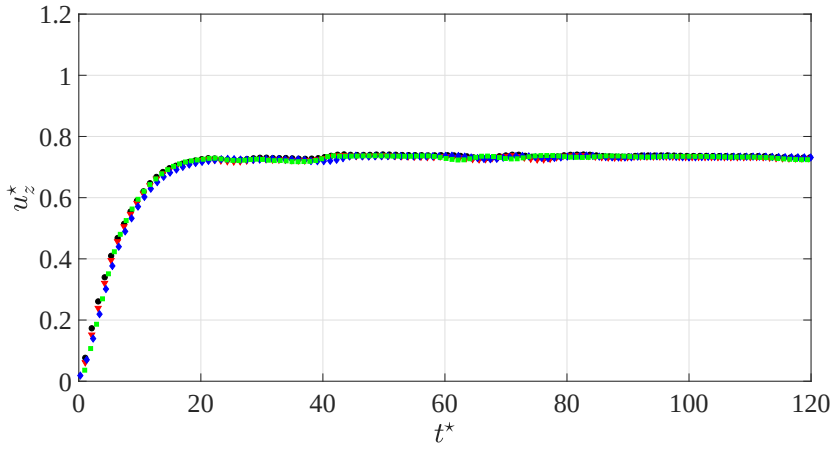

(a)

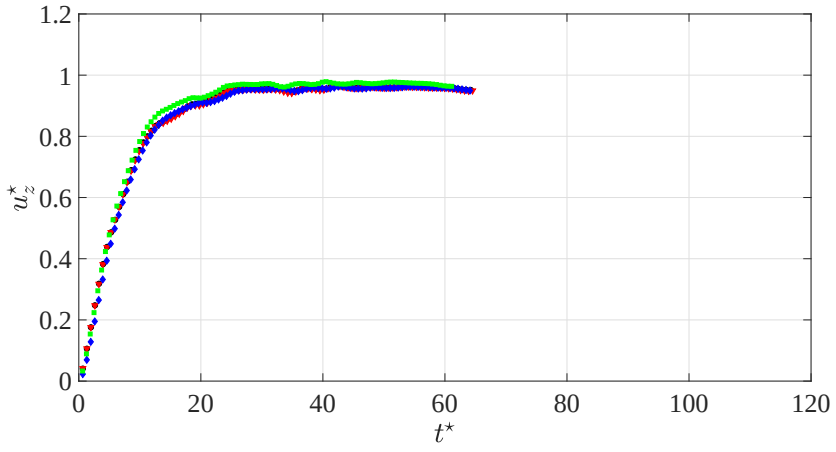

(b)

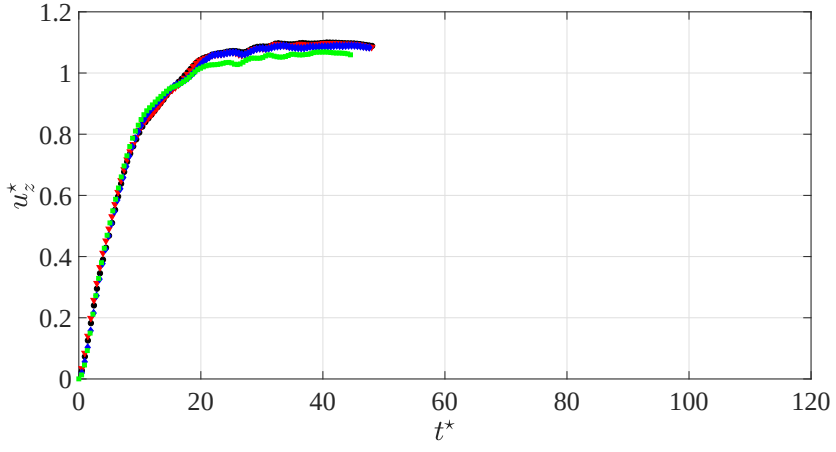

(c)

Figure F.1 – Instantaneous vertical velocity $u_z^\star$ for all the analysed coatings in the mixture $W020\_G080$. (a), $d = 5\,\mathrm{mm}$. (b), $d = 8\,\mathrm{mm}$. (c), $d = 10\,\mathrm{mm}$. The visible oscillations are due to small residual air bubbles attached to the tank lateral walls, which did not interact with the sphere falling at the centre of the tank cross-section but negatively affected the images post-processing.

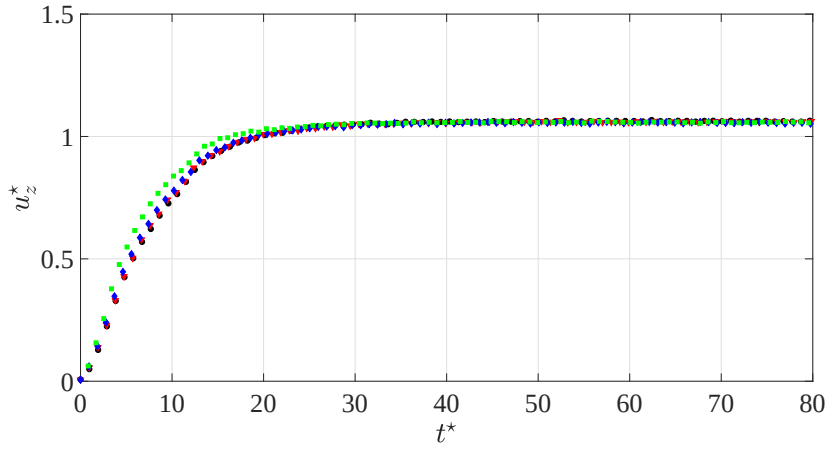

(a)

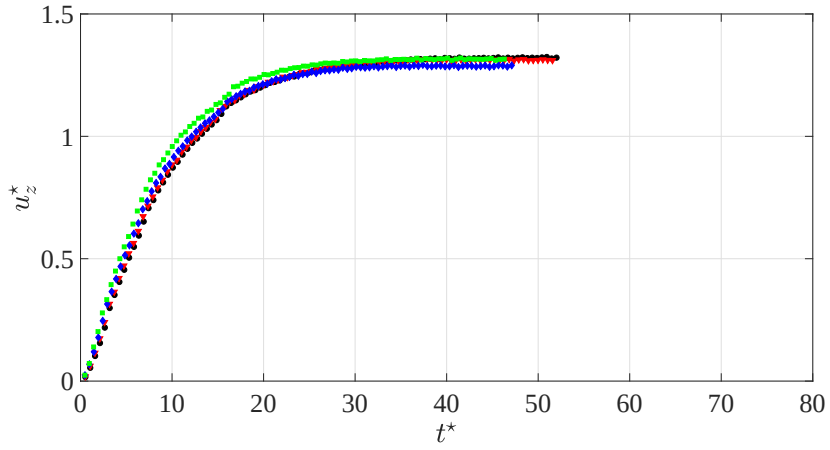

(b)

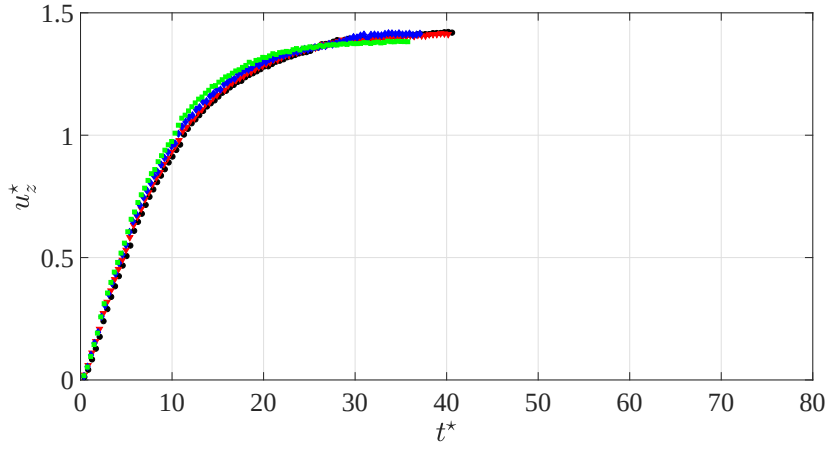

(c)

Figure F.2 – Instantaneous vertical velocity $u_z^\star$ for all the analysed coatings in the mixture $W030\_G070$. (a), $d = 5\,\text{mm}$. (b), $d = 8\,\text{mm}$. (c), $d = 10\,\text{mm}$.

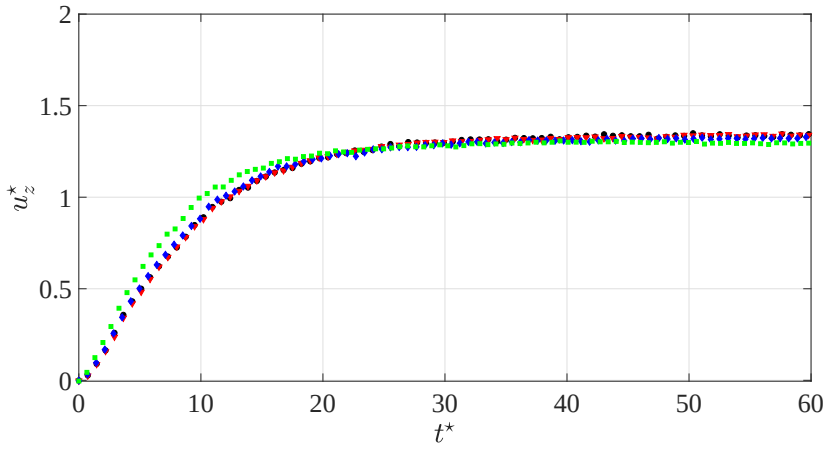

(a)

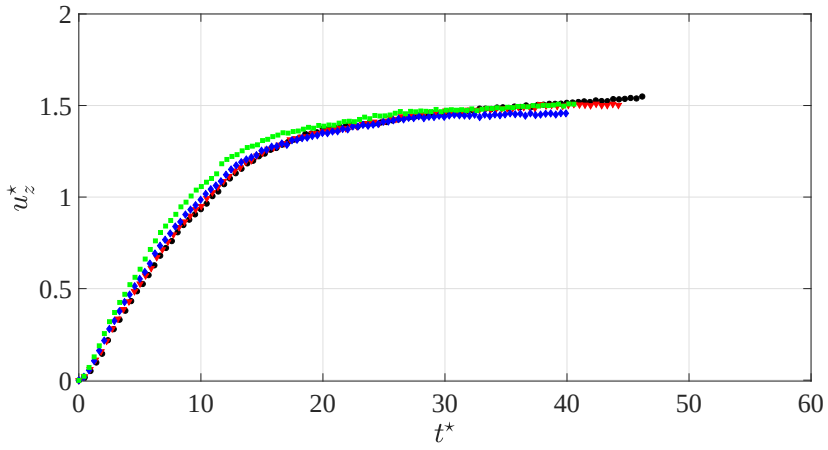

(b)

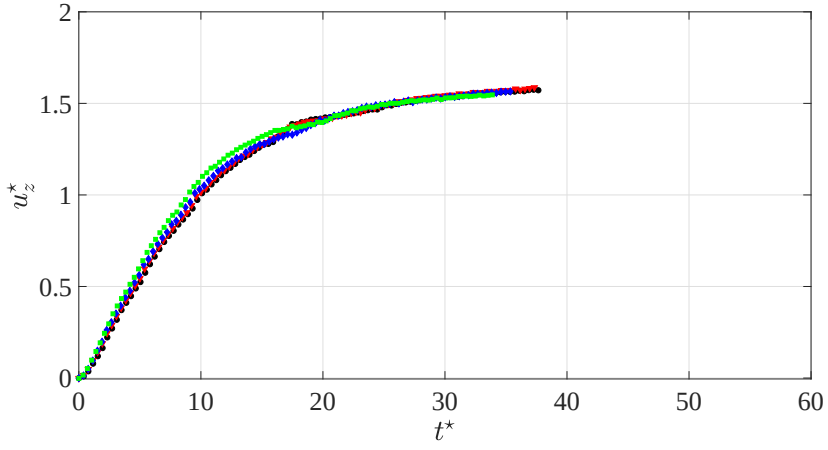

(c)

Figure F.3 – Instantaneous vertical velocity $u_z^\star$ for all the analysed coatings in the mixture $W040\_G060$. (a), $d = 5\,\text{mm}$. (b), $d = 8\,\text{mm}$. (c), $d = 10\,\text{mm}$.

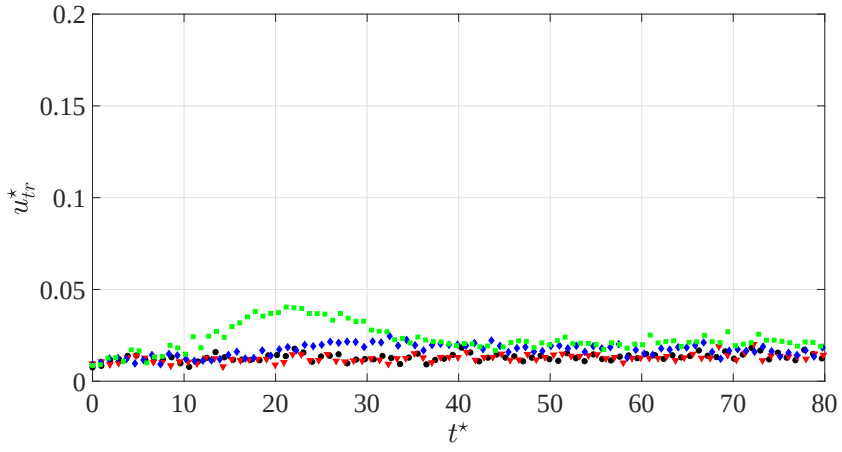

(a)

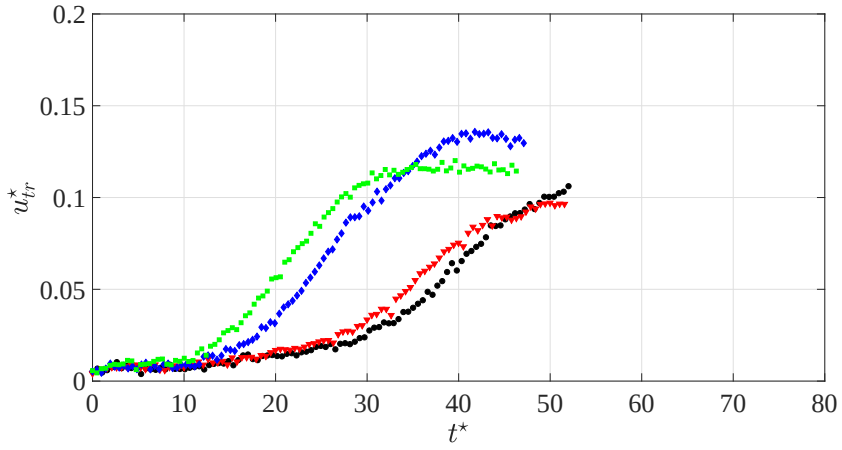

(b)

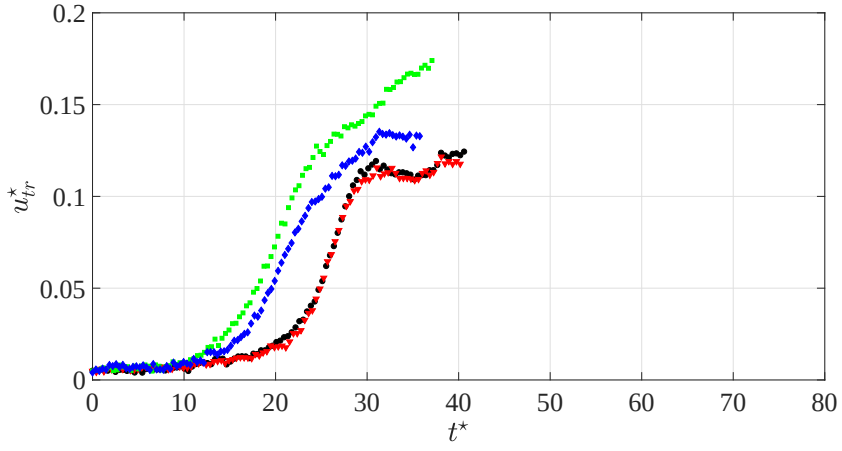

(c)

Figure F.4 – Instantaneous transversal velocity $u^\star_{tr}$ for all the analysed coatings in the mixture $W030\_G070$. (a), $d = 5\,\text{mm}$. (b), $d = 8\,\text{mm}$. (c), $d = 10\,\text{mm}$.

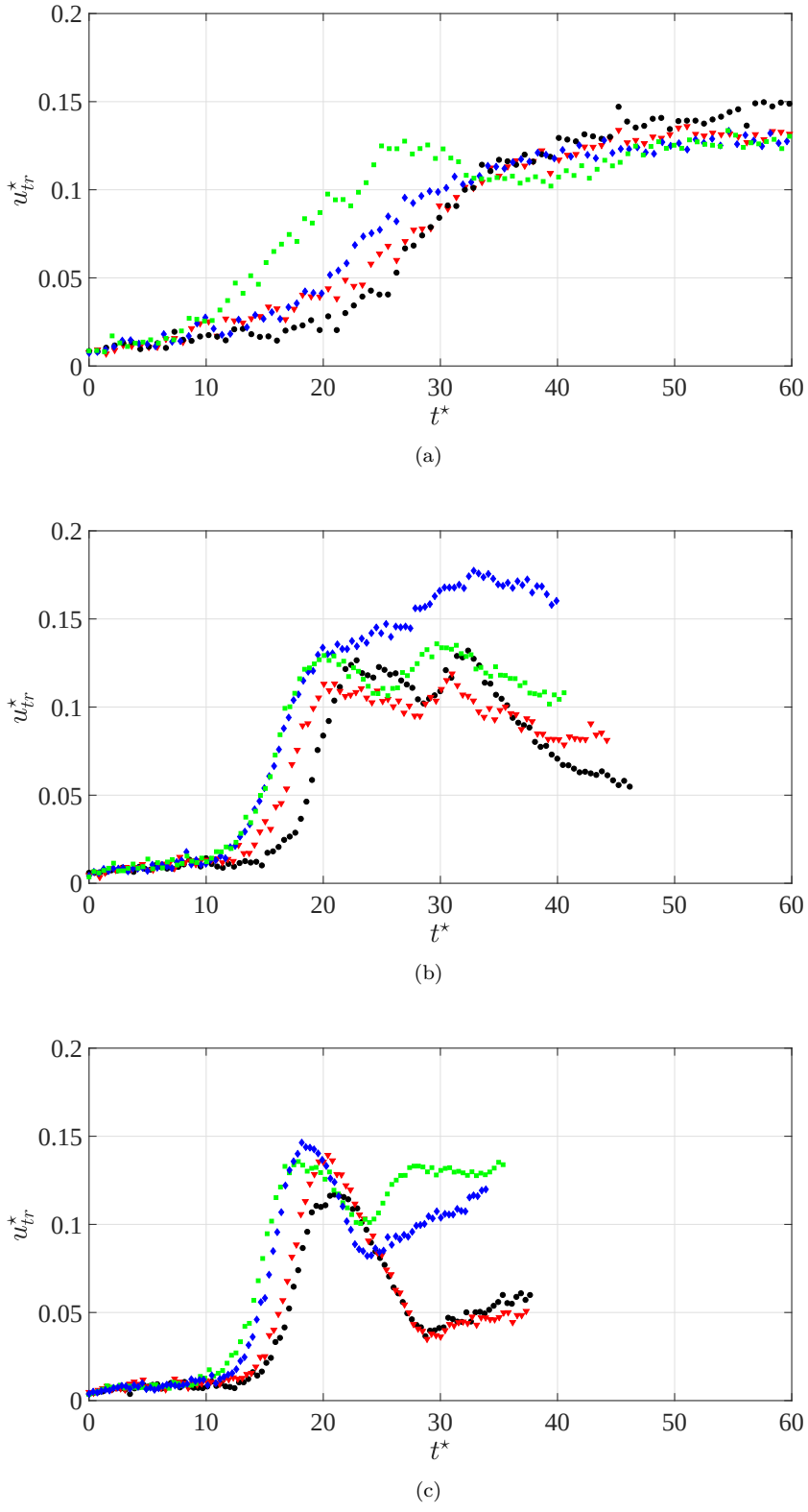

Figure F.5 – Instantaneous transversal velocity $u^\star_{tr}$ for all the analysed coatings in the mixture $W040\_G060$. (a), $d = 5\,\text{mm}$. (b), $d = 8\,\text{mm}$. (c), $d = 10\,\text{mm}$.

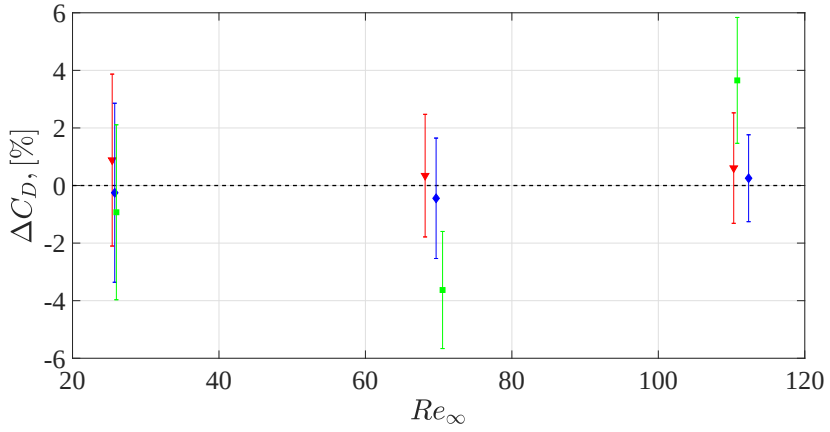

(a)

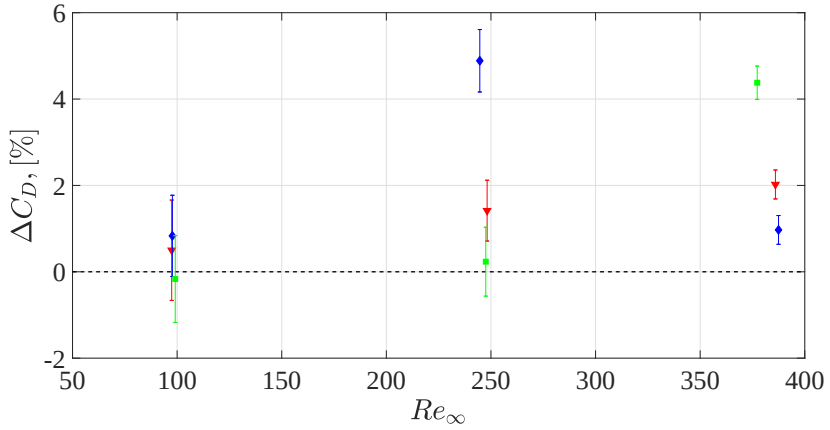

(b)

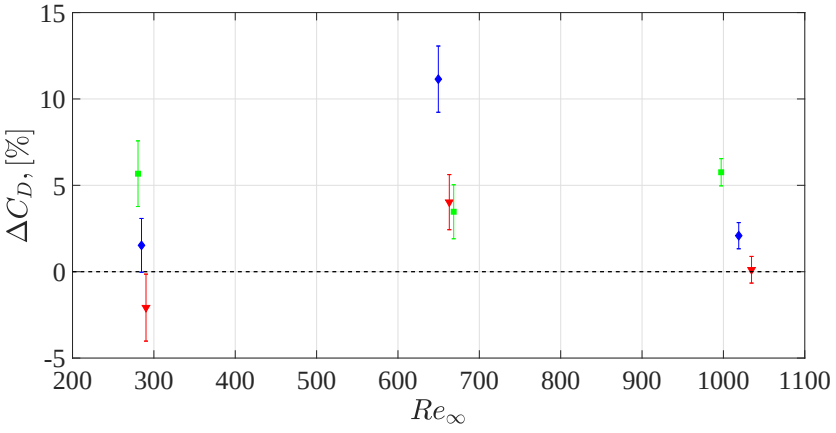

(c)

Figure F.6 – Terminal drag variation ΔC_D for all the analysed coatings and mixtures. (a), $W020\_G080$. (b), $W030\_G070$. (c), $W040\_G060$. The error bars represent the 95% confidence level. (- - -), reference value $\Delta C_D = 0$ indicating the limit between drag increase ($\Delta C_D > 0$) and decrease ($\Delta C_D < 0$) (see the ΔC_D definition in Eq. 6.3).

Appendix G

Numerical Approach Details

In this study, the Finite Volume Method (FVM) was chosen as the approach to numerically solve the incompressible flow introduced in §7.2. No attempt is here performed to provide a comprehensive discussion on the topic. An exhaustive and useful review of the subject, with also some tips on the practical implementation in OpenFOAM® (indicated as OF hereinafter), is available in Moukalled *et al.* (2016). The main steps of the technique, resumed by the schematic in Fig. G.1 (adapted from Moukalled *et al.* 2016), are the following:

1. the starting point is the definition of the analysed physical domain with the modelling of the corresponding computational domain and of the governing equations describing the physical phenomenon;
2. the computational domain is then discretised via the generation of the mesh;
3. the governing partial differential equations are discretised into an equivalent system of algebraic equations defined over the elements of the generated mesh;
4. the system of algebraic equations has to be solved with a suitable algorithm in order to estimate the desired unknown fields.

G.1 OpenFOAM Implementation

A schematic of the general structure of an OF case is reported in Fig. G.2. In the following, a brief discussion of the content of each folder and file is provided, in the attempt to connect the practical implementation of the code with the FVM steps highlighted above.

G.1.1 The *constant* Folder

The *constant* folder must contain a sub-folder named *polyMesh* where all mesh information is stored. In the present study, the mesh generation was performed via the software Pointwise® (indicated by PW hereinafter), release V18.0 (Pointwise 2019). Then, the mesh was imported into OF, which was used for the execution of the simulations. A structured mesh made of hexahedra cells was employed. The approach consisted in defining in MATLAB® the line describing the wavy lower wall of the channel. The generated *.dat* file containing the points coordinates was then imported into PW and a 2D channel geometry was constructed starting from the lower wall line (see Fig. G.3(a)). The reference system origin was always placed on the intersection between

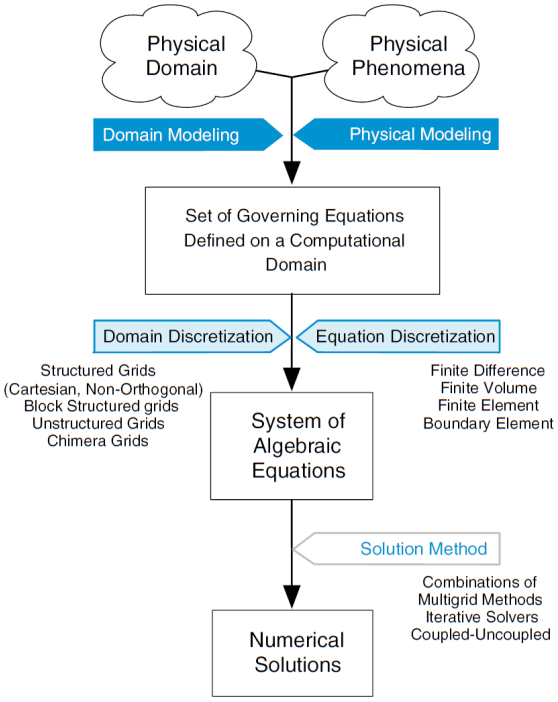

Figure G.1 – Schematic of the numerical discretisation procedure (adapted from Moukalled *et al.* 2016). The physical domain and the governing equations are modelled and discretised into the corresponding computational domain and set of algebraic equations. The latter is then solved with a suitable algorithm to estimate the desired unknown fields.

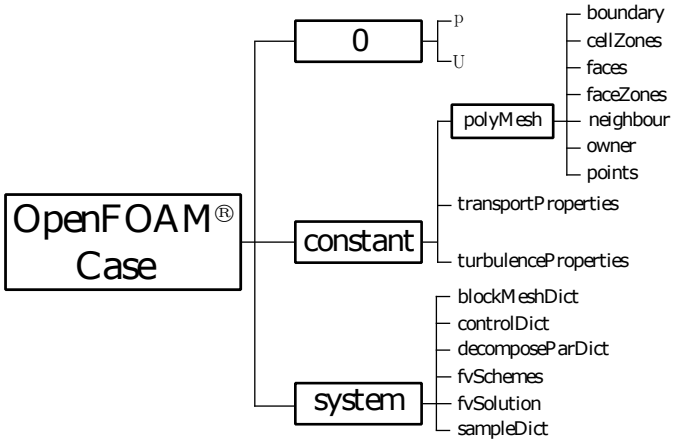

Figure G.2 – Schematic of the required general structure of an OpenFOAM® case. The folders are indicated by the black rectangles. Inside each folder, the main files that are mandatory for the execution of the code are listed. Other files may be included, depending on the particular application.

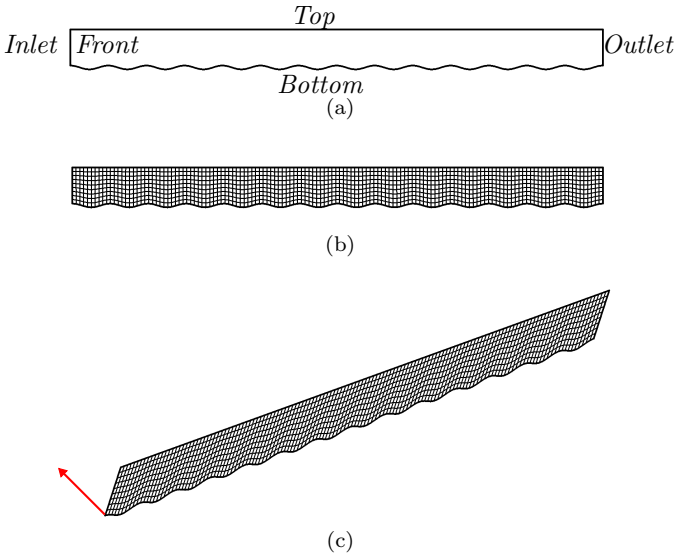

Figure G.3 – Mesh generation procedure with the software Pointwise®. (a), the 2D channel geometry is constructed over the lower wall line imported from MATLAB®. (b), the number of grid points is set for all the segments and the 2D grid is assembled. (c), the extrusion in the spanwise direction (indicated by the red arrow) is performed to generate the 3D channel geometry. The dimensions and the grid displayed are for illustration purpose only. The boundaries names are indicated next to the corresponding patch. The extrusion in (c) allows for the generation of the *Back* patch from the corresponding *Front* patch.

the lower wall average height and the inlet segment on the left of the channel geometry. Once defined the number of grid points in each created segment, the planar grid could be assembled (see Fig. G.3(b)). The extrusion in the spanwise direction was performed, creating the final 3D channel geometry (see Fig. G.3(c)). The procedure was completed by defining suitable names and boundary conditions for all the boundary faces of the mesh. Finally, the mesh was exported in a format compatible with OF, generating the files to be copied into the *constant/polyMesh* folder (see Fig. G.2). These files are mandatory for the execution of the numerical simulation since they contain all the information of the generated mesh. The described procedure makes unnecessary the use of the *blockMeshDict* dictionary inside the *system* folder, where *blockMesh* is a tool to build the mesh directly inside OF. The PW approach was preferred since the *blockMesh* utility becomes cumbersome for non-trivial geometries. Due to the importance of the boundary patches definition, the code from the OF *boundary* file is reported in Fig. G.4. For each patch the number of faces and the starting face are indicated by the corresponding value. The *empty* entry in the *Back* and *Front* patches is set when a 2D simulation is run, avoiding resolution in the spanwise direction. The *Bottom* and *Top* patches are indicated as *wall*. A generic *patch* type is indicated for the *Outlet*, which will be specified later in the boundary conditions definition. The *Inlet* is defined as *mappedPatch* since the velocity field is mapped from another region (*region0*) of the computational domain. The mapping region is specified by the *offset* entry. In this study, a uniform streamwise *offset* was imposed in order to map the *Outlet* velocity field and re-inject it in the *Inlet*. The sampling is performed by searching for the cell closest to the *offset*.

An overview of the performed simulations was provided in §7.2.2 and a resume of the investigated parameters was shown in Tab. 7.2. Here attention is focused on the mesh choice.

```
6
(
    Back
    {
        type empty;
        nFaces Value;
        startFace Value;
    }
    Bottom
    {
        type wall;
        nFaces Value;
        startFace Value;
    }
    Front
    {
        type empty;
        nFaces Value;
        startFace Value;
    }
    Inlet
    {
        type mappedPatch;
        nFaces Value;
        startFace Value;
        sampleMode nearestCell;
        sampleRegion region0;
        samplePatch none;
        offsetMode uniform;
        offset (Value 0 0);
    }
    Outlet
    {
        type patch;
        nFaces Value;
        startFace Value;
    }
    Top
    {
        type wall;
        nFaces Value;
        startFace Value;
    }
)
```

Figure G.4 – Syntax of the OF file *boundary* defining the boundary patches properties.

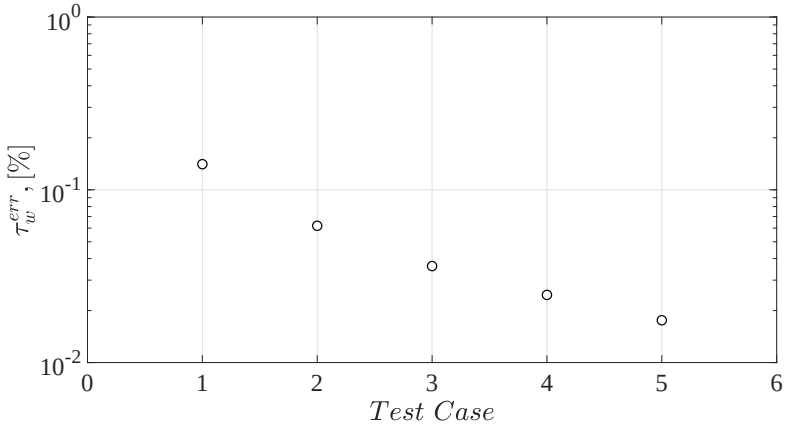

Figure G.5 – Variation of the relative error on the estimation of the wall shear stress τ_w with respect to the analytical solution (Eq. 7.9(c)) in the case of a flat, no-slip lower wall ($\frac{\Lambda}{h} = 1$ and $\frac{\delta}{h} = 0$) at $Re_m = 1000$. The grid points per each wave are increased by 50 % on each consecutive test. The mesh selected for the execution of the 2D laminar numerical simulations corresponds to the test case #2.

The starting point to establish the number of grid points per each wall wave in the streamwise direction was the analysis of turbulent channel flow DNS available in literature (Maaß & Schumann 1996; Errico & Stalio 2015). Since laminar conditions are considered, half of the points imposed in the cited works was taken as first guess. Then, the value was properly reduced and increased to analyse its influence on the control parameter $\tau_w^{err} = \frac{\tau_w^{OF} - \tau_w^{Eq.\ 7.9(c)}}{\tau_w^{Eq.\ 7.9(c)}}$, as shown in Fig. G.5. Since the relative error was 0.06 % in the tested case #2, the latter was considered satisfactory for the execution of all the simulations. In fact, an increase of 50 % of the points per each wave (test case #3) determined a relative amelioration of the evaluated result of only 0.02 %, with a six-fold increase of the execution time. Since $\frac{\Lambda}{h} = 1$, the same number of grid points was set along the channel height h. A representation of the obtained mesh typology in the region close to the wall undulation was reported in Fig. 7.5.

A preliminary control of the mesh quality could be performed via the *Examine* utility in PW. Once copied the mesh files, the OF utility *checkMesh* was exploited to further verify the mesh. In detail, some control parameters were checked in the generated grid in order to limit the possible mesh-induced errors (see e.g. Jasak 1996, Chapter 3). A sufficient mesh resolution assures a correct description of the shape of the solution, with special care in regions where the spatial variation is rapid, e.g. in the near-wall area. In this study, the grid points distribution was uniform in the streamwise and spanwise directions, while a hyperbolic tangent stretching symmetric with respect to the channel centreline (Vinokur 1983) was imposed along the direction $\mathbf{e}_y$. Two indicators connected to the grid stretching are the *smoothness* (SM) and the *aspect ratio* (AR) of the grid cells, which are schematically shown in Fig. G.6(a). The smoothness describes the transition in size between two contiguous cells, and as a rule of thumb must be kept lower than 20 %. The aspect ratio is the ratio between the longest and shortest dimension of a cell, and the maximum tolerated value in the *checkMesh* utility is equal to 1000. However, such a large value should be avoided because of effects on the gradients evaluation. High AR values could be tolerated when the solution has a strong variation in one of the directions, as in the case of a boundary layer. The analysis of practical real geometries usually results into non-orthogonal

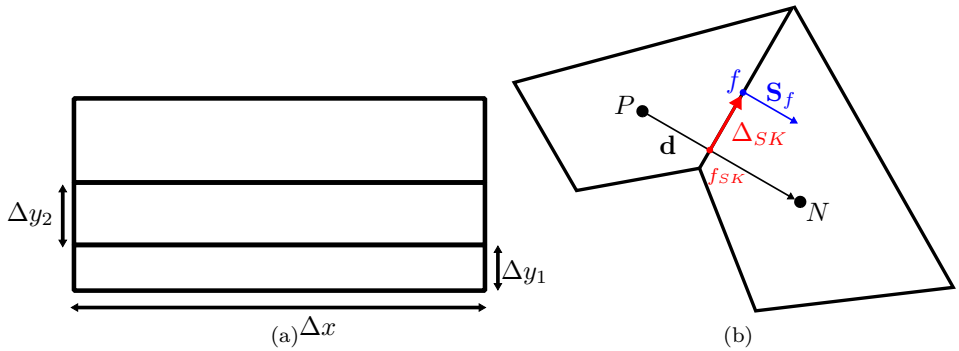

Figure G.6 – Definition of the parameters to analyse the quality of the generated mesh. (a), smoothness SM defined as the ratio between the size Δy_2 and Δy_1 of two contiguous cells. Aspect ratio AR defined as the ratio between the longest Δx and shortest Δy_1 dimension of a cell. (b), skewness SK defined as the ratio between the magnitude of the deviation Δ_{SK} of the vector $\mathbf{d}$ connecting the centroids P and N from the face centre f and the $\mathbf{d}$ magnitude. The intersection between $\mathbf{d}$ and the face is indicated by f_{SK}, while $\mathbf{S}_f$ indicates the face vector.

	$\frac{\Lambda}{h}$	$\frac{\delta}{h}$	AR	SM	$N_\perp^{max}$, [°]	$N_\perp^{ave}$, [°]	SK
FW	1	0	1.55	1.06	0	0	0
LD	1	0.05	1.60	1.06	17.2	7.4	0.2
ID	1	0.075	1.63	1.05	24.9	10.9	0.3
HD	1	0.10	1.70	1.05	31.8	14.2	0.4

Table G.1 – Quality parameters of the generated meshes, whose lower wall is described by the law introduced in Eq. 7.5, Λ being the wavelength and δ the wave amplitude. FW identifies the flat wall, LD the low deformation, ID the intermediate deformation and HD the high deformation. AR indicates the maximum aspect ratio, SM the maximum smoothness, $N_\perp^{max}$ the maximum non-orthogonality, $N_\perp^{ave}$ the average non-orthogonality, SK the maximum skewness. All the meshes were constituted of $1143 \times 39 \times 2$ grid points in the $(\mathbf{e}_x, \mathbf{e}_y, \mathbf{e}_z)$ directions, respectively.

and skewed meshes. The maximum non-orthogonality ($N_\perp$) accepted value is 70°, however high values should be avoided due to the strong influence on the evaluation of the diffusive terms. Finally, a schematic of the mesh *skewness* (SK) is reported in Fig. G.6(b), where it is defined as the deviation of the vector connecting the two centroids with respect to the face centre. Its value should be kept low since it affects both the convective and diffusive terms (the maximum accepted value in OF is equal to 4). A resume of the main quality parameters of the generated meshes is reported in Tab. G.1. The maximum AR deriving from the imposed wall stretching kept to values lower or equal to 1.7 in all cases, with a corresponding smoothness limited to 1.06 in the worst case. The effect of the wall undulation is detectable in the non-orthogonality parameter, with a maximum value reaching $\approx 32°$ in the HD case. This value, which could be improved by a modification of the mesh nature (e.g. a mesh transformation in the near-wall region), was considered acceptable since as a rule of thumb in the OF community values as high as 40° are considered *low*. Moreover, the corresponding average value was limited to $\approx 14°$ in the HD case, underlying that the highest non-orthogonal cells are limited to a small region of the channel. Finally, the SK reached an highest 0.4 value in the HD case.

```
dimensions [0 2 −2 0 0 0 0];

internalField uniform 0;

boundaryField
{
    Bottom
    {
        type zeroGradient;
    }
    Top
    {
        type zeroGradient;
    }
    Front
    {
        type empty;
    }
    Back
    {
        type empty;
    }
    Inlet
    {
        type zeroGradient;
    }
    Outlet
    {
        type fixedValue;
        value uniform 0;
    }
}
```

(a)

```
dimensions [0 1 −1 0 0 0 0];

internalField uniform (Ub 0 0);

boundaryField
{
    Bottom
    {
        type fixedValue;
        value uniform (0 0 0);
    }
    Top
    {
        type fixedValue;
        value uniform (0 0 0);
    }
    Front
    {
        type empty;
    }
    Back
    {
        type empty;
    }
    Inlet
    {
        type mapped;
        value uniform (Ub 0 0);
        interpolationScheme cell;
        setAverage true;
        average (Ub 0 0);
    }
    Outlet
    {
        type inletOutlet;
        inletValue uniform (0 0 0);
        value uniform (0 0 0);
    }
}
```

(b)

Figure G.7 – Syntax of the files defining the initial and boundary conditions for the considered variables. (a), pressure p. (b), velocity U.

Two more files are mandatory inside the *constant* folder (see Fig. G.2). The *transportProperties* file is used to specify the analysed fluid typology. In the present work a Newtonian model was selected and the kinematic viscosity $\nu_l = 10^{-6}$ m^2 s^{-1} valid for pure water at 20 °C was prescribed. The *turbulenceProperties* file specifies the typology of turbulence modelling used. This file is therefore fundamental when RANS (Reynolds-Averaged Navier-Stokes) and LES (Large-Eddy Simulations) approaches are applied. In this work, no turbulence modelling was selected.

G.1.2 The *0* Folder

The *0* folder contains the initial and boundary conditions of the tested case. One file for each variable that is going to be solved must be created. In this study, the pressure p and velocity U (the upper case follows the OF nomenclature) files were therefore generated. Two examples of the codes are shown in Fig. G.7. In both cases, the dimension of the field is firstly set. In the OF syntax, the second and third positions in the *dimensions* entry indicate the length and time units, respectively. The p variable is thus expressed in m^2 s^{-2}, being normalised by the

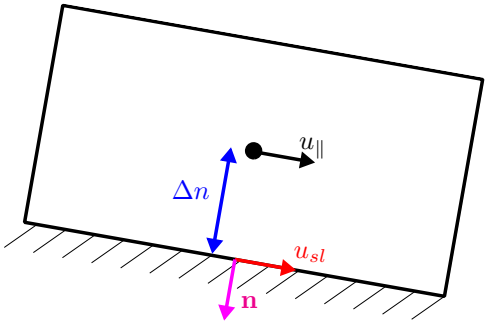

Figure G.8 – Schematic of the discretised Navier boundary condition that connects the slip velocity u_{sl} at the boundary face to the velocity component $u_{\parallel}$ parallel to the wall at the centroid of the first cell (at a distance Δn from the wall) via the slip length ℓ_{sl}. The vector $\mathbf{n}$ indicates the normal direction.

incompressible fluid density ρ_l. The canonical velocity $\mathrm{m\,s^{-1}}$ unit is considered. Then, the initial field is initialised: in both cases a *uniform* field is prescribed, with the value of the normalised pressure set to 0 and an imposed initial bulk velocity u_b along the streamwise direction. The u_b was set depending on the flow characteristics of the simulation, in order for the initial field to be quite close to the calculated field at the following timesteps. The last part of the code deals with the definition of the boundary conditions, which are practical implementations of the Dirichlet and Neumann typologies. The names of the boundary patch are user-defined and in this study were set during the mesh generation procedure in PW (see §G.1.1). The *Inlet* and *Outlet* patches were defined in the streamwise direction, while the *Front* and *Back* patches were considered in the spanwise direction. The *Top* and *Bottom* patches indicate the upper and lower walls, respectively. In the p file in Fig. G.7(a) the *zeroGradient* boundary condition is imposed at the inlet and on both walls, meaning that the normal gradient to the boundary face is set to 0. In the case of laminar simulations where a 2D configuration is considered, the *Front* and *Back* patches are set to *empty* in order to avoid the resolution in the spanwise direction. Finally, the pressure at the outlet of the channel is imposed to be equal to the reference zero value via the *fixedValue* entry. The introduced patches names are retrieved in the U file in Fig. G.7(b), where the same treatment of the p case for the *Front* and *Back* patches is shown. In the reported case, a no-slip boundary condition is imposed over both the lower and upper walls, prescribing a zero value for all the velocity components. When needed, the partial slip boundary condition was imposed on the *Bottom* patch via a discretised version of the Navier slip condition introduced in §7.1, which is depicted in the scheme in Fig. G.8. The simplified expression in Eq. 7.3 can be reformulated in a discretised version as:

$$u_{sl} = \ell_{sl}\frac{u_{\parallel} - u_{sl}}{\Delta n} = \left(1 - \frac{1}{1 + \frac{\ell_{sl}}{\Delta n}}\right) u_{\parallel} = (1 - F)\, u_{\parallel}, \tag{G.1}$$

where the slip velocity u_{sl} at the wall patch is connected to the component of the velocity parallel to the wall $u_{\parallel}$ at the centroid of the first cell via the *valueFraction* F. The latter depends on the relative size of the desired slip length ℓ_{sl} with respect to the distance Δn of the first centroid from the wall. The partial slip at the wall is thus imposed by prescribing the *a priori* calculated F value inside the boundary condition of the *Bottom* patch in Fig. G.7(b). The accuracy of the imposed Navier slip condition was a posteriori verified by investigating the velocity field in

the proximity of the lower wall of the channel. The u_{sl} and $u_{\parallel}$ values were retrieved by the calculated velocity field. Moreover, the distance Δn from the centroid to the wall was evaluated via the known coordinates of the points of the analysed mesh. The slip length ℓ_{sl} could thus be estimated by reversing Eq. G.1. The percentage error between the slip length retrieved after the simulation run and the imposed ℓ_{sl} value was $\mathcal{O}(10^{-1})$ for the whole range of investigated slip lengths. The *Outlet* boundary condition for U was of *inletOutlet* type, which imposes a *zeroGradient* condition when there is outflow and switches to a *fixedValue* (with a prescribed value *inletValue*) when there is inflow. The switch represents only a robust implementation of the *zeroGradient* condition in the case of particular applications where inflow could occur, which is not the case in the present work. The *value* entry is a dummy parameter to initialise the values at the beginning of the simulation. Finally, the *Inlet* patch was handled with a *mapped* boundary condition able to assure the bulk velocity that sustains the flow. The initial u_b value is prescribed over the whole *Inlet* patch, then in the following timesteps the velocity field is mapped from the *Outlet* patch (see Fig. G.4) and re-injected into the *Inlet*. The mapped field is rescaled via the *setAverage* entry, if necessary, in order to assure a constant bulk value equal to u_b along the whole simulation.

G.1.3 The *system* Folder

The *system* folder includes files necessary to handle the pre-run phase (e.g. the *blockMeshDict* already cited), to control the simulation and the post-processing phase. In detail, the *decomposeParDict* is the dictionary to be used when a parallel run on distributed processors is desired. The utility, which is run via the command *decomposePar*, is based on the number of specified sub-domains and on the chosen method to decompose the mesh and the initial data. The default version of the parallel run is based on the *openMPI* implementation of the Message Passing Interface library, which allows computation both on local machines and on clusters. The post-processing phase can be handled via the *sampleDict* dictionary. This utility must be run after the end of the simulation and allows for the sampling of the calculated fields over prescribed lines and surfaces inside the computational domain.

The *controlDict* file (see Fig. G.9) specifies all the parameters handling the input/output procedure at each timestep of the simulation. The sequence of mandatory entries controls the starting and ending time (*startFrom* and *stopAt*) and the timestep (*deltaT*). Optional inputs control the writing of data to the disk with the corresponding format and precision. The *runTimeModifiable* entry allows for a modification of the dictionary during the run. The *residuals* function stores the residuals and allows for their monitoring during and after the run. The mandatory *application* entry at the beginning of the dictionary sets the algorithm used for the analysed problem resolution, which is described in the following.

In the case of the incompressible Navier-Stokes and continuity equations (see Eqs. 7.6), an explicit pressure equation is missing. One possible strategy is the achievement of a relation governing the pressure behaviour from the manipulation of the available equations, in order to get an estimation of both the pressure and velocity fields. The method selected in this work is thus the *pisoFoam* solver, which is the OF implementation of the PISO algorithm (Pressure-Implicit with Splitting of Operators) developed by Issa (1985). The main steps of the solving procedure are briefly discussed in the following, using the notation proposed by Issa (1985) in his original work. Adopting a finite-difference formulation (for easiness of writing) and a Backward Euler (BE) method, the discretised incompressible continuity and momentum equations can be

```
application solver;

startFrom startTime;

startTime 0;

stopAt endTime;

endTime Value;

deltaT Value;

writeControl timeStep;

writeInterval Value;

purgeWrite Value;

writeFormat ascii;

writePrecision 12;

writeCompression off;

timeFormat general;

timePrecision Value;

runTimeModifiable true;

functions
{
#includeFunc residuals
}
```

Figure G.9 – Syntax of the file *controlDict* controlling the simulation parameters.

written in the indicial notation as follows:

$$\nabla_i u_i^{n+1} = 0, \tag{G.2a}$$

$$\frac{\rho}{\Delta t}\left(u_i^{n+1} - u_i^n\right) = H\left(u_i^{n+1}\right) - \nabla_i p^{n+1} + S_i, \tag{G.2b}$$

where n and $n+1$ are two consecutive timesteps separated by Δt, H is an operator including the convection and diffusive terms and S represents the source term. By taking the divergence of Eq. G.2(b) and exploiting Eq. G.2(a), the following implicit Poisson-type equation governing the pressure field is obtained:

$$\nabla_i^2 p^{n+1} = \nabla_i H\left(u_i^{n+1}\right) + \nabla_i S_i + \frac{\rho}{\Delta t}\nabla_i u_i^n. \tag{G.3}$$

The pressure and velocity fields are therefore estimated by a proper resolution of the coupled Eqs. G.2(b) and G.3. The originality of the PISO method lies in the handling of the coupling of these two equations, which is split in a series of predictor-corrector steps. The practical resolution of the system of equations is then performed via standard methods, e.g. Conjugate Gradient.

Predictor Step. Assuming that the solutions u_i^n and p^n at timestep n are available, a first intermediate velocity field u_i^* can be evaluated via Eq. G.2(b):

$$\frac{\rho}{\Delta t}\left(u_i^* - u_i^n\right) = H\left(u_i^*\right) - \nabla_i p^n + S_i. \tag{G.4}$$

Since the old solution p^n is used, the evaluated u_i^* will not be divergence-free.

First Corrector Step. New velocity u_i^{**} and pressure p^* fields are searched such that:

$$\nabla_i u_i^{**} = 0. \tag{G.5}$$

For this, the momentum equations can be written in terms of the intermediate fields:

$$\frac{\rho}{\Delta t}\left(u_i^{**} - u_i^n\right) = H\left(u_i^*\right) - \nabla_i p^* + S_i. \tag{G.6}$$

By taking the divergence of Eq. G.6 and exploiting Eq. G.5, a Poisson-type equation for the intermediate pressure field is obtained:

$$\nabla_i^2 p^* = \nabla_i H\left(u_i^*\right) + \nabla_i S_i + \frac{\rho}{\Delta t}\nabla_i u_i^n, \tag{G.7}$$

which is solvable since every term on the right hand side is known. The evaluated p^* field can then be injected into Eq. G.6 to evaluate u_i^{**}, which will be divergence-free.

Second Corrector Step. The same approach of the first corrector step is repeated to evaluate new velocity u_i^{***} and pressure p^{**} fields. Issa (1985) showed that the second corrector step is necessary to assure a satisfactory accuracy of the approximations $u_i^{***} \approx u_i^{n+1}$ and $p^{**} \approx p^{n+1}$. Other corrector steps could be added to the procedure, however Issa (1985) demonstrated that two corrector steps are sufficient to assure that the errors on the approximated estimation of the new solutions u_i^{n+1} and p^{n+1} are smaller than the errors introduced by the discretisation procedure.

In the *system* folder, the *fvSchemes* file controls all the techniques to be used to perform the FVM discretisation procedure. An example of the code structure is reported in Fig. G.10(a). The *ddtSchemes* specifies the technique to handle the temporal discretisation, where a Crank-Nicolson (CN) scheme with a blending factor $\psi = 0.9$ was selected in this study. The latter is an off-centering coefficient between a second order CN ($\psi = 1$) and a first order BE ($\psi = 0$). Since in practical problems a pure CN could become unstable, the chosen value, which is recommended in the OF community, is a compromise between accuracy and stability. The *gradSchemes* entry dictates the method to evaluate the gradients: in this case, a standard Gaussian integration with linear interpolation from cell centre to face centre is selected. Depending on the implemented code, several divergence terms different one another in nature may appear inside the *divSchemes* entry. For this reason, the *default* method is usually set to *none* and the technique used for each term is specified. In the example, a linear Gaussian scheme is chosen for the term containing the flux of velocity. Since the *laplacianSchemes* influence the evaluation of the diffusive terms, a Gaussian integration corrected for the effects of mesh non-orthogonality can be selected. The *interpolationSchemes* entry sets a linear interpolation as the default method to evaluate the fluxes at the faces, while the *snGradSchemes* indicates the method to evaluate the normal gradients to the face. An *orthogonal* method can be selected for orthogonal meshes, while a non-orthogonal correction can be applied when needed.

The *fvSolution* file, which is reported in Fig. G.10(b) as an example, stores information about the methods to solve the system of algebraic equations obtained via the FVM discretisation procedure. For the variable pressure p, which after discretisation generates a symmetric, positive definite matrix, the PCG (Preconditioned Conjugate Gradient) solver preconditioned via a DIC (Diagonal Incomplete Cholesky) was selected. In transient simulations it is customary to set an absolute tolerance as criterion to stop the iterations. The tolerance value was decreased of one order of magnitude in the final resolution of the pressure equation. For the variable velocity U, which generates after discretisation a non-symmetric matrix, the stabilised PBiCG (Preconditioned Bi-Conjugate Gradient) solver was chosen, preconditioned via a DILU (Diagonal

```
ddtSchemes
{
    default CrankNicolson 0.9;
}
gradSchemes
{
    default Gauss linear;
}
divSchemes
{
    default none;
    div(phi,U) Gauss linear;
        ...
}
laplacianSchemes
{
    default Gauss linear corrected;
}
interpolationSchemes
{
    default linear;
}
snGradSchemes
{
    default corrected;
}
```

(a)

```
solvers
{
    p
    {
        solver PCG;
               preconditioner DIC;
               tolerance 1e-06;
               relTol 0;
    }
    pFinal
    {
        $p;
        tolerance 1e-07;
        relTol 0;
    }
    U
    {
        solver PBiCGStab;
        preconditioner DILU;
        tolerance 1e-08;
        relTol 0;
    }
}
PISO
{
    nCorrectors 2;
    nNonOrthogonalCorrectors Value;
    momentumPredictor yes;
    pRefCell 0;
    pRefValue 0;
}
```

(b)

Figure G.10 – Syntax of the files defining the discretisation schemes and solving techniques. (a), *fvSchemes*. (b), *fvSolution*.

Incomplete LU) method. The absolute tolerance on U can be lower with respect to p since the critical part of the solving algorithm is the pressure equation. Finally, two corrector steps were imposed for the PISO loop, with a number of corrections for non-orthogonality varying depending on mesh quality. The predictor step of the momentum equation was switched on in the shown example. Since in a incompressible case the pressure is relative to a reference value, the latter was set to zero in the cell number zero.

Acknowledgments

This work was supported by the Direction Générale de l'Armement (DGA), Ministère de la Défense, République Française and the Agence Nationale de la Recherche (ANR) through the Investissements d'Avenir program under the Labex CAPRYSSES Project (ANR-11-LABX-0006-01).

A word of thanks to the staff of the GREMI Laboratory, CNRS - Université d'Orléans, for the training on the clean room operations and the related instruments.

A very special thank to Pr. Alessandro Bottaro, Universitá degli Studi di Genova, Scuola Politecnica, Dipartimento di Ingegneria Civile, Chimica e Ambientale, for the high skill in numerical simulations and the availability demonstrated all along my stay in Genova.

Personal Acknowledgments

Now that I freshly defended my thesis I have finally the time (and the energy) to dedicate my brain to one of the most complicated pages of the manuscript. As is peculiar of my personality, I'll avoid long and unnecessary sentences, going directly to the hearth of the matter.

Let me thank first of all my supervisors. My thesis director, Pr. Azeddine Kourta, for the guide that he represented to me all along my PhD, and the ability of seeing the whole picture when I was probably too much focused on the single details. Thanks to my co-advisor, Dr. Nicolas Mazellier. I will never forget the long hours spent together in front of the board trying to push a little farther our knowledge. It was an extremely enriching adventure.

A word of thanks to the members of the ESA team that, everyone with its contribution, shared with me a part of this journey. On the PhD candidates (or now Doctors) side, I want to thank Francesco, who took me under his wing when I first came to Orléans. I always appreciated your ability to enter into the depths of tough questions and to wisely advice me (which is probably a result of your advanced age...). Sophie, we spent together almost two years in that office, thank you for your availability and kindness. Thanks to Roshan and Wassim, who last joined our team: it was a pleasure for me to introduce you to the dynamics of our laboratory. Finally, a huge word of thanks to Stefano, especially for being there during the rough months of the redaction of this manuscript. Thank you for your help, advice, support and availability.
Thanks to Stéphane Loyer and Yahia Haidous, without your help I would never have been able to conceive, build and operate the experimental rigs.
Thanks also to Sylvie, for the help with administrative stuff.
Thanks to Annie and Sandrine, your politeness and smiles always impressed me.
Finally, thank you Pierre-Yves for having rocked the party during the second half of this adventure. It was a pleasure to share with you formal and more unofficial moments. I wish you the best for the following of your career.

Thanks to the PhD students of other teams, in particular Anthony and Nicolas. Of course, thank you Marco for being there since the old times at Poli in Milano.

Thank you Christian: your support and total availability, which go well beyond a simple advisor-student relationship, made this PhD possible. I'll never forget the good times of my MSc thesis in Milano.

Thanks to my old friends from high school: Carlos, Luca, Mattia, Roby, Sonia. A special thank you to Ines, who is always there for a talk over a glass.

Thanks to my athletics team-mates: Bietto, Bione, Euge, Lo and Rigo. And also thank you to coach Ado and coach Grazia.

Infine, grazie alle persone più importanti nella mia vita: Giulia, mamma e papà. Grazie per il vostro supporto che, nonostante la distanza e gli impegni, non manca mai.

TGV Paris-Milano, November 16, 2019

Marco CASTAGNA

Contribution à l'étude et à la modélisation du développement d'une couche limite sur paroi super-hydrophobe : approche couplée expérimentale et numérique

Résumé : Depuis plusieurs années, la popularité des revêtements dits super-hydrophobes (SH) est grandissante dans le secteur industriel. Pour les applications sous-marines, ces matériaux pourraient servir à réduire la traînée hydrodynamique et le bio-encrassement grâce à la présence d'un film d'air piégé au sein des rugosités. Bien que prometteurs à l'échelle du laboratoire, le comportement de ces matériaux en présence d'un écoulement dans des conditions réalistes soulève de nombreuses interrogations. Ce travail de thèse a pour objectif d'apporter une compréhension plus fine des mécanismes physiques pilotant le développement d'une couche limite sur une paroi SH pour une large gamme de régimes. Dans la première partie de ce travail des essais expérimentaux sont réalisés sur des sphères en chute libre pour analyser les effets des revêtements SH. Le montage expérimental est constitué d'un réservoir vertical rempli d'un liquide au repos. Différentes conditions de fonctionnement sont réalisées en utilisant une large gamme de diamètres des sphères et en modifiant les propriétés du liquide. Le code développé pour le post-traitement des vidéos enregistrées permet la reconstruction des efforts hydrodynamiques instantanés s'exerçant sur la sphère en chute libre. Le principal résultat obtenu pointe vers l'interaction de la couche d'air avec l'écoulement. L'intensité de cette interaction varie en fonction du régime de chute considéré. Les instabilités de trajectoire et du sillage sont amplifiées par les revêtements SH quand la perturbation hydrodynamique du sillage sur l'interface air-liquide est suffisamment importante. Pour analyser finement les mécanismes en proche paroi, la simulation numérique d'un écoulement dans un canal est considérée. La surface SH est modélisée par une condition de Navier de glissement pariétal, alors que la déformation de l'interface air-liquide est modélisée en imposant une déformation fixe de la paroi du canal. Comparativement à une surface plane SH, la paroi ainsi déformée conduit à une diminution de l'effet bénéfique du glissement pariétal.

Mots clés : Super-Hydrophobe, Sillage de Corps Épais, Instabilité, Tension Superficielle

Contribution to the study and the modelling of the development of a boundary layer over a super-hydrophobic surface: experimental and numerical coupled approach

Abstract: Super-hydrophobic (SH) surfaces are becoming more and more attractive for industrial purposes. In the framework of submarine applications, these coatings could help in reducing the hydrodynamic drag and bio-fouling thanks to the presence of an air layer encapsulated within the surface roughness. Even if promising results were obtained at laboratory scale, the extrapolation of SH coatings performance towards more realistic conditions is not straightforward. The objective of this work was to achieve a better understanding of the physical mechanisms underlying the development of a boundary layer on a SH surface over a wide range of operating conditions. In the first part of this work, SH coatings effects over bluff-bodies are studied via experiments on free falling spheres. The experimental set-up designed for the execution of the free falling tests consists in a vertical tank filled with a liquid at rest. The tests operating conditions are varied by analysing a large range of sphere diameters and liquid properties. The codes implemented to post-process the recorded videos allow for the reconstruction of the instantaneous hydrodynamic loads acting on the falling sphere. The main output of the experimental tests is the interaction between the flow around the falling sphere and the air-liquid interface. The strength of this interaction varies as a function of the analysed falling regime. Path and wake instabilities are promoted by SH coatings when the wake hydrodynamic perturbation on the air-liquid interface is strong enough. To achieve further insight on the near-wall phenomena, the experimental tests are coupled with a numerical approach in a channel configuration. The SH surface is modelled via a Navier partial slip condition, whereas the air-liquid interface deformation is modelled by prescribing a fixed deformed channel wall. The wall deformation is always found to reduce the beneficial slip effects with respect to an ideal flat SH surface.

Keywords: Super-Hydrophobic, Bluff-Body Wake, Instability, Surface Tension

Laboratoire PRISME
8 Rue Léonard de Vinci
45072 Orléans, France